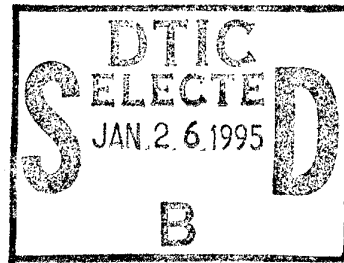


AGARD

ADVISORY GROUP FOR AEROSPACE RESEARCH & DEVELOPMENT

7 RUE ANCELLE, 92200 NEUILLY-SUR-SEINE, FRANCE

"DTIC USERS ONLY"



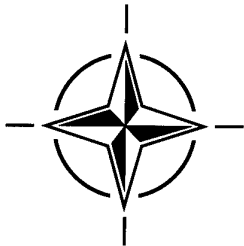
AGARD LECTURE SERIES TCP 02/LS198

Mathematical Models of Gas Turbine Engines and their Components

(Les modèles mathématiques des turbomoteurs et de leurs organes)

This publication was prepared at the request of the Propulsion and Energetics Panel of AGARD and under the sponsorship of the Technology Cooperation Programme (NACC/PfP) and will be presented on 7-8 December 1994 in Cleveland, USA, 12-13 December 1994 in Wessling, Germany, and 15-16 December 1994 in Paris, France.

19950125 001



NORTH ATLANTIC TREATY ORGANIZATION

The Mission of AGARD

According to its Charter, the mission of AGARD is to bring together the leading personalities of the NATO nations in the fields of science and technology relating to aerospace for the following purposes:

- Recommending effective ways for the member nations to use their research and development capabilities for the common benefit of the NATO community;
- Providing scientific and technical advice and assistance to the Military Committee in the field of aerospace research and development (with particular regard to its military application);
- Continuously stimulating advances in the aerospace sciences relevant to strengthening the common defence posture;
- Improving the co-operation among member nations in aerospace research and development;
- Exchange of scientific and technical information;
- Providing assistance to member nations for the purpose of increasing their scientific and technical potential;
- Rendering scientific and technical assistance, as requested, to other NATO bodies and to member nations in connection with research and development problems in the aerospace field.

The highest authority within AGARD is the National Delegates Board consisting of officially appointed senior representatives from each member nation. The mission of AGARD is carried out through the Panels which are composed of experts appointed by the National Delegates, the Consultant and Exchange Programme and the Aerospace Applications Studies Programme. The results of AGARD work are reported to the member nations and the NATO Authorities through the AGARD series of publications of which this is one.

Participation in AGARD activities is by invitation only and is normally limited to citizens of the NATO nations.

The content of this publication has been reproduced directly from material supplied by AGARD or the authors.

Published December 1994

Copyright © AGARD 1994
All Rights Reserved

ISBN 92-836-1008-3



Printed by Canada Communication Group
45 Sacré-Cœur Blvd., Hull (Québec), Canada K1A 0S7

Abstract

This Lecture Series will present and discuss the scientific problems of modern mathematical simulation of gas turbine engines and their components.

Some peculiarities of complex multicomponent and multidisciplinary models for whole flow passages of bypass gas turbine engines, core, multistage compressors and turbines, and other engine components will be studied.

Solutions of steady and unsteady problems are given using high efficiency monotone numerical methods and the theoretical bases of these methods are presented.

Many practical results of aerodynamic and thermostress simulations for engine components are shown. These results are compared widely with experimental data for accurate verification of developing computational codes.

This Lecture Series, endorsed by the Propulsion and Energetics Panel of AGARD, has been implemented by the Technology Cooperation Programme.

Abrégé

Ce cycle de conférences présente et expose les problèmes scientifiques posés par les modèles mathématiques des turbomoteurs et de leurs organes.

La conférence étudiera certaines particularités des modèles complexes multicomposants et multidisciplinaires de toute la partie de l'écoulement des moteurs à turbine, des modèles de compresseur à plusieurs étages, de turbines à plusieurs étages et d'autres composants.

Les solutions des problèmes stationnaires et instationnaires, qui sont obtenues à l'aide des méthodes numériques monotoniques et les bases théoriques de ses méthodes sont présentées.

Bon nombre de résultats de simulations aérodynamiques et de contraintes thermiques des moteurs et des composants sont présentés. Ces résultats sont comparés avec des données expérimentales pour la vérification des codes numériques développés.

Ce cycle de conférences est présenté dans le cadre du Programme de Coopération Technologique (NACC/PfP), sous l'égide du Panel de Propulsion et d'Énergétique de l'AGARD.

Accession For	
NTIS GRA&I	<input type="checkbox"/>
DTIC TAB	<input checked="" type="checkbox"/>
Unannounced	<input type="checkbox"/>
Justification _____	
By _____	
Distribution _____	
Availability Codes	
Dist	Avail and/or Special
12	

List of Authors/Speakers

Lecture Series Director: Prof. Mikhail J. IVANOV
CIAM
Aviamotornay St. 2
111250 Moscow
Russia

Dr. Vladislav G. KRUPA
CIAM
Aviamotornay St. 2
111250 Moscow
Russia

Dr. Ravil Z. NIGMATULLIN
CIAM
Aviamotornay St. 2
111250 Moscow
Russia

Dr. Valerey K. KOSTEGE
CIAM
Aviamotornay St. 2
111250 Moscow
Russia

List of Authors

Mr. V.A. Khalturin
CIAM
Aviamotornay St. 2
111250 Moscow
Russia

Mr. V.G. Sundurin
CIAM
Aviamotornay St. 2
111250 Moscow
Russia

Contents

	Page
Abstract/Abrégé	iii
List of Authors/Speakers	iv
Introduction and Overview by M. Ja. IVANOV	1
On the CFD Monotone High Accuracy Methods by M. Ja. IVANOV V. G. KRUPA R. Z. NIGMATULLIN	2
Solution of Navier-Stokes Equations Using High Accuracy Monotone Schemes by V. G. KRUPA M. Ja. IVANOV	3
The Mathematical Models of Flow Passage for Gas Turbine Engines and their Components by R. Z. NIGMATULLIN M. Ja. IVANOV	4
Simulation of Multidisciplinary Problems for the Thermostress State of Cooled High Temperature Turbines by V. K. KOSTEGE V. A. KHALTURIN V. G. SUNDURIN	5*
Application of Multicomponent Models to Flow Passage Simulation in Multistage Turbomachines and Whole Gas Turbine Engines by R. Z. NIGMATULLIN	6
Simulation of Steady and Unsteady Viscous Flows in Turbomachinery by V. G. KRUPA	7
Application of Multidisciplinary Models to the Cooled Turbine Rotor Design by V. K. KOSTEGE	8*
Verification of Multidisciplinary Models for Turbomachines by V. K. KOSTEGE	9*
Perspective Problems of Gas Turbine Engines Simulation by M. Ja. IVANOV	10

* These papers, written directly in English by their authors, have been reviewed by English speaking specialists in the field. However there may be cases in which the authors' original formulation is not fully represented.

Introduction and Overview

by

Prof. M. Ja. Ivanov,
CIAM (Central Institute of Aviation Motors)
2, Aviamotornaya St.,
Moscow, Russia, 111250

Introduction

Gas turbine engines development is directed at thermodynamic cycle parameters growth and the improvement of efficiency, capability and economy. For example, in advanced aircraft gas turbine engines in comparison with modern engines the specific weight will be 1.5÷2 times less and the efficiency will be 30÷40 % better. The gas temperature in combustion chambers of advanced engines must increase by 300 to 400 degrees. The design of these engines demands detail understanding of physical processes in all components and whole engine. Key fundamental enabling technologies include advances in mathematical modeling and computational tools. The long time and high cost of gas turbine engines design may be decreased essentially by wide application of numerical gas dynamics, heat transfer, strength and burning processes simulations.

Until recently, the use of numerical simulation in gas turbine technology development was limited mainly by analysis and recommendations for improving the characteristics of individual engine components. Examples include isolated blade rows or stages of fans, compressors and turbine, intakes, nozzles and others. The current level of development and practical application of gas turbine components simulation is presented, for example, in the observed papers [1-5]. Based on this level of achievement, the next phase of mathematical modeling will certainly include simulation of whole gas turbine engines or large multicomponent parts (as example, model of aircraft turbofan total flow passages [6]).

The next development phase will also involve solving closely related multidisciplinary problems for individual components of gas turbine engines. In such problems simulation will include simultaneously aerodynamics, heat-transfer, thermal-stressed, combustion processes, and so forth. Here the typical problem may be the thermal-stressed state of a high temperature turbine rotor, where the external viscous flow near blades, the internal cooling air flow into blades, thermal and stressed state of blades are solved simultaneously [7].

An examination of the current state of fluid dynamics computational methods may reveal trends for

the immediate future in this field. The present move seems to be toward a transition to monotone conservative high order accuracy methods for integration of Euler and Navier-Stokes equations, which describe ideal and viscous gas flows. As a typical example, we can indicate AGARD Lecture Series No.140 [8], which contains 3D computational techniques applied to internal flows in propulsion systems up to the middle 1980s. There were widely used numerical schemes of non high order of accuracy (the first and the second orders). The second order accuracy methods give oscillated solutions in regions of great parameter gradients. In present the Lecture Series only monotone high order accuracy methods are a lied to solutions of internal flow problems in propulsion systems.

Foundation for the theory of the monotone difference schemes were laid down by the Russian scientist S. K. Godunov in the late 1950s and the first stage of their development was presented in monograph [9]. Lately the term "TVD schemes" (Total Variation Diminition schemes) has been used to designate the monotone difference schemes. In the next lecture we present a more strict class of following methods, which satisfy additional conditions [5]. Highly accurate conservative difference methods now form the basis for constructing many effective algorithms and codes that solve practical internal and external aerodynamic problems.

In order to determine the advantages and shortcomings of the computational algorithms and codes being developed, it is necessary to test their serviceability and make careful comparisons with experimental data using standard model problems. Such verification must accompany any publication of numerical results and codes. Below we'll present this verification for all developing computational techniques.

Another factor affecting numerical simulation is the progress and widespread use of high efficient supercomputers. Until recently computational techniques development was constructed mainly by the availability of the efficient computational tools that, as a rule, are concentrated in large scientific research centers that grant only limited access. But the growing availability of highly efficient minicomputers, as well as personal computers and work stations with the latest

personal computers and work stations with the latest RISC processors, allows us to consider new possibilities in the development and application of numerical simulation without the need for resorting to supercomputers centers.

The achieved progress of numerical simulation and computer development allows to consider the mathematical modeling of gas turbine engines from the new positions. The gas turbine engine simulation gets on initial stage to obtain the large information for engine performances on steady and transient regimes. The steady regimes simulation includes thermodynamics cycle calculations, the equilibrium running line prediction, the flow passage design and the definition of thrust-economic, mass and cost characteristics. The transient regimes simulation includes the definition of times and performances of unsteady process (start, acceleration, throw off and oth.) by given regulation laws. The depth and completeness of gas turbine engine components presentation and interaction define the level of corresponded mathematical model. Conditionally the followed gas turbine simulation levels (table 1) can be defined.

The zero level corresponds to description of engine parameters and performances with help of tables, formal approximations and statistic dependencies. This level presents interest only for problems, where gas turbine engines have been included as one of subsystem for more complex system (for example, for performance investigation of whole aircraft).

The first level corresponds to 1D description of connections between engine components and engine geometry with help of integral balances of mass flows, powers, etc. Here it's worth to differ steady and unsteady models. Steady models of the first level simulation were presented in monographs [10,11] and papers [12,13]. Simple unsteady models of the first level were described also in papers [12,13]. More accurate unsteady models based on Euler equations with turbomachines presentations as active and passive whirl discs were considered in papers [14-16].

The second level corresponds to 2D description of the connections between engine components and engine flow passage. A few models must be defined in more details. One of them is the flow passage model on S_2 surface (as the traditional turbomachinery definition). This model bases on unsteady averaged along circular direction 2D Euler equations includes real effects of viscous losses, leakages and a selection of blowing out of cooling air as source terms in the right parts of equations. Another is the flow passage model on S_1 circular surface in various thickness layer, base also on unsteady averaged along radial direction 2D Euler equations with the same real effects. The second level of gas turbine engine simulation included the similar models on S_2 and S_1 surfaces,

The levels of gas turbine engine mathematical models

0 level	tables, formal approximations, statistics	
I level	1D steady models	1D unsteady models
II level	2D - Euler - S_1 with losses	2D - Navier-Stokes - S_1
	2D - Euler - S_2 with losses	2D - Navier-Stokes - S_2
III level	3D - Euler with averaging in axial clearances	3D - Navier-Stokes with averaging in axial clearances
	3D - Euler without any averaging	3D - Navier-Stokes without any averaging

Table 1

averaged along circular and radial direction.

The third level corresponds to 3D description of the connection between engine components and engine flow passage. It bases on the integration of Euler and Navier-Stokes equations. Here there are differed the just more simple models with circular direction averaging on one surface in the middle of axial clearances between neighborhood rows and the most complex full 3D unsteady models.

Detail descriptions of the second and third levels models are presented in this lecture series. It's worth to emphasize, that up to present time the prediction of performances designed gas turbine engines based on the zero or the first levels models and were not very accurate. Therefore some number of experiment engines must be produced for investigating performances before certification and production (this number can be up to 10 and more). Wide using of high levels mathematical model on initial stages of new engine design allows sufficiently to reduce the time and cost of new engine development and, in particular, to reduce the number of experiment engines up to a few (two or three). The high level models must accompany the all life of new engines (included design, certification, serious production, any modification and exploitation).

Central Institute of Aviation Motors (CIAM) has valuable experience and high level scientific staff for solving complex aerodynamics, heat transfer and strength problems for any components of high temperature aircraft gas turbine engines. Wide use of modern computational technologies allows us to get high efficiency of engine components and whole engine.

Overview

The lecture series illustrates the numerical simulation peculiarities, mentioned above in this introduction. The series may be divided conditionally in two parts. The first part (the lectures 2 through 5) has a more theoretical character. It describes the bases of theory for monotone high accuracy CFD methods and formulates some important problems of gas turbine engine process simulation. The second part (the lectures 6 through 10) presents many typical results of solution 2D and 3D gasdynamic and heat transfer problems, connected with gas turbine engine design.

The next lecture (by Prof. M. Ja. Ivanov, Dr. V. G. Krupa and Dr. R. Z. Nigmatullin) presents some important questions of theory for highly accurate monotone CFD methods. There Conditions for definition of monotone, TVD and following difference schemes are considered. Some details for high order of accuracy and implicit scheme's construction are described. At the end of this lecture numerical results illustrate possibilities of applied difference methods.

In the third lecture (Dr. V. G. Krupa and Prof. M. Ja. Ivanov) there a detailed description of developed method for integration 3D Navier-Stokes equations, averaged by Reynolds is presented. Two differential equations turbulence model is used. Some test solutions

of 2D and 3D viscous flow problems are presented for verification of numerical codes.

The fourth lecture (by Dr. R. Z. Nigmatullin and Prof. M. Ja. Ivanov) describes the mathematical models of flow passages for gas turbine engines and its components of various levels. First two-dimensional S_1

and S_2 models are presented and famous features of numerical algorithms are discussed. Then 3D approach with averaging in angular direction in the middle of axial gaps is considered.

In the fifth lecture Dr. V. K. Kostege presents simulation of multidisciplinary problems for thermostress state of high temperature cooled turbines. The steady and unsteady temperature fields are calculated in results of solution conjugate heat-hydraulic tasks for blade (quasi-3D model), for disk (2D model) and whole cooled rotor (3D model). Thermostress problems are solved by Finite Element Method for real complex geometry of turbomachine components.

As mentioned earlier the second part of this Lecture Series presents many practical results of numerical simulation of gas dynamics, heat transfer and stress problems for gas turbine engine design.

Dr. R. Z. Nigmatullin delivers his lecture as a review of the different applications of 2D and 3D model of flow passage's simulation in multistage turbomachines, whole core and other multicomponent problems.

Dr. V. G. Krupa presents the results of viscous turbulent flow simulation in turbomachine components. He emphasizes the treatment of boundary conditions, grid generation and turbulence modeling. Results of 2D and 3D viscous cascade flow and stator -- rotor interaction are presented. Numerical results are widely compared with available experimental data.

Dr. V. K. Kostege will deliver two lectures on a subject of application and verification of the multidisciplinary model of thermostress state for the cooled turbine rotor and stator components. Presented code package allows to carry out cooling system optimization and comparison of alternate cooling systems on design stages of high temperature gas turbine engines.

The last lecture presents the perspective problems of gas turbine engine simulations. Some review of perspective CIAM's researches in aeropropulsion systems is considered. In particular, the Computer Turbojet Test Technology based on aeroengine high 3D level simulation is presented. Some results for a big steam turbine are described. This lecture contents also the conclusion of Lecture Series.

Acknowledgments

The authors are very grateful to Ms. T. V. Weigandt and Mrs. T. S. Ivanova for their invaluable assistance in the preparation of this Lecture Series. We acknowledge Dr. A. P. Tchiaston for his generous help on the special software of numerical results presentation. The supports

software of numerical results presentation. The supports of the heads of Central Institute of Aviation Motors Prof. D. A. Ogorodnikov and Prof. V. A. Sosounov are appreciated. The authors wish to thank Drs. V. P. Pochuev, A. S. Liberson, A. N. Serebriakov and S. V. Senin for their great contributions and comments to the lectures text. Some demonstrated numerical results were obtained by our colleagues Ms. L. V. Terentieva, Mr. A. V. Kozerod, Drs. F. P. Borisov, A. M. Karelin, U. S. Kosolapov, B. I. Kurmanov, V. N. Sakharov, S. V. Rudenko and R. F. Talipov. We have pleasure to thank them for their efforts. Finally, we are obliged also to Mrs. G. A. Barjisheva, Mr. B. O. Muraviev and Ms. M. V. Kostege for their permanent help of typing manuscript.

References

1. Klineberg J. M. Advances in computational design and analysis of airbreathing propulsion systems. Papers from the 9-th International Symposium on Air Breathing Engines. Sep. 3-8, 1989, pp. 3-17.
2. Karadimas G. Application of computational system to aircraft engine components development. Papers from the 9-th International Symposium on Air Breathing Engines. Sep. 3-8, 1989, 10p..
3. Rosen R., Bowditch D. N. The future challenge for aeropropulsion. NASA Technical Memorandum No. 105613, 1992, 12p..
4. Ogorodnikov D. A., Ivanov M. Ja., Sundjiring V. G. Mathematical simulation for perspective aircraft engine design. Aircraft Technique, 1993, No.2-3, pp.1-15, (in Russian).
5. Ivanov M. Ja., Kostege V. K., Krupa V. G., Nigmatullin R. Z. Design of high-load aviation turbomachines using modern 3D computational methods. Papers from the 11-th International Symposium on Air Breathing Engines. Sep. 20-24, 1993, pp. 355-365.
6. Ivanov M. Ja., Nigmatullin R. Z. Quasi-3D numerical model of a flow passage of the aviation gas turbine engines. Papers from the 10-th International Symposium on Air Breathing Engines. Sep. 1-6, 1991, pp. 299-305.
7. Ivanov M. Ja., Kostege V. K. Application of three dimensional methods for the calculation of gas dynamic and thermal processes at the design of gas turbines for air breathing engines. Papers from the 9-th International Symposium on Air Breathing Engines. Sep. 3-8, 1989, pp. 497-505.
8. 3-D computational techniques applied to internal flows in propulsion systems. AGARD Lecture Series No. 140, 1985.
9. Godunov S. K., Zabrodin A. V., Ivanov M. Ja., Kraiko A. N., Prokopov G. P. Numerical solution of multidimensional gas dynamics problems M., Nauka, 1976, 400p., (in Russian).
10. Theory of bypass turbojet engines. Ed. by Prof. S. M. Shliakhtenko and Prof. V. A. Sosounov. M., Mashinostroenie, 1979, 432p. (in Russian).
11. Cohen H., Rogers G. F. C., Saravanamuttoo H. I. H. Gas turbine theory (third edition). Longman Scientific and Technical imprint. 1987, 414p.
12. Drouginin L. N., Shvetc L. I., Lanshin A. I. Mathematical modeling of gas turbine engines on modern computers for prediction of parameters and performances of aviation motors. CIAM Proceedings No. 832, 1979, 45p. (in Russian).
13. Fishbach L. H., Computer simulation engine systems. AIAA Paper No. 80-0051, 1980, 10p.
14. Grin V. T. On construction of mathematical model of propulsion system with air breathing engine for unsteady processes investigation. Scientific notes of TcAGI, 1976, Vol. 7, No. 6, pp. 41-49, (in Russian).
15. Grin V. T., Kraiko A. N., Miller L. G. Using of discontinuity surfaces such as active and passive discs in mathematical model of unsteady processes in propulsion system. CIAM Proceedings No. 1020, 1982, pp. 41-68, (in Russian).
16. Arutiunov G. S., Krasnov S. E., Olshtein L.E. Mathematical modeling of gas dynamics stability of turbojet engine for steady and transient regimes with inlet pressure and temperature disturbances. CIAM Proceedings No. 1093, 1984, pp. 155-169, (in Russian).

On the CFD monotone high accuracy methods

by

Prof. M. Ja. Ivanov, Dr. V. G. Krupa, Dr. R. Z. Nigmatullin
CIAM (Central Institute of Aviation Motors)
2, Aviamotornaya St.,
Moscow, Russia, 111250

Abstract

Some theoretical fundamentals of monotone high accuracy methods are presented. The conditions for the construction of monotone, total variation diminishing (TVD) and following difference schemes are described. The peculiarities of high accuracy and implicit methods design are given. The typical results of numerical solutions illustrate the principal features of developed computational techniques.

Nomenclature

t	-	time
x	-	space coordinate
a	-	convection speed
u	-	determined function
U	-	value of determined function on the cell boundaries
f	-	flux function
F	-	value of function f on the cell boundaries
p	-	pressure
V	-	velocity
M	-	Mach number
τ	-	time step
h	-	space step
c	-	coefficient of difference equation
r	-	relationship of differences
$\chi(r), \mu(r)$	-	limiting functions
b	-	parameter of limiting function
C	-	Courant number
$\nu, \varphi, \psi, \omega$	-	parameters, characterizing approximation accuracy in x direction
σ, α, β	-	parameters, characterizing approximation accuracy in t direction
λ	-	amplification factor
θ	-	phase angle

ε	-	truncation error
$G(\theta), z(\theta)$	-	functions, characterizing approximation in x direction
Q	-	point support parameter

Subscripts

j	-	cell number in x direction
q	-	current index

Superscripts

n	-	number of solution layer in t direction
$-, +$	-	parameters from the left and right cell boundaries

Introduction

Computational fluid dynamics (CFD) offers one of the most promising engineering tools for the design and development of aircraft, missiles, turbomachinery, propulsion systems etc. With the current maturity of CFD development the reader can get acquainted full enough, for example, from recently published monographs [1,2] and reviewed papers, contained in the special issues of Journal "Aerospace America" [3,4]. These publications present in detail the CFD achievements of foreign researchers (from West Europe and North America), but the CFD development in Russia is considered just shortly. Below we'll try to present a few Russian papers, which contain interesting results of effective monotone and high accuracy CFD methods development.

The theory of monotone difference methods for fluid dynamics equations solution started from the pioneering work of Russian scientist S. K. Godunov in the late 1950's [5,6]. The first stage of their development and wide application was presented in detail in the monograph, published in Russian in 1976 [7] and in French in 1981 [8]. The famous original properties of Godunov's method were not only monotonicity, but conservativeness (shock capture method) and procedure

of arbitrary " discontinuity break down" (the analogy of Riemann problem). The last procedure allows to follow closely the local flow structure on each cell boundary.

The other perspective direction of CFD difference methods became the construction of nonlinear difference scheme. One of the first works in this direction were the papers [9,10]. In these papers the limiting functions were introduced for the conservation of qualitatively right behavior of numerical solutions.

The high order of accuracy CFD methods were developed in papers [11,12], where the idea of the Runge-Kutta methods construction was used.

Compact difference schemes on minimum points support were considered in papers [13,14].

We would like to describe in more detail the papers, in which monotone difference schemes were developed.

The original Godunov method used the piecewise constant parameters distributions into each cell of grid. This method has only the first order of accuracy. The realization of a more accurate variant of the Godunov method with the piecewise linear parameters distributions into cells was proposed at the first by V. P. Kolgan and published in the paper [15]. This difference scheme has the second order of accuracy for space variables. In the paper [15] also the "minimum derivatives principle" was applied, that gave the nonlinear scheme with the simple limiting functions. The concept of the limiting functions (as the flux limiting) was independently advanced in the works [16,17], which are known very well to CFD researchers.

The monotone second order accuracy schemes were developed also in papers [18,19].

The total variation diminishing (TVD) difference schemes, introduced by A. Harten [20], became very popular CFD tool in the last decade. The general conditions for the constructions of TVD schemes have been stated and proved in paper [21]. These conditions are similar to the conditions of monotonicity.

The modification of Godunov's method with the piecewise parabolic parameter distributions into cells was developed by P. Gollala and P. Woodward [22]. The implicit variants of Godunov's method with the piecewise linear and parabolic parameters distributions into cells for integration Euler and Navier-Stokes equations were considered in papers [23,24].

The paper [25] describes the method with the piecewise cubic parameters distributions into cells for all independent variables.

This lecture presents some peculiarities of effective CFD method construction. It's worth to emphasize the main features of these modern numerical methods. They are based on finite difference schemes, which are:

- 1) conservative
- 2) monotone
- 3) following
- 4) high order accuracy
- 5) implicit

Conservative schemes allow to apply the shock capture technique for discontinuous flow simulations: monotone schemes transform any monotone difference functions into monotone functions; the schemes with the following property select the physically relevant

solution; high order accuracy schemes allow to use coarser grids in comparison with lower order accuracy schemes; implicit schemes eliminate restrictions for steps of integration.

The numerical codes using described effective methods allow to solve many engineering problems on wide spread computers of middle class of efficiency.

1. Monotone, TVD and following difference methods (the linear case)

In order to present the essentials of the methods let us begin with a simple linear convective equation, written here as follows

$$\frac{\partial u}{\partial t} + a \frac{\partial u}{\partial x} = 0 \quad a = \text{const} > 0 \quad (1.1)$$

where u is unknown function of (x, t) and a is a convection speed. This is a typical first-order hyperbolic equation and an initial value problem of this equation has initial condition

$$u(x, 0) = u_0(x) \quad -\infty < x < \infty$$

We have for (1.1) along the characteristic lines

$$a = \frac{dx}{dt} \quad \frac{du}{dt} = 0 \quad u = \text{const} \quad (1.2)$$

Using (1.2) it's easy to see that if $u_0(x)$ is increasing monotonically, then

$$u(x_j, t) \leq u_0(x_j) \quad \text{for } t \geq 0 \quad (1.3)$$

and if $u_0(x)$ is decreasing monotonically, then

$$u(x_j, t) \geq u_0(x_j) \quad \text{for } t \geq 0 \quad (1.4)$$

where $x_j = jh$, h - the space step, j - the point number.

A general two-level explicit scheme for equation (1.1) can be written as

$$u_j^{n+1} = \sum_{q=-Q}^Q c_q u_{j+q}^n \quad (1.5)$$

which has $2Q+1$ point support, and

$$u_j^n = u(x_j, t) \quad u_j^{n+1} = u(x_j, t + \tau),$$

where τ - the time step.

An implicit scheme may have the same form (1.5)

if solved relatively to unknown mesh function u_j^{n+1} [5].

Russian scientist S. K. Godunov presented convenient a criteria of monotonicity preserving schemes [5,7]:

The difference scheme (1.5) transforms any given monotone function into a monotone function with the same growth direction if and only if all coefficients c_q are non negative

$$c_q \geq 0 \quad (1.6)$$

Proof. Let $c_q \geq 0$ and u_j is monotone function. For example it's increasing monotonically, i.e. for all j $\Delta u_j^n = u_{j+1}^n - u_j^n \geq 0$. Then

$$\begin{aligned} \Delta u_j^{n+1} &= u_{j+1}^{n+1} - u_j^{n+1} = \\ &= \sum_{q=-Q}^Q c_q u_{j+q+1}^n - \sum_{q=-Q}^Q c_q u_{j+q}^n = \\ &= \sum_{q=-Q}^Q c_q (u_{j+q+1}^n - u_{j+q}^n) = \\ &= \sum_{q=-Q}^Q c_q \Delta u_{j+q}^n \geq 0 \end{aligned} \quad (1.7)$$

The sufficient condition has been proved. The necessary condition follows from the next example. Let $c_{q_0} < 0$ and

$$\begin{aligned} u_j^n &= 1 \quad \text{for } j > q_0 \\ u_j^n &= 0 \quad \text{for } j \leq q_0 \end{aligned}$$

Then

$$\Delta u_{q_0}^{n+1} = u_{q_0+1}^{n+1} - u_{q_0}^{n+1} = c_{q_0} \leq 0$$

and monotonicity of numerical solution will be destroyed. This completes the proof of monotonicity preserving criteria.

It's well known also for solution (1.1) that the total variation

$$TV(u) = \int_{-\infty}^{\infty} \left| \frac{\partial u}{\partial x} \right| dx \quad (1.8)$$

can't increase with time, i.e.

$$\begin{aligned} TV(u(t_1)) &\leq TV(u(t_0)) \\ \text{for } t_1 &> t_0 \end{aligned} \quad (1.9)$$

The idea of scheme design with total variation diminution was proposed by A. Harten [20].

The discrete total variation is\

$$TV(u_j^n) = \sum_j \left| \Delta u_j^n \right| \quad (1.10)$$

A finite difference scheme is called Total Variation Diminishing (TVD) scheme, if it satisfies a discrete version of (1.9), that is

$$TV(u_j^{n+1}) \leq TV(u_j^n) \quad (1.11)$$

For the linear case TVD schemes identify to monotone schemes [20]. In the next section it will be shown also for the nonlinear case, that the TVD conditions are the same as the conditions of monotonicity.

Now we consider more strict class of "following" schemes [25], which satisfy the conditions (1.3), (1.4). These conditions for discrete functions are rewritten as follows

$$u_j^{n+1} \leq u_j^n \quad (1.12)$$

for monotone increasing discrete functions with

$$\Delta u_j^n \geq 0 \text{ and}$$

$$u_j^{n+1} \geq u_j^n \quad (1.13)$$

for monotone decreasing discrete functions with

$$\Delta u_j^n \leq 0.$$

If for difference scheme the relations (1.12), (1.13) are fulfilled, then the scheme is following .

We will obtain the conditions for following schemes for equation (1.1), when these schemes are written in the form (1.5) and conservative form (in the next section). Previously it has been emphasized that the

coefficients c_q in (1.5) are obviously not arbitrary and have to satisfy a certain number of consistency conditions, following from approximation requirements and depending on the order of accuracy (see, for example, [1]). The first of consistency condition under the form

$$\sum_{q=-Q}^Q c_q = 1 \quad (1.14)$$

is obtained easily from the requirement that the function $u = \text{const}$ should be a solution of (1.5). Thus the scheme (1.5) can be written as

$$u_j^{n+1} = u_j^n - \sum_{q=-Q}^Q c_q (u_j^n - u_{j+q}^n) \quad (1.15)$$

For monotone increasing discrete function u_j^n ($\Delta u_j^n \geq 0$) the condition (1.12) leads in the case of scheme (1.15) to

$$\sum_{q=-Q}^Q c_q (u_j^n - u_{j+q}^n) \geq 0 \quad (1.16)$$

We can see that (1.16) will be satisfied if and only if

$$c_q \geq 0 \quad \text{for } -Q \leq q < 0 \quad (1.17)$$

$$c_q \leq 0 \quad \text{for } 0 < q \leq Q$$

From (1.6) and (1.17) we obtain the necessary and sufficient conditions for monotone following schemes in the form (1.5) as follows

$$c_q = 0 \quad \text{for } 0 < q \leq Q \quad (1.18)$$

$$c_q \geq 0 \quad \text{for } -Q \leq q \leq 0$$

For monotone decreasing discrete function from the condition (1.13) we have the same results (1.18). Hence, a two-level explicit linear monotone following schemes for equation (1.1) can be written also as upwinding schemes

$$u_j^{n+1} = u_j^n - \sum_{q=-Q}^{-1} c_q (u_j^n - u_{j+q}^n) \quad (1.19)$$

with $c_q \geq 0$, or

$$\begin{aligned} u_j^{n+1} &= u_j^n - \sum_{q=-Q}^{-1} c_q \sum_{p=q}^{-1} \Delta u_{j+p}^n = \\ &= u_j^n - \sum_{p=-Q}^{-1} \Delta u_{j+p}^n \sum_{q=-Q}^p c_q = \\ &= u_j^n - \sum_{p=-Q}^{-1} \bar{c}_p \Delta u_{j+p}^n, \end{aligned} \quad (1.20)$$

with $\bar{c}_p = \sum_{q=-Q}^p c_q \geq 0$.

As a typical examples the three widely known two-level explicit schemes for equations (1.1) are presented. They can be interpreted also as the inverse methods of

characteristics using the exact solution (1.2) with linear or parabolic interpolation over u_j^n values.

Courant-Isaacson-Rees Scheme [26]. It's written in the form (1.15) as

$$u_j^{n+1} = u_j^n - C \nabla u_j^n, \quad \nabla u_j^n = u_j^n - u_{j-1}^n \quad (1.21),$$

where $C = \alpha \tau / h$ - the Courant number. For stability of this scheme must be $0 \leq C \leq 1$.

This scheme is following monotone scheme. The original first order Godunov type scheme for equation (1.1) has the same form (1.21). In the characteristic

interpretation it uses the linear interpolation over u_j^n

and u_{j-1}^n values.

Lax Scheme [27]. It can be written

$$u_j^{n+1} = u_j^n + \frac{1}{2}(1-C)\Delta u_j^n - \frac{1}{2}(1+C)\nabla u_j^n \quad (1.22)$$

This is monotone non-following scheme. It uses the linear interpolation over u_{j-1}^n and u_{j+1}^n values.

Lax-Wendroff Scheme [28]. It has the form

$$u_j^{n+1} = u_j^n + \frac{1}{2}C(C-1)\Delta u_j^n - \frac{1}{2}C(C+1)\nabla u_j^n \quad (1.23)$$

This scheme is non-following and non-monotone scheme. It uses the parabolic interpolation over u_{j-1}^n, u_j^n

and u_{j+1}^n values.

These examples accent, in particular, the difference of monotone and following schemes.

We would like to emphasize that the conditions (1.6) for monotone schemes and (1.18) for monotone following schemes are necessary and sufficient conditions, therefore these conditions get too strict limitations. For example, in the S. K. Godunov's pioneering work [5] was shown that it's impossible to construct the linear monotone scheme with higher order of accuracy than first order. In this connection we consider in more detail the sufficient conditions, which are more convenient for practical construction of following conservative difference schemes (including the nonlinear schemes).

2. Monotone and following nonlinear schemes

The scalar nonlinear conservation law in one space dimension

$$\frac{\partial u}{\partial t} + \frac{\partial f(u)}{\partial x} = 0 \quad (2.1)$$

presents a simple enough model that already contains the phenomena of shock wave formation and expansion fans. It describes wave propagation at a speed

$$a(u) = \frac{\partial f}{\partial u}$$

and can be written

$$\frac{\partial u}{\partial t} + a(u) \frac{\partial u}{\partial x} = 0 \quad (2.2)$$

As for (1.1) the solution $u(x, t)$ is a constant along the characteristic lines $a = dx/dt$. They can't intersect which provides the formation of shock waves. We have also the properties (1.3) or (1.4) for monotone increasing or decreasing solutions.

Suppose that equation (2.1) is approximated by a conservative scheme (finite volume scheme), which for cell with number j (Fig.1) can be written as:

$$u_j^{n+1} = u_j^n - \frac{\tau}{h} (F_{j+1/2} - F_{j-1/2}) \quad (2.3)$$

where the numerical flux functions $F_{j\pm 1/2}$ are approximations of the fluxes across the cell boundaries at $x_{j\pm 1/2}$

The following difference scheme must satisfy the conditions

$$F_{j+1/2} \geq F_{j-1/2} \quad (2.4)$$

for monotone increasing mesh function with $\Delta u_j^n \geq 0$ or

$$F_{j+1/2} \leq F_{j-1/2} \quad (2.5)$$

for monotone decreasing mesh function with $\Delta u_j^n \leq 0$.

In the original monotone Godunov's scheme [5-7] the values are supposed to be the flux values taken from the exact solutions of the initial value problems defined by piece wise constant data between each cell boundaries.

For the scalar conservation law (2.1) we define

$$F_{j+1/2} = \begin{cases} f(U_{j+1/2}^-), a_{j+1/2} \geq 0 \\ f(U_{j+1/2}^+), a_{j+1/2} < 0 \end{cases} \quad (2.6)$$

where $U_{j\pm 1/2}^\pm$ are the values of function u on the right and on the left from boundary $x_{j\pm 1/2}$ correspondently. In the case $a(u) \geq 0$ equation (2.3) can be written as

$$u_j^{n+1} = u_j^n - \frac{\tau}{h} [f(U_{j+1/2}^-) - f(U_{j-1/2}^-)] \quad (2.7)$$

or, defining

$$a_j = \begin{cases} \frac{f(U_{j+1/2}^-) - f(U_{j-1/2}^-)}{U_{j+1/2}^- - U_{j-1/2}^-}, U_{j+1/2}^- \neq U_{j-1/2}^- \\ \left(\frac{\partial f}{\partial u}\right)_j, U_{j+1/2}^- = U_{j-1/2}^- \end{cases} \quad (2.8)$$

obtain

$$u_j^{n+1} = u_j^n - \frac{\tau}{h} a_j (U_{j+1/2}^- - U_{j-1/2}^-) \quad (2.9)$$

The following scheme (2.9) in our case satisfies the conditions

$$U_{j+1/2}^- \geq U_{j-1/2}^- \quad (2.10)$$

for monotone increasing mesh function with $\Delta u_j^n \geq 0$ and

$$U_{j+1/2}^- \leq U_{j-1/2}^- \quad (2.11)$$

for monotone decreasing mesh function with $\Delta u_j^n \leq 0$.

Define the boundary values at first as the explicit formula

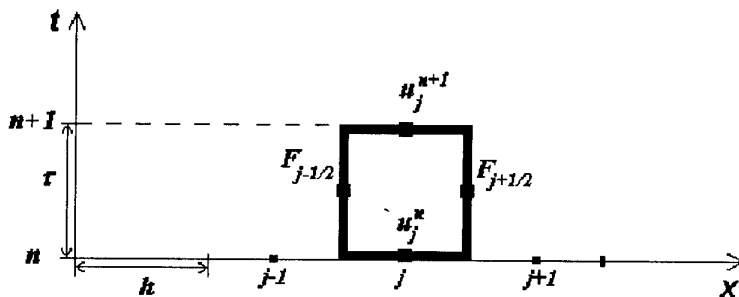


Fig. 1 Computational cell of finite volume scheme in the 1D cascade

$$U_{j+\frac{1}{2}}^- = u_j^n + \Delta u_j^n \mu_j^n \quad (2.12)$$

Here the limiting function

$$\mu_j^n = \mu(r_{j-1}^n, r_j^n, r_{j+1}^n) \quad (2.13)$$

$$r_j^n = \nabla u_j^n / \Delta u_j^n$$

can depend on various numbers of difference relationships r_j^n . For difference schemes in the following chapters the function μ_j^n depends on one, two or three (as in (2.13)) difference relationships r_j^n . Some limiting functions μ_j^n for a few concrete nonlinear schemes are presented in section 3 of this lecture.

Inserting the boundary values (2.12) into scheme (2.9) we have

$$u_j^{n+1} = u_j^n + \frac{\tau}{h} \alpha_j^n \nabla u_j^n \lambda_j^n \quad (2.14)$$

where

$$\lambda_j^n = 1 + \mu_j^n / r_j^n - \mu_{j-1}^n \quad (2.15)$$

For monotone increasing discrete function $\Delta u_j^n \geq 0$ the condition (2.10) leads to (in our case $\alpha_j^n > 0$)

$$\lambda_j^n \geq 0 \quad (2.16)$$

As we'll see below the inequality (2.16) defines the limiting coefficients for nonlinear difference schemes.

Estimating the mesh function behavior on a new level $\Delta u_j^{n+1} = u_{j+1}^{n+1} - u_j^{n+1}$ for the scheme (2.14) we have

$$\begin{aligned} \Delta u_j^{n+1} &= \\ &= \Delta u_j^n \left(1 - \frac{\tau}{h} \alpha_{j+1}^n \lambda_{j+1}^n \right) + \frac{\tau}{h} (F_{j+\frac{1}{2}} - F_{j-\frac{1}{2}}) \end{aligned} \quad (2.17)$$

Considering the equation (2.17) with the relation (2.4) we obtain the criteria of monotonicity for following explicit difference schemes:

Following explicit difference scheme (2.14) is monotone scheme if

$$\frac{\tau}{h} \alpha_j^n \lambda_j^n \leq 1 \quad (2.18)$$

for all j and n .

The relation (2.18) defines the limit for the time step τ and is a stability condition (together with (2.16)) for the linear variant of the scheme (2.14).

We consider also the implicit difference scheme in the form (2.9), when the cell boundary values are defined as

$$U_{j+\frac{1}{2}}^- = u_j^{n+1} + \Delta u_j^{n+1} \mu_j^{n+1} \quad (2.19)$$

In this case instead of (2.14) and (2.17) we have

$$u_j^{n+1} = u_j^n - \frac{\tau}{h} \alpha_j^{n+1} \nabla u_j^{n+1} \lambda_j^{n+1} \quad (2.20)$$

$$\begin{aligned} \left(1 + \frac{\tau}{h} \alpha_j^{n+1} \lambda_{j+1}^{n+1} \right) \Delta u_j^{n+1} &= \\ &= \Delta u_j^n + \frac{\tau}{h} (F_{j+\frac{1}{2}} - F_{j-\frac{1}{2}}) \end{aligned} \quad (2.21)$$

The stability condition for the linear variant of implicit scheme (2.20) is (for $\alpha_j^{n+1} \geq 0$)

$$\lambda_j^{n+1} \geq 0 \quad (2.22)$$

In this case we have from (2.21) that scheme (2.20) is a monotone scheme.

Having summarized our considerations we can formulate the next criteria:

Following stable schemes (2.14) and (2.20) are monotone schemes.

We want to emphasize once more the relations (2.16), (2.18) and (2.22) are very convenient for practice using when we construct the concrete following schemes.

Now we'll show the identity of monotone and TVD schemes with various coefficients

The general two-level difference scheme with various coefficients are presented in the same as (1.5) form as:

$$u_j^{n+1} = \sum_{q=-Q}^Q c_q(j) u_{j+q}^n \quad (2.23)$$

where coefficients $c_q(j)$ must also satisfy the first of consistency condition (see (1.14))

$$\sum_{q=-Q}^Q c_q(j) = 1 \quad (2.24)$$

Rewrite (2.23) using (2.24) in the form

$$u_j^{n+1} = u_j^n - \sum_{q=-Q}^Q c_q(j) (u_j^n - u_{j+q}^n) \quad (2.25)$$

and further

$$\begin{aligned}
u_j^{n+1} &= u_j^n - \sum_{q=-Q}^{-1} c_q(j) (u_j^n - u_{j+q}^n) + \\
&+ \sum_{q=1}^Q c_q(j) (u_{j+q}^n - u_j^n) = \\
&= u_j^{n+1} - \sum_{q=-Q}^{-1} c_q(j) \sum_{p=q}^{-1} (u_{j+p+1}^n - u_{j+p}^n) + \\
&+ \sum_{q=1}^Q c_q(j) \sum_{p=0}^{q-1} (u_{j+p+1}^n - u_{j+p}^n) = \\
&= u_j^{n+1} - \sum_{p=-Q}^{-1} (u_{j+p+1}^n - u_{j+p}^n) \sum_{q=-Q}^p c_q(j) + \\
&+ \sum_{p=0}^{Q-1} (u_{j+p+1}^n - u_{j+p}^n) \sum_{q=p+1}^Q c_q(j) = \\
&= u_j^n - \sum_{p=-Q}^{Q-1} \bar{c}_p(j) \Delta u_{j+p}^n \quad (2.26)
\end{aligned}$$

where

$$\bar{c}_p(j) = \sum_{q=-Q}^p c_q(j), \quad \text{for } -Q \leq p \leq -1$$

and

$$\bar{c}_p(j) = - \sum_{q=p+1}^Q c_q(j), \quad \text{for } 0 \leq p < Q$$

$$\Delta u_{j+p}^n = u_{j+p+1}^n - u_{j+p}^n$$

It's not difficult to get sufficient monotone conditions for nonlinear difference scheme in the form (2.26). Following the proof of the Godunov monotonicity preserving criteria, presented in previous section, we consider the monotone increasing mesh function u_j^n (with $\Delta u_j^n \geq 0$) and define difference

$$\begin{aligned}
\Delta u_j^{n+1} &= u_{j+1}^{n+1} - u_j^{n+1} = \\
&= \Delta u_j^n - \sum_{p=-Q}^{Q-1} \bar{c}_p(j+1) \Delta u_{j+p+1}^n +
\end{aligned}$$

$$\begin{aligned}
&+ u_j^n - \sum_{p=-Q}^{Q-1} \bar{c}_p(j) \Delta u_{j+p}^n = \\
&= \Delta u_j^n - \bar{c}_{Q-1}(j+1) \Delta u_{j+Q}^n - \\
&- \sum_{p=-Q+1}^{Q-1} [\bar{c}_{p-1}(j+1) - \bar{c}_p(j)] \Delta u_{j+p}^n + \\
&+ \bar{c}_{Q-1}(j) \Delta u_{j-Q}^n \quad (2.27)
\end{aligned}$$

which must be non negative for monotone scheme. Consider (2.27) we'll obtain the next sufficient conditions of monotonicity

$$\begin{aligned}
\bar{c}_{Q-1}(j+1) &\leq 0 \\
\bar{c}_p(j) &\geq \bar{c}_{p-1}(j+1), \quad p=1, \dots, Q-1 \\
1 - \bar{c}_{-1}(j+1) + \bar{c}_0(j) &\geq 0 \quad (2.29) \\
\bar{c}_p(j) &\geq \bar{c}_{p-1}(j+1) \geq 0, \quad p=-Q+1, \dots, -1 \\
\bar{c}_{-Q}(j) &\geq 0
\end{aligned}$$

for all j . The conditions (2.29) may be rewritten in form

$$\begin{aligned}
\bar{c}_{-1}(j) &\geq \bar{c}_{-2}(j+1) \geq \dots \geq \bar{c}_{-Q}(j+Q-1) \geq 0 \quad (2.30) \\
\bar{c}_0(j) &\geq -\bar{c}_{-1}(j-1) \geq \dots \geq -\bar{c}_{Q-1}(j-Q+1) \geq 0 \\
\bar{c}_{-1}(j+1) - \bar{c}_0(j) &\leq 1,
\end{aligned}$$

for all j . If coefficient $\bar{c}_p(j)$ doesn't depend on solution, then these conditions are also necessary. We can obtain the proof of the necessity the same way as it was obtained by S. K. Godunov (see the previous section).

The conditions (2.30) are exactly the same as was obtained for TVD schemes by A. Jameson and P. Lax in [21]. This is the confirmation of the identity of monotone and TVD schemes.

For semidiscrete schemes in a form

$$\frac{\partial u}{\partial t} = \sum_{p=-Q}^{Q-1} \bar{c}_p(j) \Delta u_{j+p}^n \quad (2.31)$$

the conditions of monotonicity have also the form (2.30) without the last inequality, from which we can get the stability condition for an explicit schemes (2.26).

3. Following nonlinear high order accuracy schemes

We would like to construct now following monotone high order accuracy schemes for integration of equation (2.1). For approximation (2.1) and (2.2) the difference formulas (2.7) and (2.9) are used.

Into each cell we consider piecewise polynomial distributions of function $u(x, t)$ in the form

$$\begin{aligned} u(x, t_n) = & u_j^n + v(x - x_j) \left(\frac{\partial u}{\partial x} \right)_j^n + \\ & \psi(x - x_j)^3 \left(\frac{\partial^3 u}{\partial x^3} \right)_j^n + \\ & + \omega(x - x_j)^4 \left(\frac{\partial^4 u}{\partial x^4} \right)_j^n \end{aligned} \quad (3.1)$$

where γ , φ , ψ and ω are parameters, defining below an accuracy of space derivatives. Using the same identification for discrete differences

$$\Delta u_j^n = u_{j+1}^n - u_j^n, \quad \nabla u_j^n = u_j^n - u_{j-1}^n \quad (3.2)$$

and approximate relations

$$\begin{aligned} \left(\frac{\partial u}{\partial x} \right)_j^n & \approx \frac{1}{2h} (\Delta u_j^n + \nabla u_j^n) \\ \left(\frac{\partial^2 u}{\partial x^2} \right)_j^n & \approx \frac{1}{h^2} (\Delta u_j^n - \nabla u_j^n) \end{aligned} \quad (3.3)$$

$$\left(\frac{\partial^3 u}{\partial x^3} \right)_j^n \approx \frac{1}{h^3} (\Delta u_j^n - 2\nabla u_j^n + \nabla u_{j-1}^n)$$

$$\left(\frac{\partial^4 u}{\partial x^4} \right)_j^n \approx \frac{1}{h^4} (\Delta u_{j+1}^n - 3\Delta u_j^n + 3\nabla u_j^n - \nabla u_{j-1}^n)$$

it's not difficult to obtain for an explicit scheme

$$\begin{aligned} U_{j+\frac{1}{2}}^- & = u_j^n + \frac{\omega}{16} \Delta u_{j+1}^n + \\ & + \frac{1}{16} (4v + 4\varphi + 2\psi - 3\omega) \Delta u_j^n + \end{aligned}$$

$$\begin{aligned} & + \frac{1}{16} (4v - 4\varphi - 4\psi + 3\omega) \nabla u_j^n + \\ & + \frac{2\psi - \omega}{16} \nabla u_{j-1}^n. \end{aligned} \quad (3.4)$$

The next values of parameters

$$v = 1, \quad \varphi = \frac{1}{3}, \quad \psi = -\frac{2}{3}, \quad \omega = -\frac{4}{5} \quad (3.5)$$

get for given cell the approximations of space derivative $\partial u / \partial x$ up to the fifth order of accuracy

$O(h^5)$. For variable value ω the order of accuracy decreases to the fourth, for variable values ψ and ω - to the third, for variable φ , ψ and ω - to the second.

Now obtain conditions of monotonicity for following difference schemes, which have the approximation of space derivative with order of accuracy from the second to the fifth.

We consider for relation (3.4) the modificate values of differences

$$\Delta \tilde{u}_j^n = \Delta u_j^n \chi(r_j), \quad r_j = \frac{\nabla u_j^n}{\Delta u_j^n}$$

$$\Delta \tilde{u}_{j+1}^n = \Delta u_{j+1}^n \chi(r_{j+1}), \quad r_{j+1} = \frac{\nabla u_{j+1}^n}{\Delta u_{j+1}^n} \quad (3.6)$$

$$\nabla \tilde{u}_j^n = \nabla u_j^n \chi\left(\frac{1}{r_j}\right)$$

$$\nabla \tilde{u}_{j-1}^n = \nabla u_{j-1}^n \chi\left(\frac{1}{r_{j-1}}\right), \quad r_{j-1} = \frac{\nabla u_{j-1}^n}{\Delta u_{j-1}^n}$$

where $\chi(r)$ is a limiting function and rewrite

$$\begin{aligned} U_{j+\frac{1}{2}}^- & = u_j^n + \frac{\omega}{16} \Delta \tilde{u}_{j+1}^n + \\ & + \frac{1}{16} (4v + 4\varphi + 2\psi - 3\omega) \Delta \tilde{u}_j^n + \\ & + \frac{1}{16} (4v - 4\varphi - 4\psi + 3\omega) \nabla \tilde{u}_j^n + \end{aligned}$$

$$+\frac{2\psi-\omega}{16}\nabla\tilde{u}_{j-1}^n = u_j^n + \Delta u_j^n \mu_j \quad (3.7)$$

Here

$$\begin{aligned} \mu_j &= \frac{1}{16}[\omega\chi(r_{j+1})/r_{j+1} + \\ &+(4\nu+4\phi+2\psi-3\omega)\chi(r_j) + \\ &+(4\nu-4\phi-4\psi+3\omega)\chi\left(\frac{1}{r_j}\right)r_j + \\ &+(2\psi-\omega)r_j r_{j-1}\chi\left(\frac{1}{r_{j-1}}\right) = \\ &\mu_j(r_{j+1}, r_j, r_{j-1}) \end{aligned}$$

We have the difference scheme in the form similar to (1.26)

$$u_j^{n+1} = u_j^n - \frac{\tau}{h} a_j \nabla u_j^n \lambda_j^n \quad (3.8)$$

where

$$\lambda_j^n = 1 + \mu_j^n / r_j^n - \mu_{j-1}^n$$

It can be shown (see, for example, [24]), that the conditions (1.34) or (2.17) are fulfilled, if the limiting function $\chi(r)$ has the form

$$\chi(r) = \begin{cases} 0, & r \leq 0 \\ br, & 0 \leq r \leq 1/b \\ 1, & r \geq 1/b \end{cases} \quad (3.9)$$

where $1 \leq b \leq b_{\max}$.

We present the examples of a few difference schemes. For the scheme with piecewise linear distributions of function $u(x,t)$ into cells ($\nu=1$, $\phi=\psi=\omega=0$), $b_{\max}=3$, value of Courant number $C = \alpha\tau/h \leq 0.5$.

The Godunov scheme with piecewise linear distributions of functions into cells was published first in 1972 year by V. Kolgan [15]. Realized in this work "the minimum derivatives principal" have the limiting function (3.9) with $b=1$. The Godunov scheme with piecewise parabolic distributions of functions into cells was realized in the work by P. Colella and P. R.

Woodward [22] and was published in 1984. For this scheme (with $\nu=1$, $\phi=\text{var}$, $\psi=\omega=0$), the value

$b_{\max} = (3-\phi)/(1-\phi)$, and the Courant number

$$C \leq 4/(5-\phi+(1+\phi)b).$$

For a convenient description of limiting functions we use also the "minmod" operator, which is given by

$$\begin{aligned} \min \text{mod}(a, b) &= \\ &= \frac{\text{sign}(a) + \text{sign}(b)}{2} \min(|a|, |b|) \end{aligned} \quad (3.10)$$

The "sign" operator $\text{sign}(a)$ denotes "sign of a" and is therefore ± 1 .

In the case of previous scheme with piecewise parabolic distributions into cells for the modificate values of differences in (3.7) we have

$$\Delta\tilde{u}_j^n = \min \text{mod}(\Delta u_j^n, b\nabla u_j^n) \quad (3.11)$$

$$\nabla\tilde{u}_j^n = \min \text{mod}(\nabla u_j^n, b\Delta u_j^n)$$

The explicit scheme with piecewise cubic distributions into cells (with $\nu=1$, $\phi=1/3$,

$\psi=-2/3$, $\omega=0$) has

$$b_{\max} = 9/4, \quad C \leq 1/(1+b/4+1/3)$$

and

$$\begin{aligned} \Delta\tilde{u}_j^n &= \min \text{mod}(\Delta u_j^n, b\nabla u_j^n) \\ \nabla\tilde{u}_j^n &= \min \text{mod}(\nabla u_j^n, b\Delta u_j^n) \\ \nabla\tilde{u}_{j-1}^n &= \min \text{mod}(\nabla u_{j-1}^n, 4\nabla\tilde{u}_j^n) \end{aligned} \quad (3.12)$$

The explicit scheme with parameter values (3.5) has

$$b_{\max} = 36/11, \quad C \leq 1/(1+2b/5+11/60)$$

and relations (3.6) in the form

$$\begin{aligned} \Delta\tilde{u}_j^n &= \min \text{mod}(\Delta u_j^n, b\nabla u_j^n) \\ \Delta\tilde{u}_{j+1}^n &= \min \text{mod}(\Delta u_{j+1}^n, 8\Delta\tilde{u}_j^n) \\ \nabla\tilde{u}_j^n &= \min \text{mod}(\nabla u_j^n, b\Delta u_j^n) \\ \nabla\tilde{u}_{j-1}^n &= \min \text{mod}(\nabla u_{j-1}^n, 11/2\nabla\tilde{u}_j^n) \end{aligned} \quad (3.13)$$

The value b in (3.11) - (3.13) is taken usually as b_{\max} .

Here we would like to show also that a detailed consideration of limiting functions is presented in the paper [29], a construction of high order accuracy schemes for hyperbolic equations is described in the paper [30-33].

Additional publications on this question up to 1987 we can see in the references of the monograph [1].

4. Construction of implicit following schemes.

For producing an adequate numerical solution we must use a mesh with very fine spacing in the regions with the extreme parameter gradients (in boundary layers, shock waves and others). In these regions the aspect ratio of the cells may be so large and suffer both losses of accuracy and rate of convergence and give very strict limit on time step value for explicit schemes. The present section considers the construction of implicit schemes, which are unconditional stable for any Courant number value (for the linear case).

Let us begin from the very spread two-level implicit scheme for equation (2.1) in the form (see, for example, [34])

$$\frac{u_j^{n+1} - u_j^n}{\tau} + \sigma \left(\frac{\partial f}{\partial x} \right)_j^{n+1} + (1 - \sigma) \left(\frac{\partial f}{\partial x} \right)_j^n = 0 \quad (4.1)$$

Here $\left(\frac{\partial f}{\partial x} \right)_j^n$ is the discrete approximation of the value

$\partial f / \partial x$ in a point with j and n , σ is a parameter. For $\sigma=0.5$ the scheme (4.1) has the second order of accuracy.

For the linear function $f(u) = au$ and corresponding linear difference scheme we have

$$u_j^n = \lambda^n e^{ij\theta} \quad \left(\frac{\partial u}{\partial x} \right)_j^n = u_j^n G(\theta) \quad (4.2)$$

Inserting the relations (4.2) into scheme (4.1) we obtain the amplification factor in the form

$$\lambda = \frac{1 - (1 - \sigma)Z}{1 + \sigma Z} \quad Z = Z_0 + iZ_1 \quad (4.3)$$

$$Z_0 = C \operatorname{Re}[G(\theta)], \quad Z_1 = C \operatorname{Im}[G(\theta)], \quad C = \frac{\alpha}{h}$$

For "following" difference schemes the relations (1.12) and (1.13) lead to the condition

$$Z_0 \geq 0 \quad (4.4)$$

for all θ (as earlier we consider the case $\alpha \geq 0$).

It may be shown that implicit "following" schemes with $\sigma \geq 0.5$ are unconditionally stable schemes ($|\lambda| \leq 1$).

Next we'll construct an implicit "following" scheme with third order of accuracy in time, which is unconditionally stable. Previously we would like to emphasize that the simplest way for third order scheme construction may be not successful. For example, the one parameter implicit three-level scheme with the third order of accuracy in the form

$$\begin{aligned} & \frac{1}{\tau} \left(\frac{3\sigma - 2}{4} u_j^{n+2} + u_j^{n+1} - \frac{3\sigma - 2}{4} u_j^n \right) + \\ & + \frac{1}{4} (\sigma - 1) \left\{ \frac{\partial f}{\partial x} \right\}_j^{n+2} + \left\{ \frac{\partial f}{\partial x} \right\}_j^{n+1} + \\ & + \frac{1}{4} (\sigma + 1) \left\{ \frac{\partial f}{\partial x} \right\}_j^n = 0 \end{aligned} \quad (4.5)$$

is unconditionally stable scheme. With $\sigma = -2/3$ we have the Adam's type scheme, with $\sigma = \infty$ we have the Simpson type scheme.

The amplification factor λ for scheme (4.5) is defined from the relation

$$\begin{aligned} & [(3\sigma - 2) + (\sigma - 1)Z] \lambda^2 + 4(1 + \sigma Z) - \\ & - (3\sigma + 2) + (\sigma + 1)Z = 0 \end{aligned} \quad (4.6)$$

The analysis of this equation is complex enough, therefore we consider the limited case $Z = \infty$, when roots are

$$\lambda_{1,2} = \frac{-2\sigma \pm \sqrt{3\sigma^2 + 1}}{\sigma - 1}$$

or if $\sigma \neq 0$ one of these roots is more than 1, that follows from inequality

$$\max |\lambda_{1,2}| = \max \left| \frac{-2\sigma \pm \sqrt{3\sigma^2 + 1}}{\sigma - 1} \right| \geq$$

$$\geq \frac{2|\sigma| + 1}{|\sigma - 1|} \geq \frac{|\sigma|}{|\sigma - 1|} + 1 \geq 1$$

Same way we can shown for $\sigma = 1$ or $\sigma = \infty$.

Hence, the third order accurate schemes (in time direction) in the form (4.5) aren't unconditionally stable schemes for any linear approximation of space derivative. More than three time levels for approximation give us complex numerical algorithms, which demand essential growth of computer memory and speed.

For construction of unconditionally stable third order schemes we apply the idea of recalculation (similar to the Runge-Kutte's methods).

One parameter two step three time level schemes in the form

$$\frac{u_j^{n+1+\alpha} - u_j^n}{(1+\alpha)\tau} + \frac{1}{2} \left\{ \frac{\partial f}{\partial x} \right\}_j^{n+1+\alpha} + \frac{1}{2} \left\{ \frac{\partial f}{\partial x} \right\}_j^n = 0 \quad (4.7)$$

$$\frac{u_j^{n+1} - u_j^n}{\tau} - \frac{1}{6\alpha(\alpha+1)} \left\{ \frac{\partial f}{\partial x} \right\}_n^{n+1+\alpha} + \frac{3\alpha+1}{6\alpha} \left\{ \frac{\partial f}{\partial x} \right\}_j^{n+1} + \frac{3\alpha+2}{6(\alpha+1)} \left\{ \frac{\partial f}{\partial x} \right\}_j^n = 0$$

have the third order of accuracy in time direction, where α is nonnegative parameter. At the first step we define value $u_j^{n+1+\alpha}$ on the time level $t = (n+1+\alpha)\tau$ (the predictor step), at the second step we define value u_j^{n+1} on the next time level $t = (n+1)\tau$ (the corrector step). By that the scheme (4.7) demands approximately two time more calculations, then the scheme (4.6).

Spectral stability analysis of scheme (4.7) leads to amplification factor

$$\lambda = \frac{1 + A_1 Z + B_1 Z^2}{1 + A_2 Z + B_2 Z^2}$$

$$A_1 = \frac{3\alpha^2 + 1}{6\alpha}, \quad B_1 = -\frac{3\alpha^2 + 2\alpha + 1}{12\alpha}$$

$$A_2 = \frac{3\alpha^2 + 6\alpha + 1}{6\alpha}, \quad B_2 = \frac{3\alpha^2 + 4\alpha + 1}{12\alpha}$$

We have

$$|\lambda|^2 =$$

$$= \frac{1 + C_1 Z_0 + C_2 Z_0^2 + C_3 Z_1^2 + C_4 Z_0(Z_0^2 + Z_1^2) + B_1^2(Z_0^2 + Z_1^2)^2}{1 + C_5 Z_0 + C_6 Z_0^2 + C_7 Z_1^2 + C_8 Z_0(Z_0^2 + Z_1^2) + B_2^2(Z_0^2 + Z_1^2)^2}$$

$$C_1 = 2A_1, \quad C_2 = A_1^2 + 2B_1$$

$$C_3 = A_1^2 - 2B_1, \quad C_4 = 2A_1 B_1$$

$$C_5 = 2A_2, \quad C_6 = A_2^2 + 2B_2$$

$$C_7 = A_2^2 - 2B_2, \quad C_8 = 2A_2 B_2$$

For $\alpha > 0$ the value $|\lambda| \leq 1$ scheme (4.6) is

unconditional stable ($|A_1| < A_2, |B_1| < B_2,$

$A_1^2 - 2B_1 = A_2^2 - 2B_2$). For $\alpha < 0$ we can show, that

$|\lambda| > 1$ for large enough Z .

Is similar to (4.7) a family of two parameters third order accurate schemes (α and β are positive parameters) presented.

$$\frac{u_j^{n+1+\alpha} - u_j^n}{(1+\alpha)\tau} + \sigma \left\{ \frac{\partial f}{\partial x} \right\}_j^{n+1+\alpha} + (1-\sigma) \left\{ \frac{\partial f}{\partial x} \right\}_j^n = 0$$

$$\sigma = \frac{\beta + 1}{2(\alpha + 1)} \quad (4.8)$$

$$u_j^{n+1+\beta} = u_j^n + \frac{\beta + 1}{\alpha + 1} (u_j^{n+1+\alpha} - u_j^n)$$

$$\frac{u_j^{n+1} - u_j^n}{\tau} + \frac{1}{6\beta(\beta+1)} \left\{ \frac{\partial f}{\partial x} \right\}_j^{n+1+\beta} +$$

$$+ \frac{3\beta+1}{6\beta} \left\{ \frac{\partial f}{\partial x} \right\}_j^{n+1} + \frac{3\beta+2}{6(\beta+1)} \left\{ \frac{\partial f}{\partial x} \right\}_j^n = 0$$

The schemes (4.8) with $\beta > 0$ are unconditionally stable (for $Z_0 \geq 0$), because they are similar to schemes (4.7) in the linear case.

5. Numerical examples.

An examples of application of "following" high order accuracy methods to integration of linear convective equation, Euler and Navier-Stokes equations are shown in this section. The choice of model problems demonstrates typical peculiarities of developed methods and codes. In particular, the results for linear convective equation illustrate the high order of accuracy methods.

Then the results for 2D and 3D Euler equations demonstrate the quality of shock and rare wave solutions and some other properties. At the end of section two test problems for a steady and unsteady viscous laminar flow are solved using Navier-Stokes equations.

Figure 2 and 3 show test results for the model convective problems

$$\frac{\partial u}{\partial t} + \frac{\partial u}{\partial x} = 0 \quad (5.1)$$

where

$$u(x, 0) = \sin \pi x, \quad -1 \leq x \leq 1$$

with periodical boundary conditions and using uniform grids. This results have been obtained by A. Kozerod for the authors' request. The truncation error ε from space size h is presented for the time $t = 1$. The value ε is defined for the norm l_2

$$\varepsilon = \left(\frac{1}{2} \int_{-1}^1 |u - u_e|^2 dx \right)^{1/2} \quad (5.2)$$

where u_e is the exact solution of problem (5.1). The space derivatives for all cases are calculated with the third order of accuracy, without using the limiting functions (the solid lines) and using the limiting functions in form (3.9) (the dotted lines). The index 1 relates to the implicit scheme (4.1) with $\sigma = 1$ (the first order of accuracy by t), the index 2- to the scheme (4.1) with $\sigma = 0.5$ (the second order of accuracy by t) and the index 3 - to the scheme (4.6) for the $\alpha = 0.5$ (the third order of accuracy by t). Figure 2 presents results

for the Courant number $C = \frac{\tau}{h} = 1$, figure 3 - for the

Courant number $C = 2.5$. We can see the logarithm ε depends on the logarithm h linearly with the angle tangent 1, 2 and 3. If we use the limiting functions the accuracy of the scheme (4.6) is only two times more than the accuracy of the second order scheme. When the Courant number is $C = 2.5$ (figure 3) the errors of time derivative approximation have the great role and the accuracy of the scheme (4.6) has the third order (with or without the limiting functions).

A second example for demonstration of accuracy concerns a 2D transonic turbine cascade. Figure 4 illustrates the constant entropy error lines in percents % for first (1), second (2) and (3) third order schemes. We can see very small level of errors for high order scheme. For this case the mesh contains 57×10 cells, the exit Mach number $M_2 = 0.8$.

The impressive capability of developed schemes is demonstrated by some solutions of inviscid and viscous

problems. The first results of this series present 2D and 3D inviscid flows.

Fig. 5 illustrates transonic shock flow results in model symmetric cascade under angle of attack 10° . Here the H-type mesh with 158×40 cells is used. Exit Mach number is $M_2 = 0.73$. Mach constant lines on pressure and suction sides are presented. Dotted lines are sonic lines.

Fig. 6 shows free underexpanded axisymmetric jet with value $n = p_0 / p_\infty = 2$ and the exhaust Mach number $M_0 = 2$. The computational grid contains 40 cells and is connected with the boundary jet. The pressure constant lines are given with interval $\Delta p = 0.04$. We want to emphasize the good resolution of a shock and rarefaction waves, much better than for the first order accuracy method [7,8].

The next results demonstrate the supersonic flow with the initial Mach number $M_0 = 3$ ($x_0 = 0$) into a channel (fig.7). Here also we can see very good monotone solution near shocks and other waves.

The 3D inviscid supersonic shock solution between two intersected wedges (the leading edge angle $\gamma = 12.2^\circ$) with initial Mach number $M_0 = 3.17$ is shown in fig.8. In this case we have self-similar solution with Mach shock deflection, which is presented as pressure contour lines with $\Delta p = 0.07$. A Cartesian mesh had 30×30 cells (in the plate $x = const$). This result demonstrates good 3D shock resolutions.

Now we present the 2D results of the two models viscous problems solutions, using Reynolds's averaging Navier-Stokes equations. These problems involve a steady axisymmetric flow of air first in a constant-area cylindrical duct, then through a reverse-flow angled orifice, and finally into the atmosphere as a free jet, as depicted in Fig.9. Two parameters differential turbulent model ($q - \omega$) is used [35]. Computational mesh contains 80×60 cells. Fig.9 presents velocity constant lines with interval $\Delta V = 0.03$. Velocity value relates to stagnation sound speed value. Fig. 10 presents streamline contours. The mass discharge coefficient equals 0.615.

The last viscous 2D problem is an unsteady shock and symmetric wedge interaction, as depicted in fig.11. The wedge has a base dimension of 56 cm and the symmetric leading and trailing wedge angle are 45 degrees. Fig.11 and 12 illustrate constant density contours at $t = 60$ and 87 microseconds. In these time moments the solutions have automodeling type. Here the algebraic Baldwin-Lomax turbulent model is used [36]. The mesh contains 90×70 cells. The two last solutions were presented as special benchmark problems on Canadian CFD Conference in June 93.

Results, which are presented in this lecture demonstrate a good possibility of developed numerical methods for calculation steady and unsteady flow of inviscid and viscous gas in the wide range of velocity

(for deep subsonic, transonic, supersonic and hypersonic speed).

The next lectures contain many illustrated material for solution of various practical problems of gas turbine engines and its components design and verification of computational codes.

References

1. Hirsh C. Numerical computation of internal and external flows. 1988, Vol. 1, 515 p. and Vol. 2, 691 p.
2. Applied Computational Aerodynamics, Vol. 125, Progress in Astronautics and Aeronautics, Published by AIAA, 1991, 874 p.
3. Focus '92. Computational Fluid Dynamics - Part 1. Aerospace America, 1992, No.1.
4. Focus '92. Computational Fluid Dynamics - Part 2. Aerospace America, 1992, No.2.
5. Godunov S. K. Difference method for calculation of weak solutions of fluid dynamic equations. Math. Sbornik, 1959, Vol. 47(89), No.3, pp.271-306, (in Russian).
6. Godunov S. K., Zabrodin A. V., Prokopov G. P. Difference scheme for two dimensional unsteady problems of gasdynamics and calculation flow with detach shock wave, J. of Comp. Math. and Math. Phys., 1961, Vol. 1, No.6, pp. 1020-1050, (in Russian).
7. Godunov S. K., Zabrodin A. V., Ivanov M. Ja., Kraiko A. N., Prokopov G. P. Numerical solution of gas dynamic multidimensional problems, M., Nauka, 1976, 400p, (in Russian).
8. Godunov S., Zabrodine A., Ivanov M., Kraiko A., Prokopov G. Resolution numerique des problemes multidimensionnels de la dynamique des gas. Editions Mir, Moscow, 1979, 414 p.
9. Fedorenko R. P. Application of high order accuracy difference schemes for numerical solution of hyperbolic equations, J. of Comput. Math. and Math. Phys., 1962, Vol.2, No.6, pp. 1122-1128, (in Russian).
10. Goldin V. Ja., Kalitkin N.N., Shishova T. V. Nonlinear difference schemes for hyperbolic equations, J. of Comp. Math. and Math. Phys., 1965, Vol.5, No.5, pp. 938-944, (in Russian).
11. Rusanov V.V. Difference schemes of the third order of accuracy for shock capturing solutions. Papers of Academy of Science USSR, 1968, Vol. 180, No.6, pp. 1303-1305, (in Russian).
12. Balakin V. B. On Runge-Kutta type methods for gas dynamics, J. of Comp. Math. and Math. Phys., 1970, Vol. 10, No.6, pp. 1512-1519, (in Russian).
13. Tolstykh A. I. On numerical method of solution Navier-Stokes equations for compressible gas in wide region of Reynolds numbers, Rep. Ac. of Sci., 1973, Vol. 210, No.1, pp. 48-51, (in Russian).
14. Tolstykh A. I. Compact difference schemes and their applications to fluid dynamics problems, M. - Nauka, 1990, 230 p, (in Russian).
15. Kolgan V. P. Application of minimum derivatives values principal to difference schemes construction for shock capturing gas dynamics solutions, Sci. Notes of TcAGI, 1972, Vol. 3, No.6, pp. 68-77, (in Russian).
16. Boris J.P., Book D. L. Flux corrected transport, ISHASTA, A fluid transport algorithm that works, J. of Comp. Phys. 1973, Vol.11, No.1, pp.38-69.
17. Van Leer B. Towards the ultimate conservative difference scheme. Monotonicity and conservation combined in a second order scheme, J. of Comp. Phys., 1974, Vol. 14, No.2, pp.361-370.
18. Kopchenov V. I., Kraiko A. N. Monotone second order accuracy scheme for hyperbolic systemes with two independent variables. J. of Comp. Math. and Math. Phys., 1983, Vol.23, No.19, pp.848-859, (in Russian).
19. Rodionov A. V. Monotone second order accuracy scheme for shock capture calculation of nonequilibrium flows, J. of Comp. Math. and Math. Phys., 1987, Vol.27, No.4, pp.585-593, (in Russian).
20. Harten A. High resolution schemes for hyperbolic conservation laws. J. of Comp. Phys., 1983, Vol.49, No.3, pp.357-393.
21. Jameson A., Lax P. D. Conditions for the construction of multi-point total variation diminishing schemes, Applied Numerical Mathematics, 1986, Vol.2, pp.335-345.
22. Golella P., Woodward P.R. The piecewise parabolic method (PPM) for gasdynamical simulations.- J. of Comput. Phys., 1984, Vol. 54, No.1, p.174-201.
23. Ivanov M. Ja., Nigmatullin R. Z. Implicit high accuracy Godunov's scheme for integration of Euler equation, J. of Comp. Math. and Math. Phys., 1987, Vol.27, No.11, p. 1725-1735, (in Russian).
24. Ivanov M. Ja., Nigmatullin R. Z., Krupa V. G. Implicit high order accuracy Godunov type scheme for integration of Navier-Stokes equations. J. of

- Comp. Math. and Math. Phys., Vol. 29, No.6, pp.888-901, (in Russian).
25. Ivanov M. Ja., Kostege V. K., Krupa V. G., Nigmatullin R. Z. Design of high-load aviation turbomachines using modern 3D computational methods. Papers from the 11-th International Symposium on Air Breathing Engines, Sep.20-24, 1993, pp.355-365.
 26. Courant R., Isaacson E., Rees M. On the solution of nonlinear hyperbolic differential equations by finite difference, Com. P. and Appl. Math., 1952, Vol. 5, No. 2, pp. 243-254.
 27. Lax P. D. Weak solutions of nonlinear hyperbolic equations and their numerical computations, Com. P. and Appl. Math., 1954, Vol. 7, No. 1, pp. 159-193.
 28. Lax P. D., Wendroff B. Systemes of conservation laws, Com. P. and Appl. Math., 1960, Vol. 13, No. 2, pp. 217-237.
 29. Sweby P.K. High resolution schemes using flux limiters for hyperbolic conservation laws, SIAM Journal of Numerical Analysis, 1984, Vol. 21, No.5, pp.995-1011.
 30. Chakravarthy S. R., Harten A., Osher S. Essentially non-oscillatory shock-capturing schemes of arbitrarily-high accuracy, AIAA Paper No. 86-0339, 1986, 14p.
 31. Yang J. Y. Third-order nonoscillatory schemes for the Euler equations, AIAA Journal, 1991, Vol. 29, No. 10, pp. 1611-1618.
 32. Yamamoto S., Daiguji H. High-order-accurate upwind schemes for solving the compressible Euler and Navier-Stokes equations, Computers Fluids, 1993, Vol. 22, No. 2/3, pp. 259-270.
 33. Pinchukov V. I. On construction of monotone schemes of various order of accuracy for one class of equations, J. of Comp. Math. and Math. Phys., 1994, (in Russian).
 34. Rogdestvensky B. L., Yanenko N. N., Quasilinear equations systems, M., Nauka, 1978, 687p, (in Russian).
 35. Coakley T. J. Turbulence modeling methods for the compressible Navier-Stokes equations, AIAA Paper N83-1693, 1983, 9p.
 36. Baldwin B. S., Lomax H. Thin - layer approximation and algebraic model for separated turbulent flows, AIAA Paper N78-257, 1978, 10p.

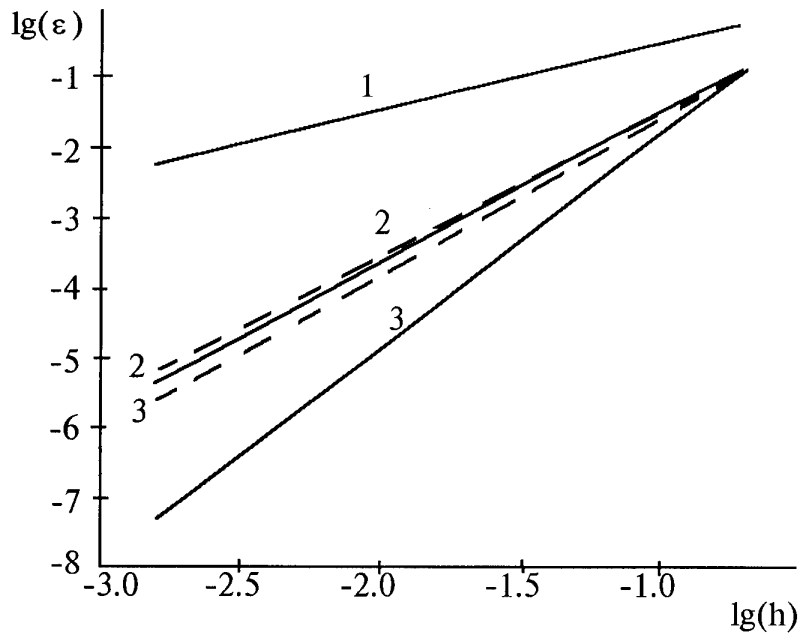


Fig. 2 Evolution of solution error ε with space mesh size.
 Courant number $C=1$.
 1 - the first order scheme;
 2 - the second order scheme;
 3 - the third order scheme;
 solid lines - without the limiting functions;
 dotted lines - with the limiting functions.

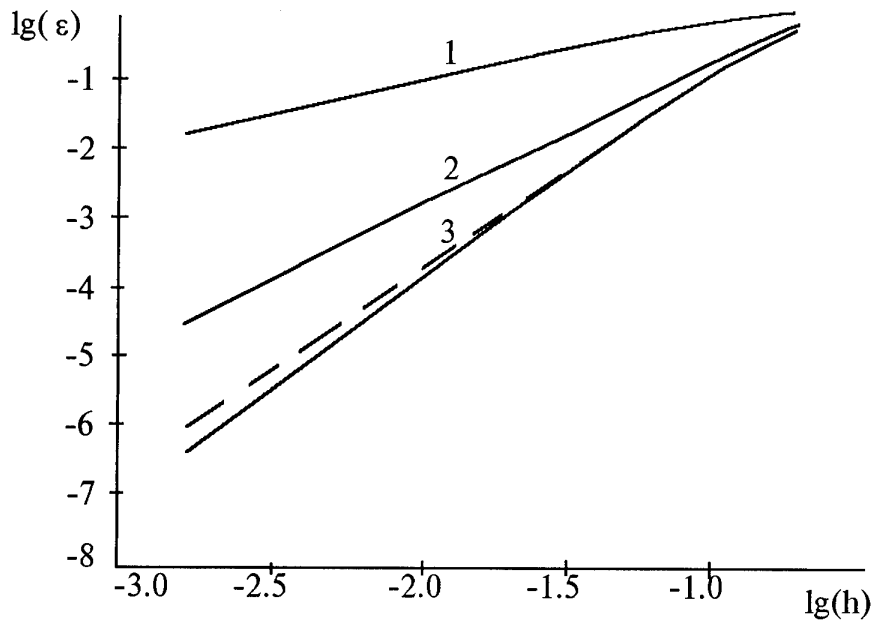


Fig. 3 Evolution of solution error ε with space mesh size.
 Courant number $C=2.5$.
 1 - the first order scheme;
 2 - the second order scheme;
 3 - the third order scheme;
 solid lines - without the limiting functions;
 dotted lines - with the limiting functions.

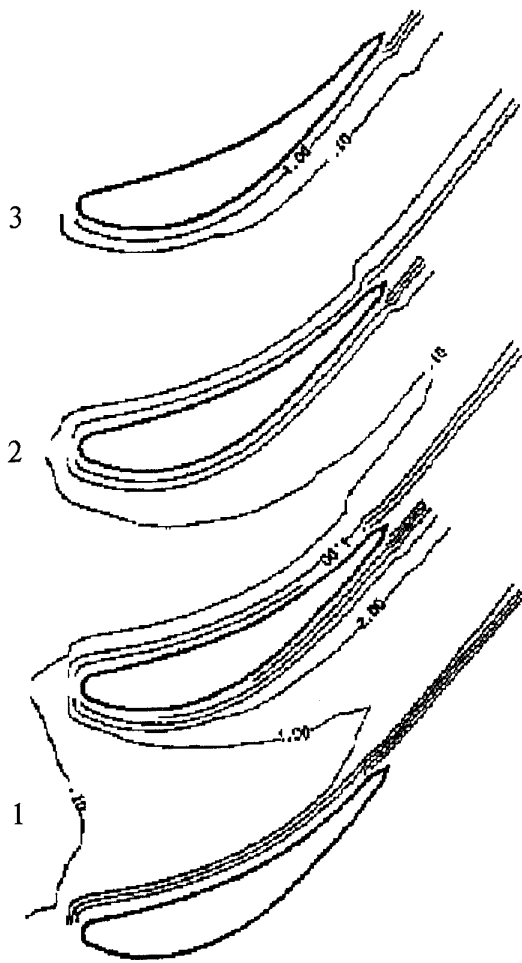


Fig. 4 The constant entropy error lines for 2D transonic turbine cascade: the mesh 57×10 , the exit Mach number - 0.8. 1 - the first order scheme; 2 - the second order scheme; 3 - the third order scheme.

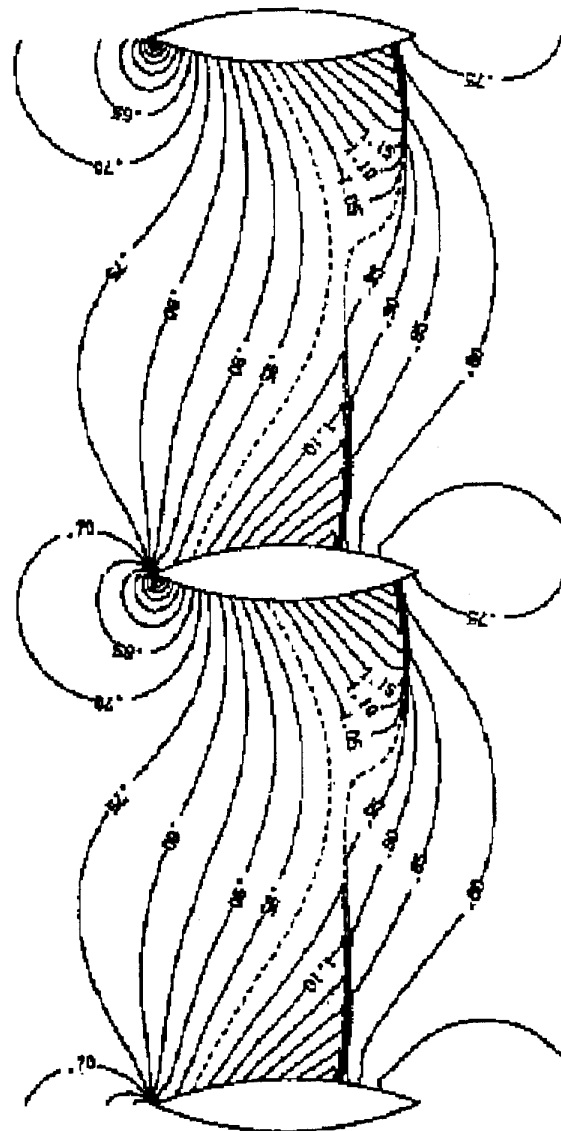


Fig. 5 Transonic shock flow in 2D symmetric cascade under angle of attack 10° . The exit Mach number - 0.73. Mach constant lines.

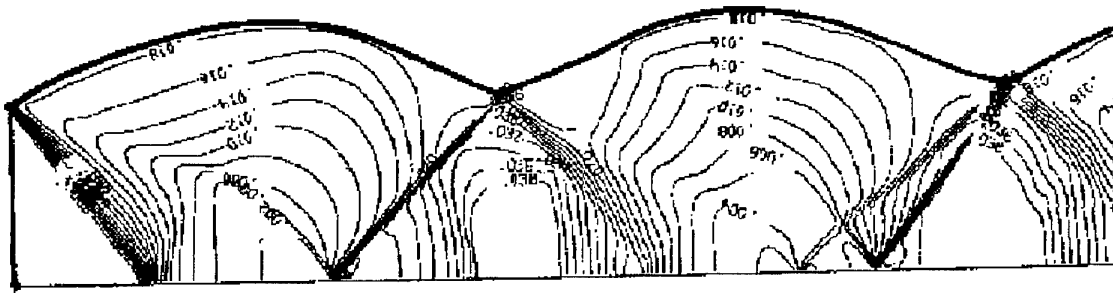


Fig. 6 The free underexpanded axisymmetric supersonic jet.
The pressure constant lines picture.
Initial Mach number $M_0 = 2$, $\rho_0 / \rho_\infty = 2$

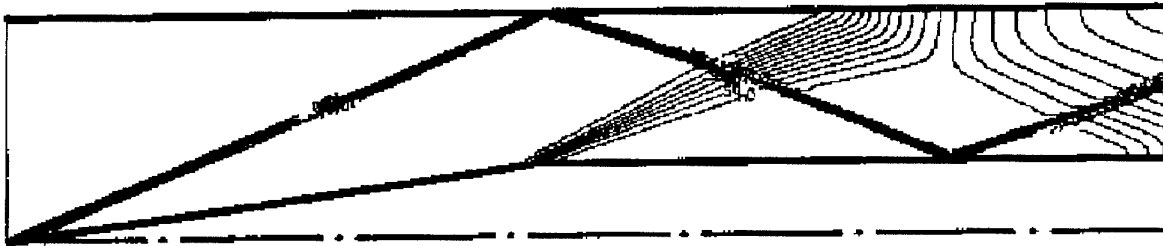


Fig. 7 Supersonic flow into 2D channel. Inlet Mach number $M_0 = 3$.

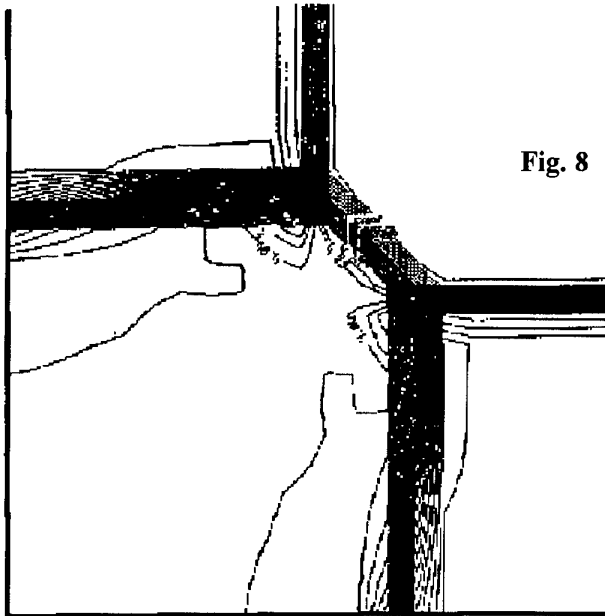


Fig. 8 The inviscid supersonic shock solution between two intersected wedge.
The pressure contour lines.
Leading edge angle $\gamma = 12.2^\circ$, the initial Mach number $M_0 = 3.17$.

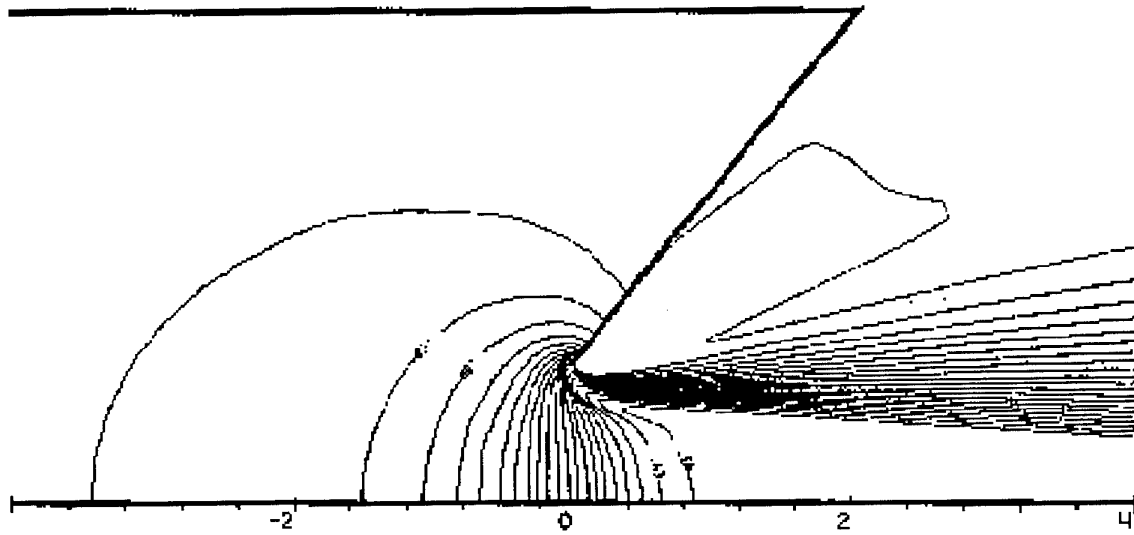


Fig. 9 Axisymmetric free - jet flow.
Velocity constant lines with interval $\Delta V = 0.03$.

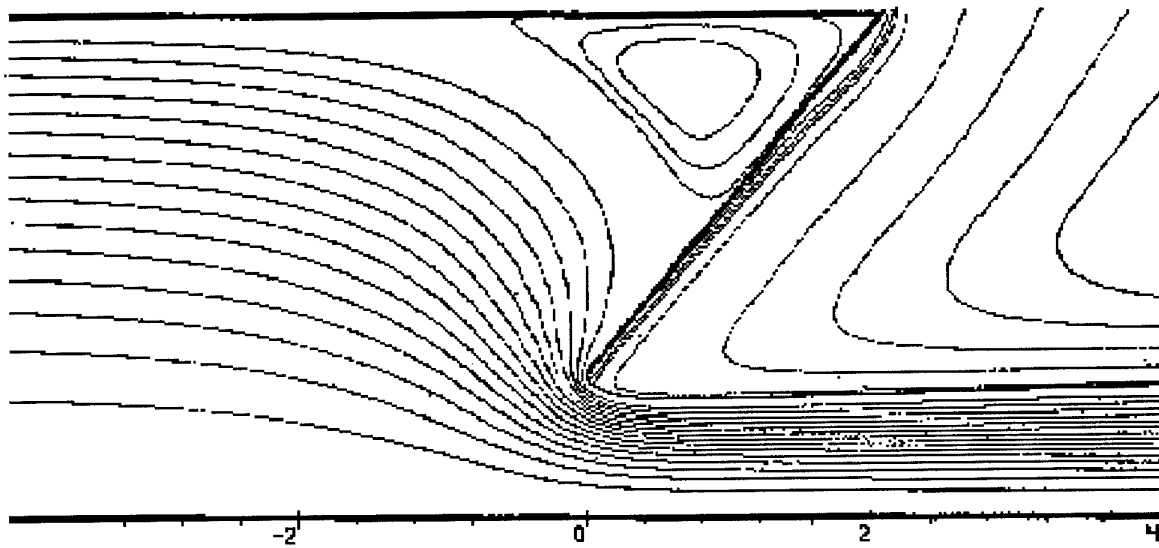


Fig. 10 Axisymmetric free - jet flow.
Streamline contour. Mass discharge coefficient 0.615

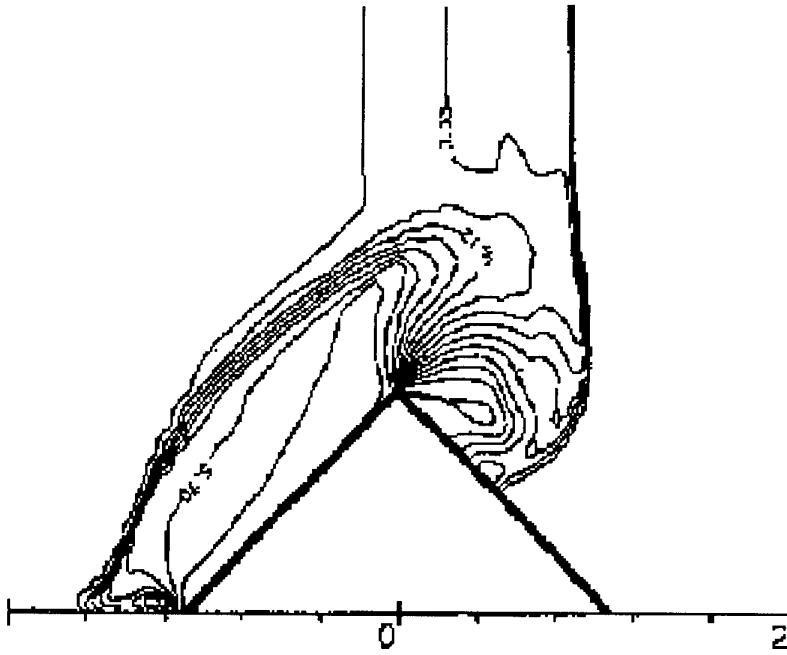


Fig. 11 Unsteady shock/symmetric wedge interaction.
Constant density contour at $t = 60$ microsecond.

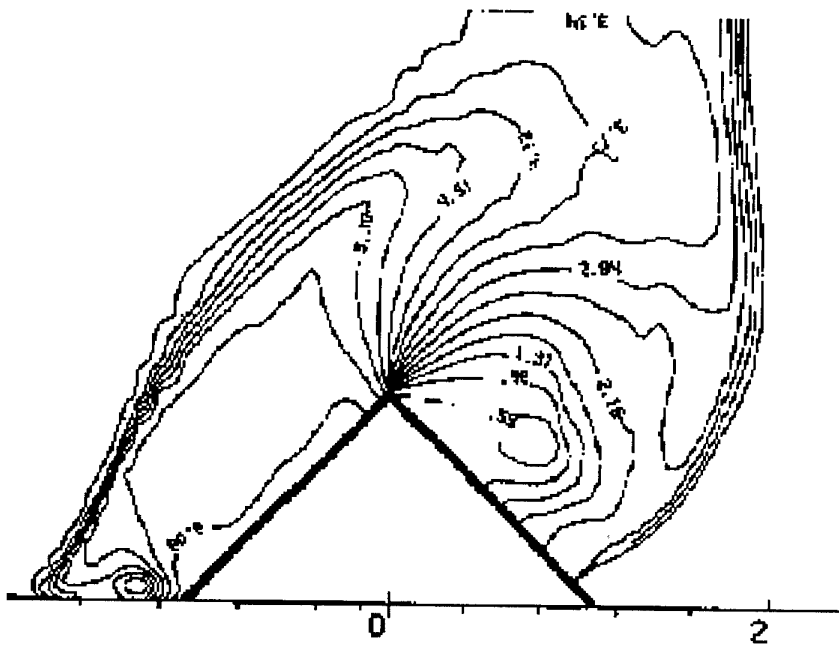


Fig. 12 Unsteady shock/symmetric wedge interaction.
Constant density contour at $t = 87$ microsecond.

Solution of Navier-Stokes equations using high accuracy monotone schemes

by

Dr. V. G. Krupa, Prof. M. Ja. Ivanov
 CIAM (Central Institute of Aviation Motors)
 2, Aviamotornaya St.,
 Moscow, Russia, 111250

Abstract

Numerical monotone methods for integration of the Reynolds averaged Navier-Stokes equations are presented. These methods employ finite volume formulation, implicit high-order accuracy Godunov type scheme and two-equation ($q-\omega$) turbulence model, based on integration up to the wall. To illustrate of the typical peculiarities of these methods the computations of viscous flows in curvilinear ducts, around 2D airfoils and 3D shock-wave boundary layer interaction are considered. Available experimental data are used for verification of the computed results.

Nomenclature

A, B, C, D	Jacobian matrices
E, F, G	mass, momentum and energy fluxes
I	identity matrix
J	transformation matrix
M	Mach number
Re	Reynolds number
Pr	Prandtl number
T	temperature
U	conservative variables
k	turbulent kinetic energy
p	pressure
t	time
v	relative velocity
(x, r, φ)	cylindrical coordinates
γ	specific heats ratio
(ξ, η, ζ)	general curvilinear coordinates
ε	turbulence energy dissipation
λ	bulk viscosity coefficient
μ	molecular viscosity coefficient
ρ	density
$\tau_{xx}, \tau_{xr}, \tau_{x\varphi},$ $\tau_{rr}, \tau_{r\varphi}, \tau_{\varphi\varphi}$	viscous shear stress

Ω - angular velocity

Superscripts

n - denotes time level
 \wedge - denotes quantities in generalized coordinates

Subscripts

i, j, k - denotes quantities in the centers of computational cells
 ξ, η, ζ - denotes differentiation in ξ, η and ζ directions, respectively.

Introduction

At present time a large number of numerical methods for the solution of Navier-Stokes equations have been developed [1,2]. We would like to indicate shortly some of these methods. One of the widely used is the Beam and Warming approximate factorization scheme [3]. An implicit method of MacCormack [4] based on a bidiagonal solution technique has been also applied successfully to solve fluid dynamic problems. The multistage Runge-Kutta time-stepping scheme with multigrid technique developed by Jameson et al. [5,6] for Euler equations has been extended to 2D and 3D Navier-Stokes equations [7,8].

Most of these methods represent non-dissipative approximations of the convective terms and frequently display oscillations in the neighborhood of shocks. To suppress (but not completely eliminate) these oscillations artificial dissipative terms have to be added. In practice, it needs a "tuning" of dissipation coefficients. Also, these methods have time-step restrictions due to either factorization errors or explicit structure of the scheme and demonstrate rather low convergence to steady-state solution.

The construction of accurate and reliable methods for solving Navier-Stokes equations can be done on the basis of high-order accuracy monotone schemes. One of the first monotone schemes was originally proposed by Godunov [9]. The method uses a piecewise constant distributions of parameters in each cell and a procedure

of arbitrary discontinuity breakdown (exact solution of Riemann problem at cell boundary). The method is conservative, have good shock-capturing properties and closely simulates wave propagation at each cell. The method was widely used for computation of inviscid flows [10], however, its application to solve Navier-Stokes equations has long been restricted because of the first order accuracy. Extension of the method to the second order accuracy in space has been carried out in [11]. To satisfy the conditions of monotonicity piecewise linear distributions of parameters were restricted to 'minimum derivatives values principle'. More recently, closely related to this method a family, of so-called high-accuracy TVD schemes [12-15] has been developed for Euler equations. These schemes are second or higher order accurate, capture discontinuities with high resolution and need no artificial dissipation. Up to now, a large number of Navier-Stokes solvers, based on TVD formulation, have been developed for computation of external and internal viscous flows (see, for example, [16-23]).

In this lecture, using ideas of the previous lecture, the numerical method for solving Navier-Stokes equations is discussed. The method is based on the implicit monotone second and third order accuracy Godunov-like scheme. The Reynolds averaged Navier-Stokes equations closed by two-equation turbulence model are written in the conservation-law form generalized curvilinear coordinate system. The main ideas of explicit Godunov scheme - principle of monotonicity and procedure of arbitrary discontinuity break-down are used. Piecewise parabolic distributions of the parameters over cells of the computational grid are used in order to increase the order of approximation [13,24]. The scheme is written in delta form [3]. The implicit operator is constructed taking into account the sign of the eigenvalues of the Jacobian matrix [25]. To avoid time-step restrictions due to factorization, the unfactored implicit operator is inverted using Gauss-Seidel line method. Extension of algorithm to third-order accuracy in time is also presented.

The Navier-Stokes solvers are the necessary tools for prediction of viscous effects in the aerodynamic design. Applications of the present numerical method to turbomachinery problems will be presented in the next lectures. In this lecture some numerical examples are considered. The computed results include turbulent flows in curvilinear ducts, over 2D airfoil and 3D shock-wave boundary layer interaction. Accuracy of the methods is estimated by comparison with available experimental data.

1. Governing Equations

Reynolds-averaged Navier-Stokes equations in a cylindrical (x, r, φ) system of coordinates rotating with angular velocity Ω are:

$$\frac{\partial U}{\partial t} + \frac{\partial F}{\partial x} + \frac{\partial G}{\partial r} + \frac{\partial E}{\partial \varphi} = K, \quad (1.1)$$

$$F = F_i - F_v, \quad G = G_i - G_v, \quad E = E_i - E_v$$

$$U = \begin{bmatrix} \rho \\ \rho v_x \\ \rho v_r \\ \rho v_\varphi \\ e \end{bmatrix}, \quad F_i = \begin{bmatrix} \rho v_x \\ \rho v_x^2 + p \\ \rho v_x v_r \\ \rho v_x v_\varphi \\ (e + p)v_x \end{bmatrix},$$

$$G_i = \begin{bmatrix} \rho v_r \\ \rho v_x v_r \\ \rho v_r^2 + p \\ \rho v_r v_\varphi \\ (e + p)v_r \end{bmatrix}, \quad E_i = \frac{1}{r} \begin{bmatrix} \rho v_\varphi \\ \rho v_x v_\varphi \\ \rho v_r v_\varphi \\ \rho v_\varphi^2 + p \\ (e + p)v_\varphi \end{bmatrix},$$

$$F_v = \frac{1}{\text{Re}} \begin{bmatrix} 0 \\ \tau_{xx} \\ \tau_{xr} \\ \tau_{x\varphi} \\ A_x \end{bmatrix}, \quad G_v = \frac{1}{\text{Re}} \begin{bmatrix} 0 \\ \tau_{xr} \\ \tau_{rr} \\ \tau_{r\varphi} \\ A_r \end{bmatrix},$$

$$E_v = \frac{1}{\text{Re}r} \begin{bmatrix} 0 \\ \tau_{x\varphi} \\ \tau_{r\varphi} \\ \tau_{\varphi\varphi} \\ A_\varphi \end{bmatrix},$$

$$K = \frac{1}{r} \begin{bmatrix} -\rho v_r \\ -\rho v_x v_r + \text{Re}^{-1} \tau_{xr} \\ \rho((v_\varphi + \Omega r)^2 - v_r^2) + \text{Re}^{-1} (\tau_r - \tau_{\varphi\varphi}) \\ -2\rho v_r (v_\varphi + \Omega r) + 2\text{Re}^{-1} \tau_{r\varphi} \\ -v_r (e + p) + \text{Re}^{-1} A_r \end{bmatrix},$$

$$\tau_{xx} = (\lambda + 2\mu) \frac{\partial v_x}{\partial x} + \lambda \left(\frac{\partial v_r}{\partial r} + \frac{1}{r} \frac{\partial v_\varphi}{\partial \varphi} + \frac{v_r}{r} \right),$$

$$\tau_{xr} = \mu \left(\frac{\partial v_r}{\partial x} + \frac{\partial v_x}{\partial r} \right), \quad \tau_{x\varphi} = \mu \left(\frac{\partial v_\varphi}{\partial x} + \frac{1}{r} \frac{\partial v_x}{\partial \varphi} \right)$$

$$\tau_{rr} = (\lambda + 2\mu) \frac{\partial v_r}{\partial r} + \lambda \left(\frac{\partial v_x}{\partial x} + \frac{1}{r} \frac{\partial v_\varphi}{\partial \varphi} + \frac{v_r}{r} \right),$$

$$\tau_{r\varphi} = \mu \left(r \frac{\partial v_\varphi}{\partial r} \frac{1}{r} + \frac{1}{r} \frac{\partial v_r}{\partial \varphi} \right),$$

$$\tau_{\varphi\varphi} = (\lambda + 2\mu) \frac{\partial v_\varphi}{r \partial \varphi} + \lambda \left(\frac{\partial v_x}{\partial x} + \frac{\partial v_r}{\partial r} + \frac{v_r}{r} \right) + 2\mu \frac{v_r}{r}$$

$$A_x = \tau_{xx} v_x + \tau_{xr} v_r + \tau_{x\varphi} v_\varphi + \frac{\mu}{\text{Pr}} \frac{\partial T}{\partial x},$$

$$A_r = \tau_{rx} v_x + \tau_{rr} v_r + \tau_{r\varphi} v_\varphi + \frac{\mu}{\text{Pr}} \frac{\partial T}{\partial r}$$

$$A_\varphi = \tau_{\varphi x} v_x + \tau_{\varphi r} v_r + \tau_{\varphi\varphi} v_\varphi + \frac{\mu}{\text{Pr}} \frac{\partial T}{r \partial \varphi},$$

$$p = \frac{\gamma - 1}{\gamma} \rho T,$$

$$e = \rho \frac{v_x^2 + v_r^2 + v_\varphi^2 - (\Omega r)^2}{2} + \frac{p}{\gamma - 1},$$

$$\mu = \mu_l + \mu_t, \quad \frac{\mu}{\text{Pr}} = \frac{\mu_l}{\text{Pr}_l} + \frac{\mu_t}{\text{Pr}_t}$$

Here, t stands for time, ρ - for density, p - for pressure, T for temperature; v_x, v_r, v_φ are the physical components of the relative velocity vector along

x, r and φ axes; μ_l and μ_t are the molecular and turbulent viscosity coefficients, $\lambda = -(2/3)\mu$, $\text{Pr}_l = 0.72$ and $\text{Pr}_t = 0.9$ are Prandtl numbers; $\gamma = 1.4$ is the specific heat ratio, and Re is the Reynolds number.

The system (1.1) has been written in dimensionless form: the components of the relative velocity vector v have been divided by the characteristic value V_∞ , the density by ρ_∞ , the pressure by $\rho_\infty V_\infty^2$, temperature by V_∞^2 / C_p (C_p is the specific heat at a constant pressure), and the linear dimensions by the characteristic length L .

The turbulent viscosity coefficient μ_t is calculated using the two-equation ($q - \omega$) model of turbulence [26]; the quantities q and ω are related with the kinetic energy of turbulence k and the dissipation ratio ε : $q = k^{1/2}$, $\omega = \varepsilon / k$. In dimensionless form (q divided by V_∞ , ω by V_∞ / L) the system of equations of the ($q - \omega$) model in rotating cylindrical system of coordinates has the form:

$$\frac{\partial U_t}{\partial t} + \frac{\partial F_t}{\partial x} + \frac{\partial G_t}{\partial r} + \frac{\partial E_t}{\partial \varphi} = K_t, \quad (1.2)$$

$$F_t = F_{ti} - F_{tv}, \quad G_t = G_{ti} - G_{tv}, \quad E_t = E_{ti} - E_{tv}$$

$$U_t = \begin{vmatrix} \rho q \\ \rho \omega \end{vmatrix}, \quad F_{ti} = \begin{vmatrix} \rho q v_x \\ \rho \omega v_x \end{vmatrix}, \quad G_{ti} = \begin{vmatrix} \rho q v_r \\ \rho \omega v_r \end{vmatrix},$$

$$E_{ti} = \frac{1}{r} \begin{vmatrix} \rho q v_\varphi \\ \rho \omega v_\varphi \end{vmatrix},$$

$$F_{tv} = \frac{1}{\text{Re}} \begin{vmatrix} \mu_q \frac{\partial q}{\partial x} \\ \mu_\omega \frac{\partial \omega}{\partial x} \end{vmatrix}, \quad G_{tv} = \frac{1}{\text{Re}} \begin{vmatrix} \mu_q \frac{\partial q}{\partial r} \\ \mu_\omega \frac{\partial \omega}{\partial r} \end{vmatrix}, \quad E_{tv} = \frac{1}{\text{Re}} \begin{vmatrix} \mu_q \frac{\partial q}{r \partial \varphi} \\ \mu_\omega \frac{\partial \omega}{r \partial \varphi} \end{vmatrix},$$

$$K_t = \left[\begin{array}{l} \frac{-\rho q v_r - \text{Re}^{-1} \mu_q \frac{\partial q}{\partial r} + \frac{\rho \omega q}{2} \left(C_\mu D \frac{P}{\omega^2} - \frac{2}{3} \frac{\text{div} \bar{v}}{\omega} - 1 \right)}{r} \\ \frac{-\rho q v_r - \text{Re}^{-1} \mu_\omega \frac{\partial \omega}{\partial r} + \rho \omega^2 \left(C_1 \left(C_\mu \frac{P}{\omega^2} - \frac{2}{3} \frac{\text{div} \bar{v}}{\omega} \right) - C_2 \right)}{r} \end{array} \right]$$

$$\mu_q = \mu_1 + \frac{\mu_t}{\text{Pr}_q}, \quad \mu_\omega = \mu_1 + \frac{\mu_t}{\text{Pr}_\omega}, \quad \mu_t = \text{Re} C_\mu D \rho \frac{q^2}{\omega}$$

$$D = 1 - \exp(-\text{Re} \alpha \rho q \frac{d_n}{\mu_1}),$$

$$D = 2 \left[\left(\frac{\partial v_x}{\partial x} \right)^2 + \left(\frac{\partial v_r}{\partial r} \right)^2 + \left(\frac{\partial v_\varphi}{r \partial \varphi} + \frac{v_r}{r} \right)^2 \right] +$$

$$+ \left(\frac{\partial v_r}{\partial x} + \frac{\partial v_x}{\partial r} \right)^2 + \left(\frac{\partial v_\varphi}{\partial x} + \frac{\partial v_x}{r \partial \varphi} \right)^2 +$$

$$+ \left(\frac{\partial v_\varphi}{\partial r} + \frac{\partial v_r}{r \partial \varphi} - \frac{v_\varphi}{r} \right)^2 - \frac{2}{3} (\text{div} \bar{v})^2$$

$$\text{div} \bar{v} = \left(\frac{\partial v_x}{\partial x} + \frac{\partial v_r}{r \partial r} + \frac{\partial v_\varphi}{r \partial \varphi} \right)$$

Here, d_n is the distance along normal to the wall. The values of the constants entering into (1.2) as follows:

$$C_\mu = 0.09, \quad C_1 = 0.045 + 0.405D, \quad C_2 = 0.92$$

$$\alpha = 0.0065, \quad \text{Pr}_q = 1, \quad \text{Pr}_\omega = 1.3.$$

2. Numerical Method

We will now describe the main features of numerical methods construction with reference to the example of system (1.1); for (1.2) the difference scheme is similarly constructed.

The initial system of equations (1.1) is written in the new curvilinear coordinates

$$\xi = \xi(x, r, \varphi), \quad \eta = \eta(x, r, \varphi), \quad \zeta = \zeta(x, r, \varphi),$$

retaining the divergent form:

$$\frac{\partial \hat{U}}{\partial t} + \frac{\partial \hat{F}}{\partial \xi} + \frac{\partial \hat{G}}{\partial \eta} + \frac{\partial \hat{E}}{\partial \zeta} = \hat{K} \quad (2.1)$$

$$\hat{U} = U/J, \quad \hat{F} = (\xi_x F + \xi_r G + \xi_\varphi E)/J,$$

$$\hat{G} = (\eta_x F + \eta_r G + \eta_\varphi E)/J,$$

$$\hat{E} = (\zeta_x F + \zeta_r G + \zeta_\varphi E)/J, \quad \hat{K} = K/J$$

The metric coefficients which appear in (2.1) are expressed using the formulae

$$\xi_x = J(r_\eta \varphi_\zeta - r_\zeta \varphi_\eta), \quad \eta_x = J(r_\zeta \varphi_\xi - r_\xi \varphi_\zeta),$$

$$\zeta_x = J(r_\xi \varphi_\eta - r_\eta \varphi_\xi), \quad \eta_\varphi = J(x_\zeta r_\xi - x_\xi r_\zeta),$$

$$\xi_r = J(x_\zeta \varphi_\eta - x_\eta \varphi_\zeta), \quad \eta_r = J(x_\xi \varphi_\zeta - x_\zeta \varphi_\xi),$$

$$\zeta_r = J(x_\eta \varphi_\xi - x_\xi \varphi_\eta),$$

$$\xi_\varphi = J(x_\eta r_\zeta - x_\zeta r_\eta),$$

$$\zeta_\varphi = J(x_\xi r_\eta - x_\eta r_\xi)$$

$$J = \frac{\partial(\xi, \eta, \zeta)}{\partial(x, r, \varphi)}$$

We shall use the generally accepted indications when constructing the difference scheme: a superscript n refers to the instant of time $t = n\tau$, where τ is the time step, while integer subscripts refer to the value of the function at the center of a computational cell, and two integers and a single half-integer refer to the value of the function at a cell boundary. Writing (2.1) at the $(n+1)$ -th time step, we carry out linearization with respect to the values at the n -th time step (see [3]). We will write the resulting difference scheme in a form that is convenient for using the iterative Gauss-Seidel method along a line $\xi, \zeta = \text{const}$ ($\Delta \xi = \Delta \eta = \Delta \zeta = 1$).

$$\begin{aligned} & (I + \mathcal{H}[A^+ + A^- + \nabla_\eta B^+ - \nabla_\eta B^- + C^+ + C^- - \\ & - D + 2(A_v + C_v) - \Delta_\eta \nabla_\eta B_v]) \Delta U_{i,j,k}^{n,p+1} = \\ & = \tau Z_{i,j,k} + \tau J_{i,j,k} [(A^+ + A_v) \Delta U_{i-1,j,k}^{n,p+1} + \\ & + (A^- + A_v) \Delta U_{i+1,j,k}^{n,p} + (C^+ + C_v) \Delta U_{i,j,k-1}^{n,p+1} + \\ & + (C^- + C_v) \Delta U_{i,j,k+1}^{n,p}] \end{aligned} \quad (2.2)$$

$$Z_{i,j,k} = \left[-J \left(\frac{\partial \hat{F}}{\partial \xi} + \frac{\partial \hat{G}}{\partial \eta} + \frac{\partial \hat{E}}{\partial \zeta} \right) \right]_{i,j,k}^n,$$

$$\Delta U^{n,p} = U^{n+1,p} - U^n, \quad \Delta_\eta f = f_{i,j+1,k} - f_{i,j,k},$$

$$\nabla_\eta f_{i,j,k} = f_{i,j,k} - f_{i,j-1,k}$$

where p is the number of the "internal" iteration. The Jacobian matrices in (2.2) have the form:

$$A = \frac{\partial \hat{F}_i}{\partial U} = A^+ - A^- = S_\xi \Lambda_\xi^+ S_\xi^{-1} - S_\xi \Lambda_\xi^- S_\xi^{-1},$$

$$B = \frac{\partial \hat{G}_i}{\partial U} = B^+ - B^- = S_\eta \Lambda_\eta^+ S_\eta^{-1} - S_\eta \Lambda_\eta^- S_\eta^{-1},$$

$$C = \frac{\partial \hat{E}_i}{\partial U} = C^+ - C^- = S_\zeta \Lambda_\zeta^+ S_\zeta^{-1} - S_\zeta \Lambda_\zeta^- S_\zeta^{-1}$$

$$\Lambda^\pm = \frac{1}{2} (|\Lambda| \pm \Lambda), \quad A_v = \frac{\partial \hat{F}_v}{\partial U_\xi}, \quad B_v = \frac{\partial \hat{G}_v}{\partial U_\eta},$$

$$C_v = \frac{\partial \hat{E}_v}{\partial U_\zeta}, \quad D = \frac{\partial \hat{K}}{\partial U}$$

Here, $\Lambda_\xi, \Lambda_\eta$ and Λ_ζ are diagonal matrices composed of the eigenvalues of the matrices A, B and C ; $|\Lambda|$ is a matrix composed of the absolute values of

Λ ; S_ξ, S_η and S_ζ are transformation matrices leading to the diagonal form. The splitting of the Jacobi matrices and the use of upwinding (in accordance with the sign of the eigenvalues) differences [25] enable one to increase the stability of the difference scheme.

The quantities U^{n+1} (for known $Z_{i,j,k}^n$) are found from the system (2.2). The direction around the computation domain was chosen as follows: for each fixed value of i (starting with $i=1$) we calculated the values of $\Delta U_{i,j,k}^n$, $k=1,2,\dots,k_{\max}$; we then passed on to the new layer ($i+1$).

The matrix of the operator on the left side (2.2) has a block (dimensions 5×5) tridiagonal form, and its inversion (determination of $\Delta U_{i,j,k}^n$,

$j=1,2,\dots,j_{\max}$, i and k fixed) is carried out by means of a three-point matrix sweep. In the case of

periodic (in j) boundary conditions for the inversion of the matrix it is necessary to use cyclic sweep formulae.

The method of calculating of right side of $Z_{i,j,k}^n$ is described in detail in [27]. The space derivatives in the viscous terms are approximated by central differences with second-order accuracy. The "inviscid" terms are calculated in terms of the flux vectors on the cell boundaries (the derivatives with respect to ξ and ζ are similarly calculated; accordingly, we will drop the indices i and k):

$$\left(\frac{\partial \hat{G}}{\partial \eta} \right)_j = \frac{\hat{G}_{j+1/2}^n - \hat{G}_{j-1/2}^n}{\Delta \eta}$$

To calculate the flux vectors, we use piecewise parabolic parameter distributions satisfying the condition of monotonicity (for linear system) [3,24]:

$$U_{j+1/2}^- = U_j^n + S_\eta \left[\frac{1+\varphi}{4} \Delta \hat{W}_j + \frac{1-\varphi}{4} \nabla \tilde{W}_j \right],$$

$$U_{j-1/2}^+ = U_j^n - S_\eta \left[\frac{1+\varphi}{4} \nabla \tilde{W}_j + \frac{1-\varphi}{4} \Delta \tilde{W}_j \right],$$

$$\Delta \tilde{W}_j = \min \text{mod}(\Delta W_j, b \nabla W_j),$$

$$\nabla \tilde{W}_j = \min \text{mod}(\nabla W_j, b \Delta W_j)$$

$$\Delta W_j = S_\eta^{-1} \Delta_\eta U_j^n, \quad \nabla W_j = S_\eta^{-1} \nabla_\eta U_j^n$$

$$1 \leq b \leq b_{\max}, \quad b_{\max} = \frac{3-\varphi}{1-\varphi}, \quad \varphi < 1.$$

$$\min \text{mod}(x, y) = \begin{cases} 0, & xy \leq 0 \\ \text{sign}(x) \min(|x|, |y|), & xy > 0 \end{cases}$$

where $U_{j+1/2}^\pm$ are the values of U^n on the right and left of the face of the cell with number $j+1/2$, respectively, and in the n *th* time layer. From the values of $U_{j+1/2}^-$ and $U_{j+1/2}^+$ using the procedure for solving the problem of the breakdown of an arbitrary discontinuity [9,10], we calculated the major quantities

from which the fluxes $\hat{G}_{j+1/2}$ are computed. This method of approximation does not require the introduction of terms with artificial dissipation and makes it possible to obtain stable solutions with second order accuracy.

3. Third-order accurate in time integration scheme

The method presented in Sec. 2 is a second order accurate in space (third-order accuracy can be achieved in one-dimensional uniform grid) and first-order accurate in time. Accuracy in time may not be crucial for the computation of steady-state solution by time-dependent method, but for computation of unsteady flows it may be desirable to increase the order of approximation in time. In this section we will describe a third-order accuracy in time scheme for integration of Navier-Stokes equations. Our consideration will be restricted to system of 2D Navier-Stokes equations; extension to 3D dimensions and turbulence model equations is quite straightforward.

A main attention will be focused on the approximation in time, the approximation of stationary part of equations being assumed to be known. In particular, the fluxes at cell boundary can be computed by formulae of Sec. 2.

The 2D Navier-Stokes equations in a moving, coordinate system $\xi = \xi(x, y, t)$, $\eta = \eta(x, y, t)$ take the form (x, y - Cartesian coordinates):

$$\frac{\partial \hat{U}}{\partial t} + \frac{\partial \hat{F}}{\partial \xi} + \frac{\partial \hat{G}}{\partial \eta} = 0 \quad (3.1)$$

$$\hat{U} = U/J, \quad \hat{F} = (\xi_t U + \xi_x F + \xi_y G)/J,$$

$$\hat{G} = (\eta_t U + \eta_x F + \eta_y G)/J,$$

$$F = F_i - F_v, \quad G = G_i - G_v$$

$$\mathbf{v} = \begin{bmatrix} \rho \\ \rho u \\ \rho v \\ e \end{bmatrix}, \quad \mathbf{F}_i = \begin{bmatrix} \rho u \\ \rho u^2 + p \\ \rho uv \\ (e+p)u \end{bmatrix}, \quad \mathbf{F}_v = \begin{bmatrix} 0 \\ \tau_{xx} \\ \tau_{yy} \\ A_x \end{bmatrix},$$

$$\mathbf{G}_i = \begin{bmatrix} \rho v \\ \rho uv \\ \rho v^2 + p \\ (e+p)v \end{bmatrix}, \quad \mathbf{G}_v = \frac{1}{\text{Re}} \begin{bmatrix} 0 \\ \tau_{yx} \\ \tau_{yy} \\ A_y \end{bmatrix}$$

$$e = \rho \left(\frac{u^2 + v^2}{2} \right) + \frac{\rho}{\gamma - 1}, \quad \mu = \mu_l + \mu_t,$$

$$\frac{\mu}{\text{Pr}} = \frac{\mu_l}{\text{Pr}_l} + \frac{\mu_t}{\text{Pr}_t}$$

where

$$\tau_{xx} = (\lambda + 2\mu)u_x + \lambda v_y, \quad \tau_{xy} = \tau_{yx} = \mu(v_x + u_y),$$

$$\tau_{yy} = (\lambda + 2\mu)v_y + \lambda u_x,$$

$$\xi_t = J(x_\eta y_t - y_\eta x_t), \quad \xi_x = Jy_\eta, \quad \xi_y = -Jx_\eta,$$

$$\eta_t = J(y_\xi x_t - x_\xi y_t), \quad \eta_x = -Jy_\xi, \quad \eta_y = Jx_\xi$$

$$J = \xi_x \eta_y - \xi_y \eta_x$$

From the considerations given in Sec. 4 of [28] we can now present a family of the third-order accuracy in time schemes for Eq. (3.1) (α - parameter)

$$\frac{\hat{U}_{i,j}^{n+1+\alpha} - \hat{U}_{i,j}^n}{\tau} + \frac{1}{2} Z_{i,j}^{n+1+\alpha} + \frac{1}{2} Z_{i,j}^n = 0, \quad (3.2)$$

$$\frac{\hat{U}_{i,j}^{n+1} - \hat{U}_{i,j}^n}{\tau} - \frac{3\alpha+1}{6\alpha} Z_{i,j}^{n+1+\alpha} + \frac{1}{6\alpha(\alpha+1)} Z_{i,j}^{n+1} + \frac{3\alpha+2}{6(\alpha+1)} Z_{i,j}^n = 0 \quad (3.3)$$

where

$$Z_{i,j} = \frac{\hat{F}_{i+1/2,j} - \hat{F}_{i-1/2,j}}{\Delta \xi} + \frac{\hat{G}_{i,j+1/2} - \hat{G}_{i,j-1/2}}{\Delta \eta}$$

Third order approximation in time of scheme (3.2), (3.3) can be justified by expansion in Taylor series at $t = (n+1)\tau$. The scheme (3.2), (3.3) for linear scalar case is unconditionally stable if $\alpha > 0$ provided that approximation of the space derivatives satisfies some conditions [28]. Note that discretization, based on the piecewise parabolic distribution (2.3), meet these conditions.

The solution at $(n+1)$ th time level can be found after two steps: at first (predictor) step we obtain values $U^{n+1+\alpha}$ ($U^{n+1+\alpha}$ can be treated as a approximate solution at $t = (n+1+\alpha)\tau$), at second (corrector) step we obtain the solution at the next time level.

Eq. (3.2), (3.3) represent a set of nonlinear equations. To solve this system some iterative approach can be used. In the present paper iterative technique is based on Newton method. For sake of brevity, we consider Eq. (3.2); iterative process for (3.3) is constructed similarly.

Assume $U^{n+1+\alpha,p}$ is an approximation to $U^{n+1+\alpha}$, when $p=0, U^{n+1+\alpha,p} = U^n$. Having written (3.2) for $U^{n+1+\alpha,p+1}$, we carry out linearization with respect to the values $U^{n+1+\alpha,p}$ [3,29]. The resulting difference scheme can be written in the following form ($\Delta\xi = \Delta\eta = 1$);

$$\begin{aligned} & \left[I + \frac{1}{2} \tau (\nabla_{\xi} A^+ - \Delta_{\xi} A^- - \nabla_{\xi} \Delta_{\xi} A_v + \right. \\ & \left. + \nabla_{\eta} B^+ - \Delta_{\eta} B^- - \Delta_{\eta} \nabla_{\eta} B_v) \right] \Delta \hat{U}_{i,j}^{n+1+\alpha,p} = \\ & = -\tau \left[\frac{\hat{U}_{i,j}^{n+1+\alpha,p} - \hat{U}_{i,j}^n}{\tau} + \frac{1}{2} (Z_{i,j}^{n+1+\alpha,p} + Z_{i,j}^n) \right] \quad (3.4) \end{aligned}$$

where

$$\Delta \hat{U}_{i,j}^{n+1+\alpha,p} = \hat{U}_{i,j}^{n+1+\alpha,p+1} - \hat{U}_{i,j}^{n+1,p}$$

$$A = \frac{\partial \hat{F}_i}{\partial \hat{U}} = S_{\xi} (\Lambda_{\xi}^+ - \Lambda_{\xi}^-) S_{\xi}^{-1} = A^+ - A^-, \quad A_v = \frac{\partial \hat{F}_v}{\partial \hat{U}_{\xi}}$$

$$B = \frac{\partial \hat{G}_i}{\partial \hat{U}} = S_{\eta} (\Lambda_{\eta}^+ - \Lambda_{\eta}^-) S_{\eta}^{-1} = B^+ - B^-, \quad B_v = \frac{\partial \hat{G}_v}{\partial \hat{U}_{\eta}}$$

Values $\Delta U_{i,j}^{n+1+\alpha,p}$ can be found from the solution of the linear system (3.4). The iterations are performed until the right-hand side of (3.4) is driven to zero.

In present method the inversion of implicit operator in left-hand side of (3.4) has been carried out by Gauss-Seidel line method. This approach described in detail in Sec. 2.

4. Computed Examples.

Now we will present some computational results obtained by this numerical method.

A steady-state solution was obtained by the time dependent method. The scheme parameters were $\varphi = 1/3$ and $b = b_{\max}$. Typical value of the Courant number (constant for each cell) was $CFL = 50-100$. The solution was assumed to be stationary if the initial value of residual had decreased by 3.5-4 orders of magnitude. Algebraic Baldwin-Lomax turbulence model [30] and two-equation $(q-\omega)$ turbulence model [26] were employed.

Figures 1 - 3 show the results related to the flow in an axisymmetric U - duct, which was experimentally investigated in [31]. Computational grid consisted of 122×82 nodes (fig. 1). The flow parameters used in calculations corresponds to the experimental conditions:

$M_{out} = 0.0925$, $Re_h = 10^5$. Figure 2 shows the comparison of the static pressure distributions between measured data and the present computations. Skin-friction results are compared in fig. 3. Note, that Baldwin-Lomax model indicates large separation regions both on the inner and outer duct walls while $(q-\omega)$ model predicts relatively small separation region on the inner wall at $\theta \approx 180^\circ$.

Computed results [36] for viscous flow with swirl in a swan necked annular interstage duct are shown in fig. 4 - 6. Calculations were made for $P_{out} = 1 \text{ atm.}$, $Re_h = 2 \cdot 10^5$ and swirl angle $\beta = 20^\circ$. Figure 4 shows constant pressure contours. The comparisons of computed skin friction coefficient (nondimensionalized by edge dynamic pressure at inlet) and total pressure distribution with experiment [32] are shown in fig. 5 and fig. 6.

Figures 7- 9 show results of transonic RAE 2822 airfoil calculations [37] compared with experimental measurements [33]. Computational grid consisted of 192×62 nodes is shown in fig. 7. Calculations were performed for $M_{\infty} = 0.73$, $Re = 6.5 \cdot 10^6$ and angle of attack at 3.19° . The computed surface pressure coefficient and skin friction coefficient, nondimensionalized by edge dynamic pressure, are shown in fig. 8a and fig. 8b correspondently. In front of the shock computed results agree very well with experiment, but behind the shock skin friction for both turbulence models is not properly predicted. Computed Mach contours are shown in fig. 9.

Fig. 10 and 11 show the computed surface pressure distributions [37] in comparison with experiment [34] and Mach contours, respectively, for an NACA 0012 airfoil at $M_{\infty} = 0.799$, $Re = 9 \cdot 10^6$ and angle of attack at 2.26° . Large difference in the shock location between Navier-Stokes and Euler solutions (fig.9) is caused by strong viscous-inviscid interaction.

Figures 12 - 15 are related to the 3D numerical simulation [38] of inclined shock wave interaction with boundary layer on a cylinder. Computations grid consisted of $61 \times 35 \times 34$ nodes (fig. 12). The free-stream Mach number was assumed to be equal to $M_{\infty} = 2.95$, the Reynolds number $Re = 1.45 \cdot 10^7 \text{ m}^{-1}$. Algebraic Baldwin-Lomax turbulence model was used in this case. Experimental oil-flow patterns [35] and computed surface limiting velocity vectors are shown in fig. 13. Measured and predicted static pressure distributions on the surface of the cylinder in the planes of symmetry $\varphi = 0^\circ$ and $\varphi = 180^\circ$ are shown in fig. 14. Fig.15 shows the comparison of the lines of constant static pressure in the plane of symmetry $\varphi = 0^\circ$ between measured data and the present computation. The calculated distribution reproduces the structure of the

flow quite well, including the system of the incident and reflected shocks.

Developed method allows to obtain a quite accurate solutions of the test problems on medium size grids. In the next lecture we will present the application of this method to solution of practical problems in turbomachinery.

References

1. Koveniya V.M., Yanenko N.N. Method of decomposition in problems of gasdynamics. Novosibirsk, Nauka, 1981, (in Russian).
2. Shang J.S. An assessment of numerical solutions of the compressible Navier-Stokes equations. *J. Aircraft*. 1985. V.22. N 5. pp. 353-370.
3. Beam R.N., Warming R.F. An implicit factored scheme for the compressible Navier-Stokes equations. *AIAA Journal*. 1978. V. 16. N 4. pp. 393-402.
4. Mac Cormack R.W. A numerical method for solving the equations of compressible viscous flow. *AIAA Journal*, 1982, V. 20, N 9, pp. 1275-1281.
5. Jameson A., Schmidt W., Turkel E. Numerical solutions of the Euler equations by finite volume methods using Runge-Kutta time-stepping schemes. *AIAA Paper* 81-1259. 1981.
6. Jameson A. Solution of the Euler equations by a multigrid method. *Appl. Math. Comput.* 1983, V. 3, pp. 327-356.
7. Swanson R.C., Turkel E. A multistage time-stepping scheme for the Navier-Stokes equations. *AIAA Paper* 85-0035. 1985.
8. Vatsa V.N., Wegan B.W., Development of a multigrid code for 3D Navier-Stokes equations and its application to a grid-refinement study. *Computers & Fluids*. 1990. Vol. 18, No. 4, pp. 391-403.
9. Godunov S.K. A difference method for the numerical calculation of discontinuous solutions of the equations of hydrodynamics. *Matem. Sb.* 47(89), 3, 271-306, 1959 (in Russian).
10. Godunov S.K., Zabrodin A.V., Ivanov M.Ja., Kraiko A.N., Prokopov G.P. Numerical solution of gas dynamic multidimensional problems. M., Nauka, 1976, 400 p. (in Russian).
11. Kolgan V.P. Application of minimum derivatives values principle to difference schemes construction for shock capturing gas dynamics solutions. *Sci. Paper of TSAGI*, Vol. 3, No. 6, 1972, p. 68-77 (in Russian).
12. Harten A. High resolution schemes for hyperbolic conservation laws. *J. of Comp. Phys.*, 1983, Vol. 49, No. 3, pp. 357-393.
13. Chakravarthy S.R., Osher S. A new class of high accuracy TVD schemes for hyperbolic conservation laws. *AIAA Paper* No. 85-0363, 1985, 11 p.
14. Chakravarthy S.R. The versatility and reliability of Euler solvers based on high-accuracy TVD formulations. *AIAA Paper* No. 86-0243, 1986, 15 p.
15. Sweby P.K. High resolution TVD schemes using flux limiters. *Lect. Appl. Math.* 1985, V. 22, No. 2, pp. 289-309.
16. Yamamoto S., Daiguji H., Ishigaki H. An implicit time-marching scheme for solving the compressible Navier-Stokes equations. *Proc. Internat. Symp. on Comput. Fluid Dynamics*. 1988. pp. 773-784.
17. Shian N., Hsu C., Chgu W. Numerical simulation of 3D transonic turbulent projective aerodynamics by TVD schemes: *AIAA Paper*, 89-0335, 1989, 8 p.
18. Richards B., Qin N., Wang Z. Numerical experiments using Navier-Stokes codes for generalized hypersonic shapes ICAS-90, pp. 1927-1937.
19. Venkatakrisnan V. Preconditioned conjugate gradient methods for the compressible Navier-Stokes equations. *AIAA Journal*, 1992, V. 29, N 7, pp. 1092-1100.
20. Rudy D.H., Thomas J.L., Kumar A., Gnoffo P.A., Chakravarthy S.R. Computation of laminar hypersonic compression-corner flows. *AIAA Journal*, 1991, V. 29, N 7, pp. 1108-1113.
21. Nozaki O., Yamamoto K., Kikuchi K., Saito Y., Sugahara N., Tanura A., Navier-Stokes computation of the three dimensional flow fields through a transonic fan blade row. *ISABE*, 1993, v. 1, pp. 340-346.
22. Aftosmis M.J. Upwind method for simulation of viscous flow on adaptively refined meshes. *AIAA Journal*, 1994, vol. 32, No. 2, pp. 268-277.
23. Yamamoto S., Daiguji H. High-order-accurate upwind schemes for solving the compressible Euler and Navier-Stokes equations. *Computers & Fluids*, 1993, vol. 22, N 2/3, pp. 259-270.
24. Collela P., Woodward P.R. The piecewise parabolic method (PPM) for gasdynamical simulations. *J. Comput. Phys.*, 1984, 54, N. 1, pp. 174-201.
25. Steger J.L., Warming R.F. Flux vector splitting of the inviscid gas dynamics equations with application

- to finite difference method. J.Comput. Phys., 1977, 24,3, pp. 372-397.
26. Coakley T.J. Turbulence modeling methods for the compressible Navier-Stokes equations. AIAA Paper N 83-1693, 1983, 13 p.
 27. Ivanov M.Ja., Krupa V.G., Nigmatullin R.Z. Implicit high order accuracy Godunov type scheme for integration of Navier-Stokes equations. J. of Comp. Math. and Math. Phys. 1989 Vol. 29, No. 6, pp.888-901 (in Russian).
 28. Ivanov M.Ja., Krupa V.G., Nigmatullin R.Z. On the CFD monotone high accuracy methods. AGARD-lecture series, N 198, 1994, LS-198.
 29. Rai M.M. An implicit, conservative, zonal-boundary scheme for Euler equations calculations. AIAA Paper, N 85-0488, 1985, 22 p.
 30. Baldwin B.S., Lomax H. Thin-layer approximation and algebraic model for separated turbulent flows. AIAA Paper N 78-257,1978,10 p.
 31. Ostermier B.J., Sharma L.K. Flowfield characteristics of an axisymmetric 180-degree turnaround duct. AIAA Paper, N 87-1357, 1987, 10.p.
 32. Abdalla H.A., Soundranayagam S. Flow in compressor in interstage ducts. ISABE, 89-7020, 1989, pp. 207-215.
 33. Cook P.H., Mcdonald M.A. and Firmin M.C.P Airfoil RAE2822 - pressure distributions and boundary layer and wake measurement. AGARD AR-138, Paper AG, 1979.
 34. Harris C.D. Two-dimensional aerodynamics characteristics of the NACA 0012 airfoil in the Langley six-foot transonic pressure tunnel. NACA TM-81927, 1981.
 35. Brosh A., Kussoy M.I., Hung C.M. Experimental and numerical investigation of shock wave impingement on a cylinder. AIAA Journal, 1985, v. 23, N 6, pp. 840-846.
 36. Krupa V.G., Talipov R.F. Calculation of turbulent flow in interstage duct of compressor. Preprint CIAM, N 4, 1991 (in Russian).
 37. Krupa V.G. Calculation of transonic flows around 2D airfoils. Preprint CIAM, N 8, 1992 (in Russian).
 38. Ivanov M.Ya., Krupa V.G. Calculation of the spatial interaction of a shock wave with a boundary layer on a cylinder. Zh. Vychisl. Mat. Mat. Fiz. Vol. 32, No. 4, pp. 623-634, 1992 (in Russian).

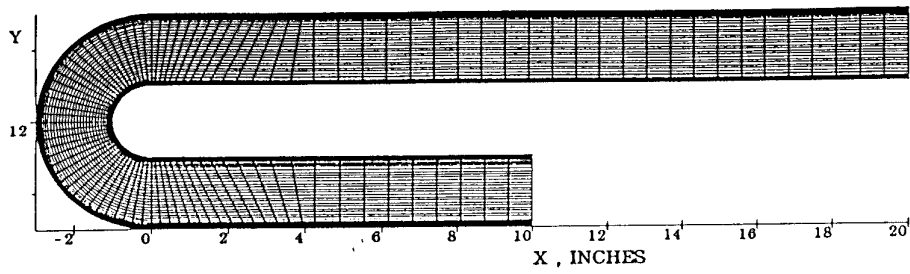


Fig. 1 100x80 U-duct grid

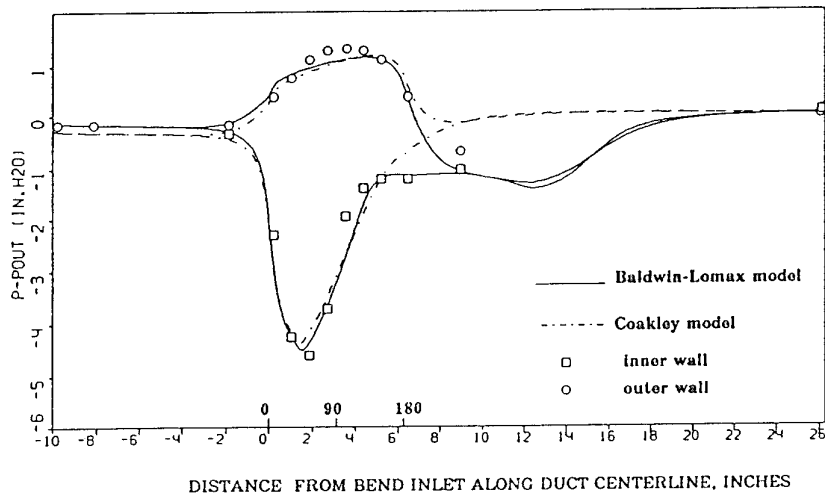


Fig. 2 Wall Static Pressure

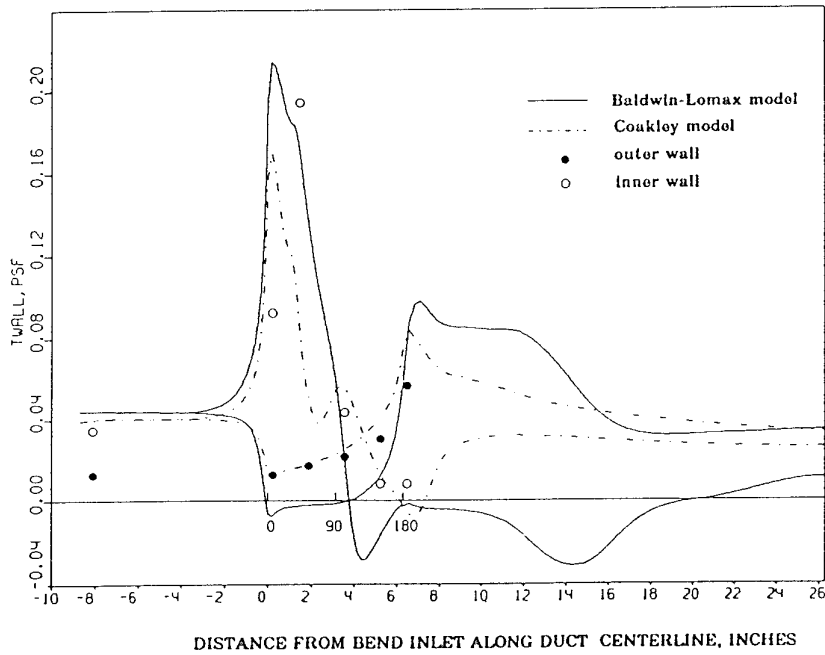


Fig. 3 Variation of Wall Shear Stress

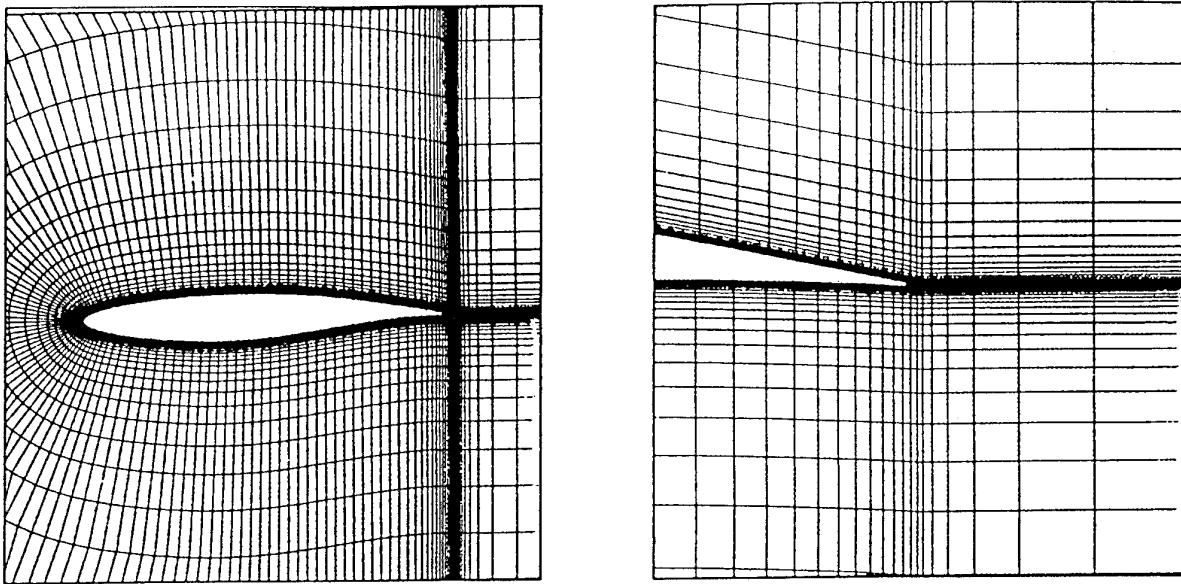


Fig. 7 192x62 grid for RAE 2822 airfoil.

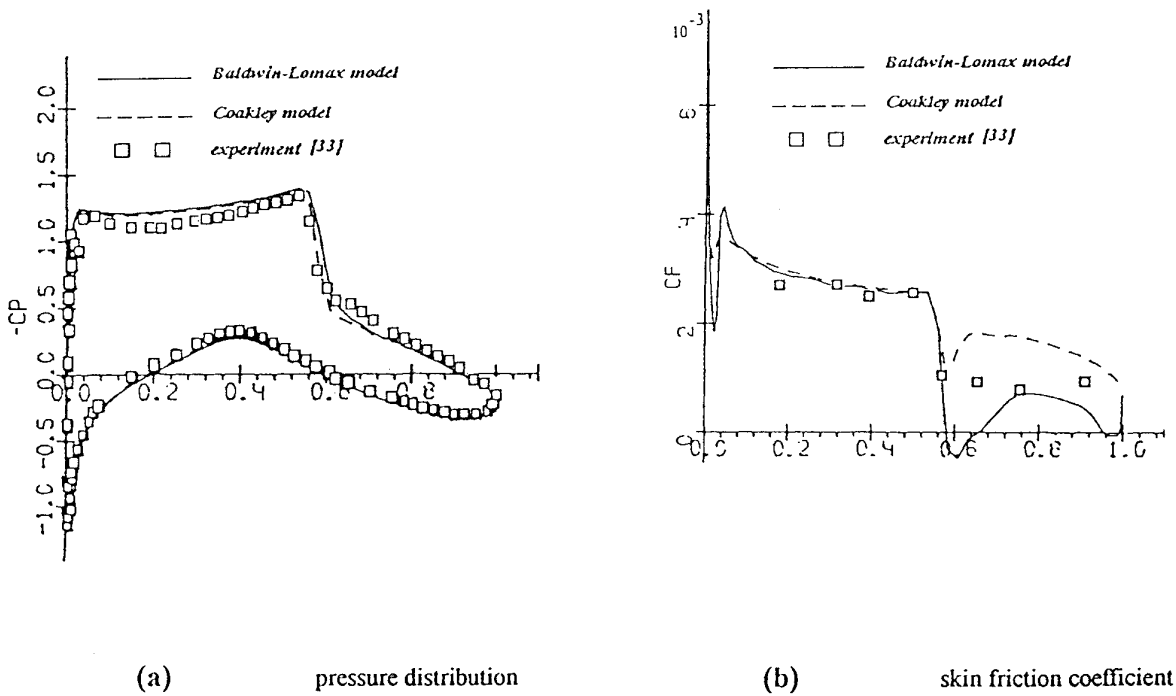


Fig. 8 RAE 2822 airfoil, $M_\infty = 0.73$, $Re = 6.5 \cdot 10^6$, $\alpha = 3.19^\circ$

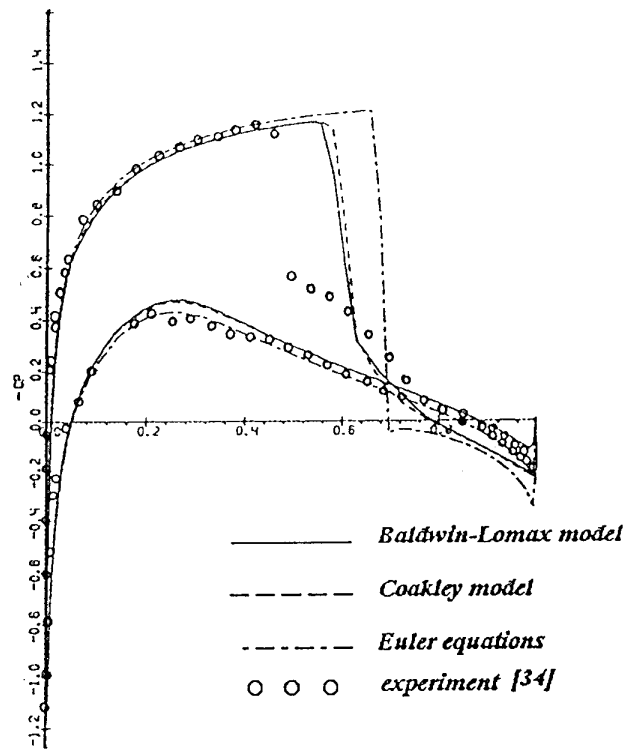


Fig.10 Pressure distribution, NACA 0012 airfoil, $M_\infty = 0.799$, $Re = 9 \cdot 10^6$, $\alpha = 2.26^\circ$

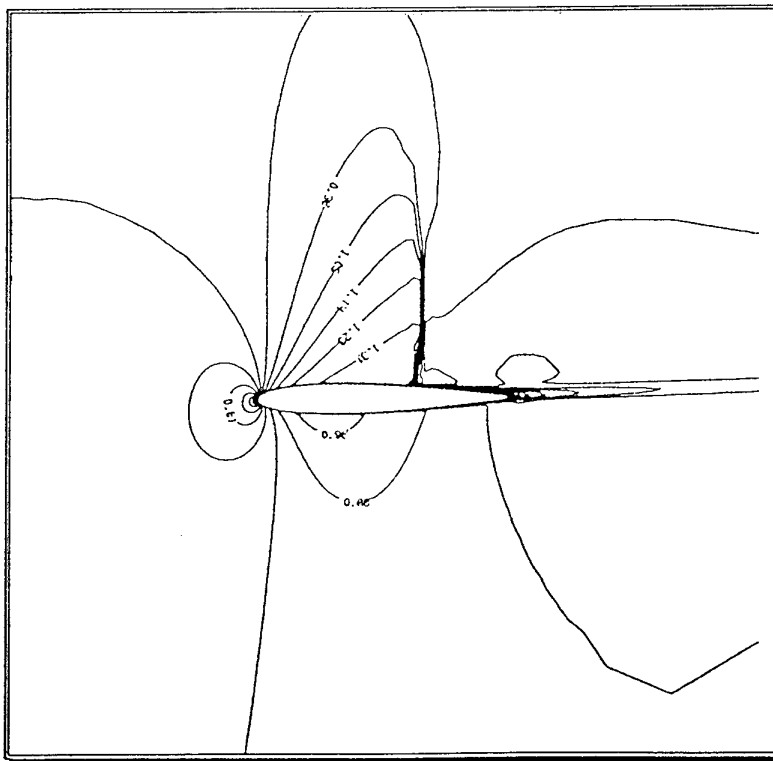


Fig.11 Mach contours (Coakley model), NACA 0012 airfoil, $M_\infty = 0.799$, $Re = 9 \cdot 10^6$, $\alpha = 2.26^\circ$

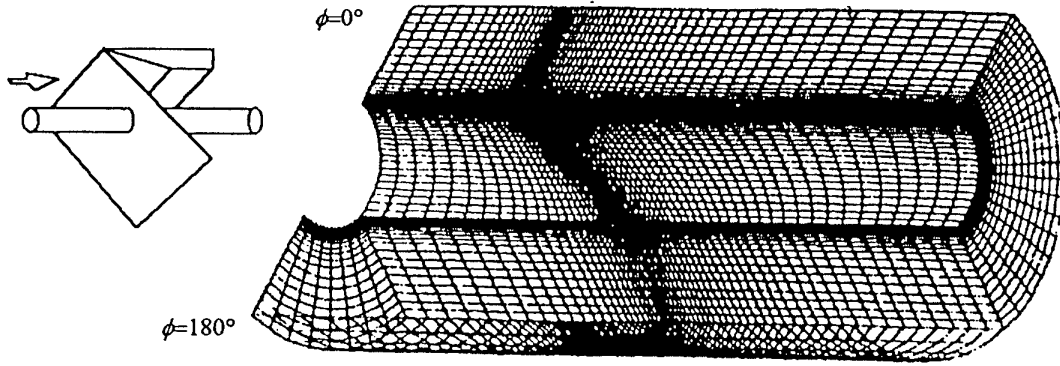


Fig. 12 Computational $65 \times 35 \times 34$ grid

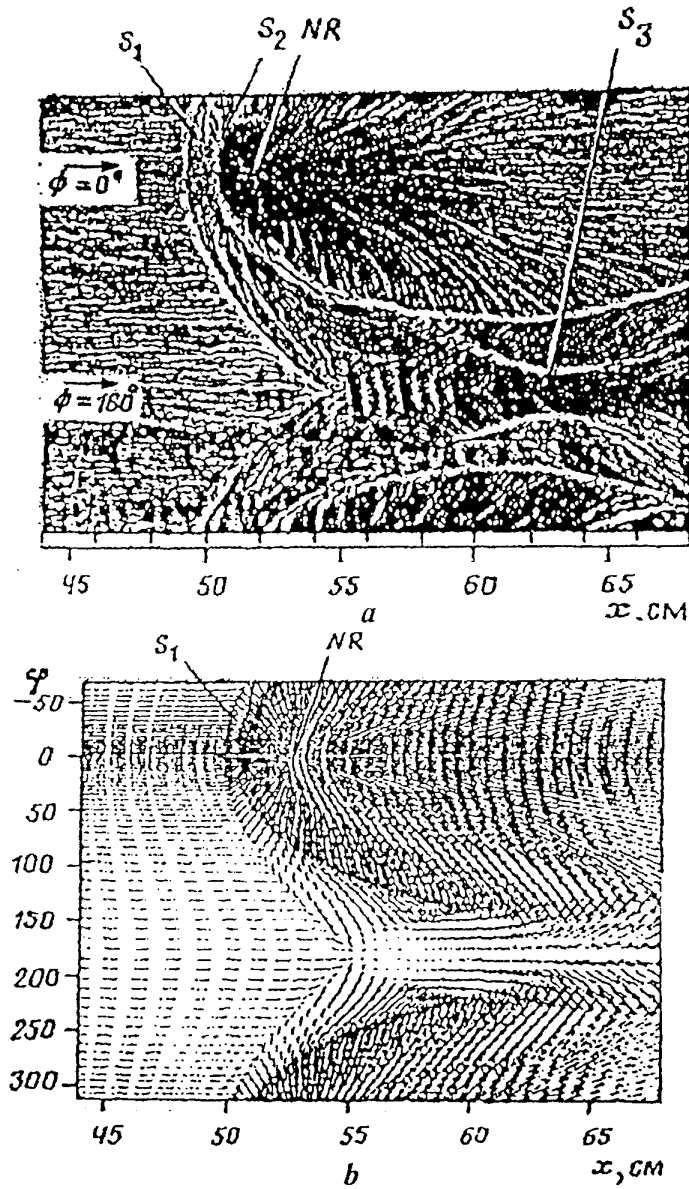


Fig. 13 Experimental oil-flow picture (a),
computed surface-velocity pattern (b)

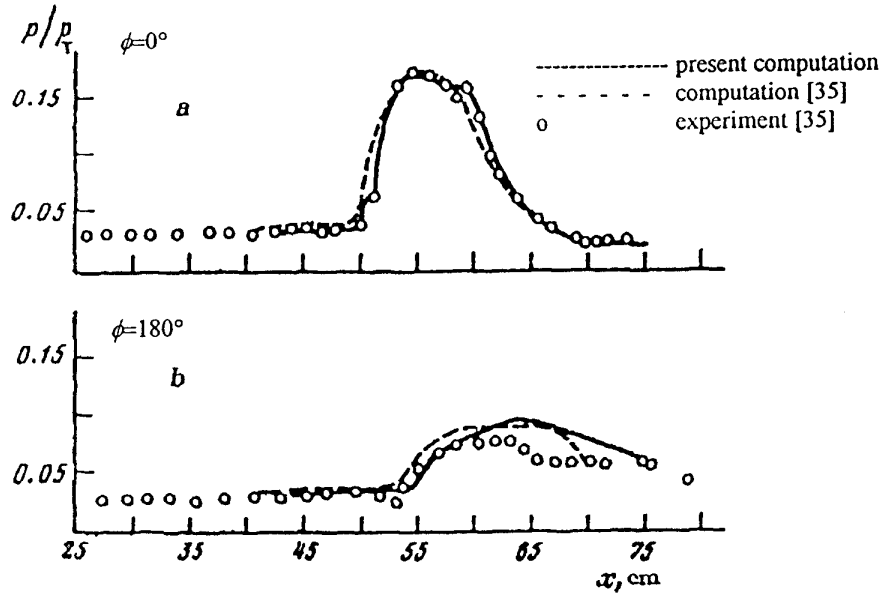


Fig. 14 Static pressure distribution on a cylinder

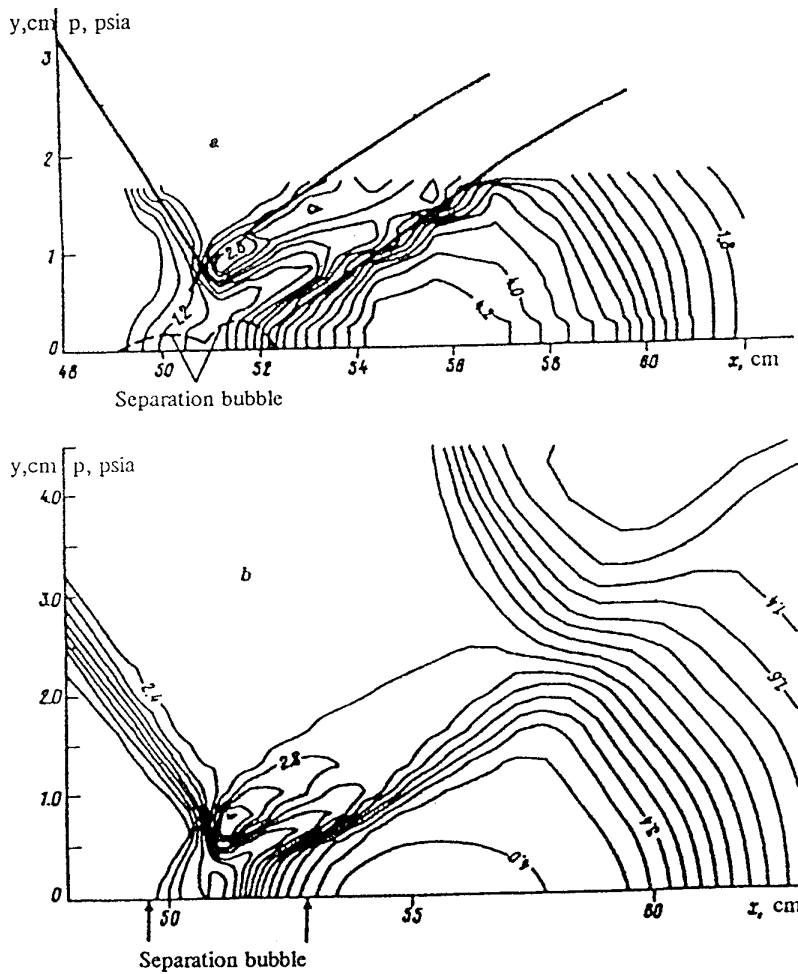


Fig. 15 Measured (a) and computed (b) static-pressure contours on the windward plane $\phi = 0^\circ$

The mathematical models of flow passage for gas turbine engines and their components

by

Dr. R. Z. Nigmatullin, Prof. M. Ja. Ivanov
CIAM (Central Institute of Aviation Motors)
2, Aviamotornaya St.
Moscow, Russia, 111250

Abstract

Mathematical models for gas turbine engines and installations components flow passages based on real 3D geometry of all components of flow passage in particular on spatial shape of blades are considered.

The models are based on numerical solving of unsteady Euler equations and so it allows to simulate some unsteady transitional functioning regimes of engines and installations together with steady ones. The models take into consideration the viscous losses, leakages in axial gaps and tip clearances, cooling air injection and selection.

The first level mathematical models are based on 2D steady and unsteady methods on S_1 and S_2 surfaces. Some features of numerical algorithms based on these methods are considered.

The second level models are based on 3D approaches anywhere in computational domains excluding the middles of axial gaps between neighboring blade rows where for the simplification of the problem the averaging in angular direction is fulfilled.

Nomenclature

t	-	time
z, r, φ	-	cylindrical coordinates
ξ, η, ζ	-	curvilinear coordinates
ξ_z, ξ_r, \dots	-	partial derivatives $\frac{\partial \xi}{\partial z}, \frac{\partial \xi}{\partial r}, \dots$
ω	-	angular velocity of rotor
u, v, w	-	velocity vector components in cylindrical coordinate system
ρ	-	density
p	-	pressure
e	-	total energy per volume
ε	-	specific internal energy
T	-	temperature

c_p, c_v	-	specific heats at constant pressure, volume
\dot{m}	-	density of sources of mass
f_z, f_r, f_φ	-	dissipative forces components
h	-	specific enthalpy
s	-	specific entropy
\vec{V}	-	velocity vector
R	-	gas constant

Introduction

Gas turbine engines and installations development depends to a great extent on the successful solution of problems of flow passage aerodynamics which may be fulfilled by numerical simulations using modern powerful computers. Experience of design gained at present time showed the urgent necessity of wide employment of mathematical tools of high complexity (2D and 3D steady and unsteady models). These models, accounting real flow passage geometry, viscous losses, leakages in axial gaps and tip clearances, selection and injection of cooling air are considered in the present lecture.

The lecture begins with the description of 2D approaches based on the consideration of S_1 and S_2 surfaces. The method of such type seems to be first considered in [1]. Mainly the approaches based on streamfunction (or vorticity - streamfunction) formulation or streamline curvature procedures were employed [1-8].

The method described here arises from work [9] and is based on solving of averaged in angular direction time dependent Euler equations. Some differences are that the basic equations are written in the another form and the conditions at the boundaries between axisymmetrical flow and bladed domains are considered. (The importance of the consideration of such type of conditions was noted in [10]). This method was widely used in design and investigation of engines and installations of a number of firms (see also, [16], [17]). It has some advantages of noted methods, among them there is the possibility of simulation of some

unsteady phenomena, lacking of problems in cases shock waves are present in flow or in transonic flow regimes where the steady equations change character from elliptic to hyperbolic, the possibility of further development of these methods by including viscous terms.

Then an approach, based on using 3D Euler equations is considered. In the middles of axial gaps the averaging of parameters in angular direction is fulfilled with conservation of mass, momentum and energy fluxes. Right hand sides of these equations include the terms that describe viscous losses effects, cooling air injection, leakages, etc. Similar approaches were considered, for example, in [11-12].

Some important details and features of the algorithms are presented in appendices **A** (for S_2 - approach) and **B** (for 3D one).

The capabilities of described mathematical solvers are demonstrated by some examples of flow fields calculations in flow passages of aviation gas turbine installations.

1. Formulation of the problem

The typical flow passage of aviation gas turbine engine in meridional plane (z, r) is shown in fig.1 (the domain **ABCD**, including core **EFGH** and bypass duct **FIJG**). Either whole flow passage or some of its components may be considered. The initial data are: full 3D geometry of flow passage (including blades, nozzles, etc.), angular velocities of rotors, specific fuel consumption and heat of combustion, air cooling scheme. It is supposed also that gas leakages are known. The boundary conditions include total parameters (pressure, temperature) and velocity direction distributions at inlet **AB** and static pressure at outlet **CD**.

Depending on the location in the flow passage either the absolute cylindrical coordinate system (stator regions) or relative one (rotor regions) will be used.

Gas turbine engine components flows will be considered using Euler equation with right hand source members for accounting of viscous losses, blowing in and blowing out of cooling air, leakages, etc. In cylindrical coordinates (z, r, φ) the conservative form of these equations is:

$$\frac{\partial}{\partial t}(r\bar{U}) + \frac{\partial}{\partial z}(r\bar{F}) + \frac{\partial}{\partial r}(r\bar{G}) + \frac{1}{r} \frac{\partial}{\partial \varphi}(r\bar{H}) = \bar{h} \quad (1.1)$$

$$\bar{U} = \begin{pmatrix} \rho \\ \rho u \\ \rho v \\ \rho w \\ e \end{pmatrix}, \quad \bar{F} = \bar{F}(\bar{U}) = \begin{pmatrix} \rho u \\ \rho u^2 + p \\ \rho uv \\ \rho uw \\ (e + p)u \end{pmatrix}$$

$$\bar{G} = \bar{G}(\bar{U}) = \begin{pmatrix} \rho v \\ \rho uv \\ \rho v^2 + p \\ \rho vw \\ (e + p)v \end{pmatrix}$$

$$\bar{H} = \bar{H}(\bar{U}) = \begin{pmatrix} \rho w \\ \rho uw \\ \rho vw \\ \rho w^2 + p \\ (e + p)w \end{pmatrix}$$

$$\bar{h} = \begin{pmatrix} r\dot{m} \\ r\dot{m}V_z + f_z \\ r\dot{m}V_r + f_r + p + \rho(w + \omega r)^2 \\ r\dot{m}V_\varphi + f_\varphi - \rho v(w + 2\omega r) - r^2\rho \frac{d\omega}{dt} \\ r\dot{m}H' + \omega^2 r^2 \rho v - r^2 \rho w \frac{d\omega}{dt} \end{pmatrix}$$

ρ - is density, u, v, w - relative velocity components in cylindrical coordinate system, ω - angular velocity of relative frame of reference, p - static pressure.

The (1.1) system is closed by state equations:

$$p = \rho RT \quad (1.2)$$

$$e = \rho \left[\varepsilon(T) + \frac{1}{2}(u^2 + v^2 + w^2) \right] \quad (1.3)$$

where T - absolute temperature, ε - specific internal energy:

$$\varepsilon = \int_{T_0}^T C_v(\tau) d\tau + \varepsilon_0, C_v > 0$$

The function $\varepsilon(T)$ may be specified using the dependence c_v on T (or $c_p = c_v + R$ on T). (V_z, V_r, V_φ) - cooling air velocity components (at the cooling locations) in the reference frame.

H' - total enthalpy of cooling air in the same frame of reference. It was supposed for simplicity that the cooling air is the same gas, as the main flow, but with different parameters (total pressure, temperature) and hence the state equations (1.2), (1.3) also take place for this air.

Cooling air injection, which really is fulfilled through slots, is modeled by spatial distributed mass sources with density \dot{m} . The distribution of \dot{m} in space is defined using the cooling air mass rates at different places of flow passage. In some cases (for example, in S_1 and S_2 formulations) the density \dot{m} may be distributed by the next way. For each kind of air injection with number $i: 1 \leq i \leq l$ (for example, for a number of perforation slots) it's specified a spatial distributed function α_i , where α_i is a mass δm_i of injected air in infinitesimal volume δV divided by the mass δm_0 of "primary" gas in this particle δV ("primary" gas is one that goes from some inflow section). The distribution of α_i may be easily fulfilled using a stream function (in two-dimensional cases). Then mass concentration of cooling air of injection with number i is

$$c_i = \frac{\alpha_i}{1 + \alpha_1 + \dots + \alpha_l}, i = 1, \dots, l.$$

Mass concentration c_0 of "primary" gas may be obtained from the equation:

$$c_0 + c_1 + \dots + c_l = 1$$

Using the conservation of primary gas mass:

$$\begin{aligned} \frac{\partial}{\partial t}(r\rho c_0) + \frac{\partial}{\partial z}(r\rho u c_0) + \frac{\partial}{\partial r}(r\rho v c_0) + \\ + \frac{1}{r} \frac{\partial}{\partial \varphi}(r\rho w c_0) = 0 \end{aligned}$$

together with the equations (1.1) it is easy to obtain the expression for $r\dot{m}$

$$r\dot{m} = r\rho c_0 \left[\frac{d\alpha_1}{dt} + \dots + \frac{d\alpha_l}{dt} \right], \quad (1.4)$$

$$\text{where } \frac{d}{dt} = \frac{\partial}{\partial t} + u \frac{\partial}{\partial z} + v \frac{\partial}{\partial r} + w \frac{1}{r} \frac{\partial}{\partial \varphi} -$$

substantial derivative.

The setting of $r\dot{m}$ by expression (1.4) is very convenient because there is no difficulty in defining the functions α_i (when the stream function exists). Also it is easy to approximate the derivatives in (1.4) so that the increasing of total mass flow rate will be achieved without any losses and errors (e.g. if we add 2% of air to main flow, then mass rate at the exit will exactly 2% more than at the inflow section). The approach described above may be applied also for taking off the air.

The terms (f_z, f_r, f_φ) are included in (1.1) for accounting of viscous losses effects.

If we set:

$$(f_z, f_r, f_\varphi) = - \frac{r\Phi}{u^2 + v^2 + w^2} (u, v, w) \quad (1.5)$$

then using (1.1) one may derive the equation:

$$\begin{aligned} r\rho T \frac{ds}{dt} = r\dot{m} \left\{ H' - h - \frac{1}{2} (V_z^2 + V_r^2 + V_\varphi^2) + \right. \\ \left. + \frac{1}{2} [(V_z - u)^2 + (V_r - v)^2 + (V_\varphi - w)^2] \right\} + r\Phi \end{aligned}$$

where $h = \varepsilon + RT$ - specific enthalpy, s - specific entropy.

Using (1.4) one may obtain another form of this equation:

$$\begin{aligned} r\rho T \frac{ds}{dt} = r\rho c_0 \sum_{i=1}^l \left\{ H'_i - h - \frac{1}{2} (V_{zi}^2 + V_{ri}^2 + V_{\varphi i}^2) + \right. \\ \left. + \frac{1}{2} [(V_{zi} - u)^2 + (V_{ri} - v)^2 + (V_{\varphi i} - w)^2] \right\} \frac{d\alpha_i}{dt} + r\Phi \end{aligned}$$

where parameters V_z, V_r, V_φ and H' with index i are corresponded to kind of air injection with number i .

According to these equations entropy changes due to changing of mixture temperature, losses in mixing process, etc.

A term Φ in (1.5) is used for simulation of viscous losses effects. Let σ be a prescribed entropy growth (from some initial point to current one) due to viscous losses. The function σ must be spatially distributed in accordance with the notions of the locations of entropy growth (e.g. near solid walls, trailing edges etc.). The

values of these losses must be defined using either experimental data or empirical correlations or boundary layers calculations.

Then one may put

$$\Phi = \rho T \frac{d\sigma}{dt}, \quad (1.6)$$

where $\frac{d}{dt}$ is substantial derivative and may be approximated by any way.

Governing equations (1.1) are solved using a body fitted coordinate transformations:

$$\begin{aligned} \xi &= \xi(z, r, \varphi), \\ \eta &= \eta(z, r, \varphi), \\ \zeta &= \zeta(z, r, \varphi). \end{aligned} \quad (1.7)$$

The system (1.1) may be rewritten in the next conservative form

$$\begin{aligned} \frac{\partial}{\partial t} \left(\frac{r\bar{U}}{J} \right) + \frac{\partial}{\partial \xi} \left(\frac{r}{J} \left(\bar{F}\xi_z + \bar{G}\xi_r + \bar{H} \frac{1}{r} \xi_\varphi \right) \right) + \\ + \frac{\partial}{\partial \eta} \left(\frac{r}{J} \left(\bar{F}\eta_z + \bar{G}\eta_r + \bar{H} \frac{1}{r} \eta_\varphi \right) \right) + \\ + \frac{\partial}{\partial \zeta} \left(\frac{r}{J} \left(\bar{F}\zeta_z + \bar{G}\zeta_r + \bar{H} \frac{1}{r} \zeta_\varphi \right) \right) = \frac{\bar{h}}{J}, \end{aligned} \quad (1.8)$$

where $J = \frac{\partial(\xi, \eta, \zeta)}{\partial(z, r, \varphi)}$, and terms ξ_z, ξ_r, \dots denote

the partial derivatives $\frac{\partial \xi}{\partial z}, \frac{\partial \xi}{\partial r}, \dots$

For modeling transient operations in engines one must add also the equations describing the acceleration of each rotor:

$$J_0 \frac{d\omega}{dt} = M_t - M_c + M_f, \quad (1.9)$$

where M is torque and suffixes t, c and f refer to turbine, compressor (fan), corresponding to this rotor and other sources of torque (for example, forces, using for the initial acceleration of rotor), J_0 is the polar moment of inertia of the rotor.

The solution of unsteady system (1.8) (maybe, together with (1.9)) even for a number of stages of the turbine or compressor is a very expensive task. For the applications it's sufficient in many cases to use some "averaging" procedures. Two types of such averaging will be considered. The first type corresponds to S_1 and

S_2 surfaces formulations, when the equations (1.8) are averaged and more simple 2D equations are obtained.

In another approach the full system (1.8) is solved and the flow parameters are averaged only on some surfaces located in the middles of axial gaps between the neighboring vanes and blade rows. (See, for example, [11], [12], [16], [17]).

2. Axisymmetrical S_2 -surface formulation

At the beginning of the 50-th Wu [1] (see also [2-8]) suggested a method of solving 3D inviscid flow equations in turbomachinery by solving 2D problems on two families of surfaces S_1 and S_2 . This method is widely used in design applications because it requires small computational efforts compared with 3D methods.

An S_2 -approach described below rises to work [9].

Governing equations that describe gas flows in hub-to-shroud S_2 -surface may be obtained from 3D ones either by averaging in angular direction or by considering the flow between two close stream-surfaces.

Gas flows are considered in channel restricted by two solid surfaces and containing blade rows (stators and rotors). The computational domain may be divided into sub-domains of two kinds.

The assumed between neighboring rows (in axial gaps) is assumed to be axisymmetrical. One may derive the equations describing gas flows in these sub-domains from (1.8) supposing: $\zeta \equiv \varphi$,

$$\xi_\varphi = \eta_\varphi = 0, \quad \frac{\partial}{\partial \zeta} \equiv 0:$$

$$\begin{aligned} \frac{\partial}{\partial t} \left(\frac{r\bar{U}}{J} \right) + \frac{\partial}{\partial \xi} \left(\frac{r}{J} \left(\bar{F}\xi_z + \bar{G}\xi_r \right) \right) + \\ + \frac{\partial}{\partial \eta} \left(\frac{r}{J} \left(\bar{F}\eta_z + \bar{G}\eta_r \right) \right) = \frac{\bar{h}}{J} \end{aligned} \quad (2.1)$$

The governing equations in bladed sub-domains may also be considered as a special case of common equations (1.8). Let (ξ, η, ζ) be such curvilinear coordinates that the surfaces defined by equations $\zeta = \text{const}$ are stream-surfaces located between two neighboring blades. Then the equation takes place:

$$u\zeta_z + v\zeta_r + w \frac{1}{r} \zeta_\varphi \equiv 0 \quad (2.2)$$

A blockage factor in angular direction may be defined by the relation:

$$k = 1/\zeta_\varphi \quad (2.3)$$

It's supposed that functions $z(\xi, \eta, \zeta_0)$, $r(\xi, \eta, \zeta_0)$, $\varphi(\xi, \eta, \zeta_0)$ at the corresponding value $\zeta = \zeta_0$ are known that is the stream-surface $\zeta = \zeta_0$ is given.

Then one may choose two different ways. The approach used in [9] corresponds to the choice of other coordinates (ξ, η) satisfying the relation

$$\xi_\varphi = \eta_\varphi = 0 \quad (2.4)$$

Then: $z_\zeta = r_\zeta = 0$, $\varphi_\zeta = k$,

$$\begin{aligned} \frac{r}{J} &= rk \begin{vmatrix} z_\xi & z_\eta \\ r_\xi & r_\eta \end{vmatrix}, & \frac{r\zeta_z}{J} &= rkr_\eta \\ \frac{r\zeta_r}{J} &= -rkz_\eta, & \frac{\xi_\varphi}{J} &= 0 \\ \frac{\eta_z}{J} &= -rkz_\xi, & \frac{\eta_r}{J} &= rkz_\xi, & \frac{\eta_\varphi}{J} &= 0 \end{aligned} \quad (2.5)$$

$$\frac{r\zeta_z}{J} = r \begin{vmatrix} r_\xi & r_\eta \\ \varphi_\xi & \varphi_\eta \end{vmatrix}, \quad \frac{r\zeta_r}{J} = -r \begin{vmatrix} z_\xi & z_\eta \\ \varphi_\xi & \varphi_\eta \end{vmatrix}$$

$$\frac{\zeta_\varphi}{J} = \begin{vmatrix} z_\xi & z_\eta \\ r_\xi & r_\eta \end{vmatrix}$$

The equation (1.8) with accounting of (2.2) leads to form:

$$\begin{aligned} \frac{\partial}{\partial t} \left(\frac{r\bar{U}}{J} \right) + \frac{\partial}{\partial \xi} \left(\frac{r}{J} (\bar{F}\xi_z + \bar{G}\xi_r) \right) + \\ + \frac{\partial}{\partial \eta} \left(\frac{r}{J} (\bar{F}\eta_z + \bar{G}\eta_r) \right) = \frac{\bar{h}}{J} + \bar{h}_1, \end{aligned} \quad (2.6)$$

where

$$\bar{h}_1 = \begin{pmatrix} 0 \\ -\frac{r\zeta_z}{J} \left(\frac{\partial \rho}{\partial \zeta} \right) - \rho \frac{\partial}{\partial \zeta} \left(\frac{r}{J} \zeta_z \right) \\ -\frac{r\zeta_r}{J} \left(\frac{\partial \rho}{\partial \zeta} \right) - \rho \frac{\partial}{\partial \zeta} \left(\frac{r}{J} \zeta_r \right) \\ -\frac{\zeta_\varphi}{J} \left(\frac{\partial \rho}{\partial \zeta} \right) - \rho \frac{\partial}{\partial \zeta} \left(\frac{\zeta_\varphi}{J} \right) \\ 0 \end{pmatrix}$$

The terms

$$\frac{\partial}{\partial \zeta} \left(\frac{r}{J} \zeta_z \right), \quad \frac{\partial}{\partial \zeta} \left(\frac{r}{J} \zeta_r \right), \quad \frac{\partial}{\partial \zeta} \left(\frac{1}{J} \zeta_\varphi \right)$$

are naturally calculated using the identities:

$$\begin{aligned} \frac{\partial}{\partial \xi} \left(\frac{r\zeta_z}{J} \right) + \frac{\partial}{\partial \eta} \left(\frac{\eta_z}{J} \right) + \frac{\partial}{\partial \zeta} \left(\frac{r\zeta_z}{J} \right) &= 0, \\ \frac{\partial}{\partial \xi} \left(\frac{r\zeta_r}{J} \right) + \frac{\partial}{\partial \eta} \left(\frac{\eta_r}{J} \right) + \frac{\partial}{\partial \zeta} \left(\frac{r\zeta_r}{J} \right) &= \frac{1}{J}, \quad (2.7) \\ \frac{\partial}{\partial \xi} \left(\frac{\xi_\varphi}{J} \right) + \frac{\partial}{\partial \eta} \left(\frac{\eta_\varphi}{J} \right) + \frac{\partial}{\partial \zeta} \left(\frac{\zeta_\varphi}{J} \right) &= 0. \end{aligned}$$

The equations system (2.2), (2.6) serves for finding of

unknowns: \bar{U} and $\left(\frac{\partial \rho}{\partial \zeta} \right)$.

This approach has the following shortcoming. One

may show using (2.2), (2.6) that $\left(\frac{\partial \rho}{\partial \zeta} \right)$ depends on

derivatives $\frac{\partial \rho}{\partial \xi}, \frac{\partial \rho}{\partial \eta}$. So if one excludes $\left(\frac{\partial \rho}{\partial \zeta} \right)$ in

(2.6) then this system would be written in nonconservative form which may cause some difficulties in trans- and supersonic flow calculations with strong discontinuities.

One may overcome this difficulty by choosing coordinates (ξ, η) so that instead of (2.4) the next relations will take place:

$$\begin{cases} \xi_z \zeta_z + \xi_r \zeta_r + \frac{1}{r^2} \xi_\varphi \zeta_\varphi = 0, \\ \eta_z \zeta_z + \eta_r \zeta_r + \frac{1}{r^2} \eta_\varphi \zeta_\varphi = 0 \end{cases} \quad (2.8)$$

That is the surfaces $\xi = const$ and $\zeta = const$ are orthogonal, and the surfaces $\eta = const$ and $\zeta = const$ are also orthogonal.

Then instead of (2.6) one obtains a system:

$$\begin{aligned} & \frac{\partial}{\partial t} \left(\frac{r\bar{U}}{J} \right) + \frac{\partial}{\partial \xi} \left(\frac{r}{J} \left(\bar{F}_{\xi_z} + \bar{G}_{\xi_r} + \bar{H} \frac{1}{r} \xi_\varphi \right) \right) + \\ & + \frac{\partial}{\partial \eta} \left(\frac{r}{J} \left(\bar{F}_{\eta_z} + \bar{G}_{\eta_r} + \bar{H} \frac{1}{r} \eta_\varphi \right) \right) = \\ & = \frac{\bar{h}}{J} + \bar{h}_1, \end{aligned} \quad (2.9)$$

where as before

$$h_1 = \begin{pmatrix} 0 \\ -\frac{r_{\zeta_z}}{J} \left(\frac{\partial p}{\partial \zeta} \right) - \rho \frac{\partial}{\partial \zeta} \left(\frac{r}{J} \zeta_z \right) \\ -\frac{r_{\zeta_r}}{J} \left(\frac{\partial p}{\partial \zeta} \right) - \rho \frac{\partial}{\partial \zeta} \left(\frac{r}{J} \zeta_r \right) \\ -\frac{r_{\zeta_\varphi}}{J} \left(\frac{\partial p}{\partial \zeta} \right) - \rho \frac{\partial}{\partial \zeta} \left(\frac{\zeta_\varphi}{J} \right) \\ 0 \end{pmatrix},$$

and

$$\frac{\partial}{\partial \zeta} \left(\frac{r}{J} \zeta_z \right), \frac{\partial}{\partial \zeta} \left(\frac{r}{J} \zeta_r \right), \frac{\partial}{\partial \zeta} \left(\frac{1}{J} \zeta_\varphi \right)$$

are calculated using (2.7). Metric coefficients may be found by equations:

$$\frac{r}{J} = rk \begin{vmatrix} z_\xi & z_\eta \\ r_\xi & r_\eta \end{vmatrix}, \quad \frac{r_{\zeta_z}}{J} = \begin{vmatrix} r_\xi & r_\eta \\ \varphi_\xi & \varphi_\eta \end{vmatrix}, \quad (2.10)$$

$$\frac{r_{\zeta_r}}{J} = - \begin{vmatrix} z_\xi & z_\eta \\ \varphi_\xi & \varphi_\eta \end{vmatrix}, \quad \frac{\zeta_\varphi}{J} = \begin{vmatrix} z_\xi & z_\eta \\ r_\xi & r_\eta \end{vmatrix}$$

$$\frac{r_{\xi_z}}{J} = r\varphi_\zeta (r_\eta - r^2 k_{\zeta_r} \varphi_\eta),$$

$$\frac{r_{\xi_r}}{J} = -r\varphi_\zeta (z_\eta - r^2 k_{\zeta_z} \varphi_\eta),$$

$$\frac{\xi_\varphi}{J} = rk r \varphi_\zeta (z_\eta \zeta_r - r_\eta \zeta_z),$$

$$\frac{m_z}{J} = -r\varphi_\zeta (r_\xi - r^2 k_{\zeta_r} \varphi_\xi),$$

$$\frac{m_r}{J} = r\varphi_\zeta (z_\xi - r^2 k_{\zeta_z} \varphi_\xi),$$

$$\frac{\eta_\varphi}{J} = -rk r \varphi_\zeta (z_\xi \zeta_r - r_\xi \zeta_z),$$

The system (2.9) together with (2.2) serves for

defining of \bar{U} and $\left(\frac{\partial p}{\partial \zeta} \right)$. It was the approach that

was used in the computations. Note that the equations describing flow fields in axisymmetrical subdomains and in bladed ones are different and so at the boundaries of these subdomains it is necessary to consider special conditions (see Appendix A).

The approach described here and based on solving of unsteady Euler equations allows to obtain stable solutions (at sub-, trans- and supersonic conditions in absence or presence of shock waves) as well as modeling of some unsteady phenomena in multistage turbomachines.

3. S_1 - surface flows calculations formulation.

Together with S_2 surface one also considers a blade-to-blade surface S_1 . The projection of this surface on the meridional plane (z, r) coincides with the projection of S_2 surface streamline. It is supposed that this S_1 surface obtained by rotating of the streamline is a stream surface.

The governing equations on S_1 surface may be obtained from (1.8) using some special curvilinear coordinate (ξ, η, ζ) . Let the surfaces $\eta = \text{const}$ be stream-surfaces, then one may consider an orthogonal coordinates system (m, η, φ) . These coordinates are related with cylindrical ones by equations: $m = m(z, r)$, $\eta = \eta(z, r)$, $\varphi = \varphi$ and it will be supposed that the coordinate m is arc length along the meridional projection of the S_1 surface: $\eta = \eta_0$.

Then along S_1 (after a choice of the direction of increasing of η) the following relations will take place:

$$\frac{\partial(m, \eta, \varphi)}{\partial(z, r, \varphi)} = b^{-1}, \quad m_z = z_m, \quad \eta_z = -\frac{r_m}{b},$$

$$r_\eta = bz_m, \quad z_\eta = -br_m, \quad z_m^2 + r_m^2 = 1,$$

where b is Lamé parameter corresponding η (the layer thickness). Considering the superposition of transformations

$$(z, r, \varphi) \rightarrow (m, \eta, \varphi) \rightarrow (\xi, \eta, \zeta)$$

one may derive the formulae (along S_1):

$$\frac{J}{r} = [b(m_\xi r \varphi_\zeta - m_\zeta r \varphi_\xi)]^{-1}$$

$$\frac{r_{\xi z}}{J} = z_m \left(\frac{r_{\xi m}}{J} \right), \quad \frac{r_{\xi r}}{J} = r_m \left(\frac{r_{\xi m}}{J} \right),$$

$$\frac{\xi_\varphi}{J} = -bm_\zeta, \quad \frac{m_z}{J} = -r_m r^2 b \left(\frac{J}{r} \right),$$

$$\frac{m_r}{J} = z_m r^2 b \left(\frac{J}{r} \right), \quad \frac{\eta_\varphi}{J} = 0,$$

$$\frac{r_{\zeta z}}{J} = z_m \left(\frac{r_{\zeta m}}{J} \right), \quad \frac{r_{\zeta r}}{J} = r_m \left(\frac{r_{\zeta m}}{J} \right),$$

$$\frac{\zeta_\varphi}{J} = bm_\xi, \quad \frac{r_{\zeta m}}{J} = rb\varphi_\zeta, \quad \frac{r_{\zeta m}}{J} = -rb\varphi_\xi.$$

$$\left(\frac{m_z}{J} \right) u + \left(\frac{m_r}{J} \right) v + \left(\frac{\eta_\varphi}{J} \right) w \equiv 0, \quad (3.2)$$

$$\begin{cases} \frac{\partial}{\partial \xi} \left(\frac{r_{\xi z}}{J} \right) + \frac{\partial}{\partial \eta} \left(\frac{m_z}{J} \right) + \frac{\partial}{\partial \zeta} \left(\frac{r_{\zeta z}}{J} \right) = 0 \\ \frac{\partial}{\partial \xi} \left(\frac{r_{\xi r}}{J} \right) + \frac{\partial}{\partial \eta} \left(\frac{m_r}{J} \right) + \frac{\partial}{\partial \zeta} \left(\frac{r_{\zeta r}}{J} \right) = \frac{1}{J} \\ \frac{\partial}{\partial \xi} \left(\frac{\xi_\varphi}{J} \right) + \frac{\partial}{\partial \eta} \left(\frac{\eta_\varphi}{J} \right) + \frac{\partial}{\partial \zeta} \left(\frac{\zeta_\varphi}{J} \right) = 0, \end{cases} \quad (3.3)$$

replacing second and third equations of (1.8) by their linear combination (multiplying 2d by z_m and 3d by r_m and adding) the new system may be obtained instead of (1.8):

$$\frac{\partial \tilde{U}}{\partial t} + \frac{\partial \tilde{F}}{\partial \xi} + \frac{\partial \tilde{H}}{\partial \zeta} = \tilde{h}, \quad (3.4)$$

where

$$\tilde{U} = \begin{pmatrix} \frac{r}{J} \rho \\ \frac{r}{J} \rho U \\ \frac{r}{J} \rho w \\ \frac{r}{J} e \end{pmatrix}$$

Using the identities

$$\vec{F} = \begin{pmatrix} \rho \left[\left(\frac{r\dot{\xi}_m}{J} \right) U + \left(\frac{\xi_\varphi}{J} \right) w \right] \\ \rho U \left[\left(\frac{r\dot{\xi}_m}{J} \right) U + \left(\frac{\xi_\varphi}{J} \right) w \right] + \rho \left(\frac{r\dot{\xi}_m}{J} \right) \\ \rho w \left[\left(\frac{r\dot{\xi}_m}{J} \right) U + \left(\frac{\xi_\varphi}{J} \right) w \right] + \rho \left(\frac{\xi_\varphi}{J} \right) \\ (e + p) \left[\left(\frac{r\dot{\xi}_m}{J} \right) U + \left(\frac{\xi_\varphi}{J} \right) w \right] \end{pmatrix},$$

$$\vec{H} = \begin{pmatrix} \rho \left[\left(\frac{r\dot{\zeta}_m}{J} \right) U + \left(\frac{\zeta_\varphi}{J} \right) w \right] \\ \rho U \left[\left(\frac{r\dot{\zeta}_m}{J} \right) U + \left(\frac{\zeta_\varphi}{J} \right) w \right] + \rho \left(\frac{r\dot{\zeta}_m}{J} \right) \\ \rho w \left[\left(\frac{r\dot{\zeta}_m}{J} \right) U + \left(\frac{\zeta_\varphi}{J} \right) w \right] + \rho \left(\frac{\zeta_\varphi}{J} \right) \\ (e + p) \left[\left(\frac{r\dot{\zeta}_m}{J} \right) U + \left(\frac{\zeta_\varphi}{J} \right) w \right] \end{pmatrix},$$

$$\vec{h} = \begin{pmatrix} \frac{\rho(w + \omega r)^2}{r} \left(\frac{r}{J} \right) r_m + p \left\{ \frac{\partial}{\partial \xi} \left(\frac{r\dot{\xi}_m}{J} \right) + \frac{\partial}{\partial \zeta} \left(\frac{r\dot{\zeta}_m}{J} \right) \right\} \\ - \frac{\rho U(w + 2\omega r)}{r} \left(\frac{r}{J} \right) r_m + p \left\{ \frac{\partial}{\partial \xi} \left(\frac{\xi_\varphi}{J} \right) + \frac{\partial}{\partial \zeta} \left(\frac{\zeta_\varphi}{J} \right) \right\} \\ \omega^2 r \rho U \left(\frac{r}{J} \right) r_m \end{pmatrix},$$

$$e = \rho \left[\varepsilon + \frac{1}{2} \rho (U^2 + w^2) \right],$$

$$U = uz_m + vr_m.$$

For accounting of viscous losses one may use either dissipative forces (similar to (1.5)) or add viscous terms to (3.4), ([13]). In the last case one must replace the

term \vec{h} in (3.4) by $\vec{h} + \vec{b}/J$, where $\vec{b} = (0, b_1, b_2, b_3)^T$.

Let

$$\sigma_{\eta\eta} = \lambda \operatorname{div} \vec{V} + 2\mu \left(\frac{J}{r} \right) \left\{ \left[U \left(\frac{r\dot{\xi}_m}{J} \right) + w \left(\frac{\xi_\varphi}{J} \right) \right] \times \right. \\ \left. \times \frac{1}{b} \frac{\partial b}{\partial \xi} + \left[U \left(\frac{r\dot{\zeta}_m}{J} \right) + w \left(\frac{\zeta_\varphi}{J} \right) \right] \frac{1}{b} \frac{\partial b}{\partial \zeta} \right\}.$$

Then

$$\frac{b_1}{J} = \frac{\partial}{\partial \xi} \left[\frac{r}{J} \left(\sigma_{mm} \xi_m + \sigma_{m\varphi} \frac{1}{r} \xi_\varphi \right) \right] + \\ + \frac{\partial}{\partial \zeta} \left[\frac{r}{J} \left(\sigma_{mm} \zeta_m + \sigma_{m\varphi} \frac{1}{r} \zeta_\varphi \right) \right] - \\ - \left(\frac{r}{J} \right) \left[\frac{1}{r} \frac{\partial r}{\partial m} \sigma_{\varphi\varphi} + \frac{1}{b} \frac{\partial b}{\partial m} \sigma_{\eta\eta} \right],$$

$$\frac{b_2}{J} = \frac{\partial}{\partial \xi} \left[\frac{r}{J} \left(\sigma_{\varphi m} \xi_m + \sigma_{\varphi\varphi} \frac{1}{r} \xi_\varphi \right) \right] + \\ + \frac{\partial}{\partial \zeta} \left[\frac{r}{J} \left(\sigma_{\varphi m} \zeta_m + \sigma_{\varphi\varphi} \frac{1}{r} \zeta_\varphi \right) \right] + \\ + \left(\frac{r}{J} \right) \left[\frac{1}{r} \frac{\partial r}{\partial m} \sigma_{\varphi m} \right],$$

$$\frac{b_3}{J} = \frac{\partial}{\partial \xi} \left[\frac{r}{J} \left(\kappa \frac{\partial T}{\partial m} \xi_m + \kappa \frac{1}{r} \frac{\partial T}{\partial \varphi} \frac{1}{r} \xi_\varphi \right) \right] + \\ + U \frac{r}{J} \left(\sigma_{mm} \xi_m + \sigma_{m\varphi} \frac{1}{r} \xi_\varphi \right) + \\ + w \frac{r}{J} \left(\sigma_{\varphi m} \xi_m + \sigma_{\varphi\varphi} \frac{1}{r} \xi_\varphi \right) + \\ + \frac{\partial}{\partial \zeta} \left[\frac{r}{J} \left(\kappa \frac{\partial T}{\partial m} \zeta_m + \kappa \frac{1}{r} \frac{\partial T}{\partial \varphi} \frac{1}{r} \zeta_\varphi \right) \right] +$$

$$+ U \frac{r}{J} \left(\sigma_{mm} \zeta_m + \sigma_{m\varphi} \frac{1}{r} \zeta_\varphi \right) + w \frac{r}{J} \left(\sigma_{\varphi m} \zeta_m + \sigma_{\varphi\varphi} \frac{1}{r} \zeta_\varphi \right) \Big].$$

$$\frac{\partial T}{\partial m} = \left(\frac{J}{r}\right) \left[\left(\frac{r\xi_m}{J}\right) \frac{\partial T}{\partial \xi} + \left(\frac{r\zeta_m}{J}\right) \frac{\partial T}{\partial \zeta} \right],$$

$$\frac{1}{r} \frac{\partial T}{\partial \varphi} = \left[\left(\frac{\xi_\varphi}{J}\right) \frac{\partial T}{\partial \xi} + \left(\frac{\zeta_\varphi}{J}\right) \frac{\partial T}{\partial \zeta} \right].$$

$$\sigma_{mm} = \lambda \operatorname{div} \bar{V} + 2\mu \left(\frac{J}{r}\right) \left[\left(\frac{r\xi_m}{J}\right) \frac{\partial U}{\partial \xi} + \left(\frac{r\zeta_m}{J}\right) \frac{\partial U}{\partial \zeta} \right].$$

$$\sigma_{m\varphi} = \sigma_{\varphi m} =$$

$$= \mu \left(\frac{J}{r}\right) \left[\left(\frac{\xi_\varphi}{J}\right) \frac{\partial U}{\partial \xi} + \left(\frac{\zeta_\varphi}{J}\right) \frac{\partial U}{\partial \zeta} + r \left(\frac{r\xi_m}{J}\right) \frac{\partial}{\partial \xi} \left(\frac{w}{r}\right) + r \left(\frac{r\zeta_m}{J}\right) \frac{\partial}{\partial \zeta} \left(\frac{w}{r}\right) \right],$$

$$\sigma_{\varphi\varphi} = \lambda \operatorname{div} \bar{V} + 2\mu \left(\frac{J}{r}\right) \left[\left(\frac{\xi_\varphi}{J}\right) \frac{\partial w}{\partial \xi} + \left(\frac{\zeta_\varphi}{J}\right) \frac{\partial w}{\partial \zeta} \right] + 2\mu \frac{\partial r}{\partial m} \frac{U}{r},$$

$$\operatorname{div} \bar{V} = \left(\frac{J}{r}\right) \left[\frac{\partial}{\partial \xi} \left\{ \left(\frac{r\xi_m}{J}\right) U + \left(\frac{\xi_\varphi}{J}\right) w \right\} + \frac{\partial}{\partial \zeta} \left\{ \left(\frac{r\zeta_m}{J}\right) U + \left(\frac{\zeta_\varphi}{J}\right) w \right\} \right],$$

$$\lambda = -\frac{2}{3} \mu \quad (\text{Stokes hypothesis}),$$

μ - eddy viscosity, κ - coefficient of thermal conductivity.

Some examples of using of S_1 - surface approach are presented in figures 2, 3, 4. Fig. 2 shows an example of calculation of inviscid flow through the turbine rotor cascade (at $r = \text{var}$, $b = \text{var}$). The calculations of such type, that take very small computational times, may be used for estimation of shock wave losses and, maybe, deviation angles (in absence of extended separation regions).

An example of inviscid unsteady calculation of flow through a turbine stage (at low rotor speed) is shown in

fig. 3. The function $r = r(m)$ and $b = b(m)$ were obtained using steady solution on S_2 - surface.

The approach with included viscous terms may be used for estimation of deviation angles and viscous ("profile") losses. An example of viscous calculation (with algebraic Baldwin-Lomax turbulence model [18]) is presented in fig. 4 (at $r = \text{const}$ and $b = \text{const}$).

4. 3D approach with averaging in the middle of axial gaps.

In this approach the gas flow within each blade row is modeled by full 3D Euler equations (1.8). At the section located approximately in the middle of the axial gap the averaging of parameters in angular direction is fulfilled, and what is more, it is required that mass, momentum and energy fluxes through the "ring" from r to $r + \delta r$ are the same for both sides of this section. (It is evident that one may calculate these fluxes either in absolute or in relative frame of reference: if they are equal in one frame then it will be true also in another frame of reference). The averaged flow parameters at this section are also the results of the solution.

5. The formulation of viscous problem on S_2 surface.

The described S_2 - approach may formally be developed by adding viscous terms. For completeness let us now write corresponding equation system for "bladed" regions (in axisymmetrical domains the equations may be obtained from usual 3D ones by

setting: $\frac{\partial}{\partial \varphi} \equiv 0$).

Instead of (2.9) we consider a system:

$$\frac{\partial}{\partial t} \left(\frac{r\bar{U}}{J} \right) + \frac{\partial}{\partial \xi} \left[\frac{r}{J} \left(\bar{F}\xi_z + \bar{G}\xi_r + \bar{H} \frac{1}{r} \xi_\varphi \right) \right] + \frac{\partial}{\partial \eta} \left[\frac{r}{J} \left(\bar{F}\eta_z + \bar{G}\eta_r + \bar{H} \frac{1}{r} \eta_\varphi \right) \right] = \frac{\bar{h}}{J} + \bar{h}_1 + \frac{\bar{b}}{J},$$

where $\bar{U}, \bar{F}, \bar{G}, \bar{H}, \bar{h}$ have the same sense as in (1.1), \bar{h}_1 is the same as in (2.9), the metric coefficients are calculated by (2.10),

$$\bar{b} = (0, b_2, b_3, b_4, b_5)^T.$$

Let

$$\gamma_1 = \left(\frac{r\xi_z}{J} \right) / c_\xi, \quad \gamma_2 = \left(\frac{r\xi_r}{J} \right) / c_\xi,$$

$$\gamma_3 = \left(\frac{\xi_\varphi}{J} \right) / c_\xi,$$

$$c_\xi = \sqrt{\left(\frac{r\xi_z}{J} \right)^2 + \left(\frac{r\xi_r}{J} \right)^2 + \left(\frac{\xi_\varphi}{J} \right)^2},$$

$$E_1 = \frac{\partial}{\partial \xi} \left(\frac{r\xi_z}{J} \right) + \frac{\partial}{\partial \eta} \left(\frac{m_z}{J} \right),$$

$$E_2 = \frac{\partial}{\partial \xi} \left(\frac{r\xi_r}{J} \right) + \frac{\partial}{\partial \eta} \left(\frac{m_r}{J} \right) - \frac{1}{J},$$

$$E_3 = \frac{\partial}{\partial \xi} \left(\frac{\xi_\varphi}{J} \right) + \frac{\partial}{\partial \eta} \left(\frac{\eta_\varphi}{J} \right),$$

$$\sigma_{\xi\xi} = \lambda \operatorname{div} \bar{V} + 2\mu \frac{v}{r} \gamma_3^2 - 2\mu \frac{w}{r} \gamma_2 \gamma_3 +$$

$$+ 2\mu \left(\frac{J}{r} \right) [uE_1 + vE_2 + wE_3].$$

Then:

$$\frac{b_2}{J} = \frac{\partial}{\partial \xi} \left[\frac{r}{J} \left(\sigma_{zz} \xi_z + \sigma_{zr} \xi_r + \sigma_{z\varphi} \frac{1}{r} \xi_\varphi \right) \right] +$$

$$+ \frac{\partial}{\partial \eta} \left[\frac{r}{J} \left(\sigma_{zz} \eta_z + \sigma_{zr} \eta_r + \sigma_{z\varphi} \frac{1}{r} \eta_\varphi \right) \right] - \sigma_{\xi\xi} E_1$$

$$\frac{b_3}{J} = \frac{\partial}{\partial \xi} \left[\frac{r}{J} \left(\sigma_{rz} \xi_z + \sigma_{rr} \xi_r + \sigma_{r\varphi} \frac{1}{r} \xi_\varphi \right) \right] +$$

$$+ \frac{\partial}{\partial \eta} \left[\frac{r}{J} \left(\sigma_{rz} \eta_z + \sigma_{rr} \eta_r + \sigma_{r\varphi} \frac{1}{r} \eta_\varphi \right) \right] - \frac{\sigma_{\varphi\varphi}}{J} - \sigma_{\xi\xi} E_2$$

$$\frac{b_4}{J} = \frac{\partial}{\partial \xi} \left[\frac{r}{J} \left(\sigma_{\varphi z} \xi_z + \sigma_{\varphi r} \xi_r + \sigma_{\varphi\varphi} \frac{1}{r} \xi_\varphi \right) \right] +$$

$$+ \frac{\partial}{\partial \eta} \left[\frac{r}{J} \left(\sigma_{\varphi z} \eta_z + \sigma_{\varphi r} \eta_r + \sigma_{\varphi\varphi} \frac{1}{r} \eta_\varphi \right) \right] + \frac{\sigma_{\varphi r}}{J} - \sigma_{\xi\xi} E_3$$

$$\frac{b_5}{J} = \frac{\partial}{\partial \xi} \left[\frac{r}{J} \left(\kappa \frac{\partial T}{\partial z} \xi_z + \kappa \frac{\partial T}{\partial r} \xi_r + \kappa \frac{1}{r} \frac{\partial T}{\partial \varphi} \frac{1}{r} \xi_\varphi \right) \right] +$$

$$+ \frac{r}{J} u \left(\sigma_{zz} \xi_z + \sigma_{zr} \xi_r + \sigma_{z\varphi} \frac{1}{r} \xi_\varphi \right) +$$

$$+ \frac{r}{J} v \left(\sigma_{rz} \xi_z + \sigma_{rr} \xi_r + \sigma_{r\varphi} \frac{1}{r} \xi_\varphi \right) +$$

$$+ \frac{r}{J} w \left(\sigma_{\varphi z} \xi_z + \sigma_{\varphi r} \xi_r + \sigma_{\varphi\varphi} \frac{1}{r} \xi_\varphi \right) \Big] +$$

$$+ \frac{\partial}{\partial \eta} \left[\frac{r}{J} \left(\kappa \frac{\partial T}{\partial z} \eta_z + \kappa \frac{\partial T}{\partial r} \eta_r + \kappa \frac{1}{r} \frac{\partial T}{\partial \varphi} \frac{1}{r} \eta_\varphi \right) \right] +$$

$$+ \frac{r}{J} u \left(\sigma_{zz} \eta_z + \sigma_{zr} \eta_r + \sigma_{z\varphi} \frac{1}{r} \eta_\varphi \right) +$$

$$+ \frac{r}{J} v \left(\sigma_{rz} \eta_z + \sigma_{rr} \eta_r + \sigma_{r\varphi} \frac{1}{r} \eta_\varphi \right) +$$

$$+ \frac{r}{J} w \left(\sigma_{\varphi z} \eta_z + \sigma_{\varphi r} \eta_r + \sigma_{\varphi\varphi} \frac{1}{r} \eta_\varphi \right) \Big].$$

Here:

$$\frac{\partial T}{\partial z} = \left(\frac{J}{r} \right) \left[\frac{r\xi_z}{J} \frac{\partial T}{\partial \xi} + \frac{m_z}{J} \frac{\partial T}{\partial \eta} \right],$$

$$\frac{\partial T}{\partial r} = \left(\frac{J}{r} \right) \left[\frac{r\xi_r}{J} \frac{\partial T}{\partial \xi} + \frac{m_r}{J} \frac{\partial T}{\partial \eta} \right],$$

$$\frac{1}{r} \frac{\partial T}{\partial \varphi} = \left(\frac{J}{r} \right) \left[\frac{\xi_\varphi}{J} \frac{\partial T}{\partial \xi} + \frac{\eta_\varphi}{J} \frac{\partial T}{\partial \eta} \right].$$

Let also: $A = \lambda \operatorname{div} \bar{V} - \sigma_{\xi\xi}$,

$$C_1 = \gamma_1 \frac{\partial u}{\partial \xi} + \gamma_2 \frac{\partial v}{\partial \xi} + \gamma_3 \frac{\partial w}{\partial \xi},$$

$$C_2 = \gamma_1 \frac{\partial u}{\partial \eta} + \gamma_2 \frac{\partial v}{\partial \eta} + \gamma_3 \frac{\partial w}{\partial \eta},$$

$$D = \frac{w}{r} \gamma_2 \gamma_3 - \frac{v}{r} \gamma_3^2,$$

$$B_1 = \mu \left[-\left(\frac{J}{r}\right) \left\{ \left(\frac{r\xi_z}{J}\right) C_1 + \left(\frac{m_z}{J}\right) C_2 \right\} - \gamma_1 D \right],$$

$$B_2 = \mu \left[-\left(\frac{J}{r}\right) \left\{ \left(\frac{r\xi_r}{J}\right) C_1 + \left(\frac{m_r}{J}\right) C_2 \right\} + \gamma_3 \frac{w}{r} - \gamma_2 D \right],$$

$$B_3 = \mu \left[-\left(\frac{J}{r}\right) \left\{ \left(\frac{\xi_\varphi}{J}\right) C_1 + \left(\frac{\eta_\varphi}{J}\right) C_2 \right\} + \right. \\ \left. + \gamma_2 \frac{w}{r} - 2\gamma_3 \frac{v}{r} - \gamma_3 D \right]$$

Then:

$$\sigma_{zz} = \lambda \operatorname{div} \bar{V} +$$

$$+ 2\mu \left(\frac{J}{r}\right) \left[\frac{r\xi_z}{J} \frac{\partial u}{\partial \xi} + \frac{m_z}{J} \frac{\partial u}{\partial \eta} \right] - \gamma_1^2 A + 2\gamma_1 B_1,$$

$$\sigma_{rr} = \lambda \operatorname{div} \bar{V} +$$

$$+ 2\mu \left(\frac{J}{r}\right) \left[\frac{r\xi_r}{J} \frac{\partial v}{\partial \xi} + \frac{m_r}{J} \frac{\partial v}{\partial \eta} \right] - \gamma_2^2 A + 2\gamma_2 B_2,$$

$$\sigma_{\varphi\varphi} = \lambda \operatorname{div} \bar{V} +$$

$$+ 2\mu \left(\frac{J}{r}\right) \left[\frac{\xi_\varphi}{J} \frac{\partial w}{\partial \xi} + \frac{\eta_\varphi}{J} \frac{\partial w}{\partial \eta} \right] + 2\mu \frac{v}{r} - \gamma_3^2 A + 2\gamma_3 B_3,$$

$$\sigma_{zr} = \sigma_{rz} = \mu \left(\frac{J}{r}\right) \left[\frac{r\xi_z}{J} \frac{\partial v}{\partial \xi} + \frac{m_z}{J} \frac{\partial v}{\partial \eta} + \right. \\ \left. + \frac{r\xi_r}{J} \frac{\partial u}{\partial \xi} + \frac{m_r}{J} \frac{\partial u}{\partial \eta} \right] - \gamma_1 \gamma_2 A + \gamma_2 B_1 + \gamma_1 B_2,$$

$$\sigma_{z\varphi} = \sigma_{\varphi z} = \mu \left(\frac{J}{r}\right) \left[\frac{\xi_\varphi}{J} \frac{\partial u}{\partial \xi} + \frac{\eta_\varphi}{J} \frac{\partial u}{\partial \eta} + \right. \\ \left. + \frac{r\xi_z}{J} \frac{\partial w}{\partial \xi} + \frac{m_z}{J} \frac{\partial w}{\partial \eta} \right] - \gamma_1 \gamma_3 A + \gamma_3 B_1 + \gamma_1 B_3,$$

$$\sigma_{r\varphi} = \sigma_{\varphi r} = \mu \left(\frac{J}{r}\right) \left[\frac{r\xi_r}{J} \frac{\partial w}{\partial \xi} + \frac{m_r}{J} \frac{\partial w}{\partial \eta} + \right. \\ \left. + \frac{r\xi_z}{J} \frac{\partial v}{\partial \xi} + \frac{m_z}{J} \frac{\partial v}{\partial \eta} \right] - \gamma_2 \gamma_3 A + \gamma_3 B_2 + \gamma_2 B_3,$$

$$+ \frac{\xi_\varphi}{J} \frac{\partial v}{\partial \xi} + \frac{\eta_\varphi}{J} \frac{\partial v}{\partial \eta} \left] - \mu \frac{w}{r} - \gamma_2 \gamma_3 A + \gamma_3 B_2 + \gamma_2 B_3,$$

where

$$\operatorname{div} \bar{V} = \left(\frac{J}{r}\right) \left[\frac{\partial}{\partial \xi} \left(\frac{r\xi_z}{J} u + \frac{r\xi_r}{J} v + \frac{\xi_\varphi}{J} w \right) + \right. \\ \left. + \frac{\partial}{\partial \eta} \left(\frac{m_z}{J} u + \frac{m_r}{J} v + \frac{\eta_\varphi}{J} w \right) \right],$$

$$\lambda = -\frac{2}{3} \mu \quad \text{(Stokes hypothesis),}$$

$$\mu = \mu_{lam} + \mu_{turb} \quad \text{- eddy viscosity,}$$

$\kappa = \kappa_{lam} + \kappa_{turb}$ - coefficient of thermal conductivity.

The equations (5.1), (2.2) are system for defining of

unknowns: U and $\left(\frac{\partial p}{\partial \xi}\right)$.

6. Numerical methods.

All described problems are based on unsteady Euler or Navier-Stokes equations. These equations may be solved by methods presented in previous lectures.

Let us briefly recall the main features of used numerical schemes. These are monotone implicit schemes of second or third order accuracy in space and time. The implicit operator was used which allows to solve the linear systems of equations by scalar three diagonal solvers. The boundary conditions were treated implicitly. In unsteady calculations additional "internal" iterations were used. And in all cases the exact solution of Riemann problem was used at the cell boundaries (high order Godunov's scheme).

7. Some numerical examples.

Here a few examples of application of described methods are presented.

First example is a flow through cooled high pressure 1 - stage turbine (fig.5). 3D approach with averaging in the middles of axial gaps was used in the calculations. The cooling air injection effects were simulated by distributed sources of mass, momentum and energy. Viscous losses values obtained from the experiments with single vane were used for stator and some simple empirical estimations were taken for rotor. Used computational grid in meridional plane is presented in fig.5. The calculated distribution of isentropic velocity coefficient (some function of static

pressure) along radius in axial gap is shown in fig .6 (solid line). Experimental results of design office are marked by squares. Fig.7 shows a distribution of exit absolute flow angle (90° corresponds to axial flow). Solid line is calculated result, a line with squares are experimental data. Some features of calculated line near tip region are connected with tip clearance losses which were accounted using some 2D - surface calculations at tip section of rotor blade. Measured and calculated mass flow rate and turbine power were in good agreement.

Another example is a calculation of gas flow through fan with mid-span shroud, low pressure compressor and by-pass duct (fig.8a,b). The results obtained by 3D approach are presented in figures 8-12. Fig.9 shows pressure contours in meridional plane (at suction side for rotors and pressure side for stator blades), fig.10 shows them at hub section and fig.11 at tip section. Fig.12 shows experimental (solid line) and calculated (squares) fan characteristic.

The gas flow through almost the same geometry (but without blade mid-span shroud) was also calculated using S_2 - approach. Used computational grid is shown at fig.13. Calculated pressure contours and stream-lines are presented at figures 14, 15. It is evident from fig.14, that used S_2 - approach allows to calculate flows with strong shock waves.

An example of steady flow calculation for bypass engine core is presented in figures 16, 17. The combustion process was modeled by sources of mass, heat. The S_2 - approach was used in this calculation. Fig.17 also shows good resolution of strong discontinuities on S_2 - surface.

This lecture contains main problem formulations and main features of used approaches. Some other details and other numerical examples will be considered later (in lecture 6).

APPENDIX A

Arbitrary discontinuity breakdown at the boundary between axisymmetrical subdomain and bladed one.

As it was mentioned above, the equations describing gas flows in bladed subdomains and in axisymmetrical regions are different (see eqs. (2.1), (2.9)). What is more, small perturbances propagate in these subdomains with different velocities. Indeed, in bladed regions local acoustic perturbances propagate in the direction perpendicular to grid lines $\xi = const$ with the

velocities $\frac{U_\xi}{c_\xi} \pm \alpha$, where α - sound speed,

$$U_\xi = u \frac{r_{\xi_z}}{J} + v \frac{r_{\xi_r}}{J} + w \frac{\xi_\phi}{J},$$

$$c_\xi = \sqrt{\left(\frac{r_{\xi_z}}{J}\right)^2 + \left(\frac{r_{\xi_r}}{J}\right)^2 + \left(\frac{\xi_\phi}{J}\right)^2}$$

and the quantities $\left(\frac{r_{\xi_z}}{J}, \frac{r_{\xi_r}}{J}, \frac{\xi_\phi}{J}\right)$ are calculated by formula (2.10). In axisymmetrical subdomains the

perturbances propagate with the velocities $\frac{U_\xi}{c_\xi} \pm \alpha$,

where $\left(\frac{r_{\xi_z}}{J}, \frac{r_{\xi_r}}{J}\right)$ are calculated by (2.5), and

$\frac{\xi_\phi}{J} = 0$. It reflects in common the physics of the flow.

It is evident from above that, first, these boundaries are in common case the discontinuity surfaces and, secondly, it is necessary to set sufficient number of boundary conditions at these surfaces which depends on number of coming and leaving perturbances. In other words it is necessary to consider an arbitrary discontinuity breakdown problem at these boundaries.

Let us first consider the boundary corresponding to leading edges. A treatment of the boundary conditions means that the usual arbitrary discontinuity breakdown procedure must be replaced by the special one described below.

Let: $\bar{\xi} = \left(\frac{r_{\xi_z}}{J}, \frac{r_{\xi_r}}{J}, \frac{\xi_\phi}{J}\right)$, where the metric coefficients are calculated by (2.10), and

$\bar{x} = \left(\frac{r_{\xi_z}}{J}, \frac{r_{\xi_r}}{J}, 0\right)$, where $\frac{r_{\xi_z}}{J}$ and $\frac{r_{\xi_r}}{J}$ are found

by (2.5). Let also $\bar{N} = \left(\frac{r_{\xi_z}}{J}, \frac{r_{\xi_r}}{J}, \frac{\xi_\phi}{J}\right) / c_\xi$ be the

unit vector normal to stream-surface $\zeta = const$,

where $\frac{r_{\xi_z}}{J}, \frac{r_{\xi_r}}{J}, \frac{\xi_\phi}{J}$ are obtained by (2.10). All parameters are related to boundaries of consideration. If it is necessary the corresponding right or left limit is used. The parameters at the bladed side will be marked by index 1 and the parameters at the axisymmetrical

subdomain will be marked by index 2. "Large" left and right parameters (at both sides of the surface) will have the indices "L" and "R".

It's convenient to consider "leading triangle" drawn

at fig. 1A (it is easy to prove that three vectors $\bar{\xi}$, \bar{x} , \bar{N}

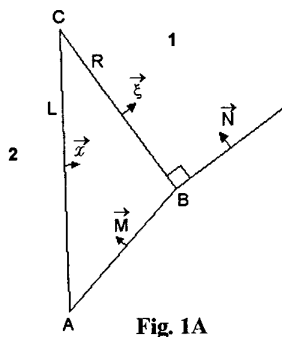


Fig. 1A

lie on one plane) This triangle may be corresponded to some real "triangle" in blade-to-blade space. (Vector M is not necessarily

perpendicular to $\bar{\xi}$ and so the models with right blockage factor values $k \neq 1$

may be considered). Let $\bar{\tau}$ be the unit vector which is orthogonal to $\bar{\xi}$ and \bar{x} . Then the $\bar{\tau}$ -projection of velocity vector \bar{V} may be eliminated from the next considerations because of the equations: $(\bar{V}_2 \cdot \bar{\tau}) = (\bar{V}_L \cdot \bar{\tau}) = (\bar{V}_R \cdot \bar{\tau})$. So below the vector \bar{V} will be considered without its $\bar{\tau}$ -component. (If \bar{V}_0 is the initial velocity vector, then $\bar{V} = \bar{V}_0 - (\bar{V}_0 \cdot \bar{\tau})\bar{\tau}$.)

Let first $\frac{V_L^2}{a_L^2} \leq 1, \frac{(\bar{V}_R \cdot \bar{\xi})^2}{a_R^2 \cdot c_\xi^2} \leq 1$, where a is sound

speed, $c_\xi^2 = (\bar{\xi} \cdot \bar{\xi})$. Then used in the present work relations at the leading edge surface may be written in the form:

$$\begin{cases} \rho_L (\bar{V}_L \cdot \bar{x}) = \rho_R (\bar{V}_R \cdot \bar{\xi}) \\ h_L + \frac{1}{2} \frac{(\bar{V}_L \cdot \bar{\xi})^2}{c_\xi^2} + \frac{1}{2} (\bar{V}_L \cdot \bar{N})^2 = h_R + \frac{1}{2} \frac{(\bar{V}_R \cdot \bar{\xi})^2}{c_\xi^2} \\ s_L = s_R \end{cases} \quad (A1)$$

$$\begin{cases} \rho_L - \rho_2 + (\bar{\rho} \bar{a}) \frac{(\bar{V}_L \cdot \bar{x}) - (\bar{V}_2 \cdot \bar{x})}{c_x} = 0, \\ \rho_L - \rho_2 - (\bar{a}^2)(\rho_L - \rho_2) = 0 \\ \bar{V}_L - \frac{(\bar{V}_L \cdot \bar{x})}{c_x^2} \bar{x} = \bar{V}_2 - \frac{(\bar{V}_2 \cdot \bar{x})}{c_x^2} \bar{x} \end{cases} \quad (A2)$$

$$\left\{ \rho_R - \rho_1 - (\bar{\rho} \bar{a}) \frac{(\bar{V}_R \cdot \bar{\xi}) - (\bar{V}_1 \cdot \bar{\xi})}{c_\xi} = 0 \right. \quad (A3)$$

where h is specific enthalpy and S is specific entropy.

The first equations (A1) are "conservation laws". Note that the momentum equation (which must include the reaction of the area AB with normal unit vector \bar{M}) in (A1) is replaced by the equation of conservation of entropy. It prevents the entropy rise at the leading edges. (The momentum equation also takes place here with some reaction of area AB).

The second equations (A2) are relations through the wave which propagates to the left of the boundary. (It is supposed here that gas flows from the left to right and

the "axial" velocity component $\frac{(\bar{V}_L \cdot \bar{x})}{c_x}$ is subsonic,

which usually takes place. If gas flows in the opposite direction then the surface is considered as the trailing edge boundary, see below). For simplicity these relations are written in linear (acoustic) form, in real algorithms it is necessary to use exact formulae for either shock or expansion wave running to the left.

The equation (A3) is the relation across the waves running to the right.

If the relations $\frac{V_L^2}{a_L^2} \leq 1, \frac{(\bar{V}_R \cdot \bar{\xi})^2}{c_R^2 \cdot c_\xi^2} \leq 1$ are valid

then the solving of equations system (A1)-(A3) has no difficulties. Indeed, expressing the parameters with index "R" from (A1), (A2) through p_L (and also through given parameters with subscript "2") one may

prove that $\left[p_R - (\bar{\rho} \bar{a}) \frac{(\bar{V}_R \cdot \bar{\xi})}{c_\xi} \right]$ is increasing

function of p_L . Therefore one may, for example,

decrease p_L beginning from some greatest value

(which is equal $\left(p_2 + (\bar{\rho}\bar{a}) \frac{(\bar{V}_2 \cdot \bar{x})}{c_x} \right)$, see (A2))

until (A3) is true. But it may occur during the decreasing of p_L that one of the inequalities

$$\frac{V_L^2}{a_L^2} \leq 1, \frac{(V_R \cdot \bar{\xi})^2}{a_R^2 \cdot c_\xi^2} \leq 1 \text{ will be broken.}$$

Let the relation $\frac{V_L^2}{a_L^2} \leq 1$ is broken. Then the system (A1) is replaced by system:

$$\begin{cases} \rho_L' (\bar{V}_L' \cdot \bar{x}) = \rho_R (\bar{V}_R \cdot \bar{\xi}) \\ h_L' + \frac{1}{2} \frac{(\bar{V}_L' \cdot \bar{\xi})^2}{c_\xi^2} + \frac{1}{2} (\bar{V}_L' \cdot \bar{N})^2 = h_R + \frac{1}{2} \frac{(\bar{V}_R \cdot \bar{\xi})^2}{c_\xi^2}, \\ s_L' = s_R \end{cases}$$

where the parameters with superscript " ' " are connected with ones (without the superscript with the shock wave relations. (This is the case of "detached" shock waves).

Another case, when the inequality $\frac{(\bar{V}_R \cdot \bar{\xi})^2}{a_R^2 \cdot c_\xi^2} \leq 1$ is

broken, is more difficult. In this case the equation (A3) must be thrown out and it is necessary to replace it by another. There are two alternative equations. The first corresponds to the choked regime, when $p_L = \bar{p}_L$ is

$$\text{found from the relation: } \frac{(\bar{V}_R \cdot \bar{\xi})^2}{c_\xi^2} = a_R^2.$$

Another relation denotes that mass flow rates from the left and from the right are equal (that is, the right and left "areas" are equal). Let $k = c_\xi^2 / (\bar{x} \cdot \bar{\xi})$ ("left blockage factor"). Then this relation may be written:

$$(\bar{V}_L \cdot \bar{x})^2 = (\bar{V}_L \cdot \bar{\xi})^2 + (\bar{V}_L \cdot \bar{N})^2 \cdot c_\xi^2 \quad (A4)$$

Using (A 2) one may transform it to the equation:

$$\frac{(\bar{V}_L \cdot \bar{x})}{c_x} =$$

$$= \frac{1}{\sqrt{1 + \frac{1 - k^2}{k^2 \frac{(\bar{x} \cdot \bar{N})^2}{c_x^2}}}} \left[\frac{(\bar{V}_2 \cdot \bar{x})}{c_x} - \frac{c_x}{(\bar{x} \cdot \bar{N})} (\bar{V}_2 \cdot \bar{N}) \right] \quad (A5)$$

This value of the pressure p_L being found using (A1), (A2), (A4) (or (A5) instead of (A4)) will be marked by \tilde{p}_L . (In this case also $\tilde{p}_R = \tilde{p}_L$, etc.)

It is the equation giving the largest value of p_L which is chosen from the alternative equations

$$\frac{(\bar{V}_R \cdot \bar{\xi})^2}{c_\xi^2} = a_R^2 \quad \text{and} \quad (A4) \quad (\text{and so}$$

$$p_L = \max(\bar{p}_L, \tilde{p}_L) \text{ together with: } \frac{(\bar{V}_R \cdot \bar{\xi})^2}{a_R^2 \cdot c_\xi^2} \geq 1).$$

Consider now what happens if the wave propagating to the left (and corresponding to relations (A 2)) stops and begins to run to right.

If it is a shock wave then one may choose the parameters with index "L" being equal to the parameters with subscript "2". At the case of expansion wave according the left wave front speed the parameters with index "L" either are equal to parameters with index "2" or are bound with them by expansion wave

relations under the condition: $\frac{(\bar{V}_L \cdot \bar{x})}{c_x} = a_L$. The third equation of (A1) is thrown out. To these two equations

one may add (A3) while $\frac{(\bar{V}_R \cdot \bar{\xi})}{c_\xi} < a_R$. If the last

condition is broken, then two alternative equations may be considered instead of (A3) (similar to the case:

$$\frac{(\bar{V}_L \cdot \bar{x})}{c_x} < a_L): \frac{(\bar{V}_R \cdot \bar{\xi})}{c_\xi} = a_R \text{ and } p_L = p_R. \text{ The}$$

condition that gives the largest value of ρ_R is chosen

(while: $\frac{(\bar{V}_R \cdot \bar{\xi})}{c_\xi} > \alpha_R$). In any case the equations are

easy solved relatively the unknown $\left(\frac{\bar{V}_R \cdot \bar{\xi}}{c_\xi} \right)$.

If gas begins to flow backward then leading edge boundary is considered as a trailing edge one. The conditions describing this case are the next.

Let

$$\rho'' = \rho_2 + (\bar{\rho} \bar{a}) \frac{(\bar{V}_2 \cdot \bar{x})}{c_x},$$

$$\rho'' = \rho_2 + \frac{1}{(\bar{a}^2)} (\rho'' - \rho_2),$$

$$\bar{V}'' = \bar{V}_2 - \frac{(\bar{V}_2 \cdot \bar{x})}{c_x^2} \bar{x},$$

$$\rho' = \rho_1 - (\bar{\rho} \bar{a}) \frac{(\bar{V}_1 \cdot \bar{\xi})}{c_\xi},$$

and ρ'' be obtained from equations:

$$\begin{cases} h(T'') + \frac{1}{2} (\bar{V}'')^2 = h(T''^*), \\ s(\rho'', T'') = s(\rho''^*, T''^*), \end{cases}$$

where $T'' = \frac{\rho''}{\rho'' R}$ (by other words, ρ''^* is total

pressure corresponding to $\rho'', \rho'', \bar{V}''$). Then at the

"leading edge" gas begins to flow backward if and

only if $\rho' > \rho''^*$.

Let us now consider the trailing edge boundary. Similar to leading edge case one may define "trailing edge triangle" (fig.2A).

Let $\bar{\ell}$ be a unit vector which lies on

the plane of the vectors $\bar{x}, \bar{\xi}, \bar{N}$ (they are similar to ones in the leading edge case) and satisfies the condition: $(\bar{x} - \bar{\xi}) \cdot \bar{\ell} = 0$.

Let its direction be the same as on fig.2A. It is convenient further to consider all vectors in the

coordinate system with basis $\frac{\bar{\xi}}{c_\xi}, \bar{N}$. (One may exclude

the $\bar{\tau}$ - direction from the consideration similar to leading edge case).

Let:

$$\frac{(\bar{V} \cdot \bar{\xi})}{c_\xi} = u, \quad (\bar{V} \cdot \bar{N}) = v,$$

$$\frac{(\bar{\ell} \cdot \bar{\xi})}{c_\xi} = \alpha > 0$$

(we have chosen such direction of $\bar{\ell}$),

$$(\bar{\ell} \cdot \bar{N}) = \beta, \quad \frac{(\bar{x} \cdot \bar{N})}{c_\xi} = \gamma,$$

$k = 1 - \frac{\gamma\beta}{\alpha}$. The value k^{-1} may be defined as "left blockage factor". The parameters at the right side of the boundary surface will be denoted further without the index "R".

Let us consider first the case when $u_L < a_L$ ("left" flow is subsonic) and $(u^2 + v^2) < a^2$ ("right" flow without the component $(\bar{V} \cdot \bar{\tau})\bar{\tau}$ is also subsonic).

Then the relations at the boundary surface used at the present work are the next:

$$\begin{cases} \rho(ku + \gamma v) = \rho_L u_L \\ s = s_L \\ h + \frac{1}{2}(u^2 + v^2) = h_L + \frac{1}{2}u_L^2 \\ \rho(ku + \gamma v)(\alpha u + \beta v) + \alpha p = (\rho_L u_L^2 + \rho_L) \alpha \end{cases} \quad (A6)$$

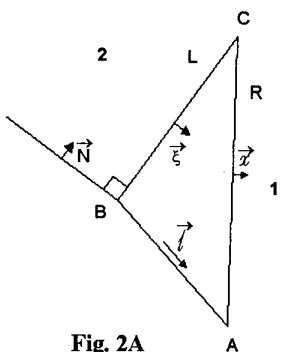


Fig. 2A

$$\begin{cases} \rho_L - \rho_2 + (\bar{\rho}\bar{\alpha})(u_L - U_2) = 0 \\ \rho_L - \rho_2 - (\bar{\alpha}^2)(\rho_L - \rho_2) = 0 \\ v_L = v_2 \end{cases} \quad (A7)$$

$$\left\{ \rho - \frac{(\bar{\rho}\bar{\alpha})}{\sqrt{k^2 + \gamma^2}} (ku + \gamma v) = \right. \quad (A8)$$

$$= \rho_1 - \frac{(\bar{\rho}\bar{\alpha})}{\sqrt{k^2 + \gamma^2}} (ku_1 + \gamma v_1)$$

The first, second and fourth equations of (A6) are mass, energy and momentum conservation laws. (The momentum equation for the direction orthogonal to \bar{l} is not included to (A6) because it serves only for the defining of reaction of the area AB. This force is supposed here to be orthogonal to AB). They are insufficient for the trailing edge case. So the equation of entropy conservation is added. Note that the number of equations (A6) is more than similar one of (A1). It is because the number of running away characteristics is more than it takes place for the leading edge.

Two first equations of (A7) are relations for the wave propagating to the left, and (A8) is the relation for the wave running to right. They are written in acoustic form, but the precise form of these equations were used in algorithms. There are not any difficulties in using these nonlinear equations because the system (A6), (A7), (A8) is solved by iterations.

Finally, as recalled in (A7), $v_L = v_2 = 0$.

Some notes about solving of the system (A6), (A7), (A8). For this the solving of (A6) is key task. Let us consider a function

$$f(\rho) = \rho(ku + \gamma v)(\alpha u + \beta v)\alpha\rho,$$

where ρ, u, v are expressed by ρ and parameters with index "L" using first three equations of (A6).

Then one may obtain the formula:

$$\frac{\partial f}{\partial \rho} = \frac{(\beta u - \alpha v)(k^2 + \gamma^2)}{\gamma u - kv} \left[1 - \left(\frac{uk + \gamma v}{\alpha \sqrt{k^2 + \gamma^2}} \right)^2 \right],$$

where $\alpha = \sqrt{\left(\frac{\partial \rho}{\partial p} \right)_s}$ is sound speed (with omitted index "R"). It is evident from (A 9) that if vector \bar{V} lies

within the angle being formed by vectors $\bar{\xi}$ and \bar{l} then f is monotone function of ρ . Considering the extreme cases, when \bar{V} is collinear to $\bar{\xi}$ or to \bar{l} , one may show that in one case f is no more than $(\rho_L u_L^2 + \rho_L)\alpha$ and at another f is no less than this value. And so the system (A6) always has the only solution relative parameters with subscript "L" (when $u^2 + v^2 < \alpha^2$).

Further one may reason similar to leading edge case. Supposing the value of ρ_L to be known one may find other parameters with subscript "L", then solve the system (A 6) and at last prove the condition (A 8). So ρ_L may be decreased beginning from some largest value until (A8) is satisfied.

But during the decreasing of ρ_L one of the relations: $u_L < \alpha_L$ or $u^2 + v^2 < \alpha^2$ may be broken.

At the first case the wave running to the left (precisely speaking its left front) and corresponding to relations (A 7) has zero speed.

It is either shock wave or expansion wave.

If it is shock wave then other relations:

$\rho_L = \rho_2, u_L = u_2, \rho_L = \rho_2$ take place instead of (A7) and one of the equations (A 6) must be excluded.

The second equation $s = s_L$ is excluded if under this condition the inequality $s > s_L$ is true, otherwise the fourth relation must be eliminated (this is the requirements of the second law of thermodynamics).

If the corresponding wave is an expansion wave then one must differ two cases. If $u_2 < \alpha_2$ then the parameters with subscripts "L" and "2" are bound by expansion wave relations under the condition: $u_L = \alpha_L$.

And if $u_2 \geq \alpha_2$ then the values of parameters with subscripts "L" and "2" are equal. In the both cases the fourth equation of (A6) is thrown out.

So the case is considered, when during the decreasing of ρ_L the relation $u_L = \alpha_L$ is broken.

Let now the condition: $u^2 + v^2 < \alpha^2$ is first broken. And so the relation $u^2 + v^2 = \alpha^2$ is fulfilled. This is the case when the flow is choked "behind the throat". Starting from this moment the values of the parameters with index "L" are constant and correspond to condition: $u^2 + v^2 = \alpha^2$. And the fourth equation of (A6) is excluded in this case.

Thus all cases are considered. (The conditions of appearing of opposite directed flows are similar to the conditions at the leading edges. In this case the "trailing edge" boundary must be considered as "leading edge" one).

If the fourth equation of (A6) is excluded then the solving of system (A6) and (A8) do not meet any difficulties.

Let us consider the system (A8) and (A6) with excluded second equation of (A6). For simplicity the case of perfect gas with constant specific heats in a ratio

$c_p/c_v = \kappa$ will be supposed. (In common case the obtained below formulae will be used in some additional iteration process using the relation:

$$\delta h = c_p \delta T = \frac{\kappa}{\kappa - 1} \delta \frac{p}{\rho}$$

Let: $\tilde{u} = \alpha u + \beta v, \tilde{v} = \beta u - \alpha v$. The system may be led to quadratic equation relative the \tilde{v} . The final formulae are:

$$\tilde{v} = \frac{2C}{-B \left(1 + \sqrt{1 - \frac{4AC}{B^2}} \right)},$$

where

$$A = \frac{1}{2} \left[\frac{\sqrt{k^2 + \gamma^2}}{(\bar{\rho} \bar{\alpha})} + \frac{\alpha^2}{\rho_L u_L} \right]^2 + \frac{\kappa}{\kappa - 1} \frac{(\kappa\beta - \gamma\alpha)^2 \sqrt{k^2 + \gamma^2}}{\rho_L u_L (\bar{\rho} \bar{\alpha})} + \frac{1}{2} \frac{\alpha^2 (\kappa\beta - \gamma\alpha)^2}{\rho_L^2 u_L^2},$$

$$B = \frac{1}{\kappa - 1} \alpha^2 (\kappa\beta - \gamma\alpha) \frac{\frac{\sqrt{k^2 + \gamma^2}}{(\bar{\rho} \bar{\alpha})} [\rho_L u_L^2 + \rho_L - \rho_1] + (\kappa u_1 + \gamma v_1)}{\rho_L^2 u_L^2} +$$

$$+ \frac{\kappa}{\kappa - 1} \frac{\sqrt{k^2 + \gamma^2}}{(\bar{\rho} \bar{\alpha})} \frac{(\kappa\beta - \gamma\alpha)}{\rho_L u_L} \left[\frac{\sqrt{k^2 + \gamma^2}}{(\bar{\rho} \bar{\alpha})} \rho_1 + \right.$$

$$\left. + \frac{\alpha^2 (\rho_L + \rho_L u_L^2)}{\rho_L u_L} - (\kappa u_1 + \gamma v_1) \right],$$

$$C = \frac{\kappa}{\kappa - 1} \frac{\alpha^2}{\rho_L^2 u_L^2} \left[\frac{\sqrt{k^2 + \gamma^2}}{(\bar{\rho} \bar{\alpha})} \rho_1 + \frac{\alpha^2 (\rho_L + \rho_L u_L^2)}{\rho_L u_L} - (\kappa u_1 + \gamma v_1) \right] \times$$

$$\times \left[\frac{\sqrt{k^2 + \gamma^2}}{(\bar{\rho} \bar{\alpha})} (\rho_L u_L^2 + \rho_L - \rho_1) + (\kappa u_1 + \gamma v_1) \right] + \frac{1}{2} \alpha^2 \frac{\left[\frac{\sqrt{k^2 + \gamma^2}}{(\bar{\rho} \bar{\alpha})} (\rho_L u_L^2 + \rho_L - \rho_1) + (\kappa u_1 + \gamma v_1) \right]^2}{\rho_L^2 u_L^2} - \left(\frac{\kappa}{\kappa - 1} \frac{\rho_L}{\rho_L} + \frac{1}{2} u_L^2 \right) \left(\frac{\sqrt{k^2 + \gamma^2}}{(\bar{\rho} \bar{\alpha})} + \frac{\alpha^2}{\rho_L u_L} \right)^2.$$

Having calculated \tilde{v} , one may find ρ :

$$\rho = \frac{(\kappa\beta - \gamma\alpha)}{\left[\frac{\sqrt{k^2 + \gamma^2}}{(\bar{\rho} \bar{\alpha})} + \frac{\alpha^2}{\rho_L u_L} \right]} \tilde{v} +$$

$$+ \frac{\left[\frac{\sqrt{k^2 + \gamma^2}}{(\bar{\rho} \bar{\alpha})} \rho_1 + \frac{\alpha \rho_L}{\rho_L u_L} + \alpha^2 u_L - (\kappa u_1 + \gamma v_1) \right]}{\left[\frac{\sqrt{k^2 + \gamma^2}}{(\bar{\rho} \bar{\alpha})} + \frac{\alpha^2}{\rho_L u_L} \right]},$$

then \tilde{u} :

$$\tilde{u} = \alpha u_L + \frac{\alpha}{\rho_L u_L} (\rho_L - \rho),$$

and, at last, ρ, u, v :

$$\rho = \frac{\rho_L u_L}{\alpha \tilde{u} + (\kappa\beta - \gamma\alpha) \tilde{v}},$$

$$u = \alpha \tilde{u} + \beta \tilde{v}, v = \beta \tilde{u} - \alpha \tilde{v}.$$

As described here and used in calculation procedures at the "internal" boundaries have the property that "subsonic" and "supersonic" cases are corresponded one to another. It denotes that at the continuous changing of values of parameters "1" and "2" fluxes at the boundaries also vary continuously (including the case when a shock wave comes to the boundary).

Note that instead of the fourth equation of (A6) any other model may be used. For example, if flow deviation angles are known (as some semi-empirical functions of other parameters), one may use them in (A6). The general scheme of reasoning will be almost the same, only same formulae will vary (and even become more simple).

APPENDIX B

The averaging of 3D flow parameters at the middle of axial gaps with conservation of mass, momentum and energy fluxes

As it was mentioned during the 3D gas flows calculations in multistage turbomachines the averaging of parameters in angular direction at the middle of axial gaps was fulfilled. On the one hand this guarantees the existence of steady solutions, on the other hand it allows to consider only one blade-to-blade channel for each blade row.

The surface which is used for averaging will be called "surface of averaging". It is the right boundary $\xi = \text{const}$ of "left" blade row and the left boundary $\xi = \text{const}$ for the "right" one. The computational grids used in the present work have the property that the "grid surface" $\eta = \text{const}$ are rotation surface located between hub and shroud.

On the surface of averaging: $\xi_\varphi = 0$. Let:

$$c_\xi = \sqrt{\left(\frac{r_{\xi z}^{\xi}}{J}\right)^2 + \left(\frac{r_{\xi r}^{\xi}}{J}\right)^2}, \quad u_k = \frac{u \frac{r_{\xi z}^{\xi}}{J} + v \frac{r_{\xi r}^{\xi}}{J}}{c_\xi},$$

$$u_t = \frac{u \frac{r_{\xi r}^{\xi}}{J} - v \frac{r_{\xi z}^{\xi}}{J}}{c_\xi}$$

It is sufficient to consider the case, when the grid surfaces $\eta = \text{const}$ are continuous at the surface of averaging.

Let the parameters with index "1" be right hand limits and with "2" the left ones. They are calculated using piece-wise parabolic distributions of characteristic variables.

"Large" values of parameters which are used to form the fluxes at all boundaries will be marked by subscripts "L" and "R" (respectively for left and right side parameters).

The averaging of parameters fulfilled under the requirement that for any ring part of the surface placed from r to $r + \delta r$ mass, momentum and energy fluxes are equal for both sides of surface of averaging. This condition can be written in the next form (for each r):

$$\left\{ \begin{aligned} \int_0^{2\pi} (\rho u_k)_L \tilde{c}_\xi d\varphi &= \int_0^{2\pi} (\rho u_k)_R \tilde{c}_\xi d\varphi \\ \int_0^{2\pi} (\rho u_k^2 + \rho)_L \tilde{c}_\xi d\varphi &= \int_0^{2\pi} (\rho u_k^2 + \rho)_R \tilde{c}_\xi d\varphi \\ \int_0^{2\pi} (\rho u_k u_t)_L \tilde{c}_\xi d\varphi &= \int_0^{2\pi} (\rho u_k u_t)_R \tilde{c}_\xi d\varphi \\ \int_0^{2\pi} (\rho u_k w)_L \tilde{c}_\xi d\varphi &= \int_0^{2\pi} (\rho u_k w)_R \tilde{c}_\xi d\varphi \\ \int_0^{2\pi} \left[\rho u_k \left\{ h + \frac{1}{2} (u_k^2 + u_t^2 + w^2) \right\} \right]_L \tilde{c}_\xi d\varphi &= A \end{aligned} \right. \quad (B1)$$

where:

$$A = \int_0^{2\pi} \left[\rho u_k \left\{ h + \frac{1}{2} (u_k^2 + u_t^2 + w^2) \right\} \right]_R \tilde{c}_\xi d\varphi$$

Let us define (for each radius) some "equivalent" axisymmetrical flow with parameters R, U, V, W, P which realize the averaging procedure. The "average" influence of right domain to left one and inversely is performed through this flow.

"Large" values of parameters (with subscripts "L" and "R") are found from the exact solution of Riemann problem (this procedure is used separately for each cell):

$$\left\{ \begin{aligned} u_{tL} &= u_{t2} \\ w_t &= w_2 \\ \rho_L - \rho_2 + (\rho a)' (u_{kL} - u_{k2}) &= 0 \\ \rho_L - \rho_2 - (a^2)' (\rho_L - \rho_2) &= 0 \\ \rho_L - P - (\rho a)'' (u_{kL} - U_k) &= 0 \end{aligned} \right. \quad (B2)$$

$$\left\{ \begin{aligned} u_{tR} &= U_t \\ w_R &= W \\ \rho_R - P + (\rho a)''' (u_{kR} - U_k) &= 0 \\ \rho_R - P - (a^2)'' (\rho_R - R) &= 0 \\ \rho_R - \rho_1 - (\rho a)'' (u_{kR} - U_{k1}) &= 0 \end{aligned} \right. \quad (B3)$$

It is supposed in (B2) and (B3), that gas flows from the left to right and the flow is "axially" subsonic which usually takes place. (If this condition is broken for some cells then one must replace these equations by corresponding others in accordance with Riemann problem solution). As earlier these equations are written in linear (acoustic) form for simplicity. Really the exact equations were used for shocks and expansion waves.

There are five unknowns R, U_t, U_k, W, P in equations system (B1) (with account of (B2), (B3)). Two of them U_t and W are found immediately, and the Newton method is used for solving of other 3 equations.

Some notes on the averaging procedure used.

If the flow for both sides of the surface is axisymmetric then as it is easy to see the parameters R, U, V, W, P are usual "large" ones, which are used in forming of fluxes. That is:

$$\rho_L = \rho_R = R, u_L = u_R = U$$

etc. In other words in this case the averaging procedure is trivial.

If the flow is "axially" supersonic then instead of (B2) the equations will take place:

$$\rho_L = \rho_2, u_L = u_2, v_L = v_2, w_L = w_2, p_L = p_2$$

and instead of (B3):

$$\rho_R = R, u_R = U, v_R = V, w_R = W, p_R = P$$

Then it is evident from (B 1) that the flow with parameters R, U, V, W, P is obtained from the flow with parameters with subscript "2" by averaging in angular direction with conservation of mass, momentum and energy.

Finally, if flows for both sides of the surface are slightly perturbed uniform axisymmetric flows then one may consider a linear problem with "frozen" coefficients replacing the flux vector

$\bar{F}(\bar{U}) = A(\bar{U})\bar{U}$ by $A(\bar{U}_0)\bar{U}$, where $\bar{U}_0 = const$ is uniform axisymmetric flow

$(A(\bar{U}) = \frac{\partial \bar{F}(\bar{U})}{\partial \bar{U}}$ is Jacobi matrix). Reasoning

similar to supersonic case and considering "plane waves" it is easy to find that considered averaging conditions are "non reflecting" ones and "Riemann invariants" are averaged in angular direction.

These notes show that used averaging procedure is quite "natural".

Note that this procedure allows also easy construct "mixed" models of flows in multistage turbines and compressors, when in some blade rows the flow is calculated by S_2 - approach and in others by 3D

method. Such method of calculation may be useful, for example, during the design of some separate blade row or stage when the influence of other stages can be accounted by more simple and less expensive way. It is evident that for this "mixed" model the averaging procedure remains the same as for fully 3D case. This model may be useful also for some unsteady simulations.

In conclusion note also that the procedures described at appendixes A and B show the convenience of using of numerical schemes based on Godunov's scheme, with use the exact solution of the Riemann problem.

REFERENCES

1. Wu Chung-Hua. A General Theory of Three-Dimensional Flow in Subsonic and Supersonic of Axial-Radial and Mixed Flow Type. Transaction ASME, 1952, 74, 8.
2. Stepanov G. Yu. Hydrodynamics of turbomachine cascade. -M., Fizmatgiz, 1962, 512p.
3. Swith L.H., Jr. The Radial Equilibrium Equations of Turbomachinery. Trans. ASME, Journal of Engineering for Power, 1966, Vol.88A, 1.
4. Novak R.A. Streamline curvature computing Procedures for Fluid Flow Problems. Trans. ASME, Journal of Engineering for Power., 1967, vol. 89A.
5. Salnikov V. S. On calculation of axisymmetrical gas flow in turbomachines. Lopatochnye mashiny i struinye apparaty.-M., Mashinostroenie, 1972, vyp. 6, pp. 45-54.
6. Hirsch C., Warzee G. A Finite - Element Method for Through Flow Calculations in Turbomachines, ASME Journal of Fluids Engineering, 1976, vol. 98, pp.403-421.
7. Denton J. E. Through Flow Calculations for Transonic Axial Flow Turbines. Trans. of ASME, Journal of Engineering for Power, 1978, Vol. 100, April 1978
8. Kioussis P., Chaviaropoulos P., Papailioni K.D. Meridional Flow Calculation Using Advanced CPD Techniques. ASME 92-GT-325.
9. Ivanov M. Ja., Kimasov Yu. I. Numerical solution of the direct definition problem of the ideal gas mean axisymmetrical flow in the turbomachinery stage. Scientific proceedings of CAHDI, 1975, Vol.6, N2.
10. Lurie K.A., Fedorov A.V., Klimovich V.I. Conditions along the boundaries of bladed zones within the flow tracts of turbines. -Intern. Journal

for numerical methods in Fluids., 1982, Vol.2, '3,
pp299-311

11. Ron-Ho R.Ni, Jeffrey C.Bogoian. Prediction of 3D Multi-Stage Turbine flow Field Using a Multiple-Grid Euler Solver. AIAA 89-0203
12. Denton J. E. A Time - Marching Method for Two and Three - Dimensional Blade - to - Blade Flows, Aeronautical Research Council, British R&M No. 3775, Oct. 1974.
13. Chima R. V. Explicit multigrid algorithm for quasi-three-dimensional viscous flows in turbomachinery. Journal of Propulsion and Power, 1987, Vol. 3, N5, pp.397-405.
14. Byvaltsev P. M., Ivanov M. Ja., Computational method for transonic potential flows in turbomachinery cascades. J. of Comp. Math. and Math. Phys., 25, pp. 447-459, 1989.
15. Consigny H., Richards B.E. Short Duration Measurements of Heat-Transfer Rate to a Gas Turbine Rotor Blade. Transactions of the ASME, Vol. 104, July, 1982.
16. Ivanov M. Ja., Nigmatullin R. Z., Quasi-3D Numerical Model of a Flow Passage of the Aviation Gas Turbine Engines. ISABE* 91-7029, pp. 299-305.
17. Ivanov M. Ja., Kostege V. K., Krupa V. G., Nigmatullin R. Z. Design of High-Load Aviation Turbomachines Using Modern 3D Computational Methods. ISABE 93-7032, pp. 355-365.
18. Baldwin B. S., Lomax H. Thin-layer approximation and algebraic model for separated turbulent flows, AIAA Paper, 1978, 78-257, p.10.

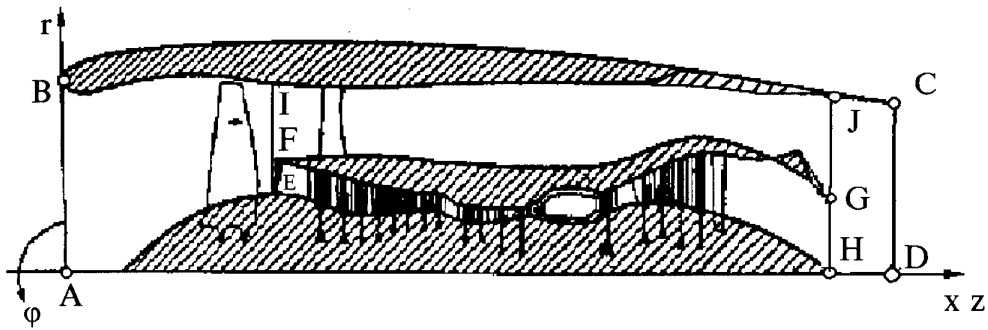


Fig. 1. Meridional plane of the computational flow passage of bypass gas turbine engine.

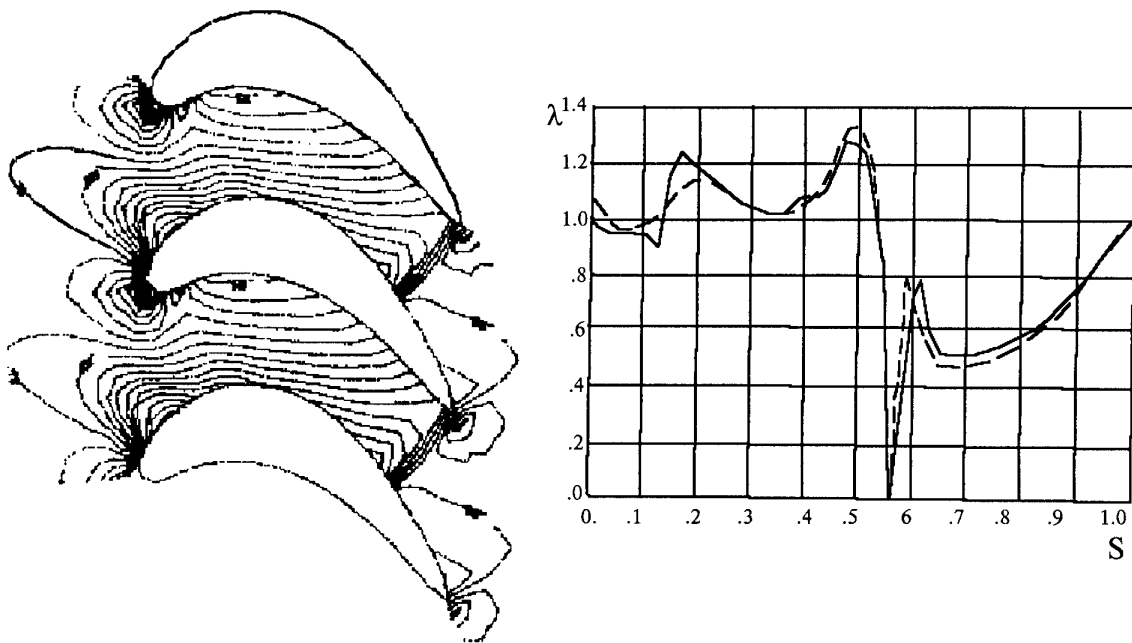


Fig. 2. Calculation of inviscid flow through the turbine cascade at S_1 -surface (dotted line is a result of solving of full potential equation [14]).

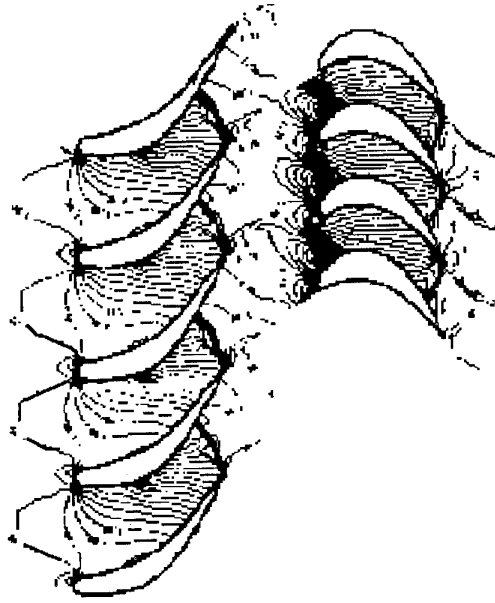


Fig. 3. Unsteady stator and rotor interaction at S_1 -surface (inviscid calculation).

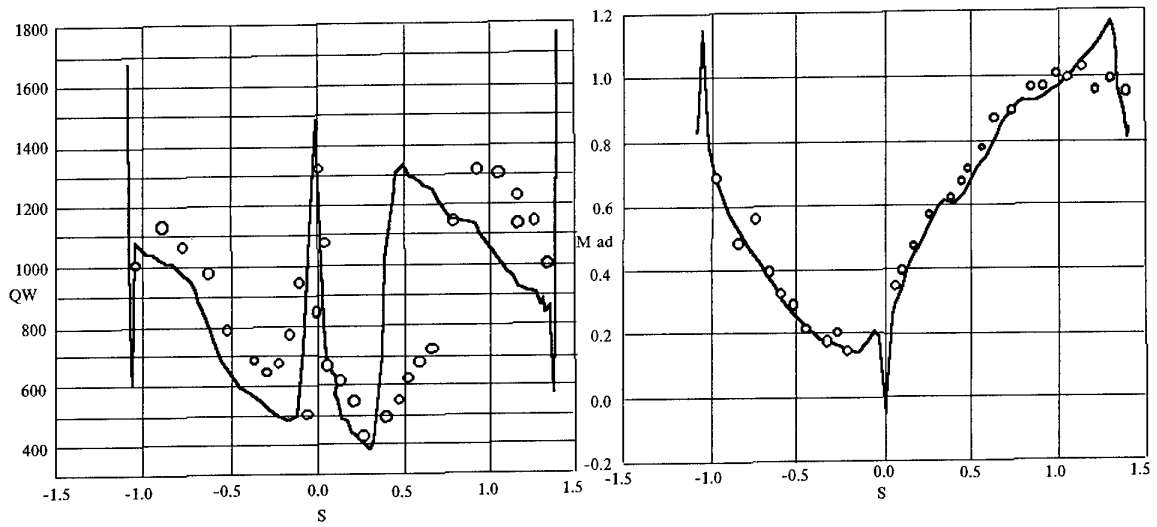


Fig. 4. Viscous flow through turbine cascade (circles - experimental data of [15]).

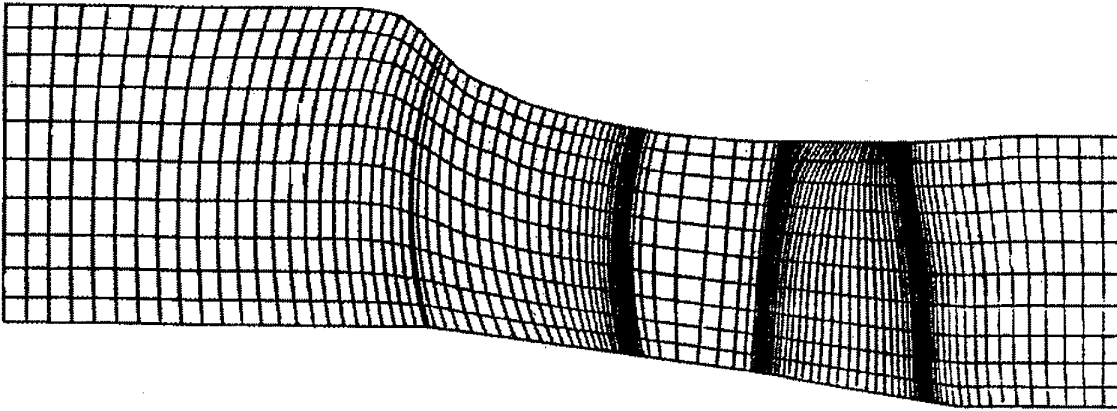


Fig. 5. Computational grid (at meridional plane) for cooled 1 stage high pressure turbine.

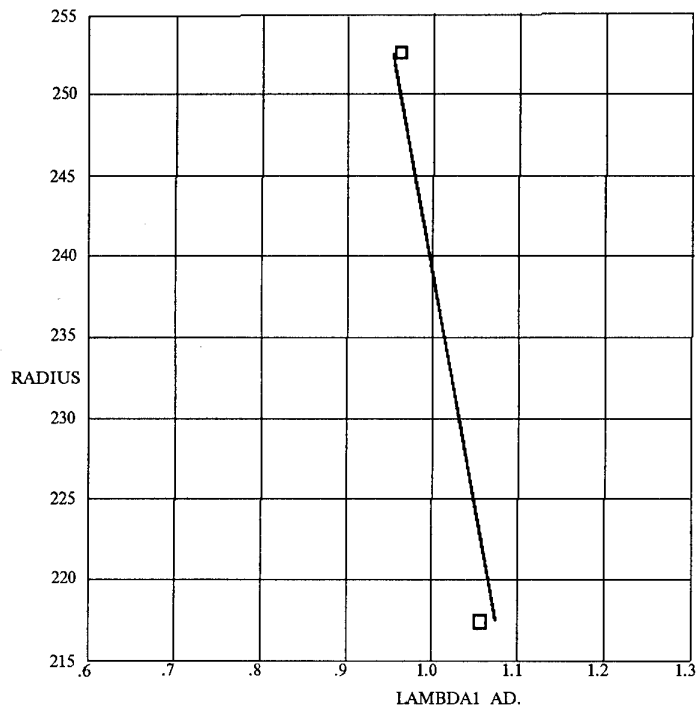


Fig. 6. Isentropic velocity

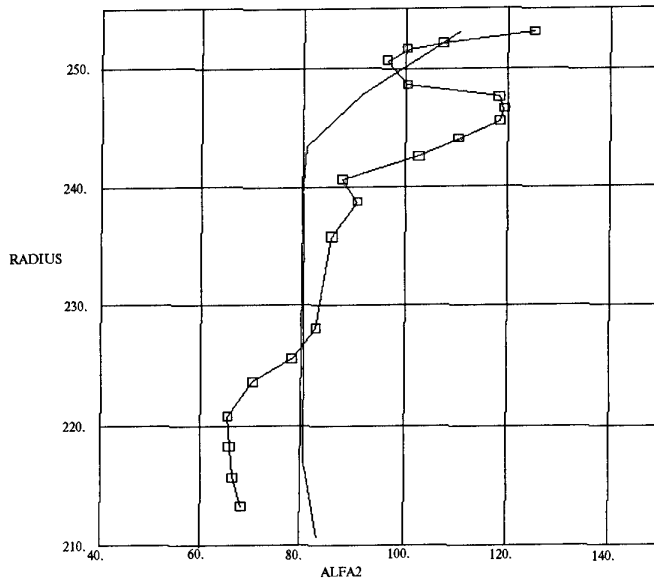


Fig. 7. Exit absolute velocity angle distribution for high pressure turbine.

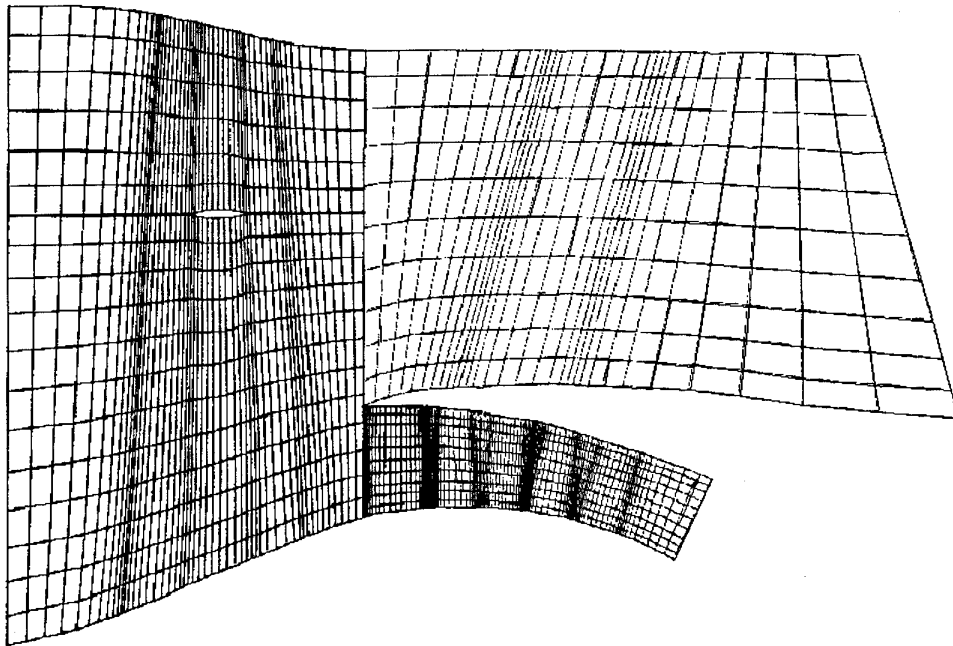


Fig. 8a. 3D computational grid for fan with blade mid-span shroud and low pressure compressor (meridional section).

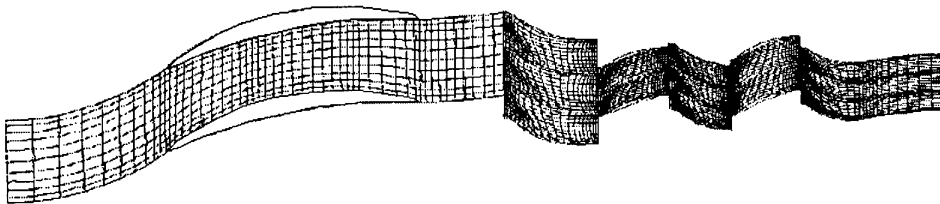


Fig. 8b. Computational grid for the fan with blade mid-span shroud and low pressure compressor (hub section).

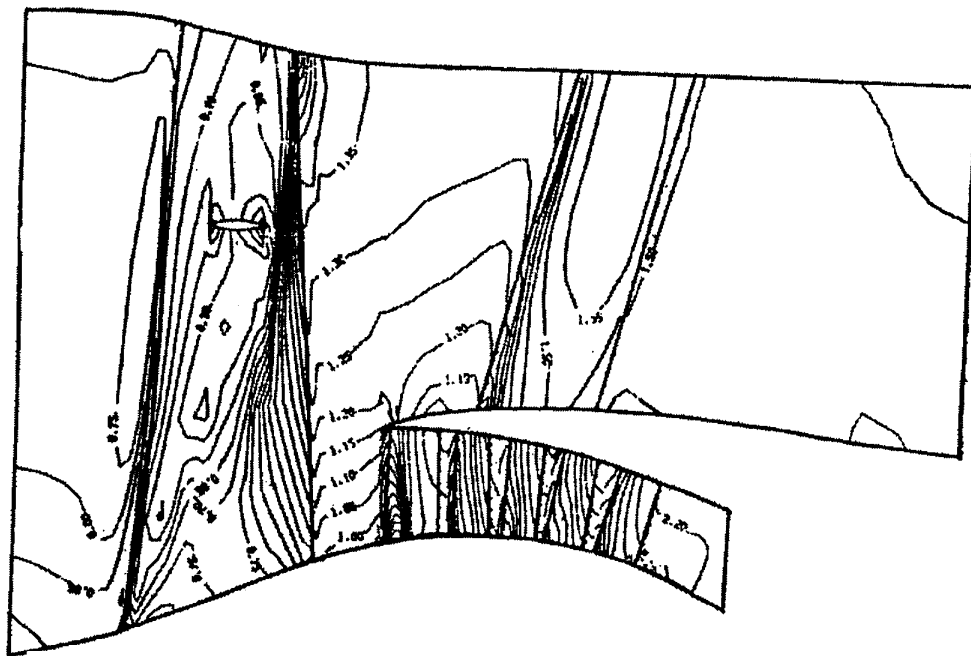


Fig. 9. Pressure contours at some meridional section.

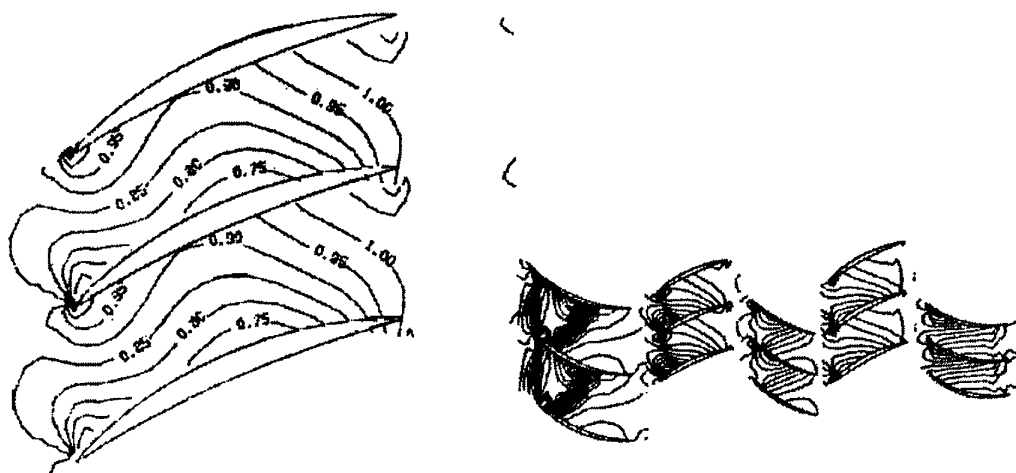


Fig. 10. Pressure control at hub section.

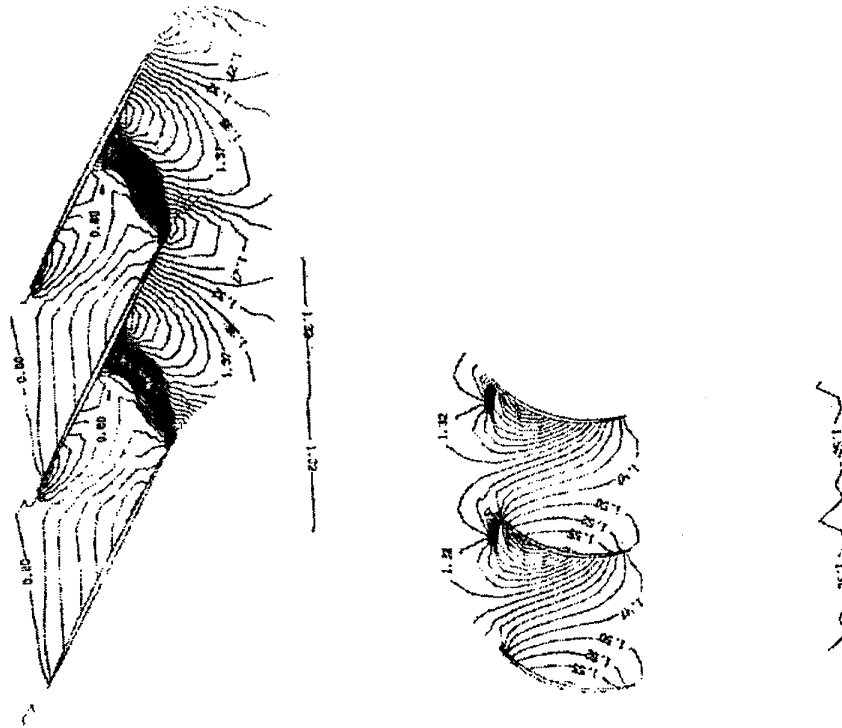


Fig. 11. Pressure contours at tip section.

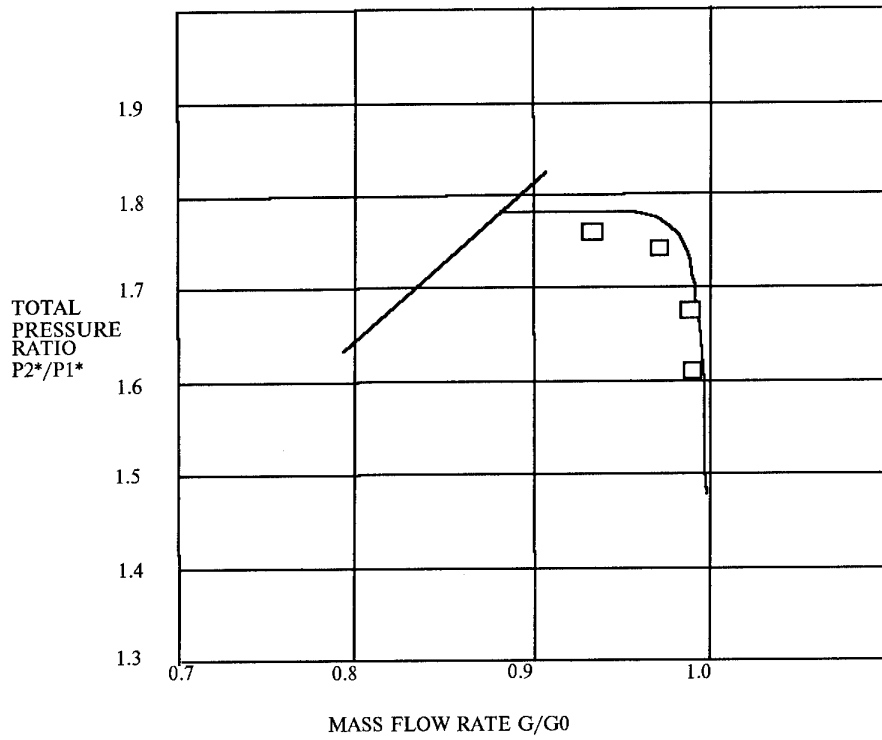


Fig. 12. Fan characteristic (solid line - experimental data, squares - calculated results) and gasdynamic stability line.

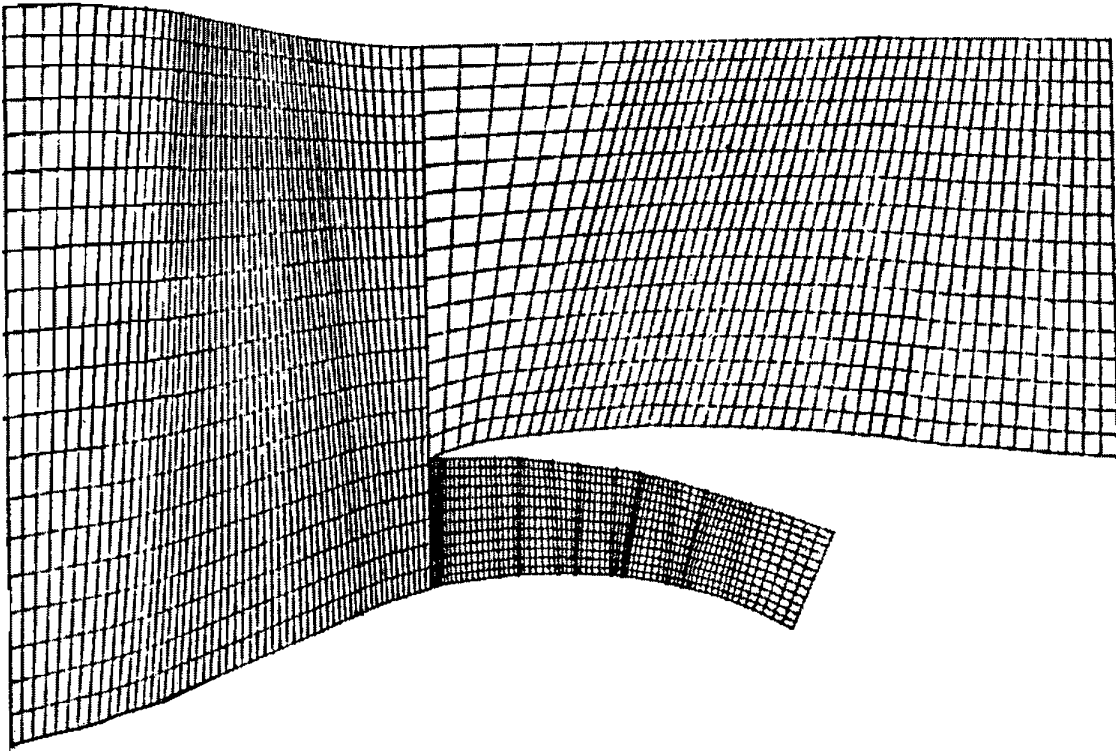


Fig. 13. Computational grid for S_2 - surface calculations.

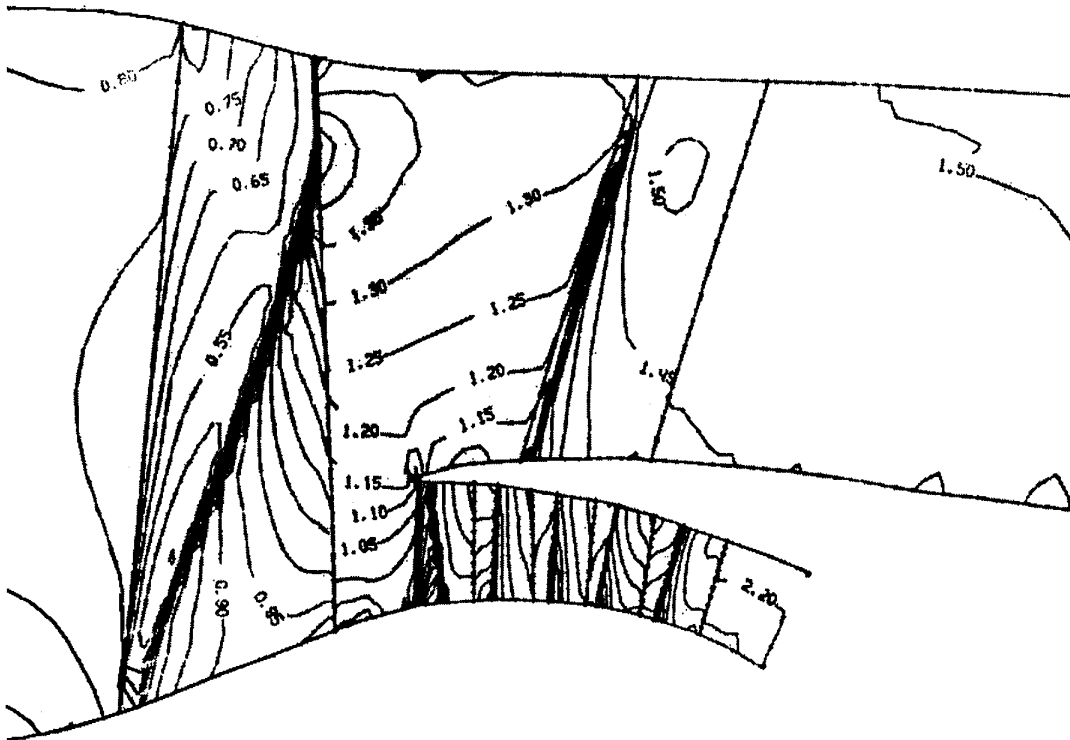


Fig. 14. Pressure contours.

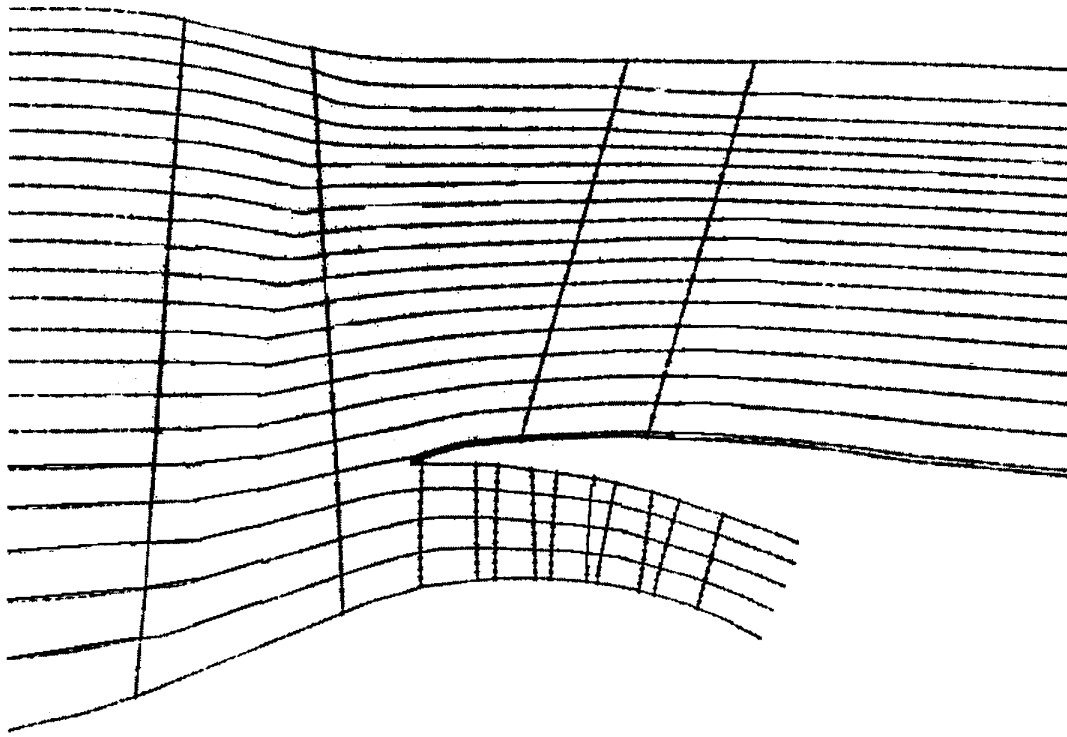


Fig. 15. Stream lines.

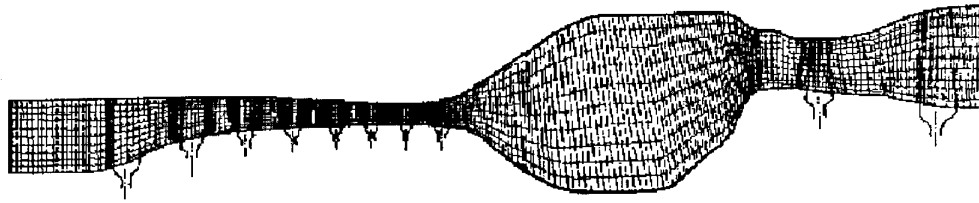


Fig. 16. Computational grid for the bypass engine core.

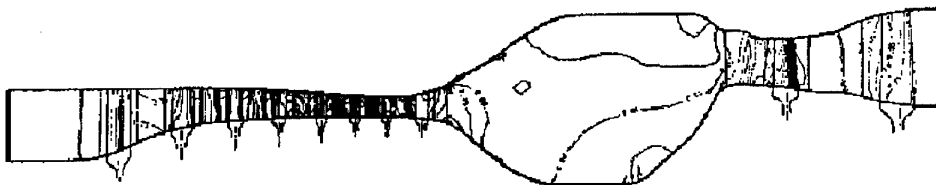


Fig. 17. Pressure contours for bypass engine core in meridional section.

Simulation of multidisciplinary problems for the thermostress state of cooled high temperature turbines

by

Dr. V. K. Kostege, V. A. Halturin, Dr. V. G. Sundurin
CIAM (Central Institute of Aviation Motors)
2, Aviamotornaya St.,
Moscow, Russia, 111250

Abstract

Numerical models for the thermostress state analysis of turbine rotor elements are discussed. Steady and unsteady temperature fields are calculated and result in solution of conjugate heat and hydraulic problems for blades (quasi three-dimensional model) for disk (two-dimensional model) and for the whole cooled rotor (three-dimensional model). A lot of attention is given to mass flow calculation in blade passages and turbine circumferential disk cavities. They are determined by using experimental data for pressure loss and generalized dependencies for friction and heat transfer coefficients on stators and rotors surfaces.

On external blade surfaces the boundary conditions are defined from the solution of two-dimensional and three-dimensional gas dynamics problems and corrected from experimental data base for film cooling. The thermostress state is calculated by a finite element method for realistic geometry using common equations of elasticity theory.

Nomenclature

c	-	heat capacity
k	-	thermal conductivity
T	-	temperature
W	-	heat source
h	-	heat transfer coefficient
N	-	shape function
t	-	time
x, y, z	-	coordinates
P	-	pressure
V	-	velocity
ξ	-	pressure loss coefficient
D	-	hydraulic diameter
l	-	passage length
G	-	mass flow
F	-	passage cross-sectional area
S	-	surface
π	-	Laval number
$\pi(\lambda) = P/P_i$		

$$q(\lambda) = \frac{\rho V}{\rho_{cr} V_{cr}} - \text{gasdynamic functions}$$

$$\varepsilon(\lambda) = \rho / \rho_T$$

R	-	gas constant
τ	-	friction tension

Subscripts

a	-	ambient
w	-	wall
con	-	contact
m	-	time moment
e	-	finite element
w	-	rotation
t	-	total
d	-	disk
ϕ	-	circular

Introduction

Complex solution of gas dynamics, heat transfer and stress conjugated problems is an important trend in the development and application of mathematics simulation in the analysis of a modern high temperature turbine. An example is the problem of an aviation engine, cooled, high temperature turbine rotor thermostress state, for which the accurate solution is provided by simultaneous calculation of air and gas mass flow in inter disk cavities, in blade cooling passages, and in the gas channel.

General purpose non-linear finite element codes, such as MAPS, ABACUS etc. are used as a solution of plasticity theory stress and for temperature field calculation with boundary conditions.

A method for the calculation of a cooling air mass flow distribution in an internal channel of a turbine blade by a multipass configuration was presented by Jen and Sobanic [1], Kumar et. al. [2]. Both methods are based on published correlations describing the heat transfer and the pressure loss. In this work, no special attention is given to temperature definition in the blade metal. A method of temperature field calculation for steady and unsteady conditions with three-dimensional and two-dimensional models, through several sections of the blade is given by

Gastebois and Lagrange [3]. Three-dimensional blade temperature distribution and internal boundary conditions are calculated using an iterative coupled procedure given by Tietz and Koschel [4]. In this work, questions of temperature calculation for blade with a film cooling system are not discussed.

Taking into account possible errors in the statement of three-dimensional boundary conditions an analysis rule is realized at the conclusion.

Lower level models are used at first. For heat state calculation, an applicable interactive system of simulation of two-dimensional and three-dimensional problems by finite elements method, is given which includes:

- modules of automated generation finite element grids in a two-dimensional and a three-dimensional compound region with minimum initial data.
- modules of calculation of one-dimensional flow and heat exchange in blade passages and in circumferential disc cavities using experimental data.
- modules of calculation of steady and unsteady nonlinear two-dimensional and three-dimensional equations of heat conduction by finite element methods with boundary conditions of second and third kind, with boundary conditions of contact heat transfer, and also with periodicity conditions.
- modules of graphic treatment of initial data and calculation results (two-dimensional and three-dimensional graphics).

In this lecture, heat transfer and hydraulic models are discussed for the profile part of blade, for disk and for rotor (which includes blade, hooks and disk). Also the practical application of results of mathematics simulation methods to analyze heat and stress processes in aviation engine elements is demonstrated.

1. Simulation of turbine element temperature state

Equations of heat conduction (1.1) with boundary conditions of the second and third kind (1.2) and with contact heat transfer conditions (1.3) are integrated.

$$c\rho \frac{\partial T}{\partial n} = \nabla(k\nabla T) + w = 0 \quad (1.1)$$

$$-k \frac{\partial T}{\partial n} = h_a(T_w - T_a) + q \quad (1.2)$$

$$\begin{aligned} -\left(k \frac{\partial T}{\partial n}\right)_1 &= h_{con}(T_{1w} - T_{2w}) \\ -\left(k \frac{\partial T}{\partial n}\right)_2 &= h_{con}(T_{2w} - T_{1w}) \end{aligned} \quad (1.3)$$

These equations describe unsteady temperature fields in a three-dimensional body with inside heat sources. On body surfaces they can be simultaneous, taking the place of convection heat flow, (determined by heat transfer coefficient and ambient temperature) and radiation heat flow (1.2). In compound constructions, such as a frame and turbine rotor, the common boundary temperature fields is wrecking break, the size of which depends on contact heat transfer. Boundary conditions on such surfaces are written down as (1.3).

Intergration of equation (1.1) with boundary conditions (1.2) and (1.3) is implemented by a finite element method. As a result we have a system of linear algebraic equations (1.4) with relatively unknown temperature values of a finite elements grid node.

$$\left(\frac{2}{\Delta t}[P] + [H] + [Q]\right)\{T\}^{m+1} = \quad (1.4)$$

$$\left(\frac{2}{\Delta t}[P] - [H] - [Q]\right)\{T\}^m + 2\{Q_1\}$$

where

$$H_{vj} = \sum h_{vj}^e,$$

$$h_{vj}^e = \int_v k \left(\frac{\partial N_\tau}{\partial x} \frac{\partial N_\tau}{\partial x} + \frac{\partial N_\tau}{\partial y} \frac{\partial N_\tau}{\partial y} + \frac{\partial N_\tau}{\partial z} \frac{\partial N_\tau}{\partial z} \right) dv,$$

$$P_\tau = \sum_e P_\tau^e, \quad P_\tau = \frac{1}{n} \int_{v'} c\rho N_\tau dv$$

$$Q_{\tau j}^e = \sum_e \int_{s_i'} h_a N_\tau N_j ds,$$

or

$$Q_j = \sum_e \int_{s_{con}'} h_{con} N_\tau N_j ds$$

$$Q_{\tau}^e = \sum_e \int_{s_i'} (h_a T_a + q) N_\tau ds + \sum_e \int_{v'} N_\tau W dv$$

$$T = [N]\{T\}$$

In computer programs for the two-dimensional case linear triangulation is used and for the three-dimensional case, a 4 - node tetrahedral and 6-node prism are used. Calculation of matrix elements $[P],[H],[Q]$ are implemented analytically for triangles and tetrahedrals.

For prisms the integration is implemented in a local system of coordinates using Gauss's quadrature.

Solution of a system of algebraic equations (1.4) is implemented by successive upper relaxation method.

To provide a unique solution, heat capacity diagonally matrices $[P]$ are used.

2. Finite elements grid generation

2.1. Two-dimensional grid.

Two-dimensional arbitrary shape construction is automatically discretized by triangular elements. Construction can include some details (calculated under regions) each of which can be multiple connected. A minimum number of nodes is needed for describing the construction boundaries, line segments between which describe sufficient exact contours of each subregion. If subregions unite in one group, then each subregion can have its own heat transfer properties, but on common boundaries, the temperature field is continuous. Between subregions which belong to different groups, we shall fix contact surfaces. An unstructured grid is generated in each subregion (Delaunay triangulation).

Printed data is array numbers which have information about the finite element grid and include: numbers of node couples which are at the beginning and end of the boundary segments calculation region, numbers of nodes forming contact segments, grid node coordinates, inter node ties and addresses of inter -node ties.

One-dimensional arrays of inter node ties for each node (for example τ) includes: node numbers connected with τ - node in order of node round-about way against pointer.

Addresses of τ - node ties in an array of inter-node ties are defined by array addresses, which includes ties beginning addresses of each node. In the ties array for each node enumerated connected with other nodes, the number of each is larger, than the τ - node number. This avoids a double description of each tie and uses thematic symmetry in equation system (1.4). The way just described demands a minimum volume of active computer memory. Also, the array of triangles and their sub region order numbers is embedded information. This information is used to define appropriate heat physical properties of the material while calculating matrix elements in equation (1.4).

2.2 . Three-dimensional finite elements grid.

A three-dimensional grid is generated based on six-node prisms and tetrahedrons. Prisms are used for grids generation in compound regions, which have a cylindrical structure. Prisms are situated in layer wise direction coinciding with cylindricity axis of a three-dimensional object. An example of objects with piece-cylindrical structure can be a turbine disk (cylindricity in circle direction), or a lock of blade (lock axis is cylinder axis).

The basis for generating a spatial prism grid is a two-dimensional plane generating a body projection on a plane, which is perpendicular to the chosen cylindricity axis), which is broken into triangles. In body projection should be contained all geometry peculiarities, which are distinguished as sub regions.

The simplest variant of generating a three-dimensional prism grid is by making a template step moving along the chosen direction - cylindricity axis.

Key information for grid generating is a layer filling array. Each sub region of the template in each layer can be the volume element basis. If the sub region is empty (in this layer the sub region presents a cavity) an appropriate array cell includes zero. Also in the sub region some details is define. Consider that between elements, there are contact surfaces with thermal resistance. Between sub regions of one element contact is ideal. This information allows the formulation of a list of node numbers for compound finite elements (prisms).

To define the real node coordinate of each layer, a row procedure is used. Templet accommodation as the whole thing on the chosen cylindricity axis, complete in space at first. In consequence we have a regular structure in the axis direction for which each layer is plane. For grid generation for example in disks, the templet is situated as a fan from section to section around the given disk axis. Also for grid generation in such regions as a profile part of blade, reflection of the whole templet or only its part on a piece-linear spatial surface is used.

Also there can be the possibility of a templet crook. To local two-dimensional templet node coordinates, a third coordinate is added, creating a local three-dimensional cartesian coordinates system. This crooked templet can move by steps along cylindricity axis creating nonplaner sections. For example, for a grid generation in the region of a perforated blade leading edge, the plane profile part of a blade section is a templet. Templet crookedness happens in the case of holes inclined to a section plane.

After calculation of all global node coordinates, grid smoothing is realized, it means the node situation changes without the calculation region external shape changing , improving grid quality.

Simultaneously with a volumetric finite element grid, on the templet base spatial hydraulic net of cooling system with bond to triangle or four -cornered surface grid elements is generated. Also, geometric characteristics of net branches are calculated. In this way liaison between the three-dimensional finite element and hydraulic models is provided, needed for solution of conjugated heat conduction analysis.

3. Calculation of air mass flow and parameters in the turbine cooling system.

Calculation of cooling air mass flow through blade cooling system passages is implemented by using hydraulic type resistances.

Air mass flow in the turbine air cooling system channels, and mass flow velocity components, pressure and air temperature in circumferential disk cavities are defined from calculation of one-dimensional flow on branches of the generated hydraulic model.

3.1 Calculation of the hydraulic net, simulating the blade cooling system.

Cooling air mass flow in blade passages is simulated by the flow in hydraulic net branches. It signifies in an appropriate model of united hydraulic resistances. Net generation is realized using blade geometry, given in a simpler way with the help of layered rows by height. On each layer is an appropriate plane blade section. Net branches simulate hydraulic resistance of a particular part of the blade. To each appropriate τ branch appoint area F and hydraulic resistance ξ . Drop of the total pressure on branches m for incompressible flow between node τ and j is written down in : (3.1.1)

$$P_{\tau} - P_j + \Delta P_{\omega} = \xi \frac{1}{2\rho} \left(\frac{G}{F} \right)^2 \quad (3.1.1)$$

In order to make the equation (3.1.1) linear, we write down an expression for mass flow in (3.1.2)

$$G = \frac{P_j}{\xi_f G_0} (P_{\tau}^{K+1} - P_j^{K+1} - \Delta P_{\omega}) \quad (3.1.2)$$

where $\xi_f = \frac{\xi}{2F^2}$;

$$G_0 = \sqrt{\frac{(P_{\tau}^k - P_j^k - \Delta P_{\omega}) \rho_j}{\xi_f}}$$

Pressure characterization in hydraulic net nodes $\{P_i\}^{k+1}$ is defined from the solution of a linear system of algebraic equations, received from the mass flow balance equation for inside nodes by using previous $\{P_i\}^k$:

$$\sum G_m = 0 \quad (3.1.3)$$

(m -branches index, which have common node).

For compressible flow equation (1.3.1), it is written down inform (3.1.4):

$$P_{ii} - P_j + \Delta P_{\omega} = \frac{\xi_f}{\rho_j} \left(\frac{0.3964 P_{ij} q(\lambda) F}{\sqrt{T_i}} \right)^2 \quad (3.1.4)$$

$$\rho_j = \frac{P_j^k}{RT_{ij}^k} \varepsilon(\lambda);$$

Air temperature at inside nodes is defined by equation (3.1.5) by taking into account flows turbulence, air heating as a result of heat exchange with the blade and from centrifugal forces acting.

$$T_{ij}^k = \frac{\sum [(T_{ii}^k + \Delta T_h + \Delta T_{\omega}) G_0 c_p]_m}{\sum (G_0 c_p)_m} \quad (3.1.5)$$

here m -indexes branches, which have a common j node.

Air heating on branches from heat exchange with the blade is defined as :

$$\Delta T_h = \frac{hS [T_w - (T_{ij}^k + T_{ii}^k) 0.5]}{c_p G_0}$$

Air pressure variation and air heating in a branch from centrifugal forces acting is defined from dependence on rotation frequency and hydraulic net node radii.

Hydraulic resistance to air mass flow in cooling passages defines flow capacity of each passage and also for the whole cooling system. Total pressure losses coefficient $\xi_{\tau j}$ on each branch is presented as the sum $\xi_{\tau j} = \xi_{\tau} + \xi_j$, where ξ_{τ} - friction losses on the branch, and ξ_j - local losses, for example passage entrance losses or passage exit losses.

Friction losses are defined using friction coefficients λ_f by correlation

$$\xi_{\tau} = \lambda_r \frac{l}{D}$$

To define friction coefficient in smooth passages (taking into account wall roughness) and in rib passages well-known experimental data from many authors are used. Friction losses coefficients for sudden section narrowing or broadening depend on correlation of narrow and wide section areas and entrance (and exit) flow conditions. A lot of experimental data for local losses are in reference books on hydraulic resistance.

3.2. Calculation of air parameters in the turbine rotor cooling system.

For the calculation of heat exchange boundary conditions of disk surfaces it is very important to have air parameter distribution in turbine circumferential disk cavities. It can be approximately defined from the solution of a system of one-dimensional differential equations by giving average parameters at entrance and exit of circumferential disk cavity. By this, tangent friction stress values on revolving and immovable surfaces are calculated using criterial equations.

Changing flow parameters by radius in the clearance between revolving disks or between disk and immovable wall can be defined by numerical solution of equation system. (3.2.1)

$$G \frac{\partial}{\partial r}(rV_{\varphi}) = 2\pi r^2 \tau_{\Sigma};$$

$$V_r \frac{\partial V_r}{\partial r} - \frac{V_{\varphi}^2}{r} = -\frac{I}{\rho} \frac{\partial P}{\partial r} - \frac{I}{\rho} \frac{\tau_r}{\delta_r};$$

$$\frac{\partial}{\partial r} \left(T_a + \frac{V_{\varphi}^2}{2c_p} + \frac{\partial V_r}{2c_p} \right) \frac{I}{c_p G} \frac{\partial L}{\partial r} + \frac{h_a r}{c_p G} (T_a - T_{w_1}) +$$

$$\frac{h_{w2} r}{c_p G} (T_a - T_{w_2}) \quad (3.2.1)$$

$$\frac{\partial}{\partial r} (\rho F_r V_r) = 0;$$

$$\rho = \frac{P}{RT}$$

where $\tau_{\Sigma} = kF_1 \tau_1 + kF_2 \tau_2$ -for flow between the disk and immovable wall.

$\tau_{\Sigma} = 2kF_1 \tau_1$ - for flow between two disks.

τ_1 and τ_2 -tangent friction tensions on the disk and wall, calculated by relations:

$$\tau_1 = \frac{0.535}{Re_{rel}^{0.2}} \rho \frac{(V_{\varphi} - V_d)^2}{2},$$

$$Re_{rel} = \frac{(V_{\varphi} - V_d)r}{\nu}$$

$$\tau_2 = \frac{0.535}{Re^{0.2}} \rho \frac{V_{\varphi}^2}{2}, Re = \frac{V_{\varphi} r}{\nu}.$$

(τ_1 is positive for a centrifugal flow. In other cases τ_1 is negative); $kF_1(kF_2)$ -correlation of real disk (wall) surfaces to annular surface on integrated part.

$\partial L = 2\pi r \tau \omega r \frac{I}{G} \partial r$ -operating, which made by revolving disk

($V_{\varphi} - V_d < 0$) -or twirling flow ($V_{\varphi} - V_d > 0$);

$\tau_1 = 2\tau_2$ -while flow in clearance between two disks;

$\tau_1 = 1$ -while flow in clearance between disk and wall.

Substitution in the equation system integrated variable R to Z, and equation of momentum conservation in radial direction to momentum conservation equation in axis direction leads to:

$$2\pi r \delta \frac{\partial (V_z^2 \rho)}{\partial z} = 2\pi r \tau - 2\pi r \delta \frac{\partial P}{\partial z}$$

which describes one-dimensional swirling flow in an annular clearance of constant width δ ($\delta \ll r$) between disk and shaft or between disk and stator.

Because parameters of entrance in some circumferential disk cavities depend on flow history, then parameter calculation in circumferential disk cavities of type (8) needs common solution of equations systems.

In common cases the hydraulic air admission system model consists of branches which look similar in order of parts with appointed flow type (such as flow between revolving disk and wall; in the annular clearance between disk and shaft; labyrinth between rotor and stator; in the revolving radial passage; in apparatus of preliminary

annular air introduction) with typical hydraulic resistance or with given mass flow characteristic.

Calculation of such a hydraulic net is made by a successive approach method, in two stages on each approach. At the first stage equation system (3.2.2) is solved, analogous to (3.1.1)

$$\frac{P_i}{\pi(\lambda_i)} - \frac{P_j}{\pi(\lambda_j)} + \Delta P_\omega = \frac{\xi_f}{\rho_j} G_0 G_{ij} \quad (3.2.2)$$

If the equation is solved for a branch, simulating flow in circumferential disk cavities, then the pressure change on the branch is defined by quantity ΔP_ω (first items in (3.2.1) it is small because of the small speed mass flow component). Relative to the quantity ΔP_ω , there are successive approaches. If ΔP_ω is zero, from equation system solution (3.2.1) mass flow values G_{ij} are defined on hydraulic net branches with given average parameters in boundary nodes. Then for received values from equation system solution type (3.2.1) we have parameters at the end of the branch on the exit of this cavity) also this turbulence at nodes is defined by the circumferential speed component and the temperature is according to:

$$V_{\varphi\tau} = \frac{\sum V_{\varphi\tau} G_\tau}{\sum G_\tau}, T_{\tau\tau} = \frac{\sum T_{\tau\tau} G_\tau}{\sum G_\tau}.$$

here m - indexes branch nodes, which have common node τ . For previous values $\{G_{ij}\}$, $\{P\}$ and new values $\{V_\varphi\}$, $\{T\}$ equation systems (3.2.2) are solved. At the end of the stage ΔP_ω is defined as

$$\Delta P = P_{ij} - P_{ii} - \frac{\xi_f}{\rho} G_{ij}^2.$$

with received vector ΔP_ω the first stage is implemented again.

The calculation succession described continues until the establishment of vectors $\{P\}$. As a solution result we have average parameters in net nodes and parameters distribution in circumferential disk cavities.

4. Simulation of temperature fields in a turbine element.

4.1. Simulation of temperature fields in blades (quasi three-dimensional model).

The calculation model of the profile part of the blade heat state includes a finite element and hydraulic model, boundary condition models and heat conduction model in the profile part of blade.

For a chosen plane profile parts of blade sections with appropriate geometry, we generate two-dimensional finite element grids. The profile part of the blade section numbers is chosen in a way, that it will take into account peculiarities of the profile part of the blade cooling system. Separate finite element grids generated in each section and united in one whole grid is more expedient than generating one whole grid simultaneously in all sections.

For mutual crossing excepting, it is very important for calculation results visualization to make section displacement relative to each other by one axis Y.

The cooling system hydraulic model generated and branches bound to appropriate blade section contours is accompanied by use of a graphic dialogue regime. Geometric branch characteristics are defined using point coordinates on section contours and some drawing data.

Boundary condition models generated include requirement of criteria dependence for heat transfer coefficient calculation on different blade section parts. For blades with convective film cooling systems on the finite element grid generation stage cornering passage projections on a section are distinguished as sub regions.

In the graphic dialogue regime, ties between perforations and the appropriate hydraulic net branch are established. For heat transfer coefficient calculation in passages needed in the editor regime, passage hydraulic diameter and passage step by height and passage inclination corner to section plane are also given. In perforated passages, local heat transfer coefficients and air heating are calculated. Received values are used in heat sources, which simulate heat exchange in perforated passages. Source intensity is defined as

$$W_\tau = h_\tau F_\tau (T_a - T_w) / V_\tau = h W_g (T_a - T_w)$$

here T_a - air temperature in passage limits of τ finite element; T_w - middle temperature of τ element; V - volume of region with source; W_g - source geometric characteristic (for cylindrical passage $W_g = \pi / S, m^{-1}$, defined only by hole step.)

For film cooling characteristic calculations, which depend on cooler mass flow, hole step, blowing ratio, Mach's number of basic flow, blade curvature is used in experimental dependence.

(A.Trishkin, CIAM)

$$\theta_{fc} = K \left\{ \frac{t}{d} + 0.017 \frac{(\bar{\rho}v)_g F_\eta}{G_0} / \left[1 + A \left(\frac{x}{R} \right)^{0.8} \text{Re}_R^{-0.2} \right] \right\}^{-1},$$

$$\text{where } \theta_{fc} = \frac{t_g - t_{fc}}{t_g - t_a}$$

K - coefficient, which taking into account flow blowing out corner to section plane.

K=1 t with $\alpha = 30^\circ$

K= 0,63 with $\alpha = 90^\circ$ (pressure side)

K= 0,73 with $\alpha = 90^\circ$ (suction side)

$(\bar{\rho}v)_g$ - mass flux on film coverage surface till calculation point ;

A = 4,5 for suction side

A = -7,1 for pressure side

x - distance from blowing site

R - middle surface curvature radius from blowing site.

In case of multi row blowing while θ_{fc} and film temperature t_{fc} calculation take into account calculation results for holes, situated up stream, it means that instead of gas temperature at the blowing site we take the previously calculated value t_{fc} .

On the external blade surface, heat transfer coefficient is defined using two-dimensional boundary layer calculation programs and correlated coefficients, taking into account film injection.

Calculation models that were described, are the basis of program complex Quasi 3D. Account of mutual influence of models is implemented by an iteration process. Some calculation results of turbine blade heat state with using this program complex are presented in Fig.4.1.1. Here are presented hydraulic and geometric models, external boundary conditions and temperature fields in a middle section and also the temperature distribution of blade's suction side.

4.2 Simulation of temperature fields in disks (axis symmetric model).

For disk heat state calculation, a solution to conjugate the heat transfer problem is needed. It means simultaneous calculation of heat exchange and heat

conduction. For calculation time minimization (especially while calculating unsteady heat regimes) one-dimensional air mass flow calculation in circumferential disk cavities and by air admission system channels are put in a separate stage.

Calculation model generation started with finite elements grid generation in meridional disk section and in stator details around them. Passages in the disk for air admission to the blade are distinguished in separate sub regions. With air blowing through clearance of roots this part of rotor can be in aspect a sub region row. In all these sub regions temperature field calculation heat sources of appropriate intensity are given.

The next stage is the air admission system hydraulic model generation. On the air admission scheme are distinguished parts with assigned flow type or typical hydraulic resistance. Information preparation for hydraulic net calculation is made in the graphic dialogue regime. One of the net branches is the blade mass flow characteristic, which is calculated by using the turbine blade hydraulic calculation program.

Calculation model generation is finished with tie establishment between the finite element grid and the hydraulic net. It means that appointed net branches show appropriate geometric model contour parts or sub region - heat sources.

Flow and average parameter calculation in circumferential disk cavities are implemented for all regimes, which are given in the description of turbine work. Mass flow, pressure, temperature, flow swirl and also flow temperature change the branch because admission (or pipe - bond) to revolving disk work are used for heat transfer coefficients and flow temperature calculation. Some calculation results steady and unsteady state of a whole cooled turbine rotor are presented on Fig. 4.2.1

The hydraulic model includes labyrinth for the compressor, cavities between stator and rotor elements, and preliminary calculated air mass flow characteristic of a cooled blade. In each cavity one - dimensional swirling flow parameters are calculated. The finite element model includes an easier model of the blade root.

4.3. Simulation of three -dimensional temperature fields in turbine rotor.

Temperature field in the turbine rotor is defined by using a three - dimensional finite element model and boundary conditions on the profile part of the blade external surface and disk side surface, defining in QUASI - 3D and 2D heat hydraulic models.

Inside flow and heat exchange passages are calculated as in a QUASI - 3D model for blade. On

platform surface, heat transfer is calculated by using experimental data and results of gas flow calculations.

Some examples of calculated three - dimensional temperature fields are presented on Fig. 4.3.1 - 4.3.4. The heat state of the blade with the developed convection - film cooling system together with the disk was calculated, taking into account boundary conditions of contact and periodicity conditions, which allowed the calculation of temperature fields without distortion within the limits of one blade root.

5. Simulation of stress - strain state turbine elements

One of the most important trends in the development of aviation engines is the spreading adoption of the numerical study of the stress-strain state of engine components in the initial design process. It includes rigorous application of finite element methods, using high level models, including two-dimensional and three-dimensional SSS models. The application of these models in the initial stage allows detection of potentially dangerous stress concentration zones; and development of the details of constructive changes for reducing these stress-except in the study of crack origine.

In practice the widest applications have SSS mathematics models which are based on numerical solutions with the help of finite elements methods, solve two-dimensional and flat and axisymmetric elasticity theory problems (especially for stress concentration zones). Also, as practice showed, in development and qualification of aviation engines in many cases, only three-dimensional calculation analyses allowed adequate descriptions of SSS details and only on this basis received reliable estimation of its lifetime in the development process.

As examples, you can see some calculation results, which illustrate application effectiveness of three-dimensional mathematics models for SSS aviation engines detailed components analyses. As three-dimensional, we mean models, based on using common elasticity theory equations in three-dimensional form, and also common shell theory equations.

We know that injection holes system geometric parameters influence stress level in the blade near from these holes, this should be taken into account while working out blade constructions with convection film cooling.

In Fig.5.1 there are spatial SSS calculation results in the cooled blade suction side near injection hole inclines, which are inclined relative to the normal to the suction side surface in blade cross section. As you can see from calculated data in the picture, the blade suction side near the inclined hole has a large stress concentration, characterized by theoretical concentration coefficient

$\alpha_{\sigma} = 5,4$. This is much more than estimated results on two-dimensional calculation base.

As you can see from the example, while designing effective convection film blade cooling systems, one should check strength conditions in stress concentration zones while taking into account spatial effects, because these strength conditions can place limits on choices of geometric parameters for convection - film cooling system.

While working out cooled turbine blade constructions from heat strength, single crystal nickel - based alloys there appears the problem of choice of rational, spatial, crystallographic lattice single crystal orientation, which provides for blade maximum lifetime while giving exploitation conditions.

The crystallographic lattice of single NI-base alloys is a cube, the mechanical characteristics of which are different in different directions. Because a blade constructed from such alloys is an anizotropic body, it is very important to use three-dimensional mathematical models for SSS calculations; taking into account the anizotropic elasticity and single crystal strength peculiarities.

There are some results of single crystal turbine blade SSS calculation on steady engine operating regime. You can see in Fig.5.2 the profile part of blade temperature field on this regime. Calculation is implemented in a common three - dimensional construction for two types of single crystal crystallographic lattice orientation. Centrifugal force N is acting in the axial orientation :[001] (cube's rib is parallel to force N acting direction) and [111] (the main cube's diagonal is parallel to force N acting direction).

Elasticity strains are defined on the basis of an orthotropic body three - dimensional elasticity theory , and plastic strains and creep strains on the basis of plastic and creep flow theories for an orthotropic body with izotropic hardening (Hill's theory). This task was solved with the help of FEM in three - dimensional construction.

Calculation results from Fig.5.3 show that the examined blade is better when axial orientation of single crystal [001], is that by which blade stress is minimum. Maximum values of stresses occur for orientation [111]. The given effect is linked with elasticity modules (and it means thermal stress, proportional to elasticity module) of single crystal in direction [001] is as much as 1,5 times, lower than in direction [111].

Next stress reduction and blade's strength durability are cast with direction of crystallization [001] probably by way of rational selection of secondary azimuthel crystallographic lattice orientation while its rotation in the most dangerous plane blade section remains flat.

These examples show that for the right estimation of stress and strain distribution in highly loaded engines, correct details of grids and nodes are very important for implementation of three-dimensional mathematical SSS models. Only on the basis of such details in the initial stage of a design can be a reliable result, which allows correct estimation of component life. But in a large number of cases, acceptable results can be obtained by using simpler, two-dimensional mathematical SSS models.

References

1. Jen H.F. and J.B. Sobanik : Cooling air flow characteristics in gas turbine components, ASME Paper No. 81 - Gt - 76 , December 1980.
2. Kumar , G.N. ; Roelky , R. J. and P.L. Meitner: A generalized one dimensional computer code for turbomachinery cooling passage flow calculations AIAA Paper No. 89 - 2574 , July 1989.
3. Gastebois Ph et J.P. Lagrange "Dimensionnement et thermomecanique des aubes de turbine aeronatiques " revue generale de thermique N 282 - 283 de Juin/ Juillet 1986.
4. T. A. Tietz, W.W. Koschel: Computer code to the calculation of the temperature distribution of cooled turbine blades Institute for Jet Propulsion and Turbomachinery. AIAA Paper , 1991.

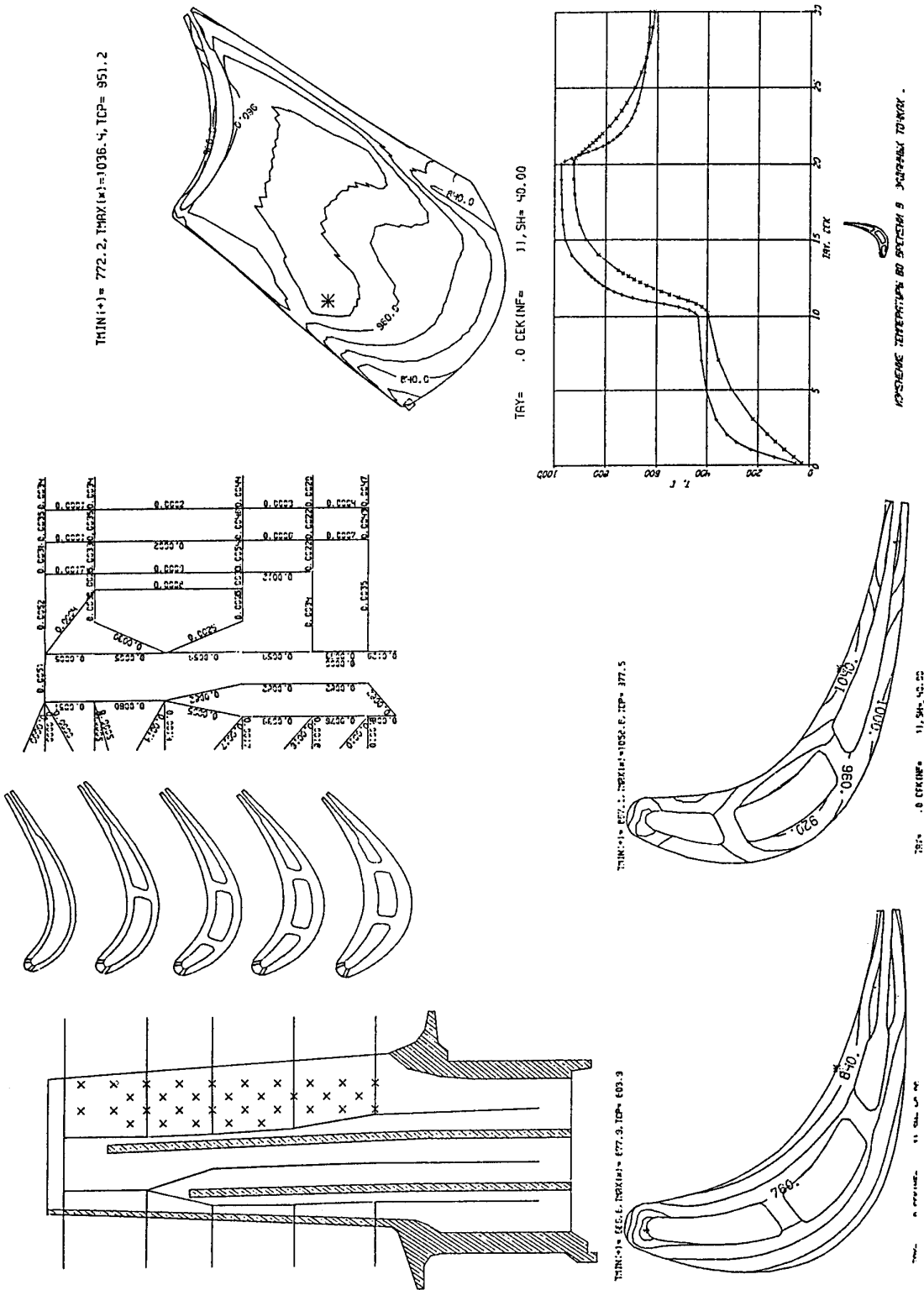


Fig.4.1.1 Quasi -3D heat hydraulic simulation of cooled turbine blade.

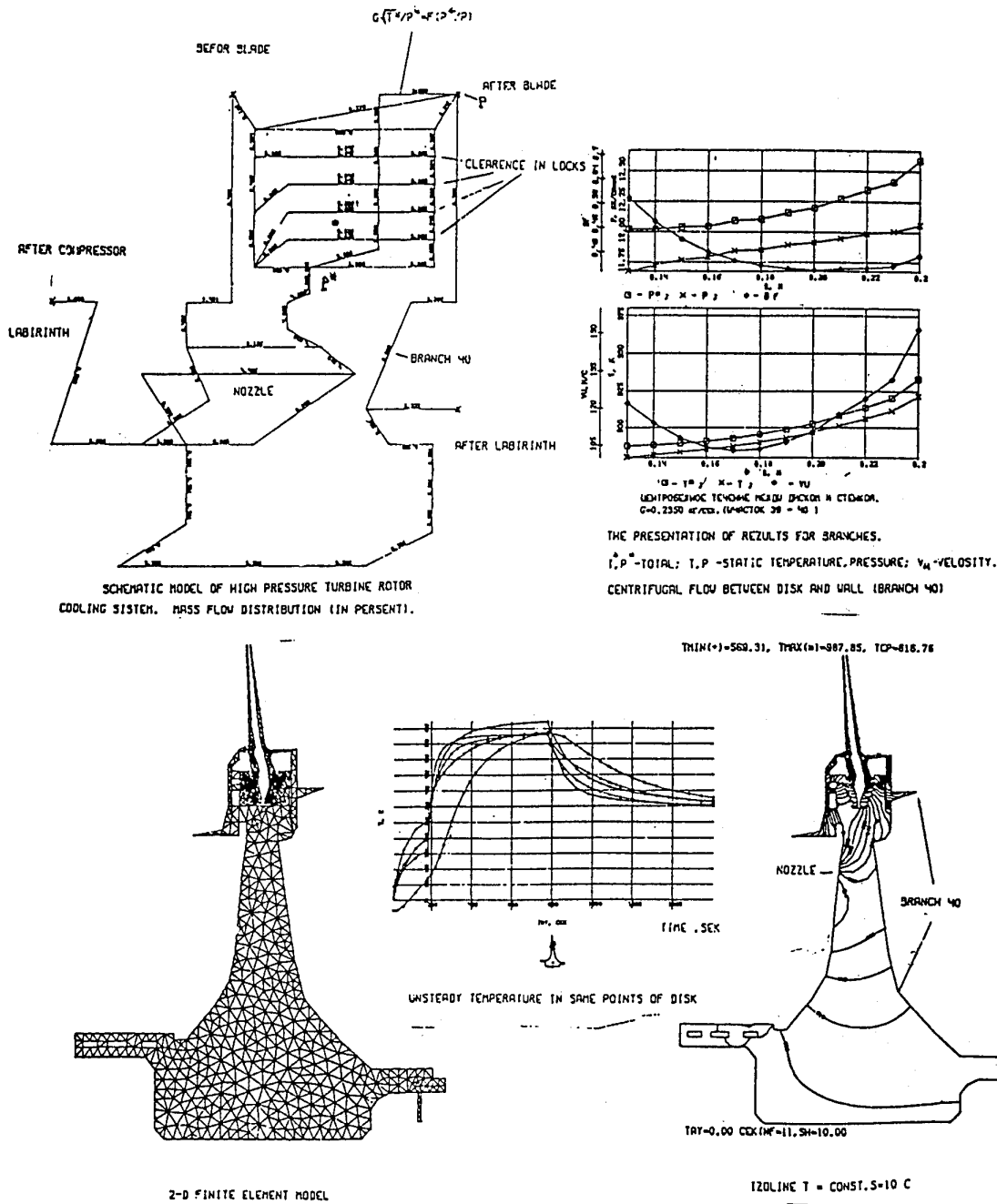


Fig.4.2.1 Steady and unsteady heat - hydraulic model of whole cooled turbine rotor.

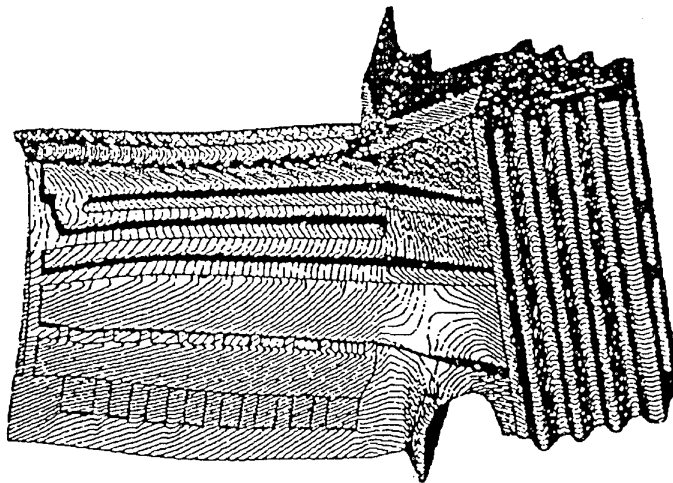


Fig.4.3.1

Cooled blade.

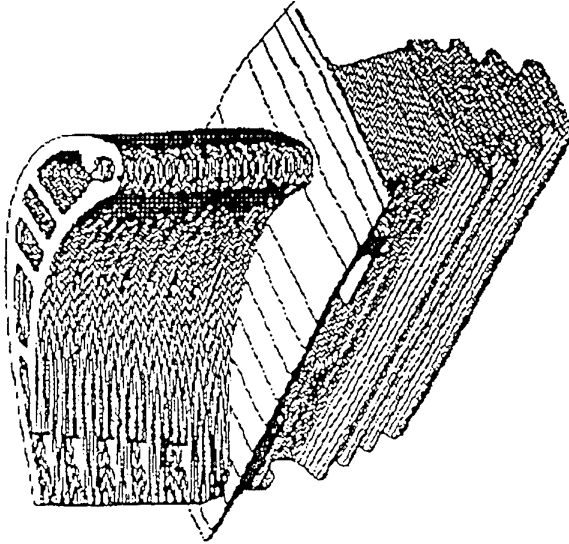
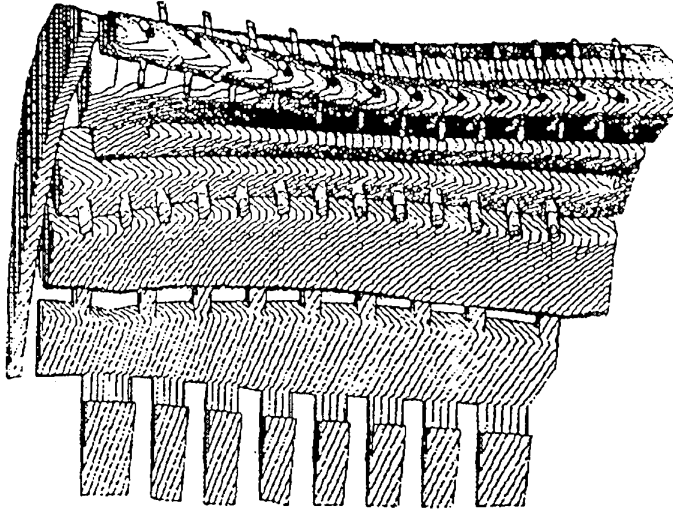
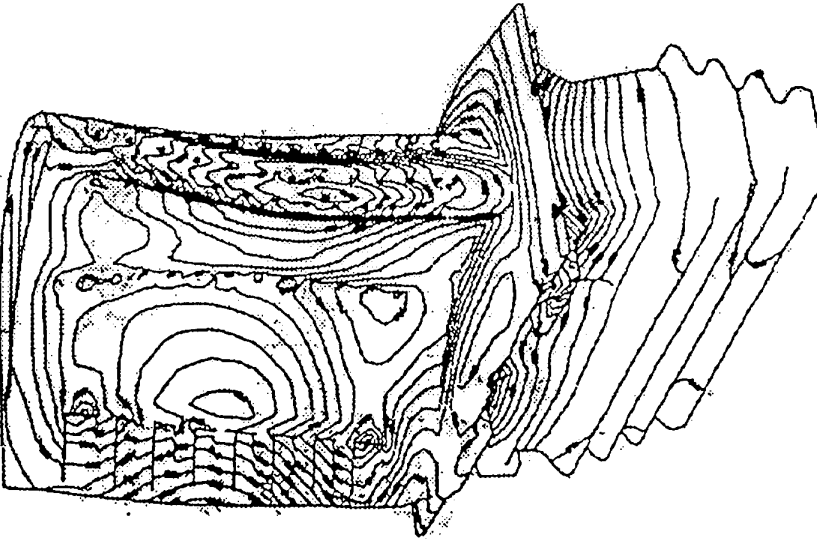


Fig.4.3.2

Internal channels of cooled turbine blade.



TRIM(2) = 508.3, THRX(1) = 1091.0, TCP = 789.4



TRY = .0 CEK(NF = 1), SH = 20.00, F = 155.1 = 25

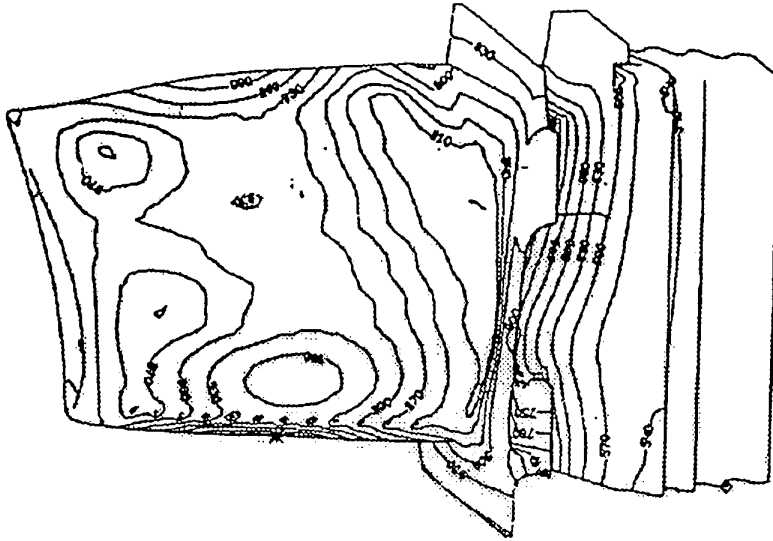


Fig. 4.3.3 Temperature field of blade.

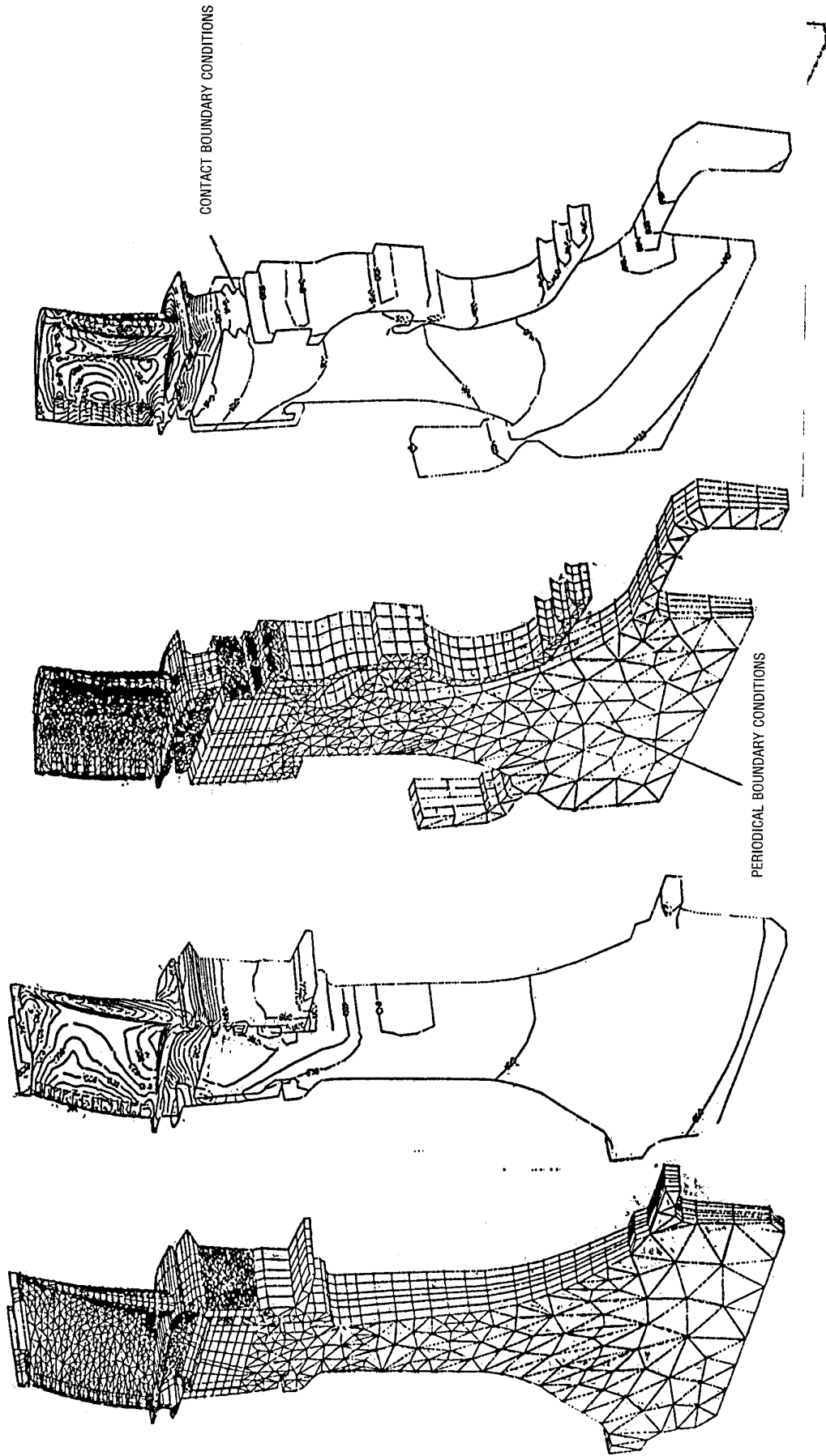


Fig.4.3.4 3D thermal simulation of whole cool turbine rotor.

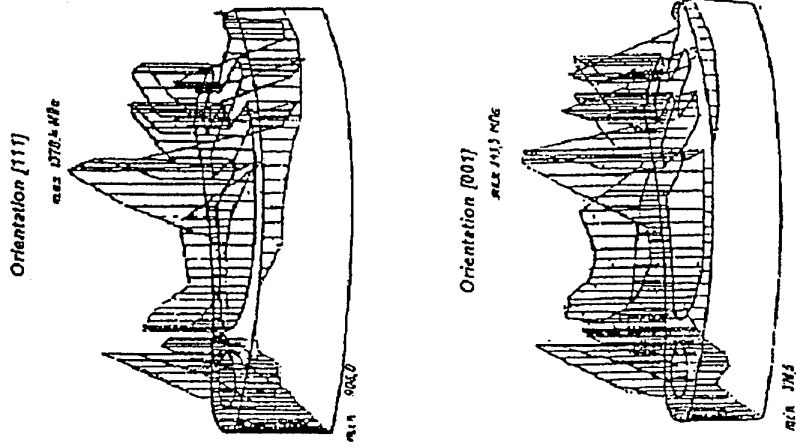


Fig. 5.3 Orientation [111]. Orientation [001]
Distribution of longitudinal stress σ_1 in middle plane blade's section.

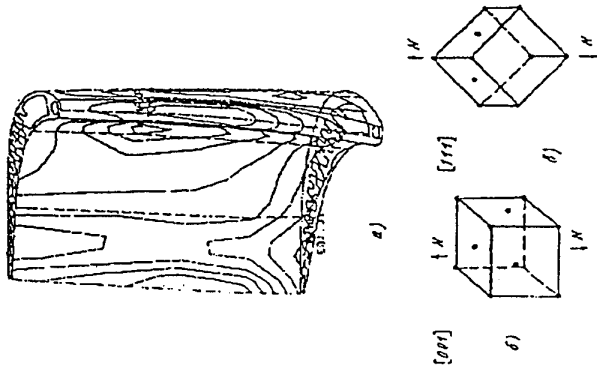


Fig. 5.1 Plane section of film-cooling blade (a) and stretch main stress σ_1 near inclined injection holes.

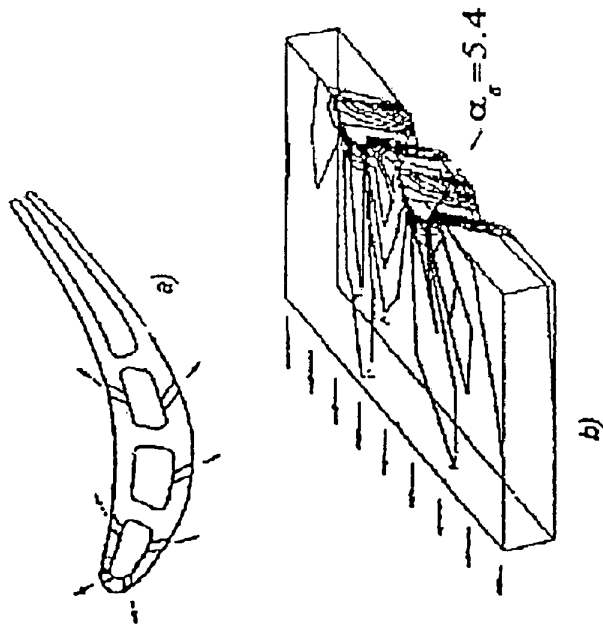


Fig. 5.2 Profile part of blade of cooling single crystal blade with temperature isolines on external surface (a) and types of single crystal [001] (b), [111] (c) crystallographic lattice previous orientation.

Application of multicomponent models to flow passage simulation in multistage turbomachines and whole gas turbine engines

by
Dr. R. Z. Nigmatullin,
 CIAM (Central Institute of Aviation Motors)
 2, Aviamotornaya St.,
 Moscow, Russia, 111250

Abstract

Some features of used numerical algorithms for gas turbine engines components flow simulation are considered. Among them are topology of computational grids in 2D and 3D cases for flow passages of complex geometry, details of realization of conservative scheme at joints of different grids. In S_2 -calculations it is necessary to consider the problem of inlet and outlet angles, in Euler calculation the ways of accounting for viscous loss effects are briefly described. Examples of calculations of flow through by-pass engine components are presented.

Introduction

Gas flow through the gas turbine engine flow passage is a very complex phenomenon. It is unsteady 3D turbulent gas motion in a traveling domain of complex geometry. So various simplified models are used for its simulation. It leads to the necessity of using some empirical or semi-empirical data.

For instance, while using Euler equations system for description of such flows it is necessary to simulate viscous loss effects. The simplest way is to use on experimental data. But even in case there is the problem of distribution of these losses within the blade-to-blade domain. Some loss components may be roughly estimated using simple models. Number of models of such type is considered, for example, in [1], [2]. Empirical formulae of various type, based on generalization of experimental investigation data, are widely used in design offices. This generalization can be fulfilled, for example, using the methods of regression analysis [3]. Losses may also be calculated by means of numerical solution of boundary layer equations or Navier-Stokes equations.

If one uses 2D approaches (gas flows on S_2 - surface) it is necessary to add to this empirical data the information about inlet and outlet flow angles.

When these data together with gas dynamic and geometrical information are gathered (by other words, when the problem is formulated) it is necessary for gas flow calculation to discretize the computational domain. Because this computational domain in many cases has

complex geometry it is convenient to use composite grids. The choice of grid configuration depend on the model used. In many cases it is necessary to consider special conditions at different grid joints. Gas flows in many modern gas turbine engine components are transonic and so it is desirable to require the conservation of mass, momentum and energy in this case.

These problems are briefly considered in the present lecture.

In conclusion examples of gas flow calculations in multistage turbines, compressors and whole by-pass engine are presented. A simple model of processes in combustion chamber used in simulation for whole engine is described.

1. Computational grids used and some features of realization of numerical scheme at joints of different grids.

Gas flow passages of gas turbine engine components may be of fairly complex geometry. As an example, let us consider gas flow through fan with low pressure compressor and by-pass duct (see figures 8-15 of lecture 4). This problem was considered both in 2D and 3D formulation. It is convenient to use composite computational grids for calculation of gas flows through such channels. For instance, a composite grid for 2D problem (see fig. 13 of lecture 4) for the fan without blade mid-span shroud consist of three components generated by simple algebraic method. In addition to ensure the scheme to be conservative it is convenient to require that neighboring grids have a common boundary. Then it is sufficient to form the combined distribution of boundary nodes of different grids, to interpolate corresponding "left" and "right" limit values of parameters to middles of formed segments, then to call arbitrary discontinuity breakdown procedure (in accordance with the main order of calculations, described in the previous lectures) and to obtain each flux as the sum of fluxes of the "combined grid" at the boundary. It is obvious, that resulting scheme is conservative. This property of the scheme is very important for transonic flows calculations.

The computational grids and algorithms of calculation for a 3D case are constructed almost in the

same way. The grid geometry in meridional plane is similar to a 2D problem (see fig. 8a of lecture 4). In addition it is natural to require that the joints of neighboring component grids are parallel to the pitch of the cascades (for averaging of parameters in angular direction), see fig. 8b of lecture 4. And a separate grid is generated for each vane or blade row. The inlet and outlet boundaries of these grids coincide with the averaging surfaces (see Appendix B of lecture 4) or with inlet or outlet boundaries of the total computational domain. Numerical calculation results show, that the method of calculation at the joints briefly described here allows to ensure the continuity of space distribution of parameters, guarantees that the scheme is conservative, which is important for transonic gas flows calculations when there may exist shock waves or other discontinuities in flow.

2. Some features of numerical algorithms of gas flow calculations on S_2 - surface.

If one uses 2D approach based on consideration of gas flow on S_2 - surface, it is necessary to have the spatial distributions of two functions: $\varphi = \varphi(\xi, \eta)$,

$k = k(\xi, \eta)$ (see lecture 4). The solution essentially depends on the choice of these functions.

The simplest way is to specify as a stream surface

$\varphi = \varphi(\xi, \eta)$ the mean blade surface, formed from mean profile lines for some family of blade sections (for example, plane sections) and to choose for

$k = k(\xi, \eta)$ the geometrical blockage factor defined

as: $1 - \frac{|\varphi_{suc} - \varphi_{pr}|}{t}$, where φ_{suc} - value of angular coordinate, corresponding to suction side of blade, and

φ_{pr} - one, related to pressure side, t - angular pitch of

cascade: $t = \frac{2\pi}{N_{bl}}$, N_{bl} - number of blades in cascade.

But this way in many cases leads to unsatisfactory results. So one often modify these functions $\varphi(\xi, \eta)$,

$k(\xi, \eta)$. One may, for example, "correct" functions

φ, k in such way that resulting "triangles" at leading and trailing edge lines (see Appendix B of lecture 4) correspond (in some sense) to "real triangles" in blade-to-blade space. As a variant of this method (for gas turbines) one may consider such modification of

$\varphi = \varphi(\xi, \eta)$ (and, may be, also $k = k(\xi, \eta)$) for which the flow velocity angle at trailing edges is equal

to "arccos-angle" (when "exit channel area" is equal to "throat area") and the triangle at fig. 2A of Appendix A of lecture 4 is right-angled. An example of using of such an approach is presented at figures 1-4 (of present lecture), where S_2 -surface gas flow calculation results are shown for a 2-stage high pressure turbine.

Figure 1 shows stream-lines (contours of mass flow rate of "primary" gas). Pressure contours are shown in figure 2. Note, that because of the property of scheme to be conservative the calculation is fulfilled both in axial gaps and within the bladed domains and it becomes easier to calculate the axial and angular loadings on blades (corresponding integrals are easily calculated using numerical fluxes without any additional simplifications). Figure 3 shows calculated distribution of degree of reaction for the first stage along the radius. The results of design office are marked by squares. Distributions of inlet gas velocity angles along radius are presented in figure 4. (lines with crosses correspond to calculated results using the present methods, squares - to design office data, solid line is distribution of geometrical inlet angles for rotor profiles; one can see that there are considerable angles of attack; later the geometry of this turbine was modified).

At the next example one can see the comparison of gas flow calculation results using 2D (S_2 -surface) and 3D formulation. The gas flow through 1-stage turbine with additional vane at outlet was considered (see fig. 5, where the used computational grid for 2D problem is presented). Viscous losses in both cases were accounted for using dissipative forces, and the values of these losses were defined using generalized empirical relations of CIAM. Figures 6 and 7 shows corresponding stream-lines and pressure contours (for 2D case). Distribution of degree of reaction along radius is shown in figure 8. Line with marks "+" corresponds to 2D approach, line marked by "x" - to 3D case, squares show experimental values at tip and at hub. Note that both approaches give satisfactory results for degree of reaction. Mass flow rates and power were also in good agreement one with another and with experimental data. (The difference of calculated and measured mass flow rates was less than 1% for both cases). But distribution of absolute velocity vector angle behind the rotor shows that the 3D approach gives results which are along whole height in better accordance with experimental data than the 2D one (fig. 9). One can see from figure 10 that this difference between 2D and 3D calculation results is related to the difference in relative velocity vector angles behind the rotor (here lines with crosses correspond to 2D case and lines with squares to 3D one. All angles in these figures are counted from the cascade pitch; β_1 is rotor inlet relative angle, β_2 is rotor outlet relative angle). The 2D approach evidently does not describe all three-dimensional features of gas in blade rows. So for accounting for these effects and also viscous effects one may introduce empirical dependence of deviation angles from some number of geometrical and gas dynamic

parameters (see, for example, [1], [5]). It is more convenient to introduce them to arbitrary discontinuity breakdown procedure at trailing edge line (see concluding notes of Appendix A of lecture 4).

3. Modeling of viscous losses effects.

If viscous losses are modeled using dissipative forces it is necessary to know loss coefficient values. (It is not important here, what one means by losses coefficient ζ : in various cases it may be a different function of flow parameters; it is supposed only that $\zeta = 0$ when there are no losses in gas flow). Supposing that losses are small one usually write:

$$\zeta = \zeta_{fr} + \zeta_{tr} + \zeta_{endwall} + \zeta_{tip\ cl.} + \zeta_{ax.\ gap} + \zeta_{cooling} + \dots, \quad (3.1)$$

where ζ with subscript corresponds to losses, which either are concentrated in some domains ($\zeta_{tr}, \zeta_{endwall}, \dots$) or are caused by any process ($\zeta_{cooling}, \dots$). Such division is conventional and although really the different types of losses are not independent, it helps to estimate the loss coefficient values and to distribute them in space in Euler calculations. In (3.1): ζ_{fr} is "friction" losses in boundary layers at blade profiles surfaces, ζ_{tr} - trailing edge losses, $\zeta_{endwall}$ - endwall losses, $\zeta_{tip\ cl.}$ - losses related to leakages in tip clearance, $\zeta_{ax.\ gap}$ - friction losses in axial gaps, $\zeta_{cooling}$ - losses which appear in cooling processes, etc. Some kinds of losses in (3.1) may be further divided into components. Considering "friction" losses ζ_{fr} one may select "angle of attack" losses ζ_i , shock waves losses ζ_{shock} , distinguish viscous losses before the "throat" section and after it, etc.

Note that when one uses Euler equations system with spatially distributed mass sources for gas flow simulation, some kinds of losses are accounted for automatically. Among them there are the losses in shock waves. In some cases (for example, in some fan blade rows) they may be the main component of losses. Losses in mixing processes (for cooling turbines and compressors) are generated also automatically.

Losses in boundary layers of blade profiles ζ_{fr} ideally are losses in cascades at S_1 - surface (excluding trailing edge losses). They may be defined by boundary layer flow calculations (in absence of extended separation zones) or by numerical solving of 2D Navier-Stokes equations (in this case ζ_{tr} are also defined). The last way is relatively costly and so during the design process some semi-empirical correlations are

often used obtained by generalization of experimental data (see, for example, [3], [6]). Similar relations exist also for endwall losses (for example, [7]) and other loss components. Many design offices have own correlations for losses most suited to using families of profiles.

One may also directly use experimental data for losses for considering blade rows (if they exist), but the models for loss components are useful also in this case for spatial distribution of losses in computational domain.

Loss components may be estimated using simple physical models (see, for example, [1], [2]).

Let us consider in conclusion two attempts of simulation of gas flow through blade row passage with unshrouded blades.

In experiment [8] "tip" clearance was at hub, turbine blade row of constant profile along height was motionless and hub surface could move. In the first example gas flow was simulated using a viscous S_2 - surface formulation (in thin-layer approximation, see lecture 4). Two cases were considered: $\delta = 0$ and $\delta = 2.2$ mm (δ is hub clearance thickness), blade height was 55mm, exit isentropic velocity coefficient was: $\lambda = 0.8$. Gas leakage in hub clearance was modeled by the same way, as flow in axial gap domain

($\frac{\partial}{\partial \varphi} \equiv 0$, see lecture 4). Hub surface was motionless.

Algebraic Baldwin-Lomax turbulence model [9] was used in the calculation.

Calculated loss coefficient ζ distribution along radius at exit section for the cases: $\delta = 0$ and $\delta = 2.2$ mm are shown correspondingly in figures 11, 12, the distribution of axial velocity (for $\delta = 2.2$ mm) is shown in figure 13 (gas flows from right to the left). Circles corresponds to experimental data of [8]. Here,

loss coefficient ζ is defined as: $\zeta = \frac{V_{ad}^2 - V^2}{V_{ad}^2}$ where

V is velocity vector magnitude, V_{ad} is "isentropic" velocity and is calculated (together with T_{ad}) from the next system:

$$\begin{cases} h(T_{ad}) + \frac{1}{2} V_{ad}^2 = h(T_*) \\ s(p, T_{ad}) = s(p_*, T_*) \end{cases}, \quad (3.2)$$

where p_*, T_* - total pressure and temperature at the inlet section of channel, p is outlet pressure, $h(T)$ and $s(p, T)$ - specific enthalpy and entropy (see lecture 4).

Constant "profile" losses $\zeta = 0.05$ (some arbitrary value) were added using dissipative forces. (If one does not add these forces, the solution will be almost the same, as presented in figures 11-13, but far from the wall ζ will be equal to 0).

As shown in figure 11, 2D viscous calculation allows to account losses in boundary layer at hub section but does not describe "secondary flows losses" ζ_{sec} . In the case $\delta \neq 0$ this calculation qualitatively describes some features of distribution of losses along radius, but there are large quantitative differences.

The probable cause is that the flow in this region is essentially three-dimensional and so 2D calculations cannot clearly simulate it. But this approach could be useful for calculations in extended channels, nozzles, etc. "Secondary" and other loss components could be accounted for using dissipative forces or by other ways.

Another simple model can be used in 3D Euler approach with averaging in the middles of axial gaps (see lecture 4). Let us consider the same example for the case $\delta = 2.2$ mm. Together with usual 3D flow computational domain an inviscid flow on S_1 -surface which coincides with butt-end of the blade is considered. Let m be arc length along the meridional projection of hub surface, $r=r(m)$ - radius of current point at this projection, $b=b(m)$ is variable relative thickness of radial clearance (thickness divided by δ - one at leading edge of the blade, for example). Then the flow at this surface is described by equations (3.4) of lecture 4. The simple algebraic grid was used in this S_1 -surface domain (this domain is shown in fig.14, where one can see also streamlines for the case $\delta = 2.2$ mm). The boundary conditions for this problem are found from 3D flow field by extrapolation at current time step. The "non-reflecting" conditions were used for this 2D task. On the other hand some numerical fluxes at the boundary of S_1 -surface multiplied by δ are used for calculation of corresponding source terms $r\dot{m}$, $r\dot{m}V_z$, $r\dot{m}V_r$, $r\dot{m}V_\phi$, $r\dot{m}H$ on right hand side of equations (1.8) of lecture 4. Usual boundary conditions are used on solid boundaries in 3D computational domain. Thus both 3D and 2D problems are solved simultaneously. Although one must solve 2D steady problem at each time step of 3D one. It is not very costly because the 2D solution at previous time step is used as initial condition for the current iteration.

In this example the terms $r\dot{m}, \dots$ were distributed along one row of cells around the blade hub section profile (although one may also consider other variants). No empirical coefficients were used in this simulation (for applications one may use, for example, coefficients for velocity (V_z, V_r, V_ϕ) , etc.).

Calculated distribution of the loss coefficient ζ averaged in angular direction is shown in figure 15 for two different grids: the first one is more fine in radial direction (solid line; the cell radial size at hub was equal to $\delta = 2.2$ mm), and the other one is more coarse near the hub (dashed line, the cells were almost of equal size in radial direction; both grids had $60 \times 11 \times 11$ nodes). Circles show experimental data of [8]. Although radial distribution of ζ in calculation does not reflect all features of experimental ones, integral values of losses are close. One can see it in figure 16, where ζ_δ is an average value of losses for the clearance thickness δ :

$$\zeta_\delta = \frac{1}{h_{bl}} \int_0^{h_{bl}} \zeta dh$$

where h is height and $h_{bl} = 50$ mm (see [8]). The value $\zeta_{\delta=0}$ corresponds to the case $\delta = 0$. The experiments and calculations were performed for the cases: $\delta = 0$, $\delta = 0.25$ mm, $\delta = 0.5$ mm, $\delta = 1.0$ mm, $\delta = 2.2$ mm. Line with "+" corresponds to calculated results, and line with squares to experimental data. These results show that described approach could be useful for estimation of this component of losses. Figures 17-19 show velocity vector field at various sections of 3D computational domain for the case: $\delta = 2.2$ mm. Note, that this approach may be convenient for unsteady calculations when δ can depend on time: $\delta = \delta(t)$.

Similar simple models may be considered also for some other kinds of losses using known current spatial distributions of all parameters in 2D and 3D computational domain.

Some examples of gas flow calculations in gas turbine engine components.

The described methods were used in gas flow calculations through a number of multistage turbomachines. Some examples are shown in figures 20, 21 (see also [10], [11]).

In conclusion let us consider an example of gas flow calculation through a by-pass gas turbine engine. The computational grid for this task (on S_2 -surface) is presented in figure 22. The domain of calculation consists of nine sub-domains. It includes the fan (one sub-domain), the compressor (three sub-domains), the annular combustion chamber (three sub-domains), the turbine with nozzle (one sub-domains) and by-pass duct (one sub-domain). Flame-tube surface is the boundary of computational sub-domain. Note also that the grid includes the space within the turbine first stator blades where gas can flow, and so some area is covered by

computational cells twice (but different sub-domains in this area has different values of blockage factor k and the sum of these values at the same point in meridional plane is equal to 1).

Because in bladed regions the Euler equations (with additional terms in right hand side) were used, we do not need to model chemical reactions in this simulation. The effects of these reactions were modeled by source terms \dot{m} , $\dot{m}V_z$, $\dot{m}V_r$, $\dot{m}V_\varphi$, $\dot{m}H$. It was supposed that the heat of combustion is released along the half of the flame-tube. Some empirical data were used for estimation of combustion efficiency [12].

It was assumed that the flame-tube surface has infinite number of infinitesimal holes and the ratio σ of the area of these holes to the corresponding flame-tube surface element area was considered as a given function of tube point. Jets through the holes were modeled using the mass, momentum and energy sources. The values of this terms were obtained by special procedure of arbitrary discontinuity breakdown at the flame-tube surface, see Appendix. (It was assumed that air accelerates up to hole section without losses and then mixes with the air or gas within the tube along some distance defined by empirical relations). The cooling of the flame-tube through narrow annular gaps was modeled in similar way (but instead of normal direction to the tube surface one must consider the tangential direction and obtained source terms are proportional to ε - annular gap thickness). This approach, of coarse, contains a number of empirical coefficients which are necessary to obtain realistic total temperature distributions at turbine inlet. Some results of steady state calculation are presented in figures 23-26. Main integral characteristics of flow (mass rates, power consumption, total pressure ratios, etc.) were in satisfactory agreement with design office data. Figure 23 shows "mass flow rate" contours. These are the streamlines anywhere except in the domain within the flame-tube (because of the source terms). Static pressure and absolute pressure contours are presented in figures 24,25. One can see that the most significant total pressure increase occurs in compressor diagonal rotor cascade. Although the integral level of total temperature at inlet of the turbine is in good agreement with design office data, some features of its distribution (figure 26) show that the model of flow in the combustion chamber must be further developed.

Some results of 3D calculations for this engine can be seen in figures 27,28.

After verification by experiments (correction of empirical information for steady solutions) the models may then be used for unsteady simulations.

APPENDIX

Some used simple models for flow near the flame-tube elements.

Let S be the flame-tube surface with infinite number of infinitesimal holes with relative area σ (fig. 1A). The values of parameters for different sides of the surface will be marked by subscripts "1" and "2".

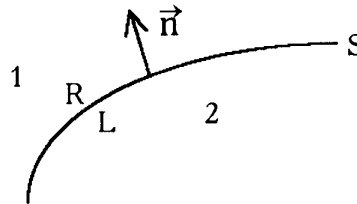


Fig. 1A

Let u be the normal component of the velocity $\vec{V}:u = (\vec{V} \cdot \vec{n})$. As earlier (lecture 4) the relations through shocks and expansion waves will be written in acoustic form (for simplicity).

Let: $p_R^* = p_1 - (\overline{\rho\alpha})^* u_1$, $p_L^* = p_2 + (\overline{\rho\alpha})^* u_2$. The inequality: $p_L^* > p_R^*$ denotes, that air (gas) flows in positive direction (from 2 to 1, see fig. 1A) and, inversly: if $p_R^* > p_L^*$ then air flows in negative direction.

It will be assumed further that $p_L^* > p_R^*$. Then the next relations are considered (v, w - tangential to the surface component of velocity):

$$\left\{ \begin{array}{l} p_L - p_2 + (\overline{\rho\alpha})(u_L - u_2) = 0 \\ s_L = s_2 \\ (v, w)_L = (v, w)_2 \end{array} \right. \quad (A1)$$

$$\left\{ \begin{array}{l} p = p_R^* \\ \rho u \sigma = \rho_L u_L \\ s = s_L \\ h + \frac{1}{2}(u^2 + v^2 + w^2) = h_L + \frac{1}{2}(u_L^2 + v_L^2 + w_L^2) \\ (v, w) = (v, w)_L \end{array} \right. \quad (A2)$$

$$\begin{cases} p_R = p_R^* \\ u_L = 0 \end{cases} \quad (A3)$$

The parameter's values with subscripts "R" and "L" are used for the calculation of numerical fluxes for different sides of the surface. The values without subscripts are related to parameters at "hole section" and are used for the calculation of the source terms:

\dot{m} , (velocity components are multiplied by some empirical coefficients).

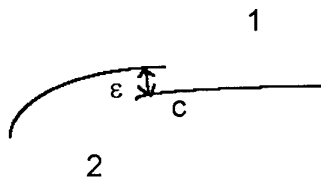


Fig.2A

Similar simple procedure was applied for modeling of the flow through narrow annular gaps which are used for cooling (fig. 2A). In calculation this gap was replaced by the nearest grid node C (fig. 3A).

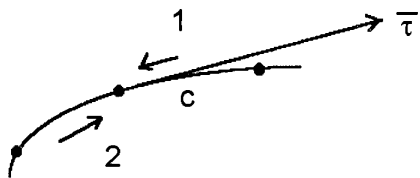


Fig.3A

The extrapolated values of parameters served then as initial data for usual arbitrary discontinuity breakdown procedure (for tangential direction $\bar{\tau}$: see fig. 3A) and obtained "large" values of parameters were used for calculation of source terms for both sides of the surface (and the term \dot{m} in this case was proportional to ϵ - gap thickness).

References

1. Stepanov G. Yu. Gasdynamics of turbomachine cascades. - M., Fizmatgiz, 1962, 512p.
2. Denton J. D. Loss mechanisms in turbomachines. ASME Paper 93-GT-435.
3. Venediktov V. D. Gasdynamics of cooled turbines. Moscow, Mashinostroenie, 1990, 240p.
4. Denton J. D. Through Flow Calculations for Transonic Axial Flow Turbines. Trans. of ASME,

Journal of Engineering for Power, 1978, Vol. 100, April 1978.

5. Lieblein S. Incidence and Deviation-Angle Correlations for Compressor Cascades. Trans. of ASME. Journal of Basic Engineering, Ser. D, Vol. 82, September 1960, pp. 575-587.
6. Lieblein S. Loss and Stall Analysis of Compressor Cascades, Trans. of ASME. Journal of Basic Engineering, Vol. 81, 1959, pp. 387-400.
7. Kacker S. C., Okapuu U. A Mean Line Method for Axial Flow Turbine Efficiency. Trans. of ASME. Journal of Engineering for Power, Vol. 104, 1982, N1.
8. Rechkoblit A. Ja., Izmailov Sh. A. Influence of inlet angle and the level of flow velocity on flow structure and endwall losses in cascades of unshrouded blades.- Bladed machines and jet apparatus. CIAM Proceedings, N1234, 1989, pp. 156-170.
9. Baldwin B. S. , Lomax H. Thin - layer approximation and algebraic model for separated turbulent flows, AIAA Paper, 1978, 78- 257, p. 10.
10. Ivanov M. Ja., Nigmatullin R. Z., Quasi-3D Numerical Model of a Flow Passage of the Aviation - Gas Turbine Engines. ISABE 91-7029, pp. 299-305.
11. Ivanov M. Ja., Kostege V. K., Krupa V. G., Nigmatullin R. Z. Desigh of High-Load Aviation Turbomachines Using Modern 3D Computational Methods. ISABE 93-7032, pp. 355-365.
12. Doroshenko V. E. On combustion process in gas turbine engine chamber. CIAM Proce-edings, N354, 1959, 26p.

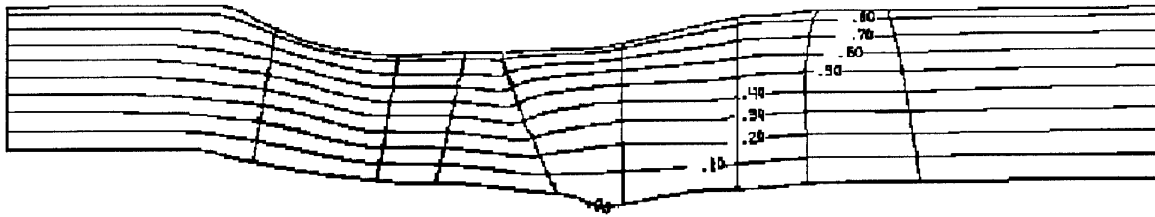


Fig. 1. Streamlines of gas flow through 2-stage high pressure turbine

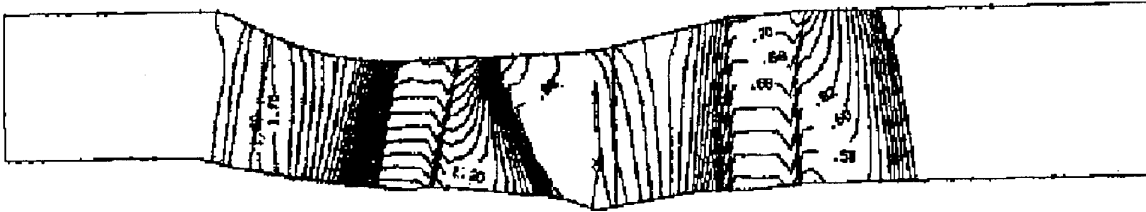


Fig. 2. Pressure contours

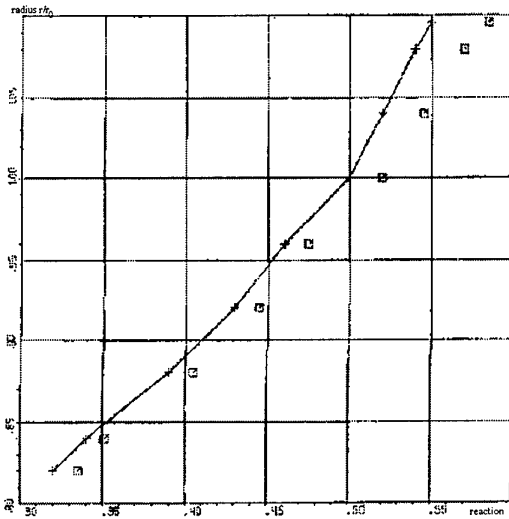


Fig. 3. Radial distribution of degree of reaction of the first stage (solid line - calculated results, squares - design office data)

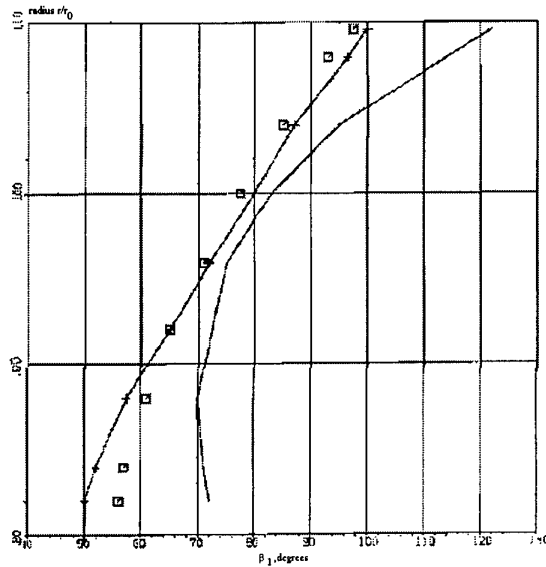


Fig. 4. Inlet relative velocity angles distribution for 1-st stage rotor blades

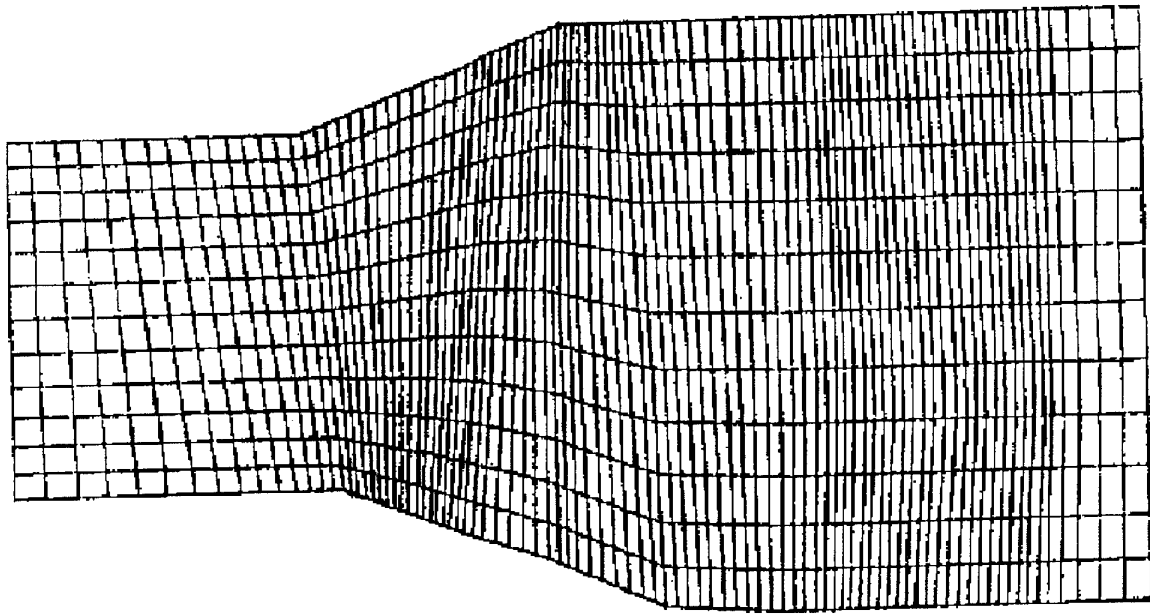


Fig. 5. Computational grid for experimental turbine

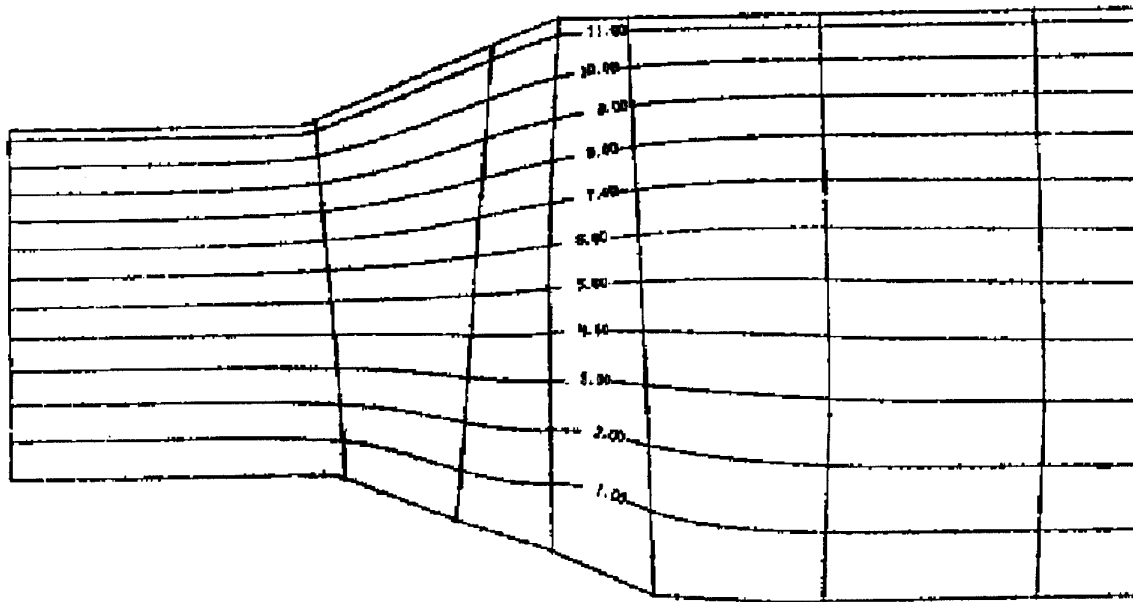


Fig. 6. Streamlines for experimental 1-stage turbine

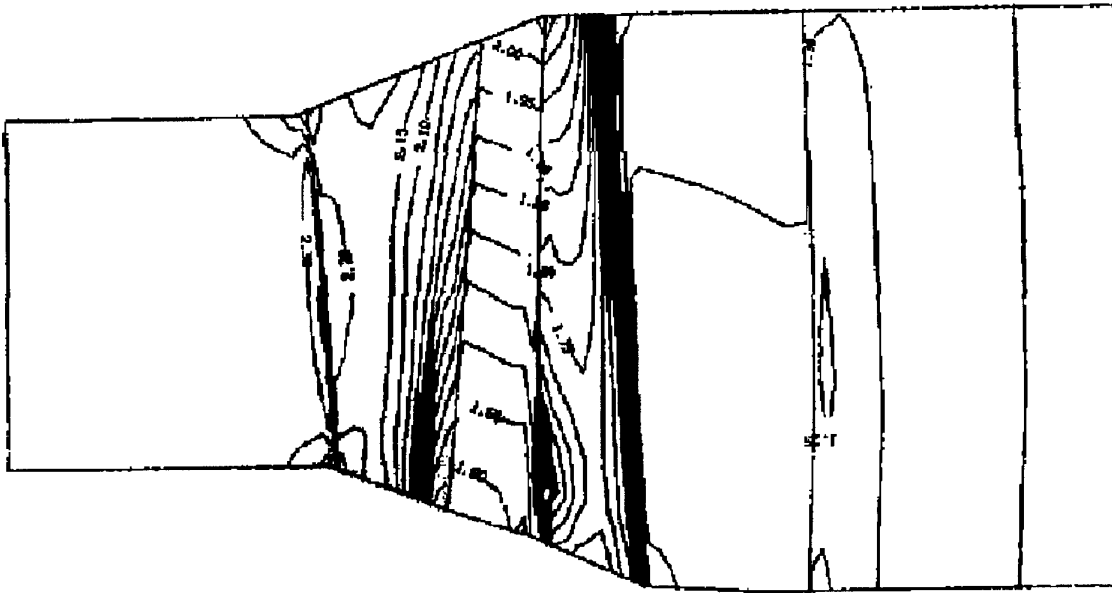


Fig. 7. Pressure contours (S_2 - solution)

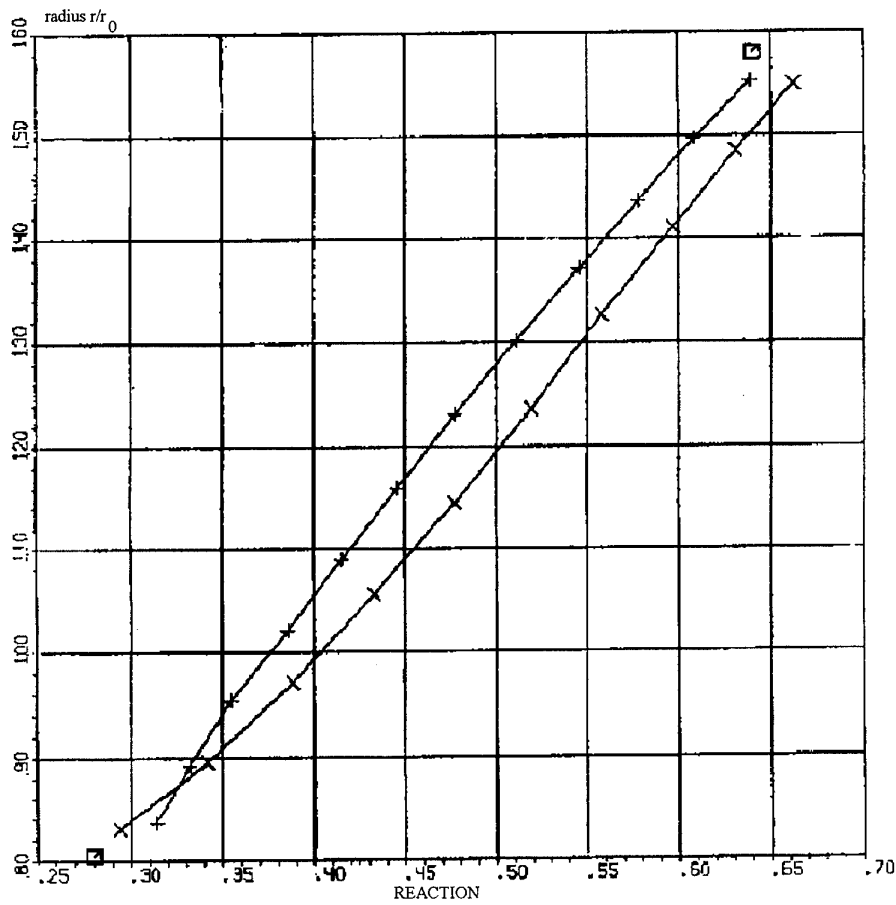


Fig. 8. Radial distribution of degree of reaction

- +---- - S_2 - solution
- x---- - 3D - solution
- - experimental data

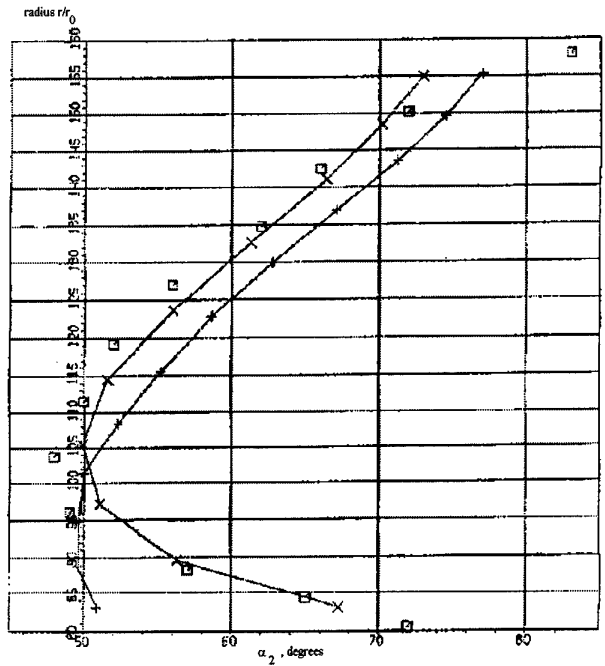


Fig. 9. Absolute velocity angles distribution behind the rotor blade row
 ---+--- - S_2 - solution
 ---x--- - 3D - solution
 □ - experimental data

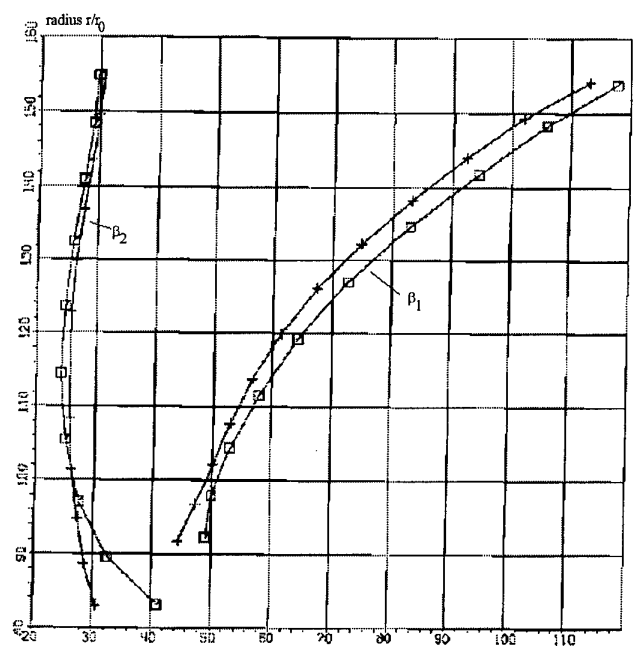
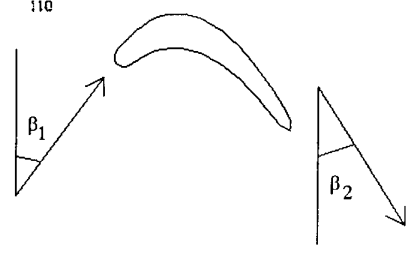


Fig. 10. Rotor relative velocity angles
 ---+--- - S_2 - solution
 ---x--- - 3D - solution



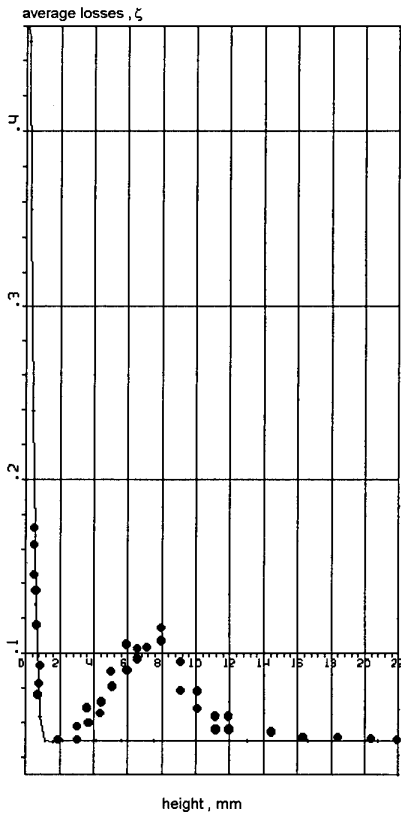


Fig. 11. Averaged in angular direction losses coefficient distribution at exit ($\delta=0$ mm)
 — - calculated results,
 ● - experimental data of [8]

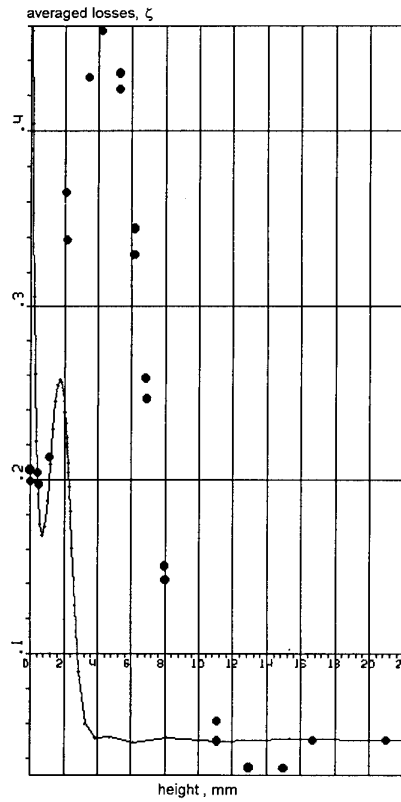


Fig. 12. Averaged in angular direction losses coefficient distribution at exit ($\delta=2.2$ mm)
 — - calculated results,
 ● - experimental data of [8]

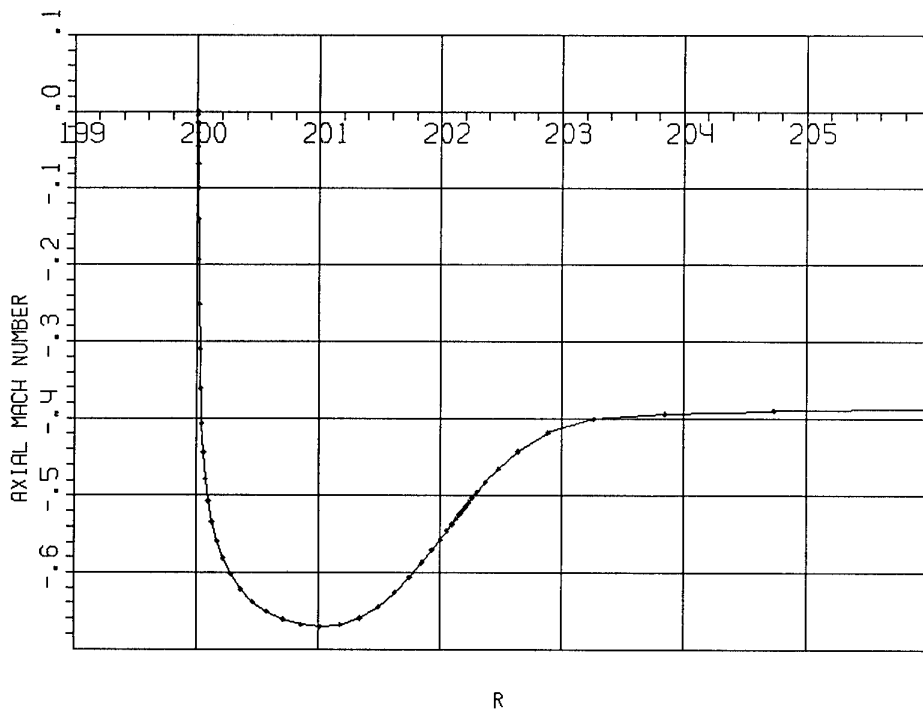


Fig. 13. Axial Mach number distribution in the case $\delta=2.2$ mm (calculation)

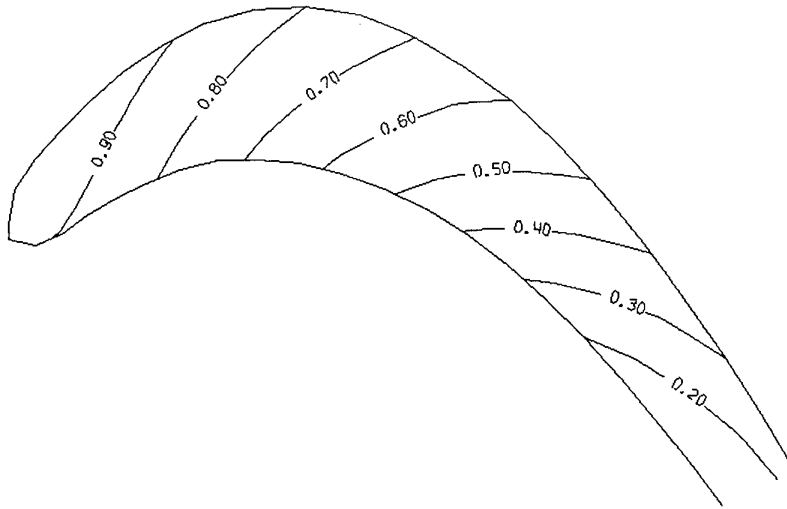


Fig. 14. Stream-lines on S_1 -surface (on butt-end of the blade), $\delta=2.2$ mm

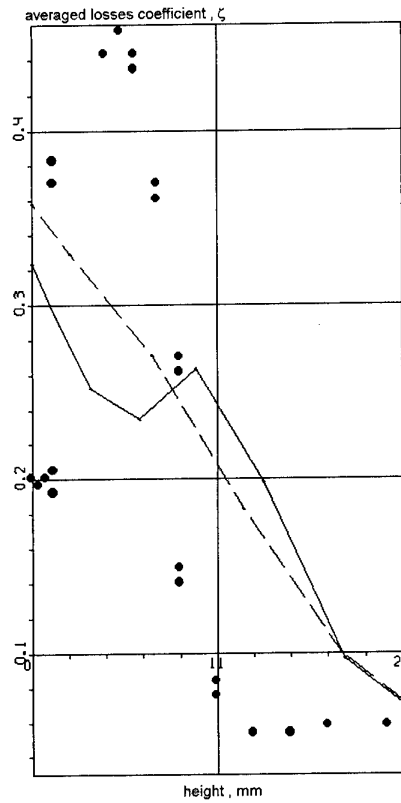


Fig. 15. Radial distribution of losses coefficient ($\delta=2.2$ mm)
 ——— - calculation (more fine grid at radial clearance)
 - - - - - calculation (with more coarse grid at this region)
 ● - experimental data of [8]

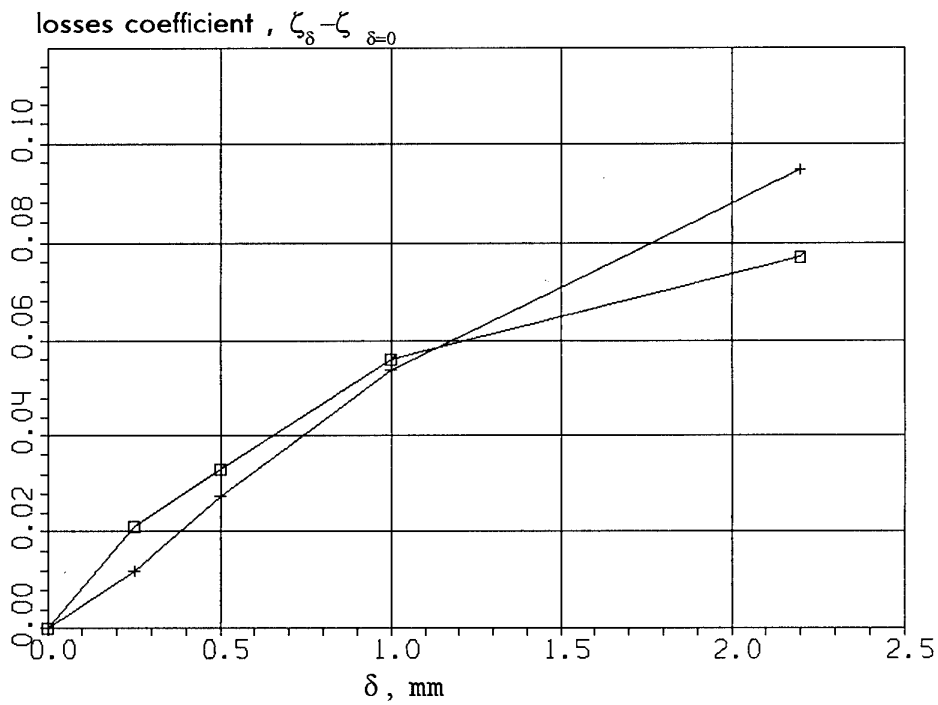


Fig. 16. Dependence of endwall losses coefficient upon radial clearance thickness

—+— - calculation
 —□— - experimental data of [8]

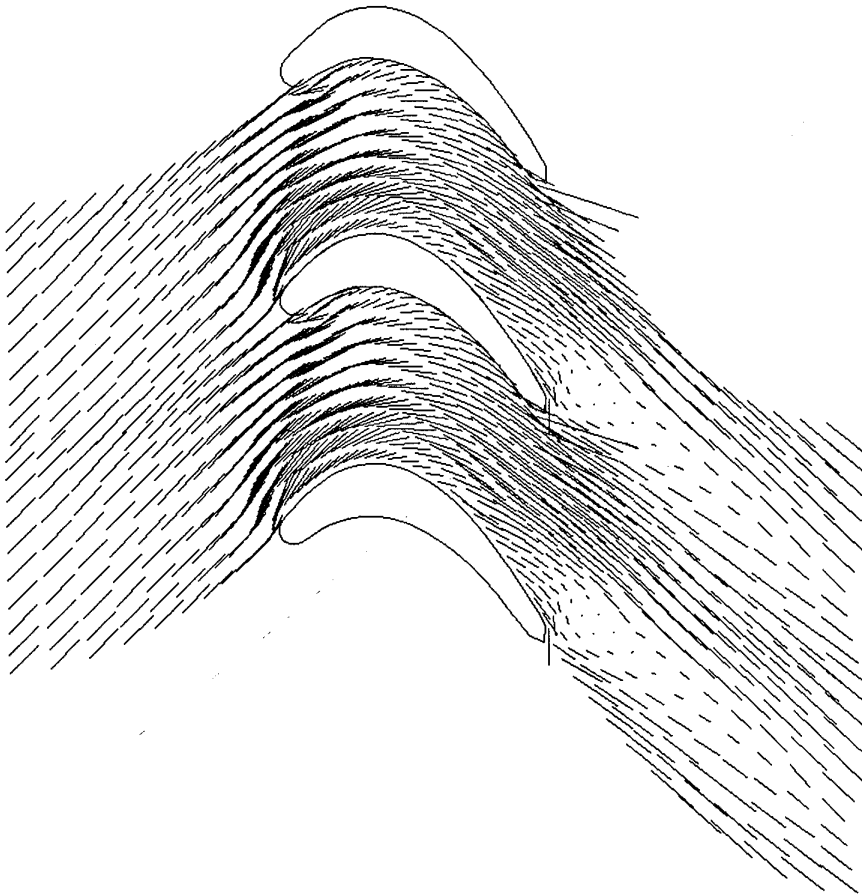


Fig. 17 Velocity vector field at hub section ($\delta=2.2$ mm)

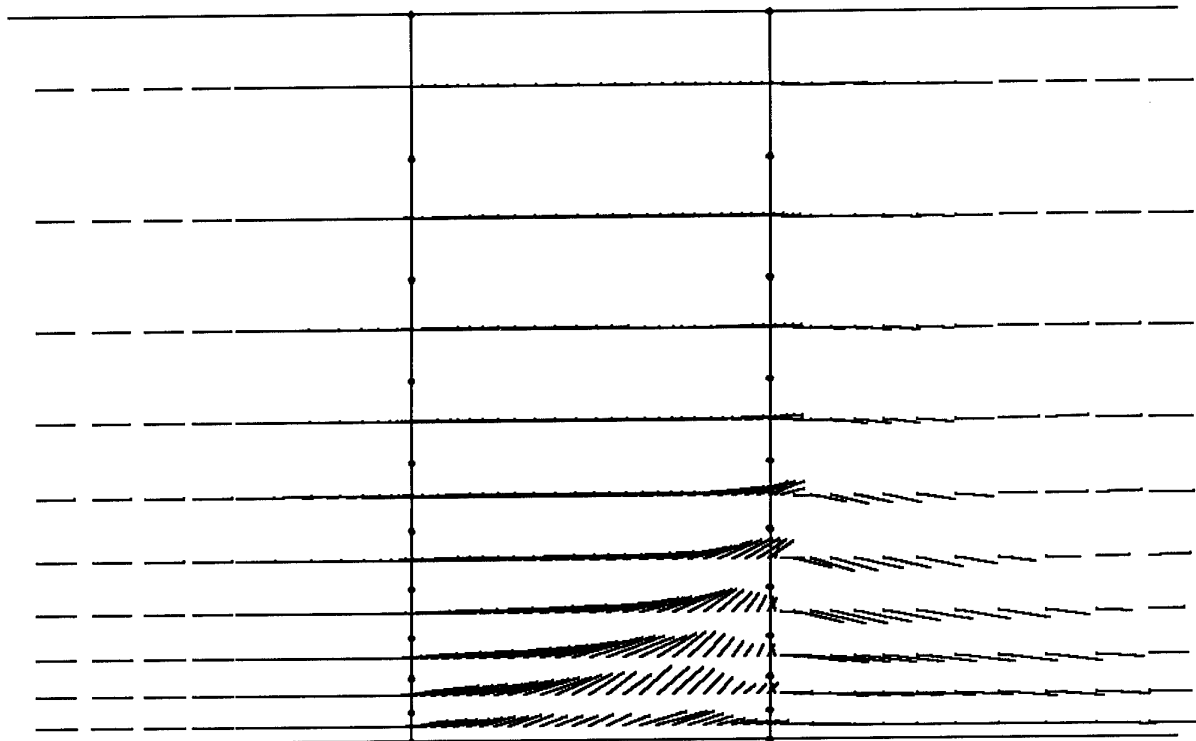


Fig. 18. Velocity vector field at suction side ($\delta=2.2$ mm)

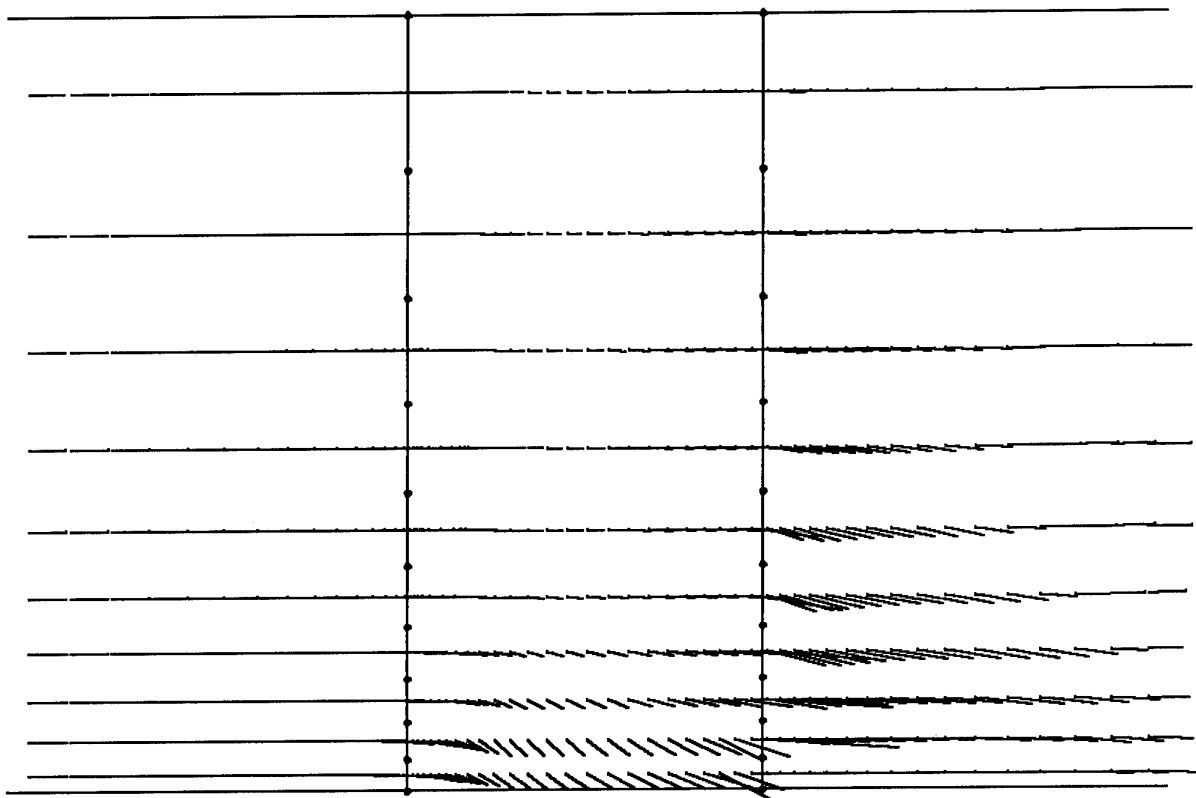


Fig. 19. Velocity vector field at pressure side ($\delta=2.2$ mm)



Fig. 20. Constant pressure contours in blade mid-span plane for the four stage high pressure compressor

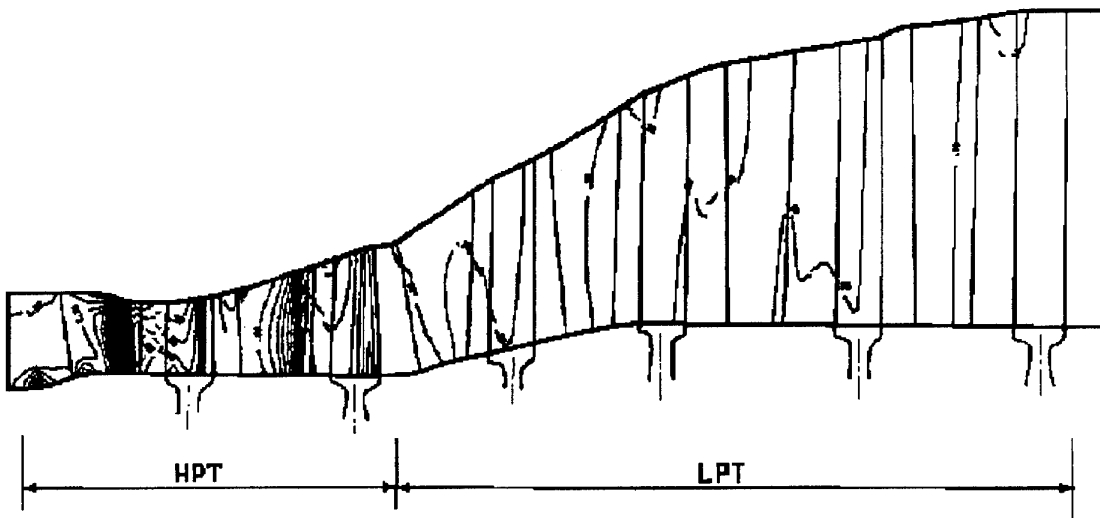


Fig. 21. Constant pressure contours in meridional section of the six stages turbine

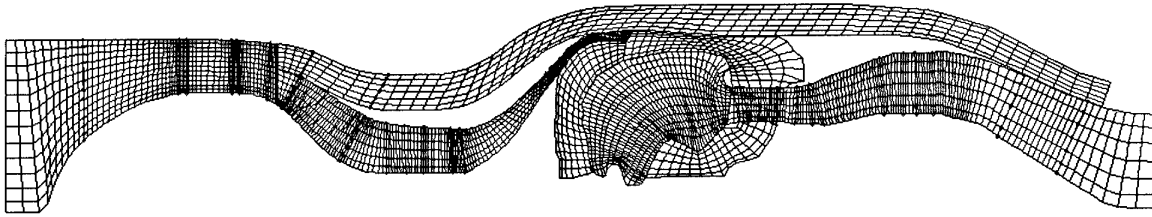


Fig. 22. Computational grid for by-pass gas turbine engine

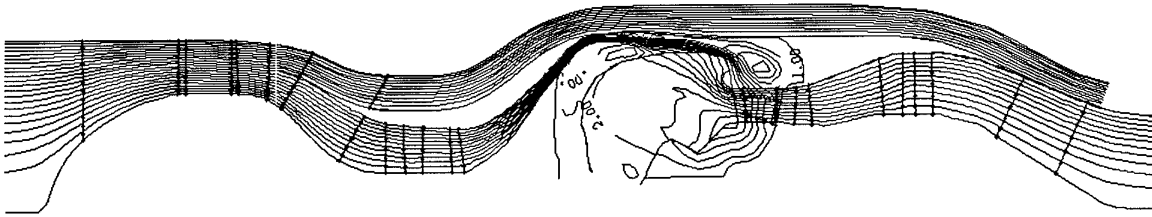


Fig. 23. "Mass flow rate" contours (streamlines)

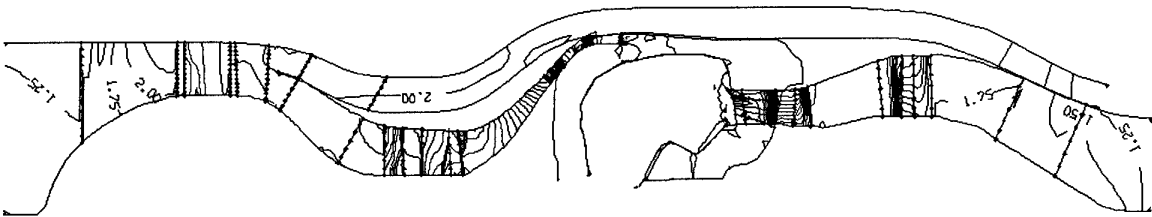


Fig. 24. Static pressure contours

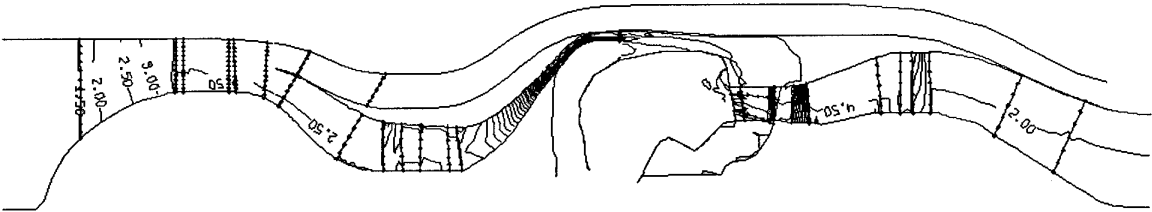


Fig. 25. Absolute total pressure contours

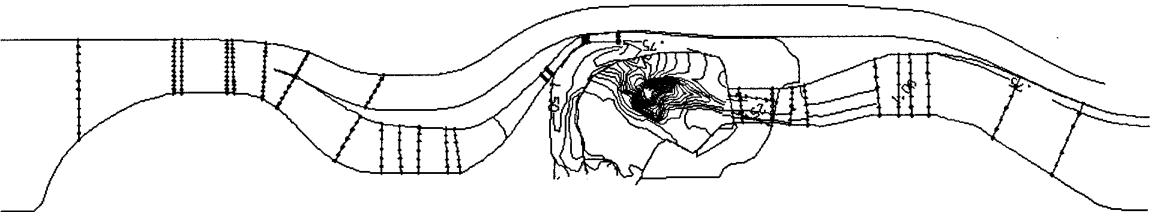


Fig. 26. Absolute total temperature contours

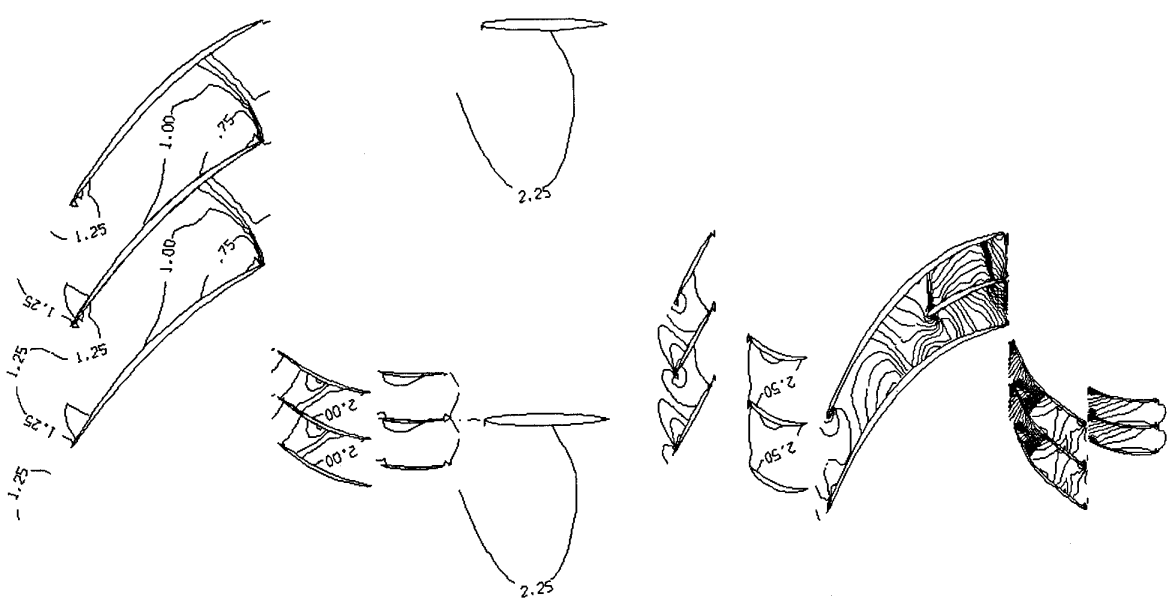


Fig. 27. Pressure contours in mid-span plane for compressor with fan (3D solution)

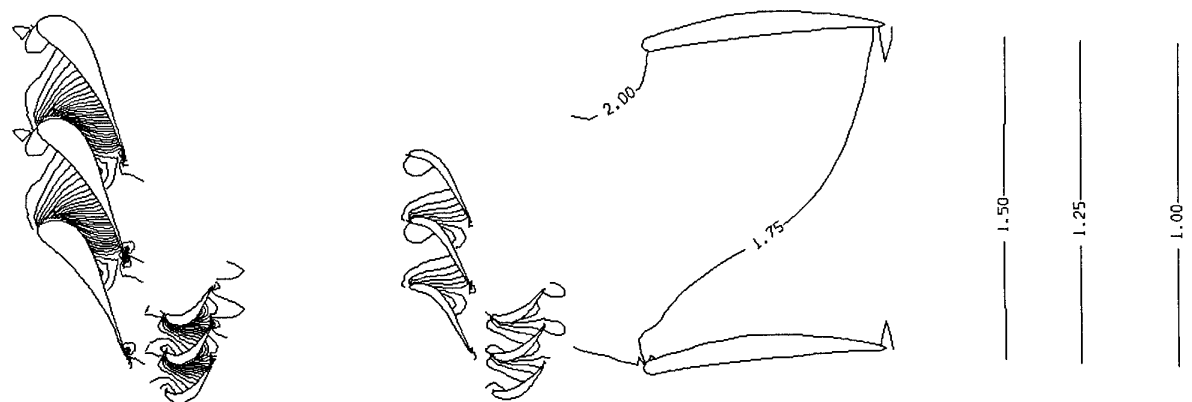


Fig. 28. Pressure contours in mid-span plane for turbine with nozzle (3D solution)

Simulation of steady and unsteady viscous flows in turbomachinery

by
V.G.Krupa,
 CIAM (Central Institute of Aviation Motors)
 2, Aviamotornaya St.,
 Moscow, Russia, 111250.

Abstract

A Navier-Stokes code has been used to compute the viscous turbulent cascade flows. The numerical method employs implicit high-order accurate Godunov scheme and a two-equation $(q - \omega)$ turbulence model based on the integration to the wall. The generation of the O-H grid system for viscous cascade flow simulations is discussed. Numerical solutions were obtained for 2D and 3D turbine cascade flows and 2D unsteady rotor-stator interactions. Available experimental data are used for verification of the computed results.

Introduction

The drive towards higher jet performance has increased demands for accurate and detailed flowfield predictions. Cascade flowfields in turbomachinery are usually very complex due to existence of many complex flow phenomena including for example shocks and shock boundary layer interactions, horseshoe and passage vortices, secondary flows and boundary layer separation. Many of these effects are greatly affected by viscosity therefore the development of the reliable numerical simulation of the viscous flows is of primary importance.

At the present time 2D and 3D inviscid codes based on solving Euler equations are extensively used for turbomachinery flow predictions. These relatively high-speed codes enable to assess aerodynamic performance of very complex turbomachinery configurations [1] but often require empirical correlations to account for viscous effects. Boundary layer codes are restricted to relatively simple geometry and can not be used for the calculation of separated flows.

More accurate and reliable simulation of viscous flows in turbomachinery can be done on the basis of the Reynolds averaged Navier-Stokes equations. In the past decade due to progress of computers a large number Navier-Stokes solvers have been developed for turbomachinery applications (see, for example, [2-9]). These codes employ different numerical techniques and turbulence models. So the validation of the Navier-Stokes solvers has become increasingly important.

In the present lecture some 2D and 3D testcase viscous flows in turbomachinery are considered. The Navier-Stokes equations are integrated by implicit high-

order accurate Godunov scheme. For turbulence modeling the two-equation $(q - \omega)$ turbulence model [10] with viscous sublayer resolution is employed. The detailed formulation of the numerical procedure was given in the previous lecture. Here, the method to generate O-H grid systems for 2D and 3D cascade geometries is discussed. To test the capability of the code to predict thermal characteristics and total pressure losses a number of 2D viscous cascade calculations were performed. The 3D viscous turbulent flows in the turbine cascades are considered. Although these calculations have been made on rather coarse grids they can illustrate the accuracy of the present method. And finally, the calculations of the viscous unsteady 2D rotor-stator interaction are presented.

Boundary conditions

In viscous cascade flow calculations the boundary conditions were formulated as follows. For solid boundaries on the airfoil surfaces and endwalls non-slip conditions for velocities, adiabatic $(\partial T / \partial \eta = 0)$ or isothermal $(T = \text{const})$ condition for temperature and for turbulent quantities $q = \partial \omega / \partial \eta = 0$ are imposed. On the inlet and outlet boundaries of the computational domain the boundary conditions are propagated by taking into account the direction of propagation of the characteristics for one - dimensional (in projection on the boundary normal) unsteady gas flow. For (axially) subsonic inlet in the boundary layer the velocity profile and the value of the total temperature are specified while in the inviscid core of the flow the total pressure, the total temperature and two flow angles are fixed. The fifth necessary parameter was determined from the computation domain using the characteristic relations.

The (q, ω) profiles in the inlet boundary layer were determined from the 'equilibrium' condition and the condition of the equality of the values of turbulent viscosity coefficient calculated from $(q - \omega)$ model and the Baldwin-Lomax algebraic model. In the inviscid flow the values of q_∞ and ω_∞ are imposed. For an (axially) subsonic exit the static pressure is fixed, the other quantities are extrapolated from the interior. Along the periodic gridlines the periodicity conditions are enforced.

Grid generation

To achieve high-quality numerical results in the computation of viscous flows in turbomachinery cascades an efficient and robust grid generation procedure is needed. The important properties of the grid generation procedure are the ability to control grid point distribution in the thin regions (boundary layers) and the ability to achieve grid points periodicity between the upper and lower parts of the outer boundary of the computational domain. The first condition is necessary to resolve effectively turbulent boundary layers with viscous sublayers - in practice several near wall nodes must be located in the region $y_+ \leq 5$. The second condition is generally required for implicit numerical methods - in order to maintain numerical stability the periodic conditions must be treated in an implicit manner.

The algebraic H-grid (fig.1) meets both conditions but often results in a highly skewing grid system. Also H-grid has rather poor resolution in the rounded leading and trailing edges of the blade. Nevertheless, H-grids have been successfully used in many 2D and 3D viscous cascade flow calculations [2,5,8,11]. Widely used C-grids [3,9,7] also do not remove deficiency in the trailing edge. Detailed calculations in the vicinity of the trailing edge are important in terms of predicting both heat transfer and base pressure. The O-grid system, based on an algebraic technique [12], often does not allow to achieve periodicity of the coordinate derivatives at the outer boundary.

One way to avoid above-mentioned difficulties is to use the combined O-H system. This approach was applied in [4] for computation of viscous stator-rotor interaction. The systems of O-grid and H-grid had overlapping regions so interpolation of the variables in these regions was needed. The combined O-H grid based on an algebraic technique was used in viscous cascade flow calculations [13]. In [14], to achieve a greater smoothness of the grid an elliptic grid optimization procedure was developed.

In the present lecture we will also describe a method for construction of the O-H topology grid for viscous cascade flow computations. We start with 2D case.

The procedure involves two stages. In the first stage the O-grid around blade is generated by an algebraic method. In this stage the $\xi = \text{const}$ lines can be constructed orthogonal to the surface of the blade and grid points distribution near the rigid wall can be easily controlled. In the next stage H-grid system is generated by solving the system of equations [15,16]

$$\alpha \bar{r}_{\xi\xi} - 2\beta \bar{r}_{\xi\eta} + \gamma \bar{r}_{\eta\eta} = -(\alpha P \bar{r}_\xi + \gamma Q \bar{r}_\eta), \quad (1)$$

where $\bar{r} = (x, y)$, $\alpha = \bar{r}_\eta \cdot \bar{r}_\eta$, $\beta = \bar{r}_\xi \cdot \bar{r}_\eta$,

$$\gamma = \bar{r}_\xi \cdot \bar{r}_\xi,$$

x, y - Cartesian coordinates; ξ, η - general curvilinear coordinates; P, Q - control functions.

As well-known, a second-order elliptic system of eq.1 allows to be specified either point locations on the boundary or the coordinate line slope at the boundary but not both. In our case, for example for boundary $\eta = \text{const}$, point locations are defined either by grid points distribution on the outer boundary of the O-grid or by grid points distribution on the line of periodicity of H grid. As it was shown in [16] it is possible to achieve a specified line slope and the specified spacing of the first coordinate surface at the boundary by iteratively adjusting control functions P, Q in eq. (1). We used a similar technique to generate H-grid.

Consider the $\eta = \text{const}$ boundary line (the treatment of $\xi = \text{const}$ boundary line is similar). On this line r_ξ and $r_{\xi\xi}$ are known. Quantity r_η can be found from specification of the desirable slope of line $\xi = \text{const}$ and spacing of the next coordinate line $\eta = \text{const}$ at the boundary. From eq.1 one can easily obtain:

$$P = -(\alpha \bar{r}_\xi - \beta \bar{r}_\eta) \cdot (\alpha \bar{r}_{\xi\xi} - 2\beta \bar{r}_{\xi\eta} + \gamma \bar{r}_{\eta\eta}) / (\alpha J^2), \quad (2)$$

$$Q = -(\gamma \bar{r}_\eta - \beta \bar{r}_\xi) \cdot (\alpha \bar{r}_{\xi\xi} - 2\beta \bar{r}_{\xi\eta} + \gamma \bar{r}_{\eta\eta}) / (\gamma J^2),$$

$$J = x_\xi y_\eta - x_\eta y_\xi$$

The iterative procedure can proceed as follows

(1) Assume initial grid point distribution for H-grid. In this step H-grid system can be constructed by algebraic method.

(2) Evaluate $r_{\eta\eta}$, $r_{\xi\eta}$ on $\eta = \text{const}$ boundaries,

and $r_{\xi\xi}$, $r_{\xi\eta}$ on $\xi = \text{const}$ boundaries, from the previous grid points distribution, using central difference formulae. (For evaluation $r_{\xi\eta}$, $r_{\eta\eta}$ points of O-grid system or condition of periodicity can be used). Evaluate control function P, Q from eq. 2 at the boundary. Evaluate the control functions in the field by interpolation from boundary values.

(3) Solve eq. (1) to generate the grid.

Steps (2) and (3) are repeated until convergence.

Computational grid obtained by this method for a 2D viscous cascade calculations are shown on fig. 2. The O-grid system has 120x25 points, the H-grid system has 95x40 points. In order to solve system of eq. (1) an ADI-method was employed and about 600 iterations was required to achieve convergence.

The construction of a 3D-grid system can be performed applying a 2D grid generation procedure on each radial surface. In the general case, when the radius of a radial surface is varying with axial distance, the orthogonality of the grid can't be retained. Figure 3 shows a 3D view of an O-H grid system obtained by this method for a typical rotor blade.

Computational results

The computational codes based on the numerical schemes described in the previous lecture have been extensively tested for 2D and 3D viscous cascade flow calculations. Here we would like to present some computational results obtained by this method.

Figures 4-7 show the computational results [17] for a rotor blade, which was experimentally investigated by Consigny and Richards [18]. In this case an H-grid system consisting of a 100x60 grid points was employed. The minimum distances from the nodes of the grid to rigid surfaces were $3 \cdot 10^{-5} c$, where c is chord-length, which corresponded to $y^+ \approx 0.3$. Courant number Cu was varied from $Cu = 5 \div 8$ in initial steps to $Cu = 50 \div 100$, after which the calculations were continued with a constant value of Cu (for each cell). Figure 4 shows a typical history of convergence where ϵ is a maximum residual, n is a number of iterations. Lower and upper curves correspond, respectively, to the residual of the Navier-Stokes equations and the $(q - \omega)$ turbulence model equations. The computations have been performed for an exit Mach number $M_{out} = 0.92$, Reynolds number based on the inlet conditions and blade chord $Re = 9.42 \cdot 10^5$ and the temperature of the wall $T_w = 294^\circ K$. Figure 5 shows the comparison between the predicted and the measured isentropic Mach number along the blade. The Mach contours are shown in fig. 6. Figure 7a,b,c shows the predicted heat transfer coefficient $Q = q_w / (T_{QW} - T_w)$ on the cascade surface in comparison with experimental data for three different levels of inlet turbulence: $Tu_\infty = 0.8\%$ (fig.7a), $Tu_\infty = 3.0\%$ (fig.7b), $Tu_\infty = 5.0\%$ (fig. 7c). On the suction surface the $(q - \omega)$ turbulence model displays at least qualitatively the capability to predict laminar to turbulent transition. However, on the pressure side the $(q - \omega)$ model underpredicts the heat transfer. Note that the Baldwin-Lomax algebraic model allows to achieve a better agreement with experiment on the pressure wall for low level of inlet turbulence (fig.7a). (In this case the locations of the transition have been inferred from experimental data).

A set of the computations have been performed to assess the capabilities of the developed Navier-Stokes solver to predict accurately losses in turbine cascades.

For comparison, a vast experimental data conducted in CIAM [19] was used. We will present some computational results for turbine cascades designated as BL40, BL48, BL53, BL108, BL157, BL166. The main geometrical characteristics of these cascades are presented in Table 1; details of the blade geometry are available in [19].

For calculations O-H grid system consisted of the 6800 points was used. The free-stream values of q_∞

and ω_∞ imposed at the inlet based on specified free stream turbulence intensity and length scale:

$$Tu_\infty = \sqrt{2/3} q_\infty / u_\infty = 5.5\%,$$

$$l_\infty = q_\infty / \omega_\infty = 0.005t.$$

Figure 8 shows the predicted isentropic number λ (λ - is the velocity coefficient) on the surface of the blade BL40 in comparison with experiment [19] for various values of the exit number λ_{out} . The agreement with experiment is generally good. The Mach number contours for $\lambda_{out} = 1.07$ are shown in fig 9. The shock system associated with the trailing edge is clearly resolved. The loss coefficient and the base pressure coefficient are shown in fig. 10. The loss coefficient and base pressure coefficient are defined as:

$$\zeta = 1 - \left(\frac{\lambda_2}{\lambda_{2is}} \right)^2, \quad \Delta p_{tr} = \frac{P_{t2} - P_2}{\frac{1}{2} \rho_{2is} V_{2is}^2}$$

The index 2 corresponds to the averaged values at the outlet.

The predicted results are in good agreement with experiment results for exit subsonic and supersonic velocities.

To assess the accuracy of the numerical method several computations have been performed on fine grid contained 27200 points. Computed Mach number contours for blade BL48 at $\lambda_{out} = 1.27$ are shown in fig. 11a (6800 points grid) and in fig. 11b (27200 points grid). The predicted and the measured loss and base pressure coefficients are plotted in fig. 12. The numerical results obtained on the different grids are in reasonable agreement. The predicted loss coefficient is generally in a good agreement with experiment while for the base pressure a quite large difference is observed. Since grid refinement does not allow to achieve a better agreement with experiment, this discrepancy is associated rather with turbulence modeling than with numerical errors.

The predicted and the measured distributions of the isentropic velocity coefficient λ on the surface of the blade BL166 are shown in fig. 13. A discrepancy can be observed on the pressure side of the blade where a quite large $(-0.8 < s/t < -0.15)$ separation zone exists. Mach number contours for subsonic and supersonic exit velocities are shown in fig. 14. Figures 15-18 show the

predicted loss coefficient and base pressure coefficient for blades BL166, BL53, BL108, BL157 respectively. For most cases the agreement between measured and predicted loss coefficients is quite satisfactory.

The 3D calculations have been performed for the low-pressure turbine cascade, which the flow was investigated experimentally in [20]. The cascade had the following principle geometric parameters: axial chord $c_x = 52.5$ mm, chord $c = 55.9$ mm, pitch $t = 31.5$ mm, and height of the cascade $h_1 = 95.8$ mm at the inlet and $h_2 = 101.6$ mm at the outlet. The vane profile was constant over the height of the cascade; the profile coordinates are given in [20].

The flow parameters used in the calculations corresponded to the flow in a low pressure turbine cascade at its design condition: the isentropic exit Mach number $M = 0.702$, the isentropic exit Reynolds number $Re = 2.9 \cdot 10^5$, inlet flow angle 38.8° . The endwall boundary layer specified at the inlet plane are in accordance with experiment. In view of the symmetry of the problem the calculations were carried out to half of the height of the cascade.

The H-grid consisted of $81 \times 27 \times 40$ nodes in the axial (x), radial (y) and azimuthal (z) directions.

The predicted and measured midspan isentropic Mach number distribution is presented in fig. 19.

The limiting streamlines near the endwall are shown in fig. 20 in comparison with experimental data [20]. Fig. 21 shows the predicted and measured secondary velocity vectors in the traverse plane at $x = 1.42c_x$. Total loss pressure contours ζ are plotted in fig. 22. Here, $\zeta = (p_{0\infty} - p_0) / (p_{02} - p_2)$, p_0 is a total pressure, the index ∞ relates to the free stream value, the index 2 corresponds to the averaged values at the outlet. The calculation reproduces the main features of the flow although the predicted locations of the centers passage and trailing shed vortex are different from experiment. The predicted spanwise distributions of pitchwise averaged total pressure loss coefficient and exit flow angle with comparison of the experiment are given in fig. 23. The computed results are in reasonably good agreement with the experiment.

The calculations have also been performed for this turbine cascade at its off-design conditions [27]. Figure 24 a,b shows the limiting streamlines on the suction side for $Re = 1.5 \cdot 10^5$ and $Re = 6 \cdot 10^5$, respectively. At $Re = 1.5 \cdot 10^5$ a large separation zone can be observed, at $Re = 6 \cdot 10^5$ the boundary layer is turbulent (in calculation and experiment [21]) on the suction side, which prevents separation. The pitchwise - averaged total pressure loss coefficient and exit flow angle are compared with the experiment in fig. 25 and fig. 26.

Although the predicted maximum in distribution of ζ is in a fairly good agreement with experiment, the calculations exaggerate the losses in the central part of channel.

Figure 27 shows the predicted and measured midspan isentropic Mach number for angles of attack $\alpha = -20.3^\circ$ and $\alpha = +8.6^\circ$. For a positive angle of attack the flow remains attached except in the small region near the leading edge. For $\alpha = -20.3^\circ$ the separation zones at the midsection are located at $0.69c_x \leq x \leq 0.98c_x$ on the suction side and at $0.02c_x \leq x \leq 0.31c_x$ on the pressure side. This is roughly correct with experiment. The spanwise distributions of pitchwise-averaged total pressure loss coefficient and exit flow angle are shown in fig. 28 and 29.

Computations have been performed for linear turbine cascade with straight endwalls studied experimentally at CIAM [28]. The main geometrical characteristics of cascade were: chord length $c = 63$ mm, pitch $t = 41$ mm, height $h = 100$ mm. The profile of the blade corresponded to hub section of the rotor blade of fourth turbine stage. A total number of 217600 grid points were used for O-H grid system (fig. 30). The flow parameters were: inlet angle $\alpha = 40.3^\circ$, exit Mach number $M_{out} = 0.565$, isentropic exit Reynolds number $Re = 7.4 \cdot 10^5$. To reduce the losses the original cascade was redesigned [28]. Fig. 31 shows the limiting streamlines on the suction side of the original (fig. 31 a) and modified (fig. 31b) blade. For original cascade a separation zone can be observed while for modified cascade the flow remains attached. Experiment [28] also indicates the separation on the suction side of the original blade but the extension of separation zone is underpredicted in calculation. For this reason, a quite large discrepancy between predicted and measured total pressure coefficient exists for original cascade (fig. 32), for modified cascade the computed distribution in a good agreement with experiment.

The calculation has been performed for supersonic stator cascade (CA-2) studied experimentally at CIAM. The detailed cascade geometry and experimental conditions are available in [29]. The inlet flow assumed to be axial, the exit Mach number $M_{out} = 1.35$. A total number of 248000 grid points were used for this case. Figure 33 shows the O-H grid system for a blade-to-blade plane, and the H-grid system for a meridional plane. Computed Mach number contours at midspan are shown in fig. 34. The distributions of mass-averaged total pressure loss coefficient and exit flow angle are presented in comparison with experiment in fig. 35a and 35b, respectively. The computed results are in a good agreement with experiment.

Now we will present some computational results for a 2D unsteady rotor-stator interaction. The rotor-stator configuration considered herein is the large scale turbine model of Dring et al. [22]. Several Navier-Stokes analyses [4,23,24] have been performed for this configurations but in all of them an algebraic turbulence model was used. This may not be quite appropriate for unsteady rotor-stator interaction especially for the

region where the rotor blade intersects the wake of the stator blade. In the present calculations the two-equation

$(q - \omega)$ turbulence model was employed. Three different numerical schemes of different levels of accuracy in time have been used in the present calculations: first-order (implicit Euler scheme), second-order (Crank-Nicolson scheme) and implicit third-order accurate in time schemes [25]. The details for numerical integration procedure are given in a previous lecture [25].

The actual experimental configuration consisted of 22 stator vanes and 28 rotor blades. Since in the present calculations the number of stators and rotors was assumed to be equal, the rotor geometry was rescaled by a factor 28/22.

Patched O-H grid systems were used for calculations. The computational grid (fig. 36) consisted of 18000 nodes. The minimum distance from the first point to the wall is about $10^{-5} t$, where t is a pitch-length. An axial gap between the stator and the rotor was assumed to be equal to 15% of average axial chord.

The rotor rotational speed Ω was $1.28u_\infty$, where u_∞ is the free-stream velocity at the inlet of the stage. The value u_∞ (unknown before the solution) was calculated from the assumption that inlet Mach number was $M=0.07$. The inlet flow angle was assumed to be axial.

The value of the static pressure was $P = 0.96P_{0\infty}$, where $P_{0\infty}$ is the free-stream total pressure. The values of the turbulent quantities were $q_\infty / u_\infty = 0.01$, $\omega_\infty t / u_\infty = 6.5$, the free stream Reynolds number was 10^5 per inch. The treatment of the patched boundaries between the O- and the H-grids in the stator and rotor regions and at the stator and rotor H-grids was based on the technique developed in [4]. This approach allows to preserve the conservation of fluxes across a patch line.

Calculations have been performed a with time step $\tau = 0.002T$, where T (period) is the time during which rotor blade completes one cycle. A rotor cycle corresponds to the motion of the rotor through a distance equal to pitch. Four iterations of the iterative algorithm were performed at each step. About six rotor cycles was required to achieve a periodic solution.

Figure 37 shows the time-averaged stator surface pressure distribution in comparison with experimental data [22]. The time averaged pressure coefficient is defined as:

$$C_p = \frac{p - P_{0\infty}}{\frac{1}{2}\rho_\infty\Omega^2}$$

where p is the time-averaged (for period) pressure, ρ_∞ is the time-averaged inlet free stream density. The predicted results obtained by different schemes are

practically identical and in a good agreement with experimental data. Figure 38 shows the time-averaged pressure coefficient for the rotor. Computed results obtained by a third-order accurate scheme are in a slightly better agreement with the experiment.

The pressure amplitude C_a on the surface of the stator are plotted in a fig. 39 . The C_a is defined as

$$C_a = \frac{P_{\max} - P_{\min}}{\frac{1}{2}\rho_\infty\Omega^2}$$

where P_{\max} and P_{\min} are the maximum and minimum pressures that occur over a cycle at a given point.

The predicted and measured pressure amplitude distributions for the rotor are shown in fig. 40 . Note, that the difference in the magnitude of pressure amplitude obtained by different schemes may achieve 15-20 %; the application a of second and third order accurate schemes in comparison with a first order accurate scheme does not allow to obtain a much better agreement with experiment. The computed Mach number contours at instants $t = 0.23; 0.567; 0.9T$ are shown in fig. 41 a,b,c.

Numerical results have shown the developed Navier-Stokes solver is able to predict quite accurately the total pressure losses for 2D viscous transonic flows in widely varying cascade geometries. For 3D viscous cascade flows the agreement between computed and measured results is also satisfactory in most cases. Reasonably good predictions have been obtained for 2D unsteady rotor-stator interaction.

References

1. Nigmatullin R.Z. Application of multicomponent models to the flow passages simulation in multistage turbomachines and whole gas turbine engines. AGARD lecture series. No 198, 1994, LS-198.
2. Hah C. A Navier-Stokes Analysis of Three-Dimensional Turbulent Flows Inside Turbine Blade Rows at Design and Off-Design Conditions. ASME Journal of Engineering for Power, Vol. 106, pp.421-429, 1984.
3. Chima R.V. Inviscid and Viscous Flows in Cascades with an Explicit Multi-Grid Scheme. AIAA Journal, Vol.23, No.10, pp.1556-1563, 1985.
4. Rai M.M. Navier-Stokes Simulation of Rotor-Stator Interaction Using Patched and Overlaid Grids. Journal of Propulsion and Power, Vol. 3, pp. 387-396, 1987.

5. Knight C.J., Choi D. Development of a viscous cascade code based on scalar implicit factorization. AIAA Paper, No. 2150, 1987.
6. Daws W.N. Development of a 3D Navier-Stokes Solver for Application to all Types of Turbomachinery. ASME Paper, No. 88-GT-70, 1988.
7. Nakahashi K., Nozaki O., Kikuchi K., Tamura A. Navier-Stokes Computations of Two- and Three-Dimensional Cascade Flow Fields. AIAA Paper, No. 87-1315, 1987.
8. Kunz R. and Lakshminarayana B. Explicit Navier-Stokes computation of cascade flows using the $k-\epsilon$ model. AIAA Journal, Vol. 30, No. 1, 1992.
9. Davis R.L., Ni R.H., Carter J.E. Cascade viscous flow analysis using Navier-Stokes equations. AIAA Paper, No. 86-0033, 1986.
10. Coakley T.J. Turbulence modeling methods for the compressible Navier-Stokes equations. AIAA Paper, No. 1693, 1983.
11. Yamamoto S., Daiguji H., Ishigaki H. An implicit time-marching scheme for solving the compressible Navier-Stokes equations. Proc. Internat. Symp. on Comput. Fluid Dynamics. North-Holland, 1988. pp. 773-784.
12. Eiseman P.R. A coordinate system for a viscous transonic cascade analysis. Journal of Computational Physics, 26, 1978, pp. 307-338.
13. Lee D., Knight C. Evolution of an O-H grid formulation for viscous cascade flows. AIAA Paper, No. 89-0207, 1989.
14. Choi D., Knight C.J. A study on H and O-H generation and associated flow codes for gas turbine 3D Navier-Stokes analyses. AIAA Paper, No. 91-2365, 1991.
15. Godunov S.K., Zabrodin A.V., Ivanov M.Ja., et al., Numerical Solution of Multidimensional Problems of Gas Dynamics (in Russian). Nauka, Moscow, 1976.
16. Thomson J.F., Warsi Z.U.A., Mastin C.W. Numerical grid generation: Foundations and Applications, North-Holland. 1985.
17. Ivanov M.Ja., Krupa V.G., Implicit unfactorized method of calculating turbulent viscous heat-conducting gas flows in turbomachinery cascades. Zh. Vychisl. Mat. Mat. Fiz., 31, 754, 1991.
18. Consigny H., Richards B.E. Short duration measurements of heat-transfer rate to a gas turbine rotor blade. J.Engng Power . V. 104. No.3. 1982. pp. 542-551.
19. Venediktov V.D., Granovsky A.V., Karelin A.M., Kolesov A.N., Muhtarov M.X. Atlas of the experimental characteristics of 2D cooled gas turbine cascades (In Russian). CIAM, 1990, 393 p.
20. Hodson H.P., Dominy R.G. Three-dimensional flow in a flow-pressure turbine cascade at its design condition. ASME Paper, No. 86-GT-106, 1986.
21. Hodson H.P., Dominy R.G. The off-design performance of a low-pressure turbine cascade. Trans. of the ASME (Russian translation), No. 2, 1988, pp. 127-137.
22. Dring R.P., Joslyn H.D., Hardin L.W., Wagner J.H. Turbine rotor-stator interaction Journal of Engineering for Power. Vol. 104, 1982. pp. 729-742.
23. Gibelung H.J., Buggeln R.C., Chen S.Y., McConaughy H.V. An implicit Navier-Stokes analysis of turbine rotor-stator interaction. AIAA Paper, No. 88-3090, 1988.
24. Dorney D.J., Davis R.L., Edward D.E., Madavan N.K. Unsteady analyses of hot streak migration in a turbine stage . AIAA Paper, No. 90-2354, 1990.
25. Krupa V.G., Ivanov M.Ja. Solution of Navier-Stokes equations using high accuracy monotone schemes. AGARD - lecture series, No 198, 1994, LS-198.
26. Ivanov M.Ja., Krupa V.G. Computation of 3D viscous cascade flow. Izv. RAN, Mech. Zhidcosti i Gaza, No. 7, pp. 58-68, 1993 (in Russian).
27. Krupa V.G. Numerical investigation of 3D flow in low-pressure turbine cascade at its off-design conditions. Preprint CIAM, No 11, 1993 (in Russian).
28. Granovsky A.V., Danilkin A.V., Rogkov S.G., Rudenko S.V. Numerical and experimental investigation of gasdynamic effectiveness of the rotor blades. Otchet CIAM, No 11636, 1990 (in Russian).
29. Gavrikov I.F., Krasavin A.A., Koristov V.V., Miyskin G.V., Mironov V.R. Experimental investigation of a aerodynamic performance of the supersonic turbine vane. Otchet CIAM, No 17-018, 1992 (in Russian).

Table 1.

Cascade	Chord, c (mm)	Axial chord-chord ratio, c_x/c	Pitch-chord ratio, t/c	Throat-chord ratio, a/c	Design inlet angle (deg)	$\text{SIN}^{-1}(a/t)$	Leading edge diameter-chord ratio	Trailing edge diameter-throat ratio
BL40	84.32	0.592	0.652	0.190	86.46	16.94	0.107	0.150
BL48	85.00	0.745	0.734	0.271	82.83	21.68	0.168	0.113
BL53	80.85	0.567	0.680	0.194	81.73	16.59	0.111	0.153
BL108	65.00	0.932	0.623	0.256	46.38	24.32	0.124	0.254
BL157	65.32	0.924	0.696	0.348	38.81	29.99	0.110	0.148
BL166	62.81	0.961	0.799	0.418	35.89	31.53	0.127	0.154

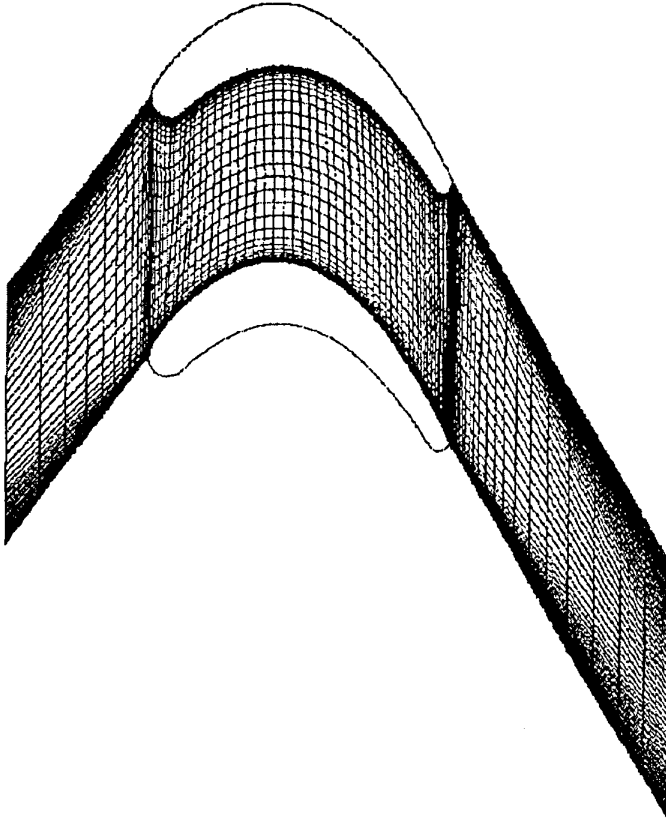


Fig. 1 100x60 H grid .

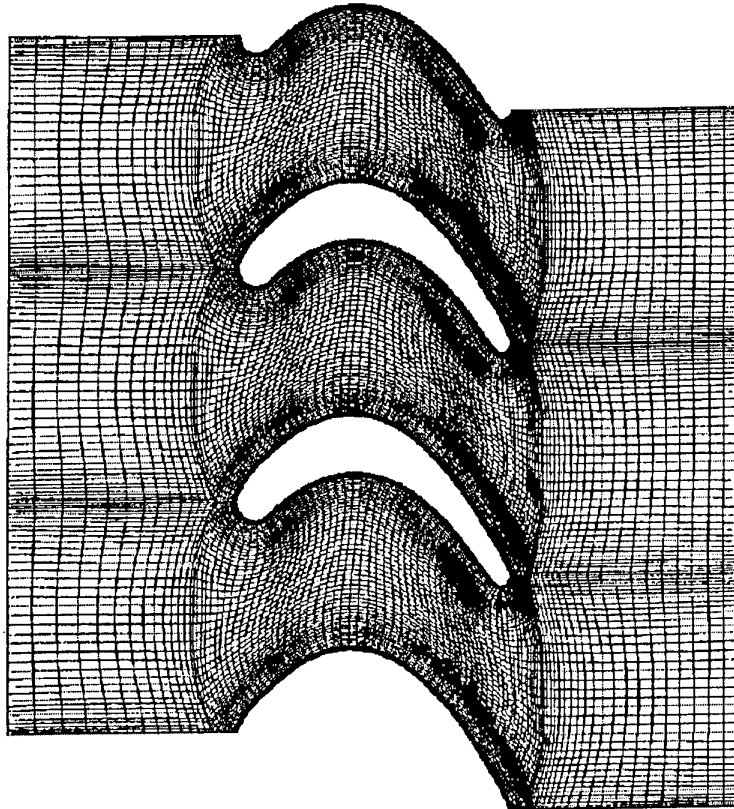


Fig. 2 a 6800 O-H grid .

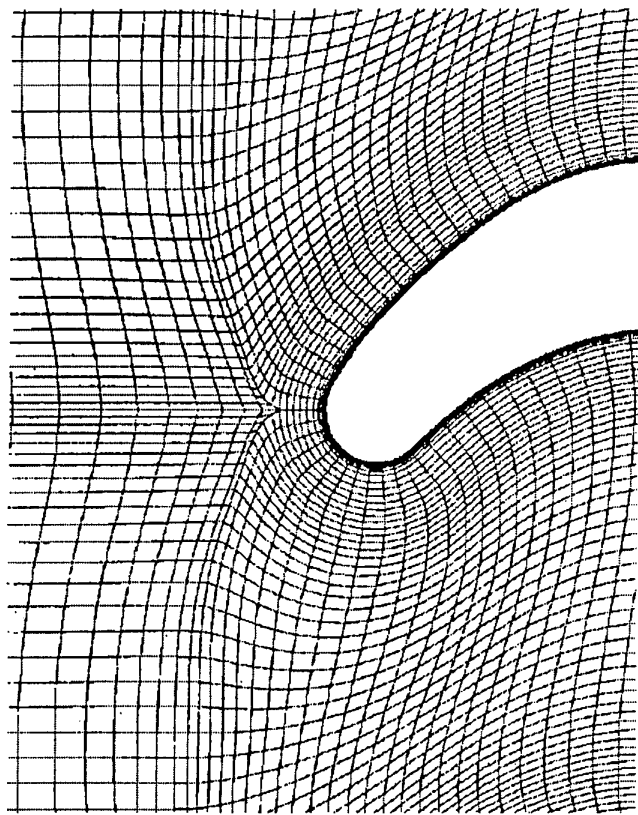


Fig. 2b Zoomed view of the leading edge .

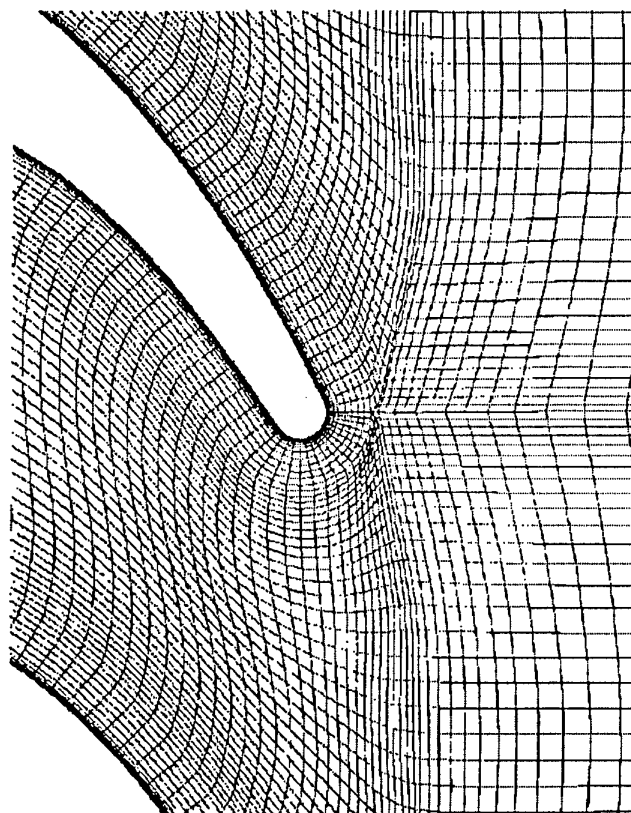


Fig. 2c Zoomed view of the trailing edge .

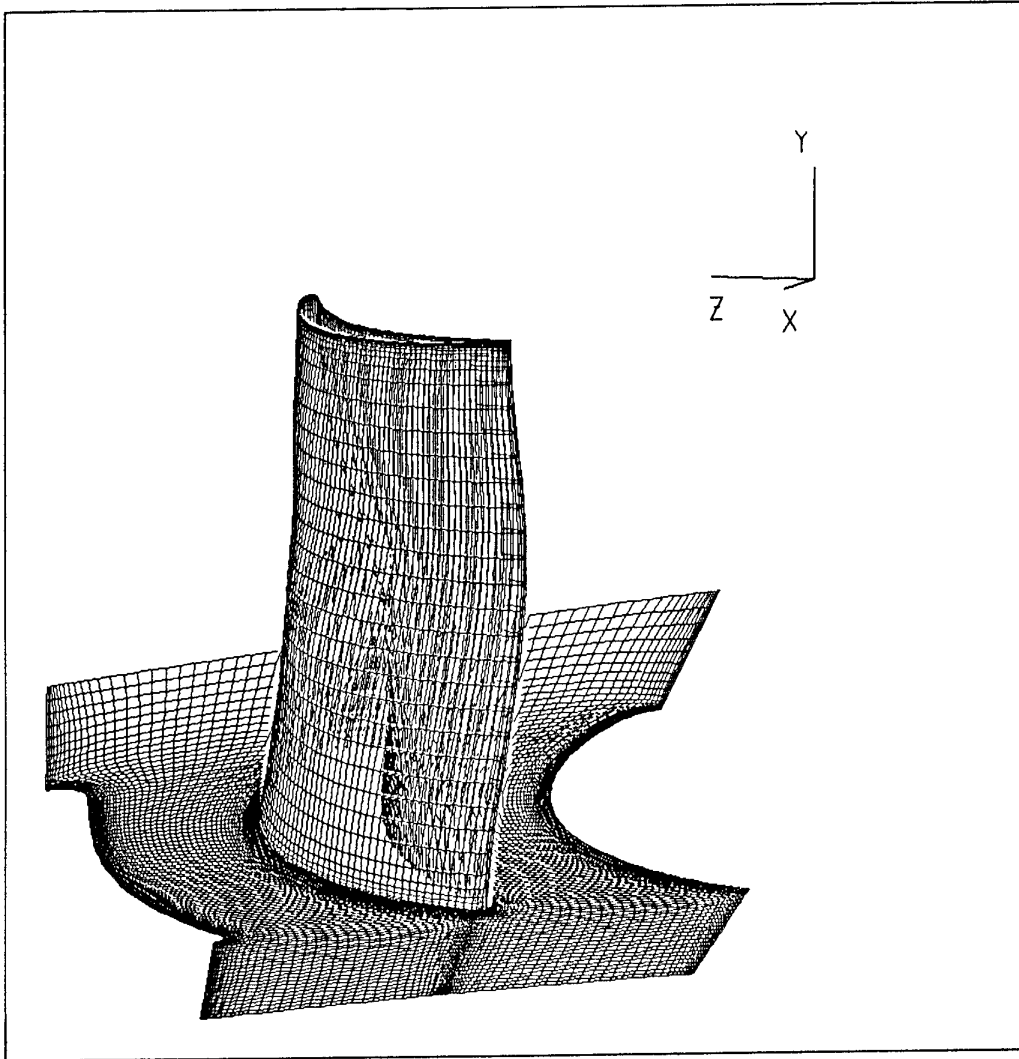


Fig. 3 3D view of O-H grid system for rotor blade .

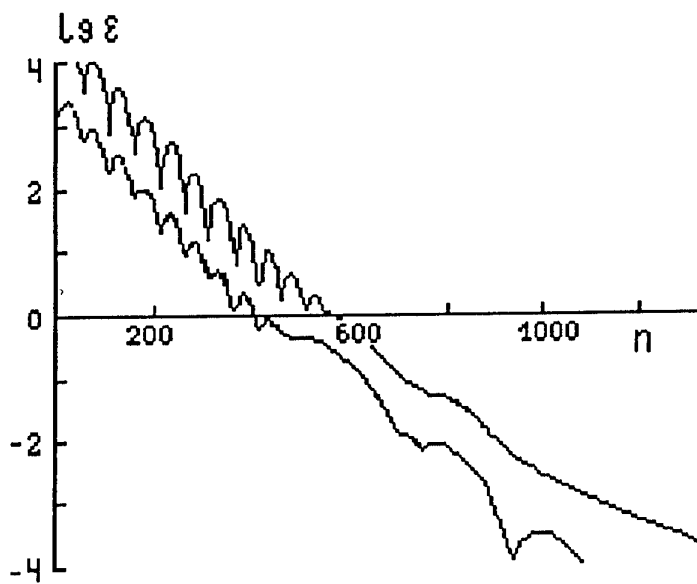


Fig. 4 Convergence for 2D viscous cascade flow calculations .

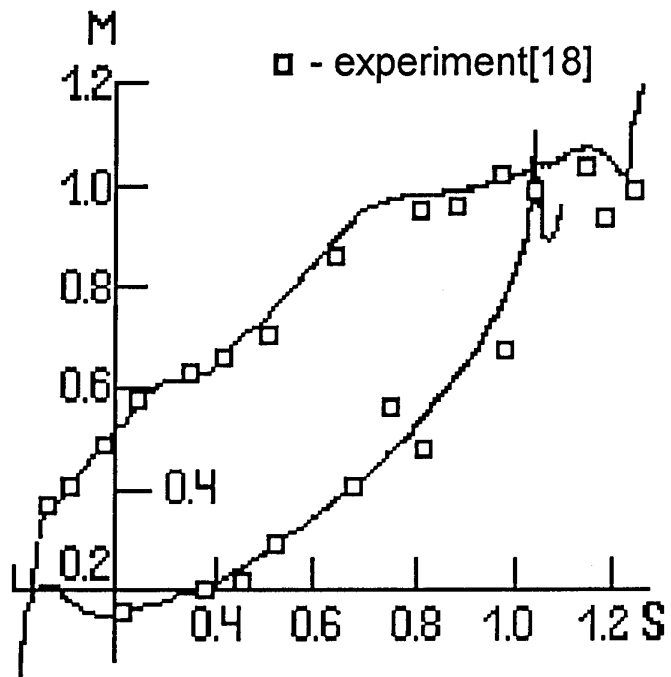


Fig. 5 Isentropic Mach distribution

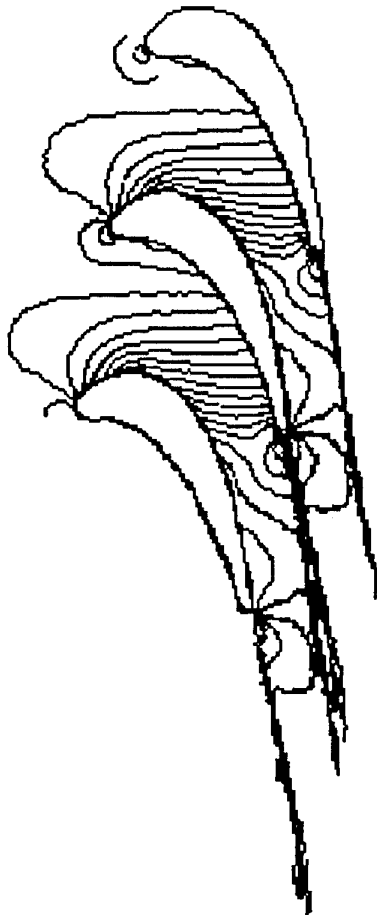


Fig. 6 Mach number contours

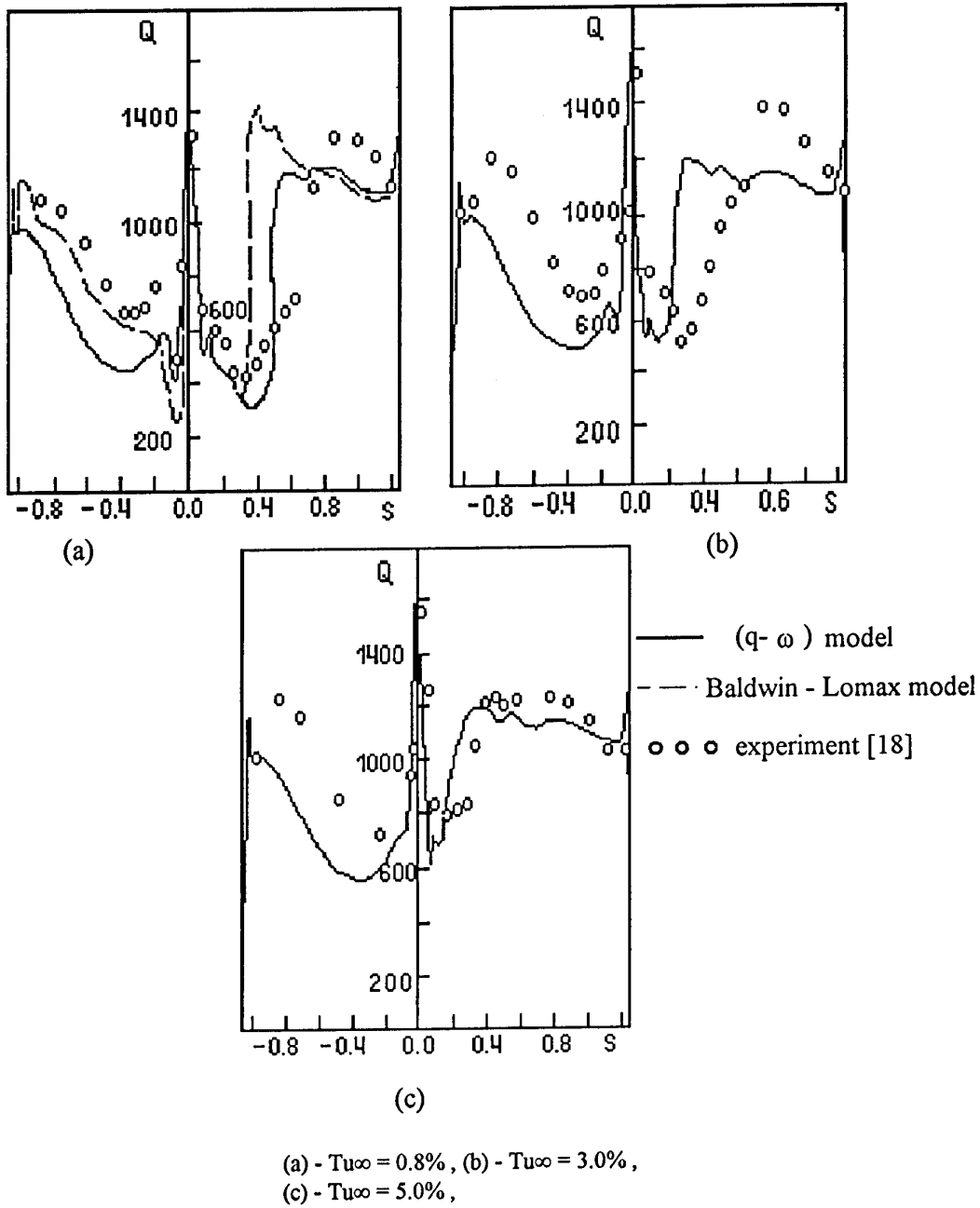


Fig. 7 Heat transfer coefficient .

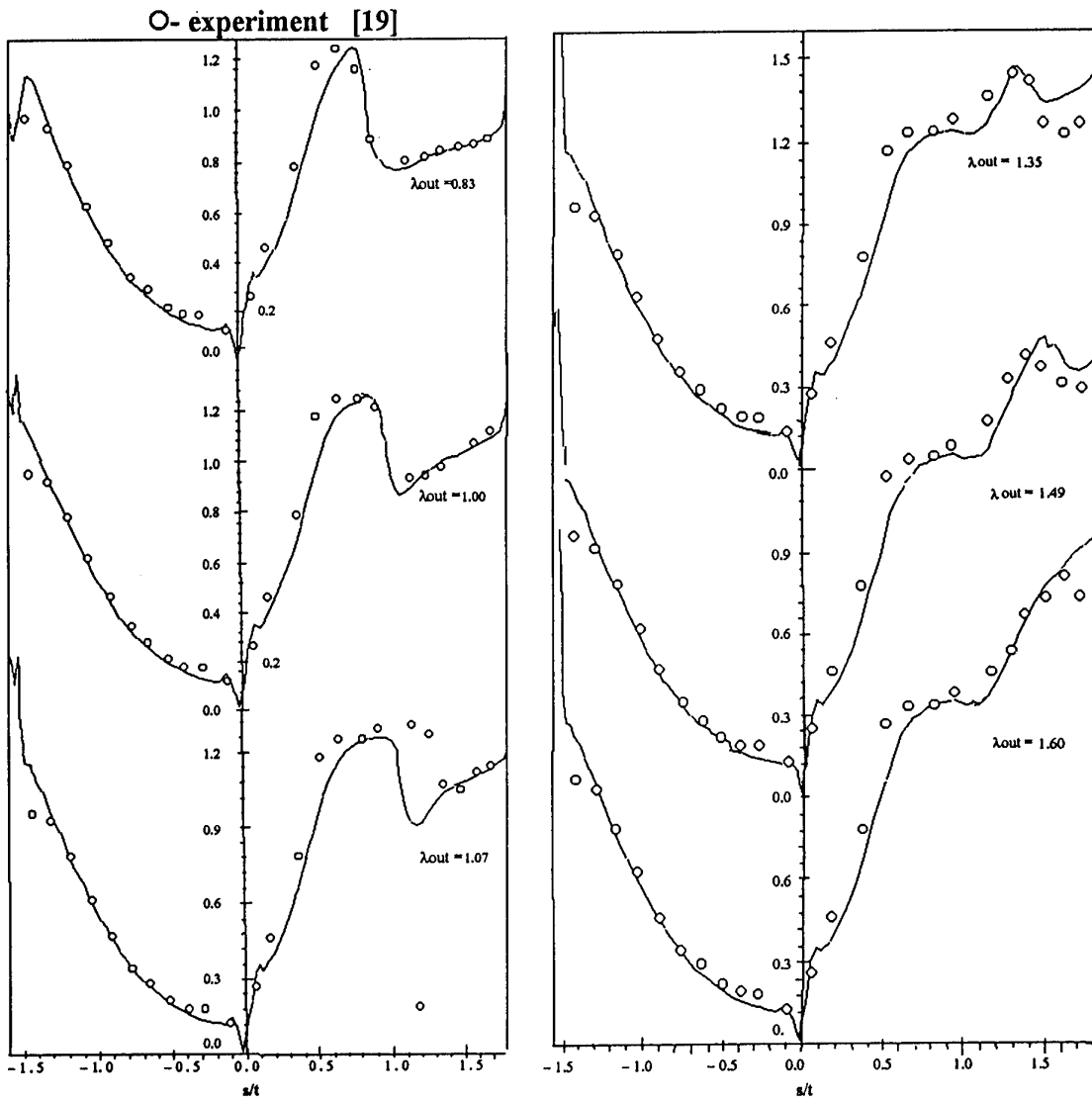


Fig. 8 Isentropic λ - number distribution for the BL 40 cascade .

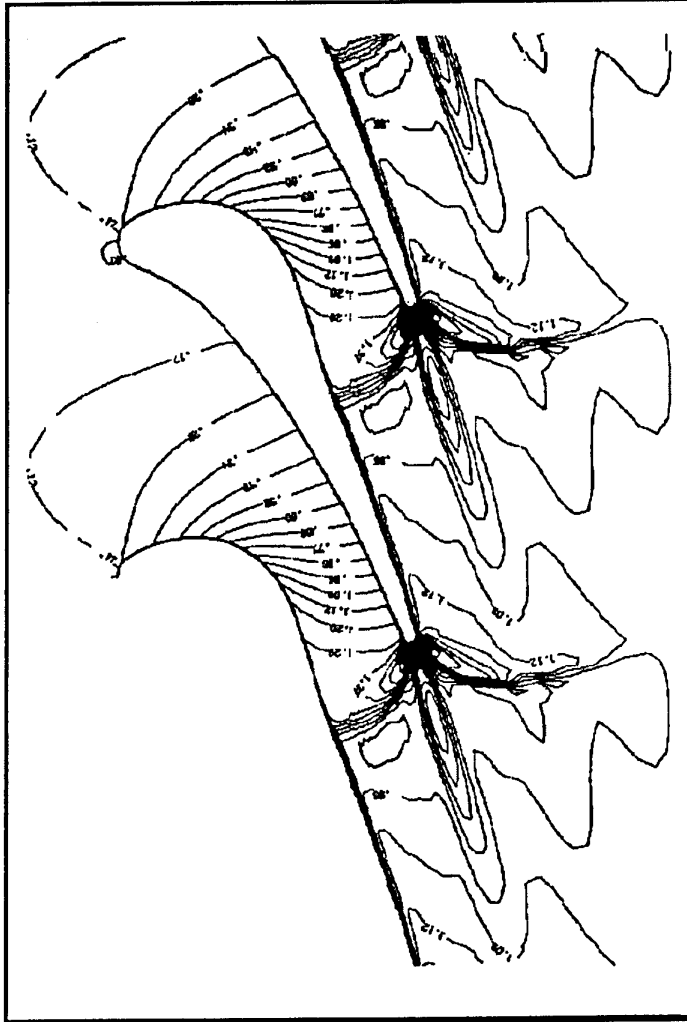


Fig. 9 Mach number contours for the BL 40 cascade ,
 $\lambda_{out} = 1.07$.

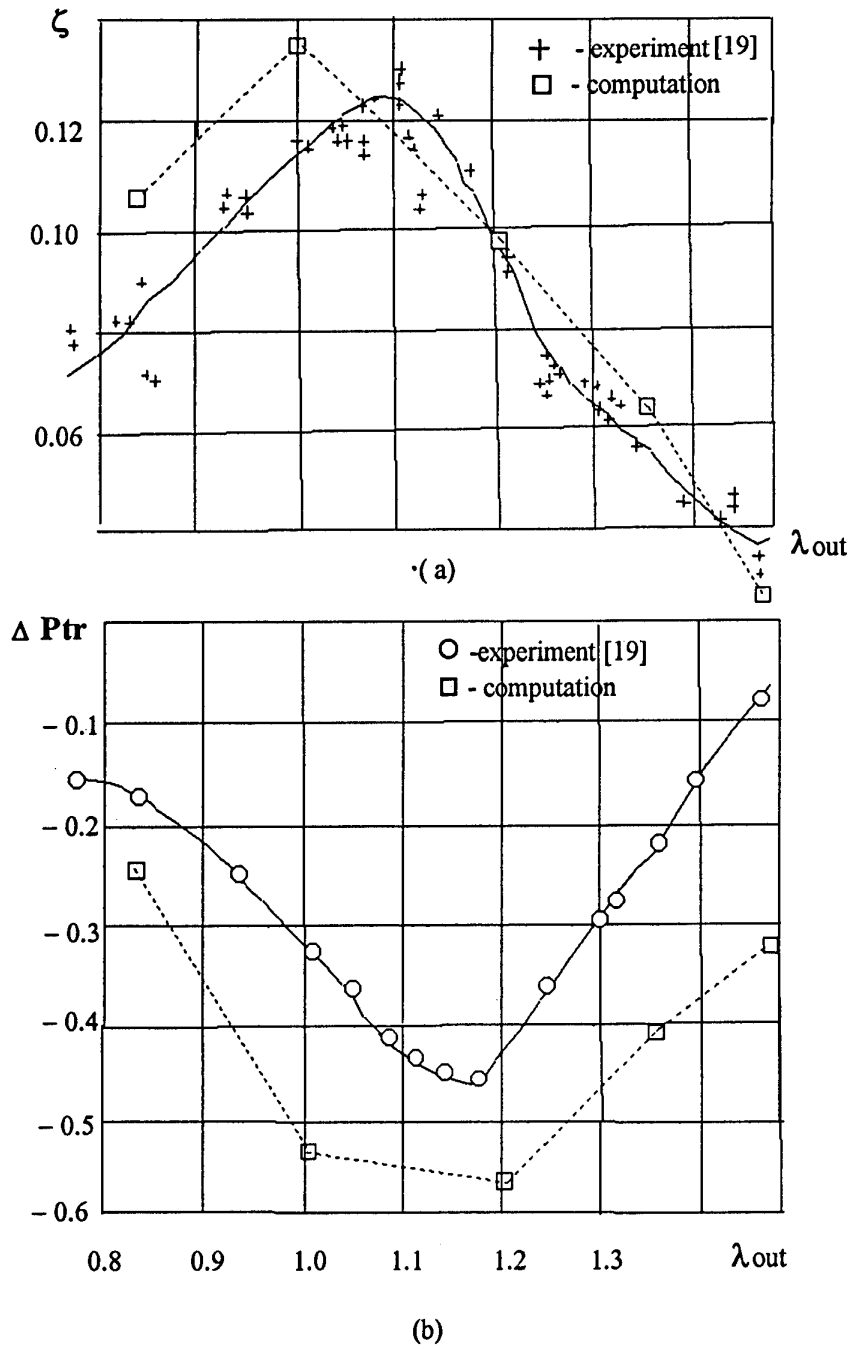
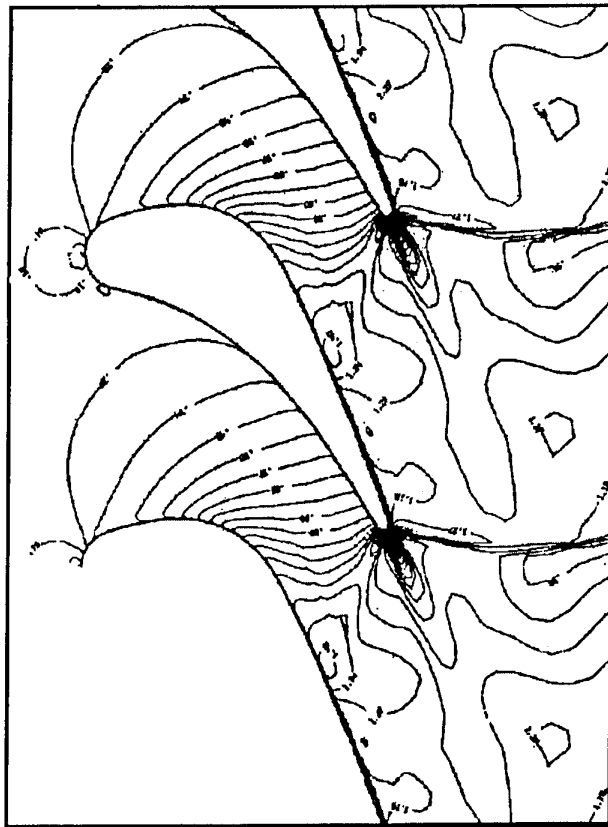
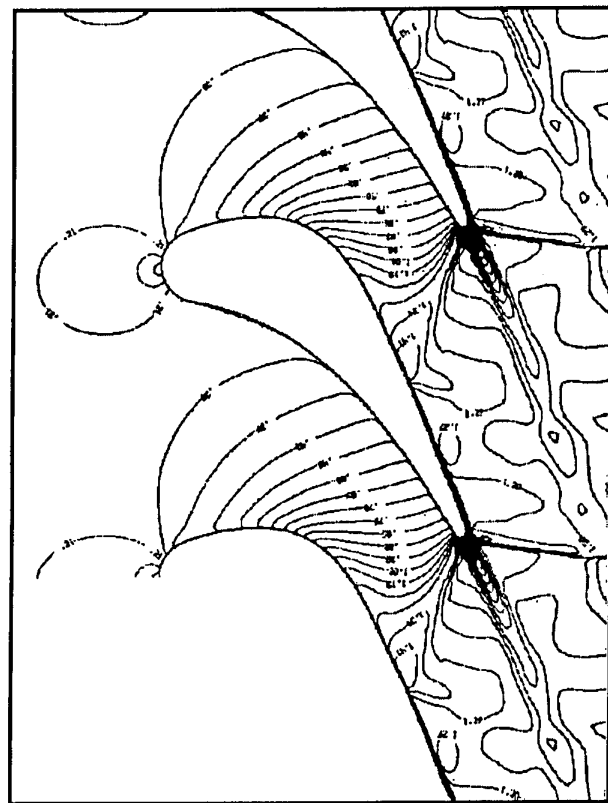


Fig. 10 Total pressure loss coefficient (a) and base pressure coefficient (b) vs exit λ_{out} .



(a) 6800 grid points



(b) 27200 grid points

Fig. 11 Mach number contours for the BL 48 cascade, $X_{out} = 1.27$.

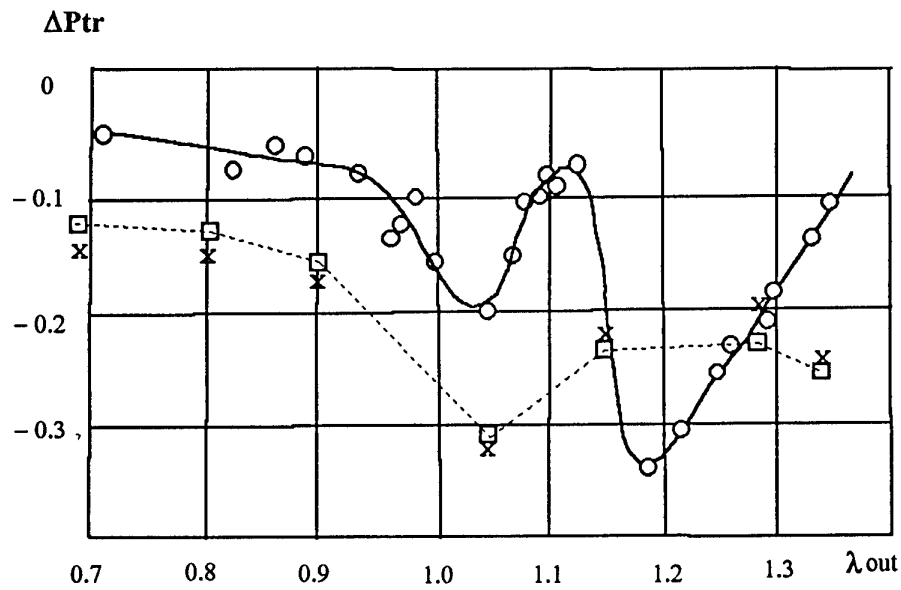
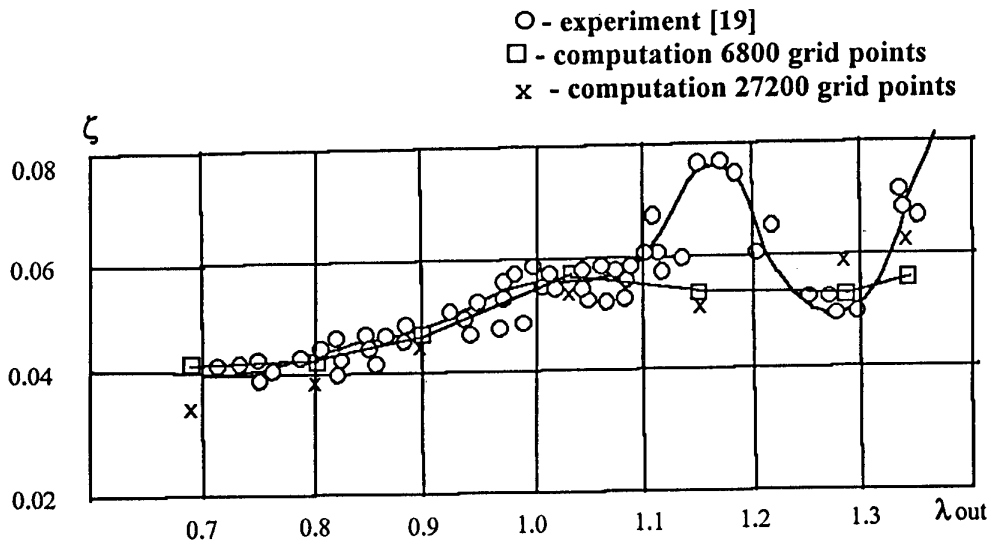
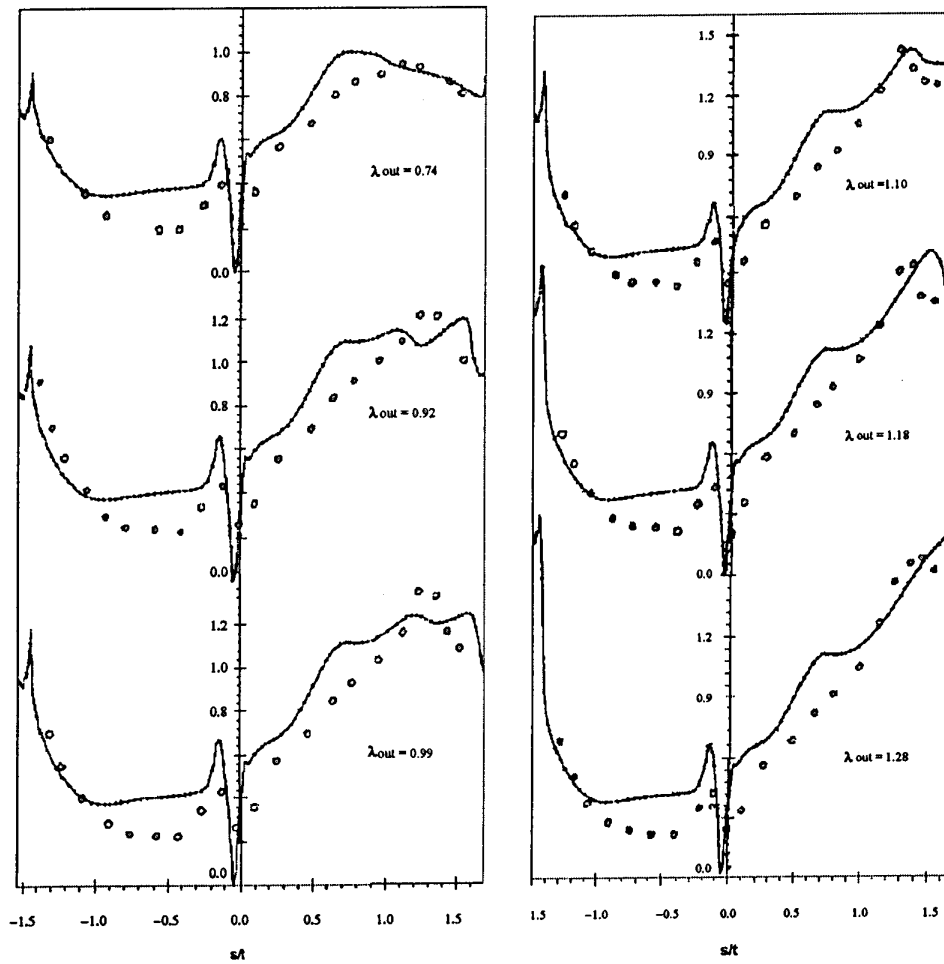


Fig. 12 Total pressure loss coefficient (a) and base pressure coefficient (b) for the BL48 cascade vs exit λ_{out} .

○ - experiment [19]

**Fig. 13** Isentropic λ - number distribution for the BL 166 cascade .

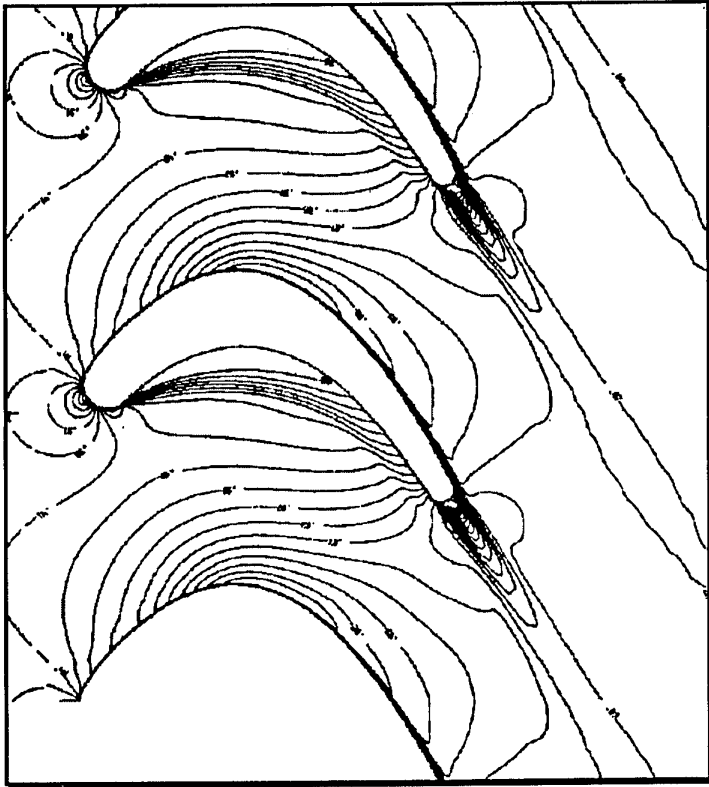


Fig. 14 a $\lambda_{out} = 0.74$

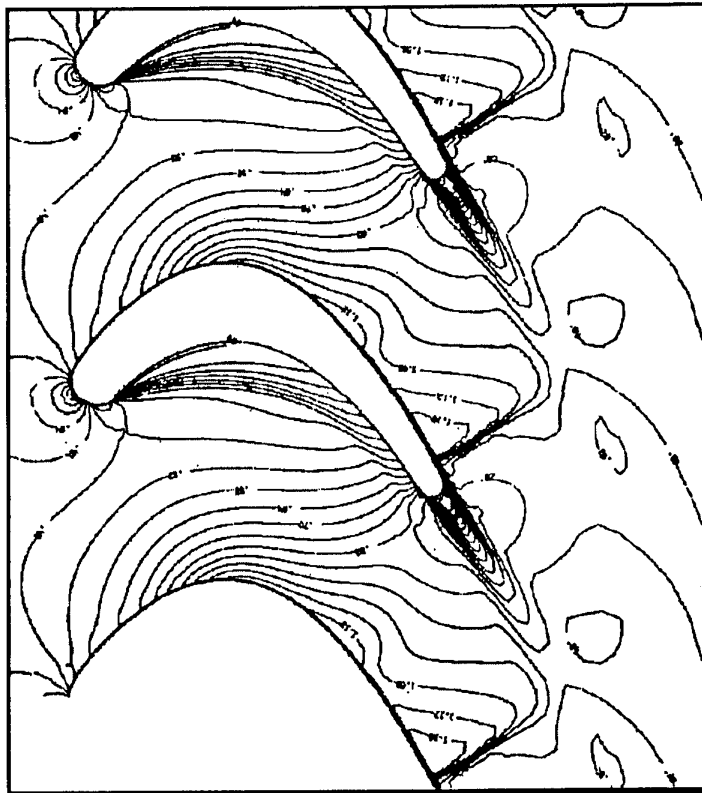


Fig. 14 b $\lambda_{out} = 0.92$

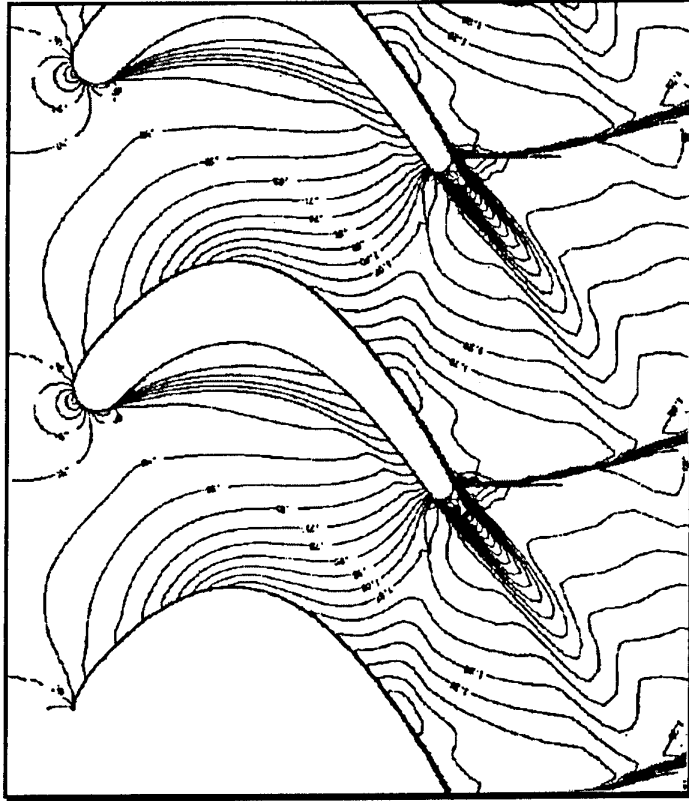


Fig. 14 c $\lambda_{out} = 1.1$

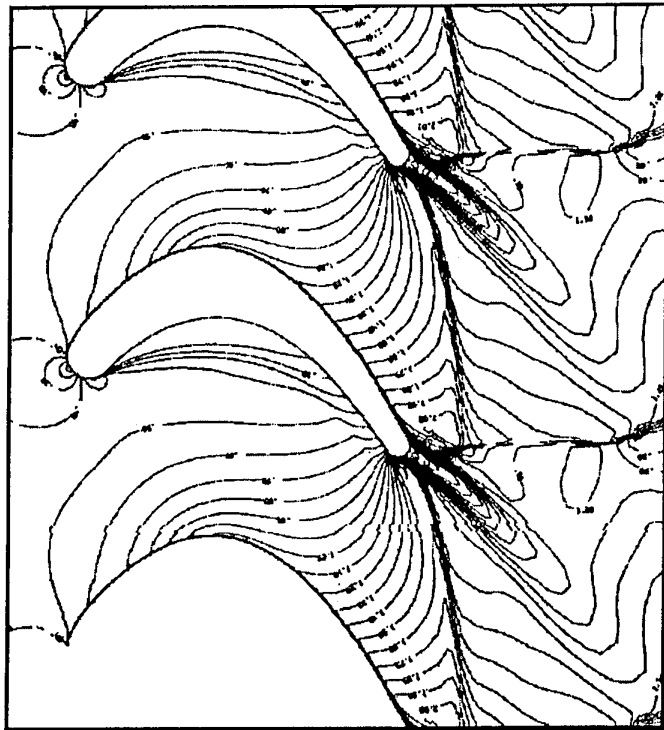


Fig. 14 d $\lambda_{out} = 1.23$

Fig. 14 Mach number contours for the BL 166 cascade

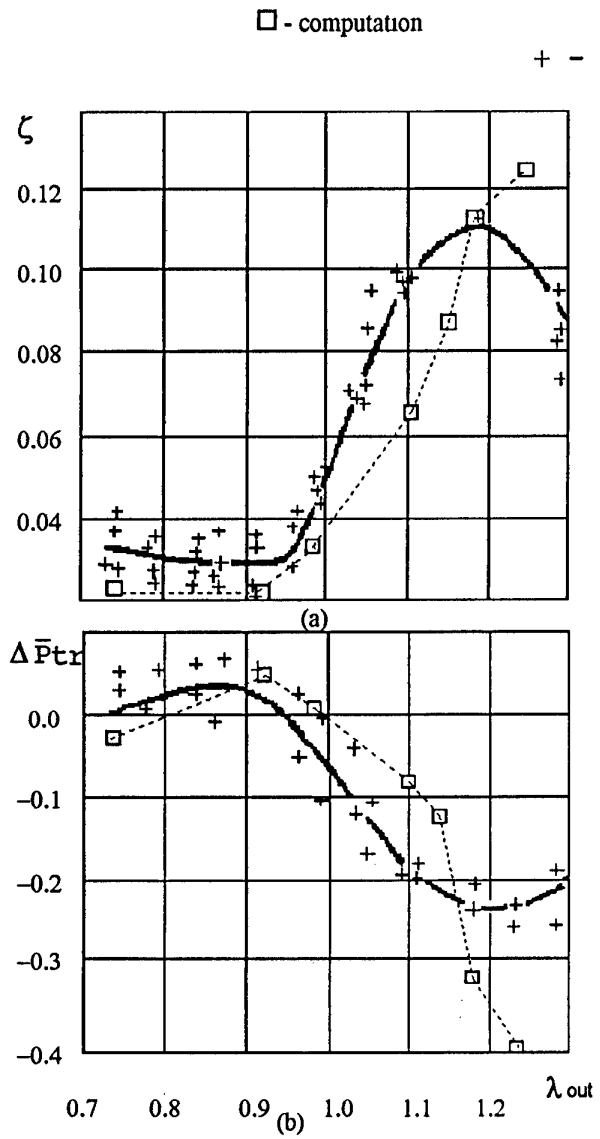


Fig. 15 Total pressure loss coefficient (a) and base pressure coefficient (b) for the BL 166 cascade vs exit λ_{out} .

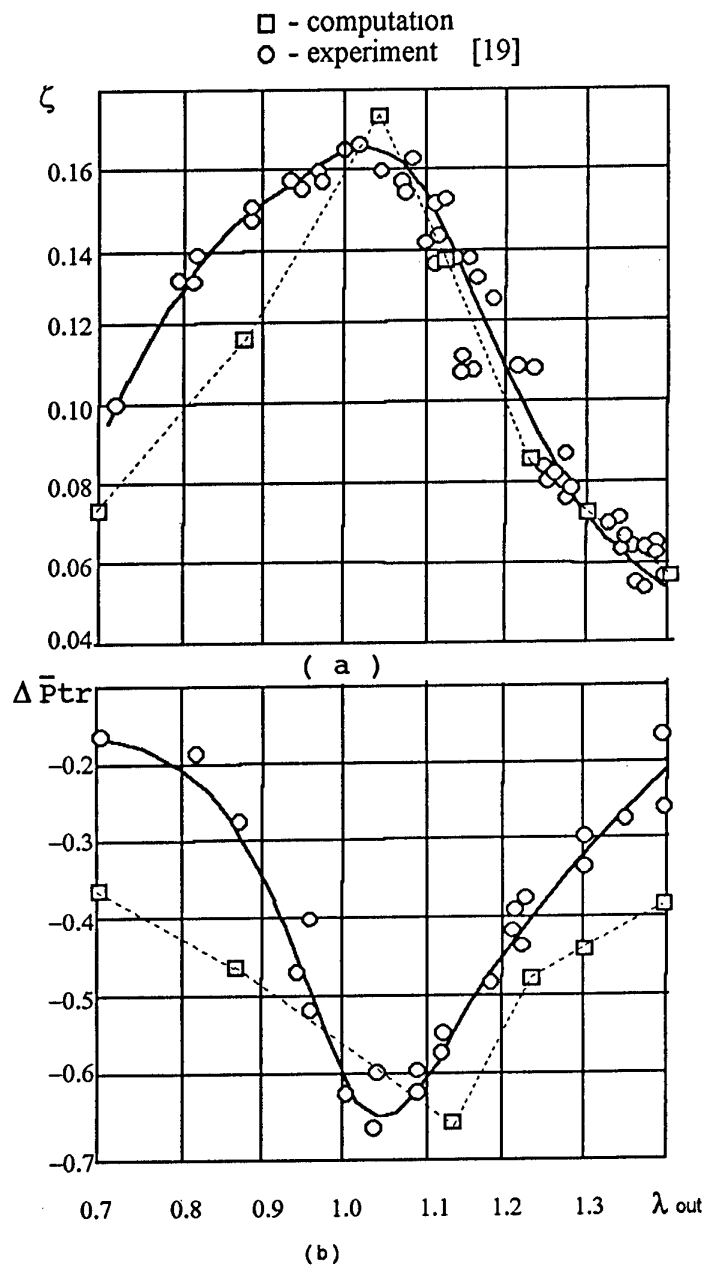


Fig. 16 Total pressure loss coefficient (a) and base pressure coefficient (b) for the BL 53 cascade vs exit λ_{out} .

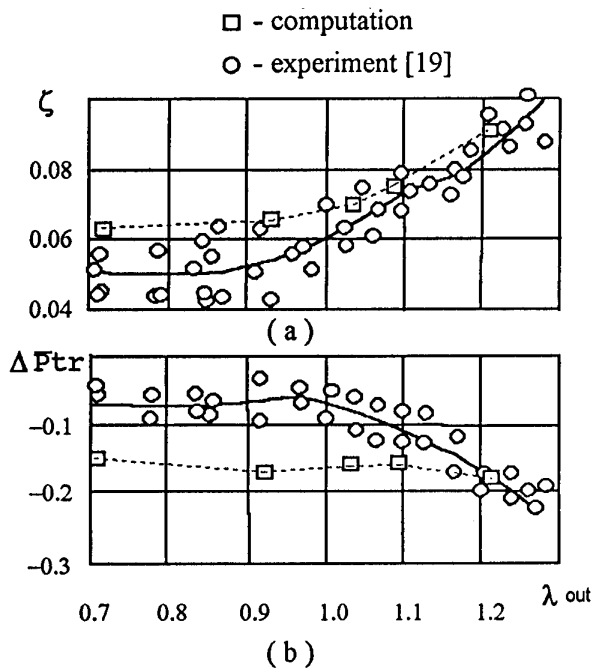


Fig. 17 Total pressure loss coefficient (a) and base pressure coefficient (b) for the BL 108 cascade vs exit λ_{out} .

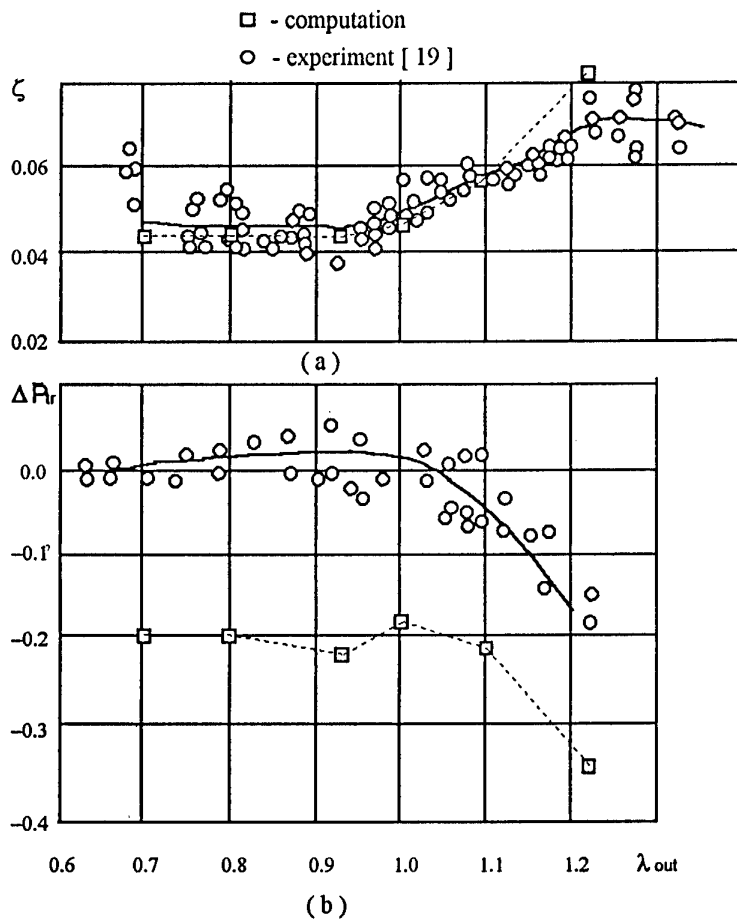


Fig. 18 Total pressure loss coefficient (a) and base pressure coefficient (b) for the BL 157 cascade vs exit λ_{out} .

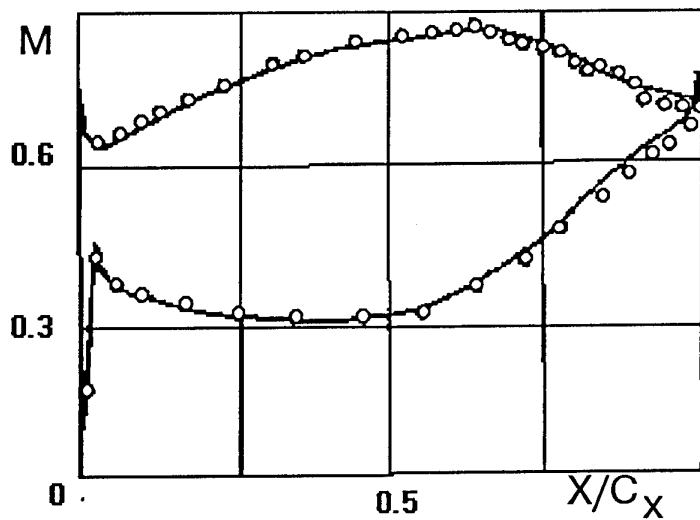
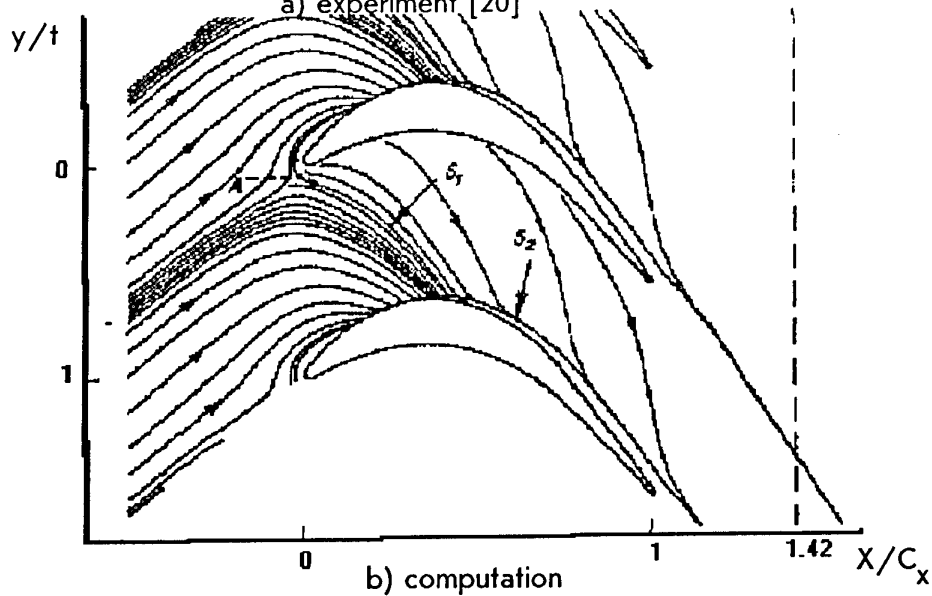


Fig. 19 Midspan isentropic Mach number distribution
 ○ - experiment [20]

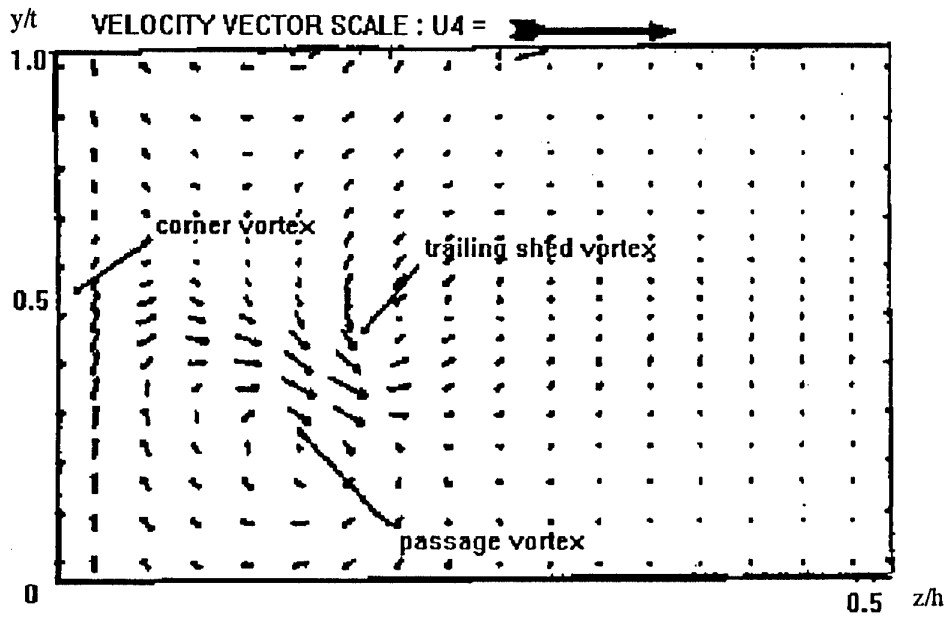


a) experiment [20]

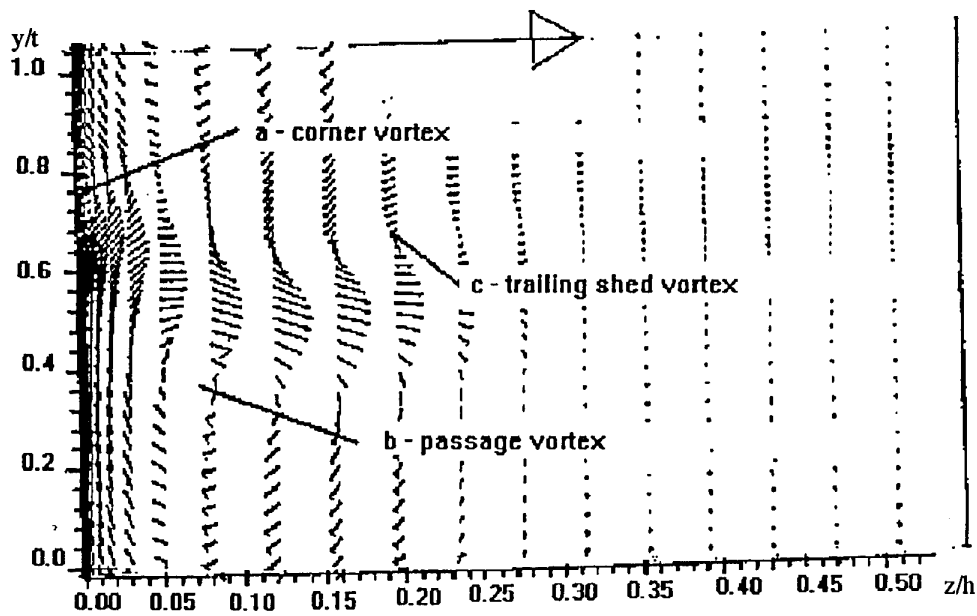


b) computation

Fig. 20 Limiting streamlines on the endwall



a) experiment



b) computation

Fig. 21 Secondary velocity vectors at $1.42 C_x$

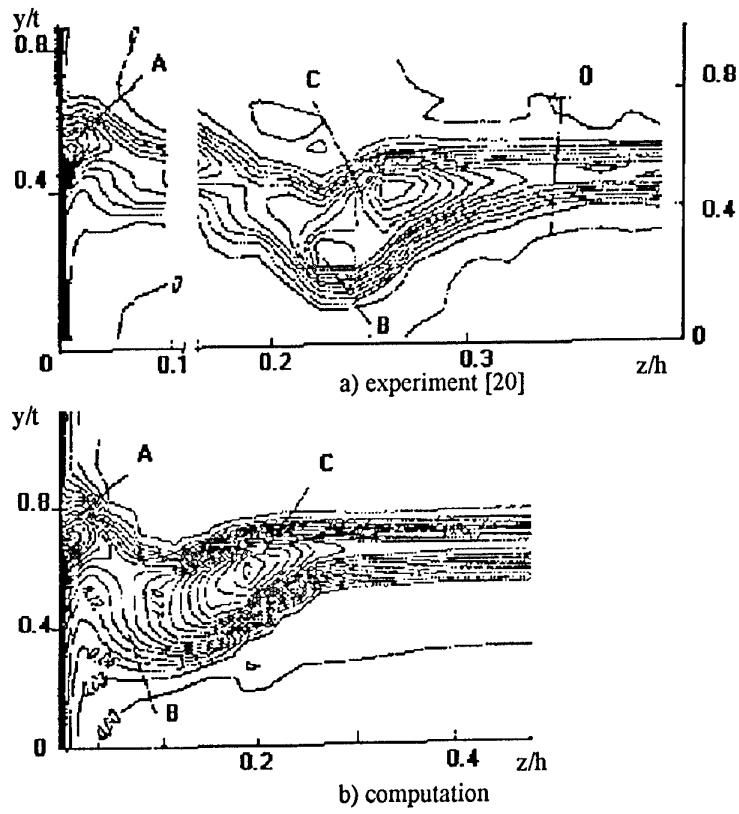


Fig. 22 Total pressure loss coefficient contours at $1.42 C_x$

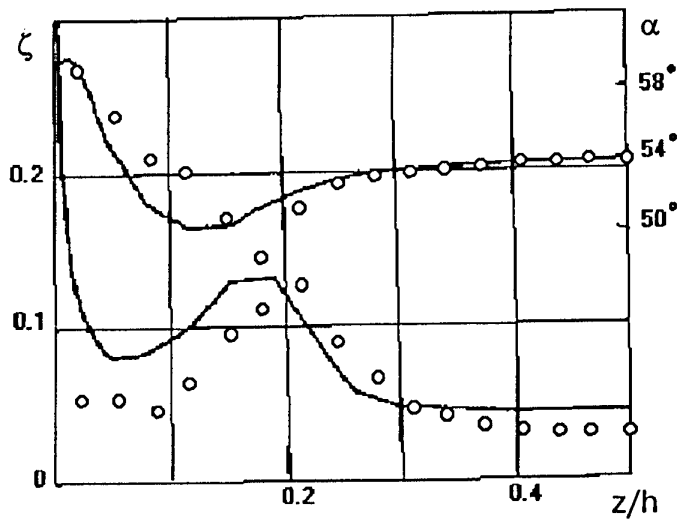
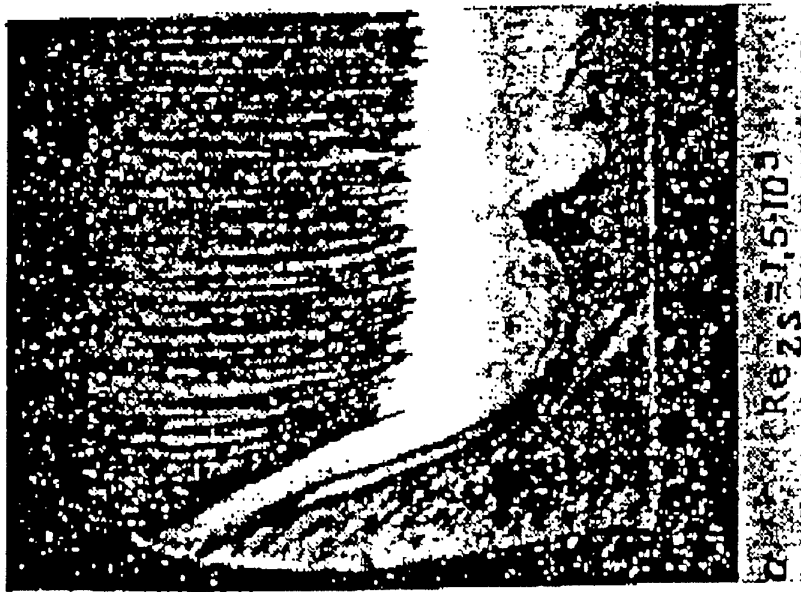
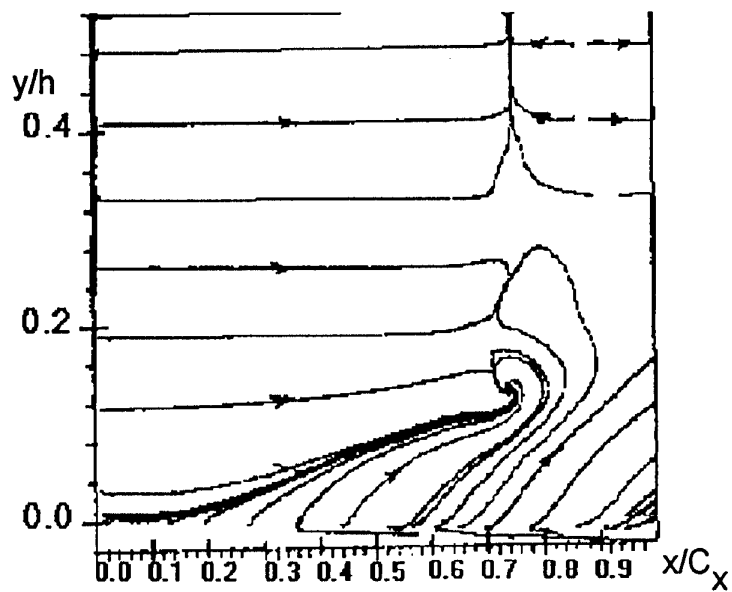


Fig. 23 Span wise variation of pressure loss and exit angle at $1.42 C_x$
 O - experiment [20]

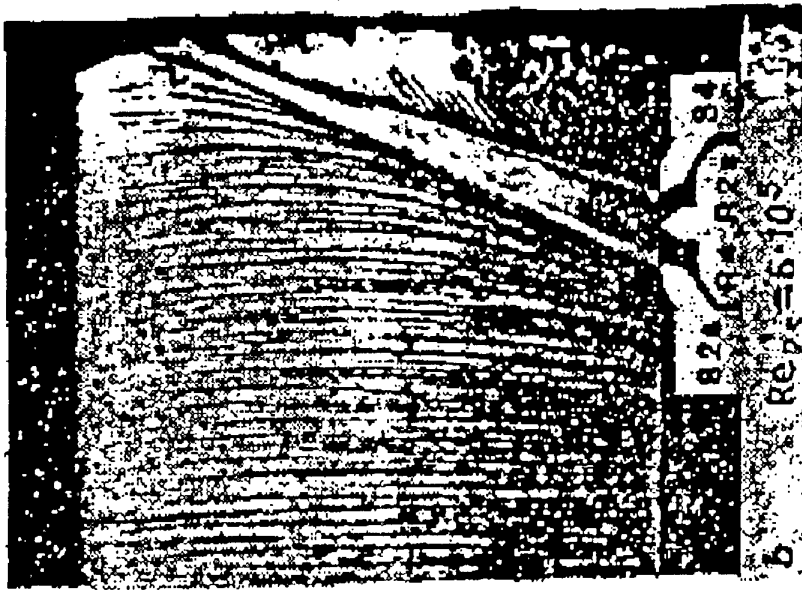


a) experiment [21]

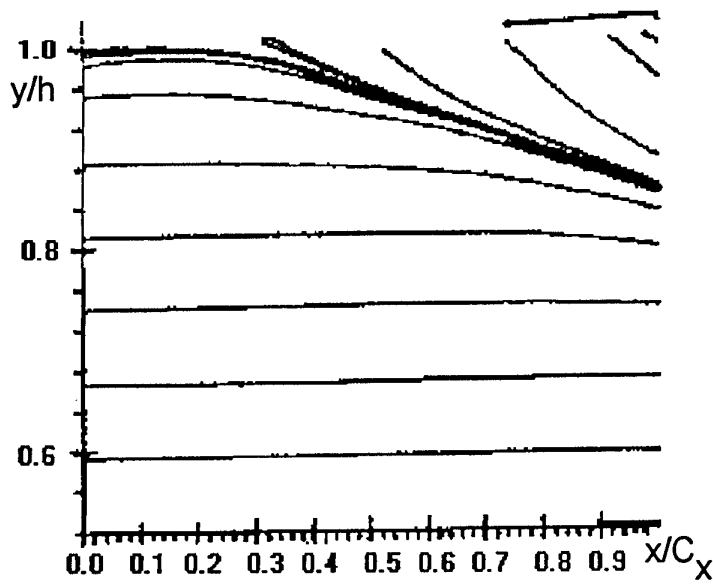


b) computation

Fig. 24a Limiting streamlines on the suction side, $Re=1.5 \cdot 10^5$



a) experiment



b) computation

Fig. 24b Limiting streamlines on the suction side, $Re=6 \cdot 10^5$

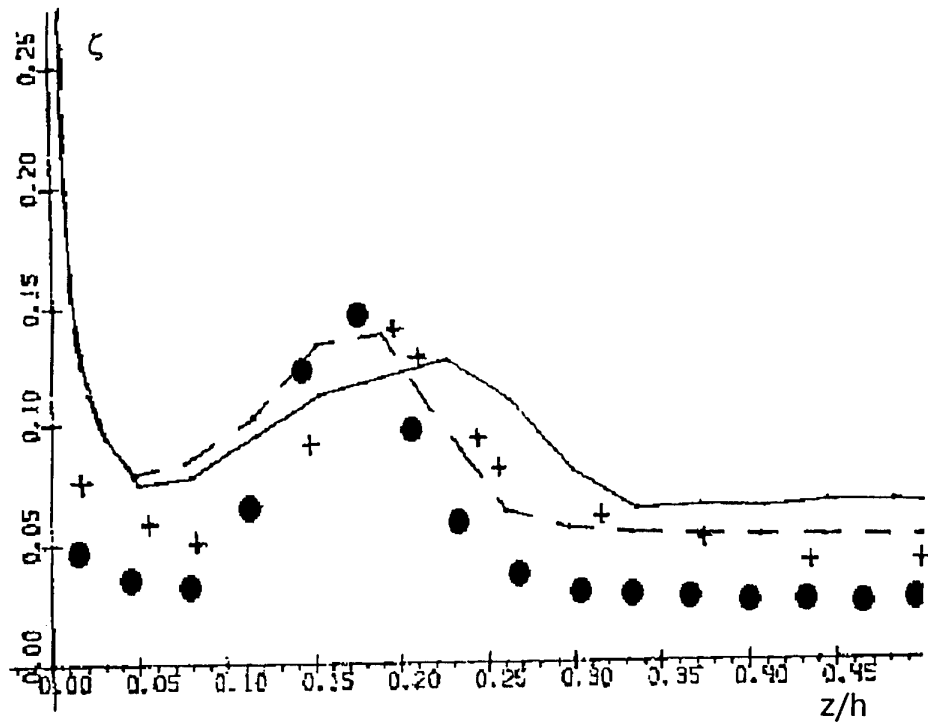


Fig. 25 Spanwise variation of total pressure loss coefficient
 + - $Re=1.5 \cdot 10^5$ experiment [21]
 O - $Re=6 \cdot 10^5$ experiment [21]
 — — — - $Re=1.5 \cdot 10^5$ computation
 - - - - - $Re=6 \cdot 10^5$ computation

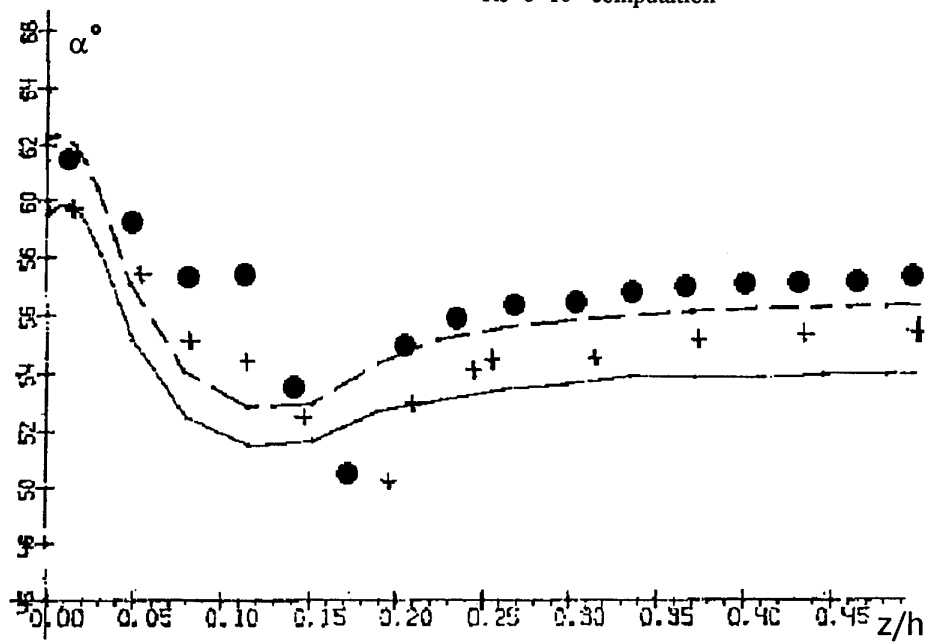


Fig. 26 Spanwise variation of exit flow angle

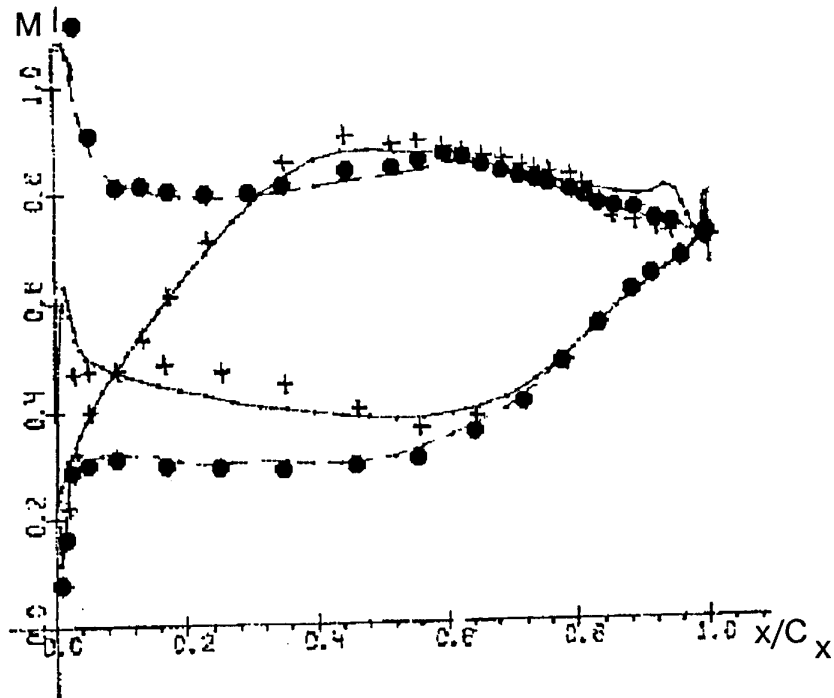


Fig. 27 Midspan Mach number distribution
 + $\alpha = -20.3^\circ$ experiment [21]
 O $\alpha = +8.6^\circ$ experiment [21]
 — $\alpha = -20.3^\circ$ computation
 - - - $\alpha = +8.6^\circ$ computation

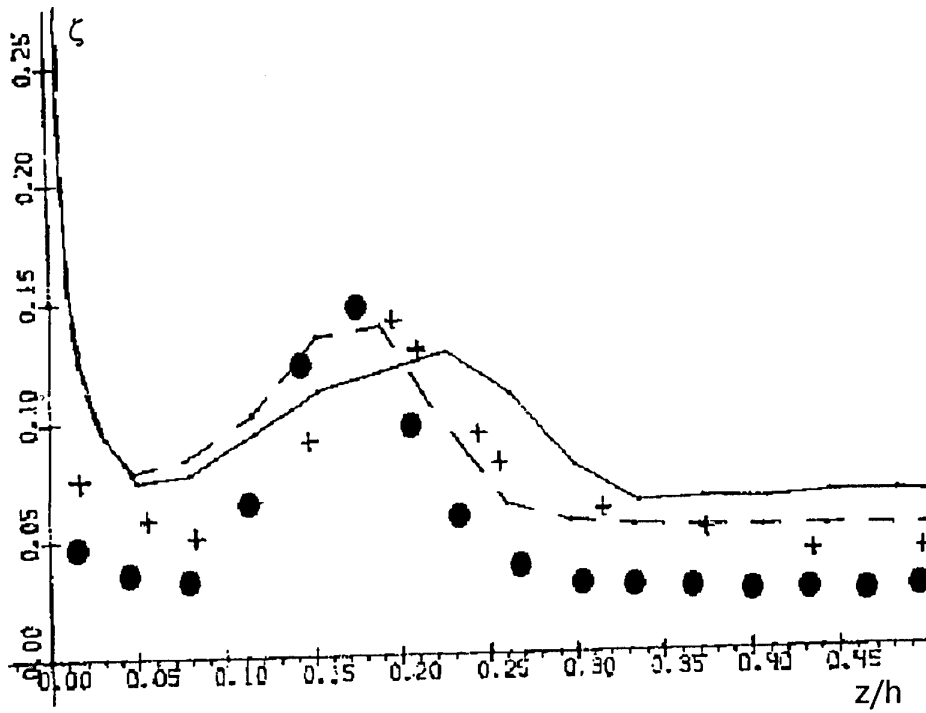


Fig. 28 Spanwise variation of total pressure loss coefficient

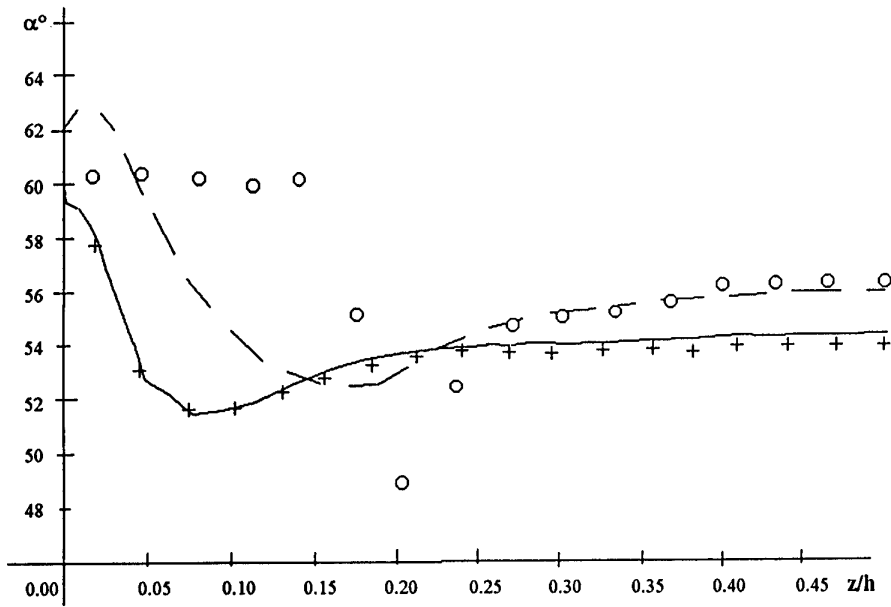


Fig. 29 Spanwise variation of exit flow angle

+	- $\alpha = -20.3^\circ$ experiment [21]
O	- $\alpha = +8.6^\circ$ experiment [21]
—	- $\alpha = -20.3^\circ$ computation
- - -	- $\alpha = +8.6^\circ$ computation

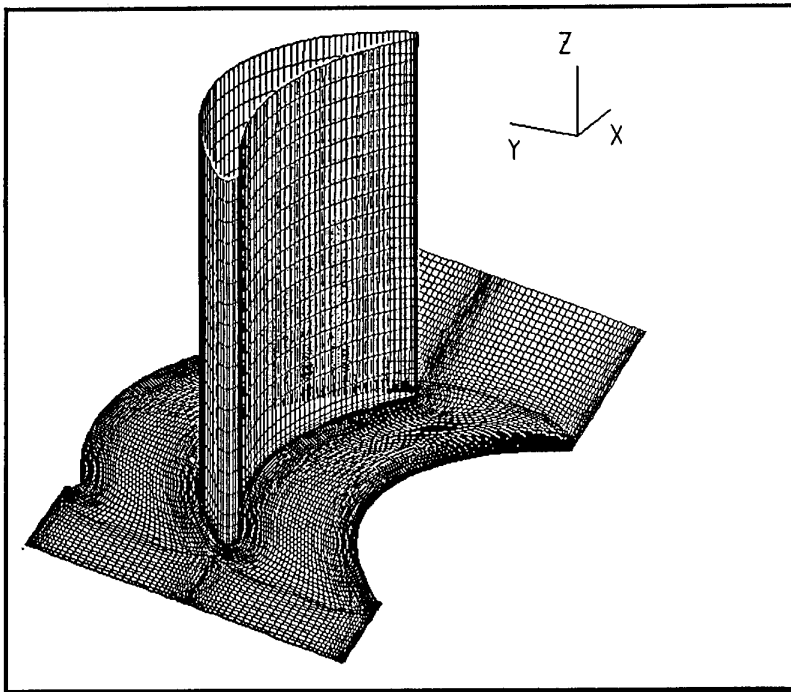
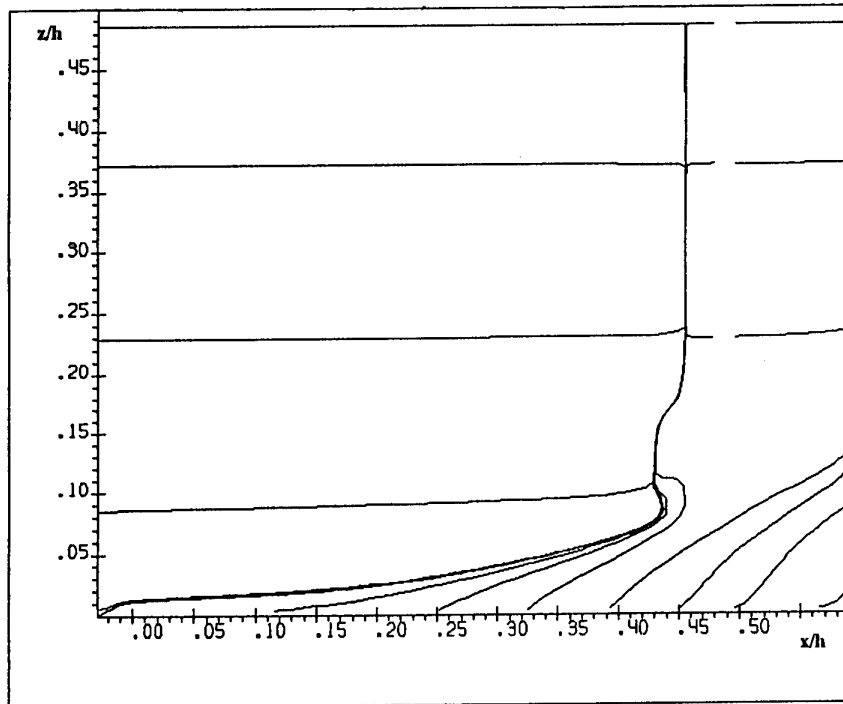
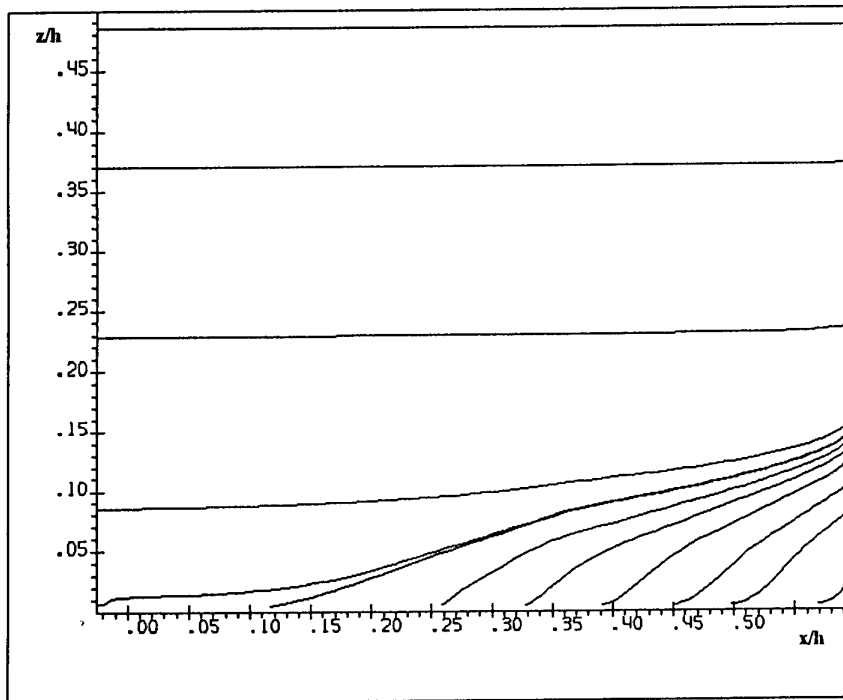


Fig. 30 3D view of 217600 O-H grid system for linear turbine cascade .



a)



b)

Fig. 31 Limiting stream lines on the suction side of the original (a) and modified (b) blade .

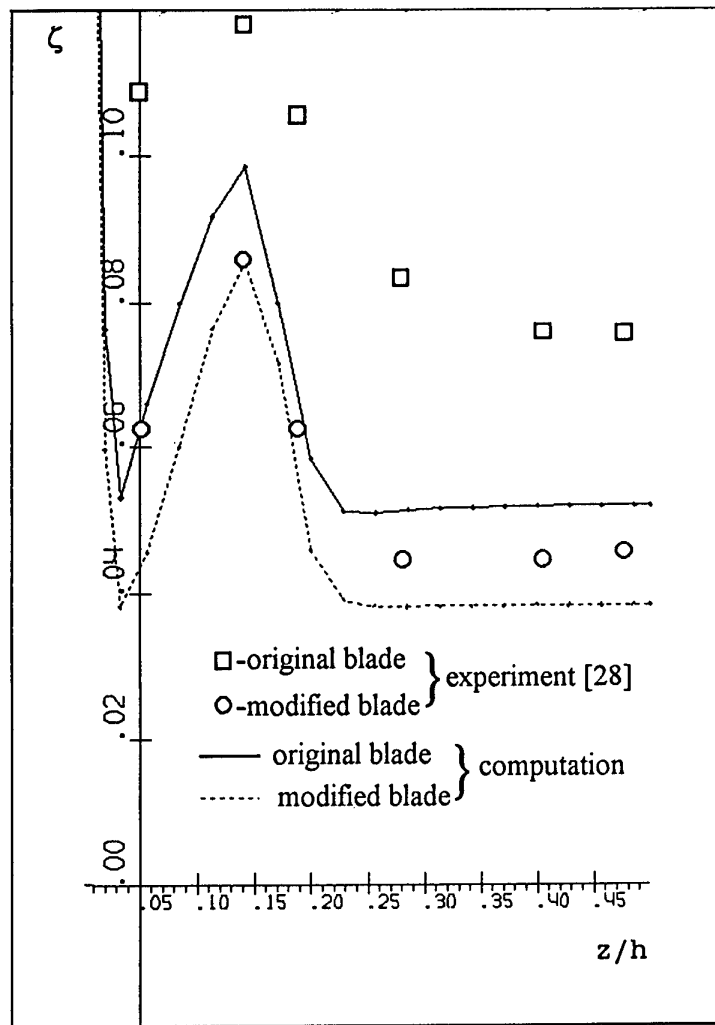
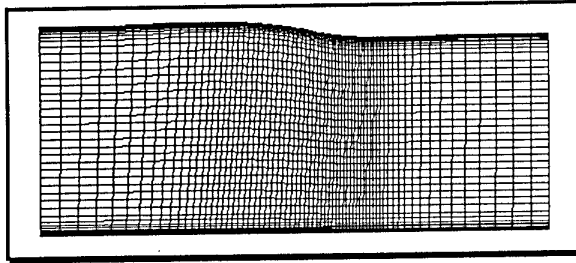
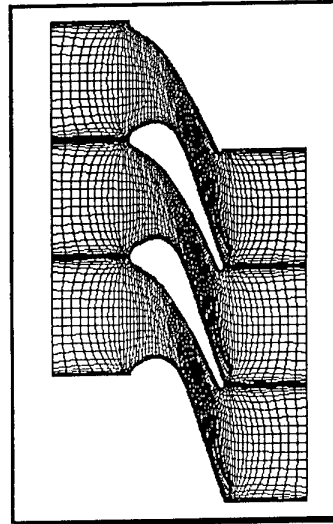


Fig. 32 Spanwise total pressure loss distribution for linear turbine cascade .



72x66 H-grid on a meridional plane .



3800 O-H grid on a blade to blade plane .

Fig. 33 Computational grid for the CA-2 vane .

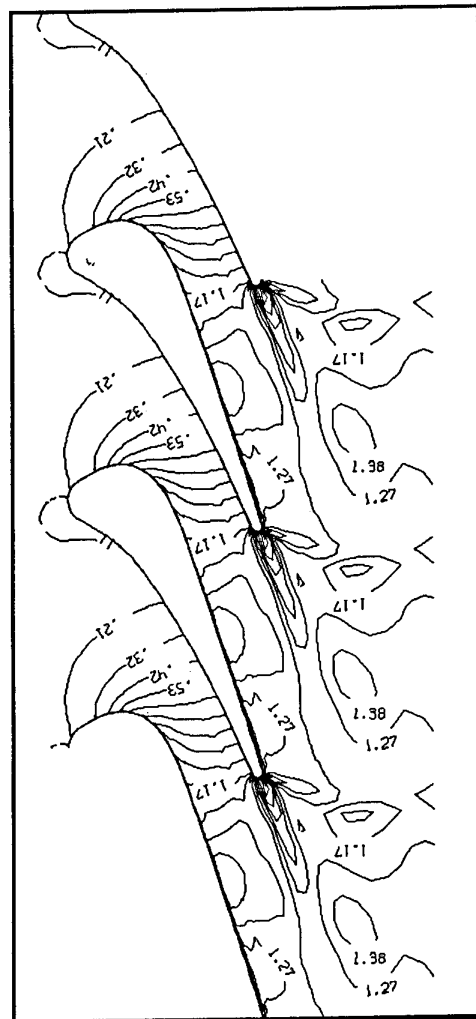
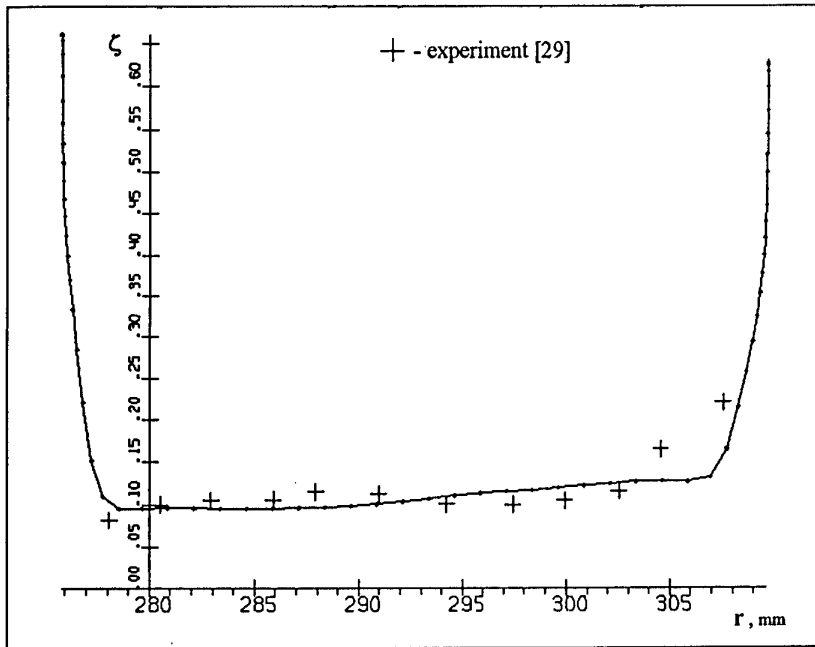
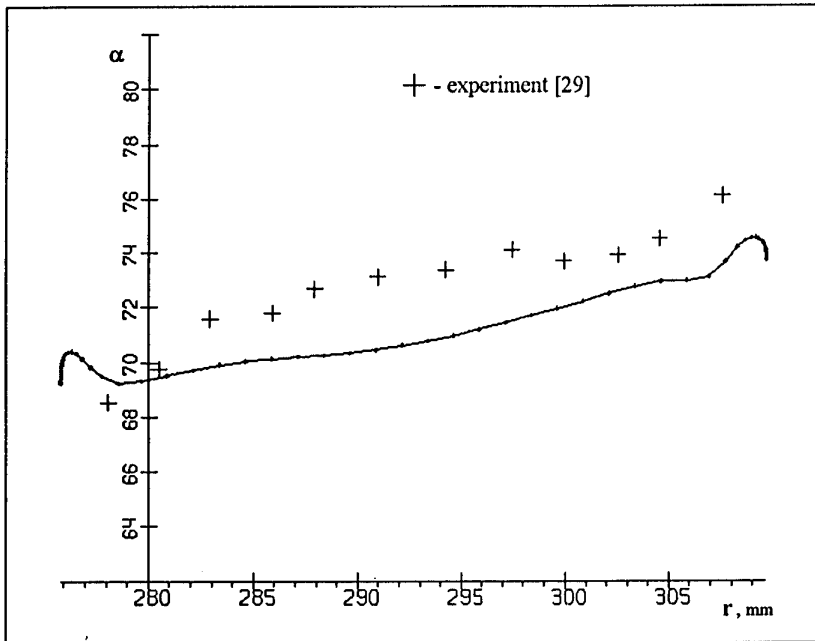


Fig. 34 Mach number contours at midspan for the CA-2 vane .



(a)



(b)

Fig. 35 Spanwise total pressure loss (a) and exit angle (b) for the CA-2 vane.

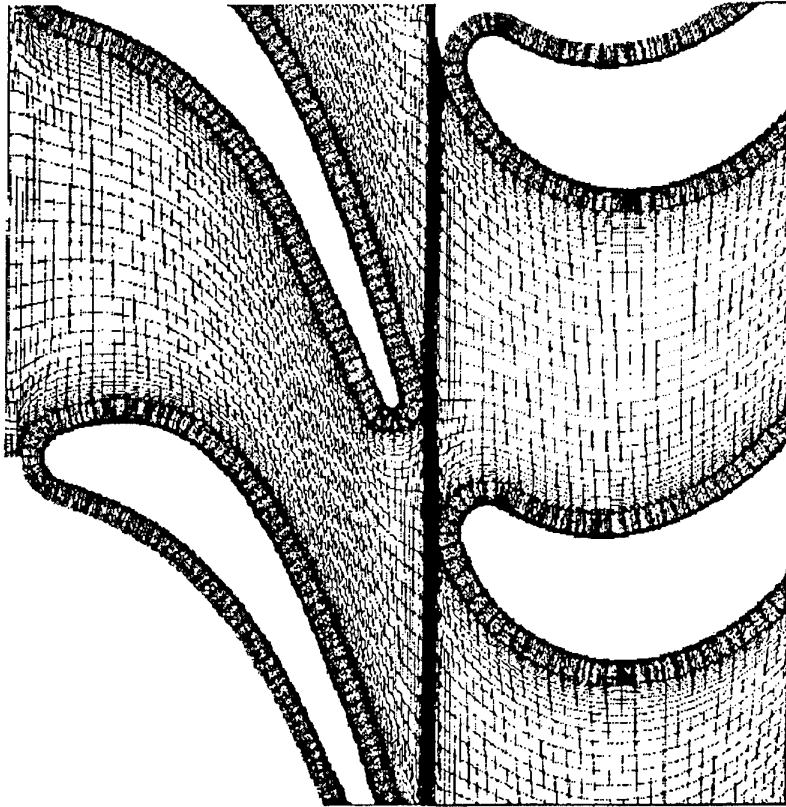


Fig. 36 Computational grid for 2D rotor-stator interaction

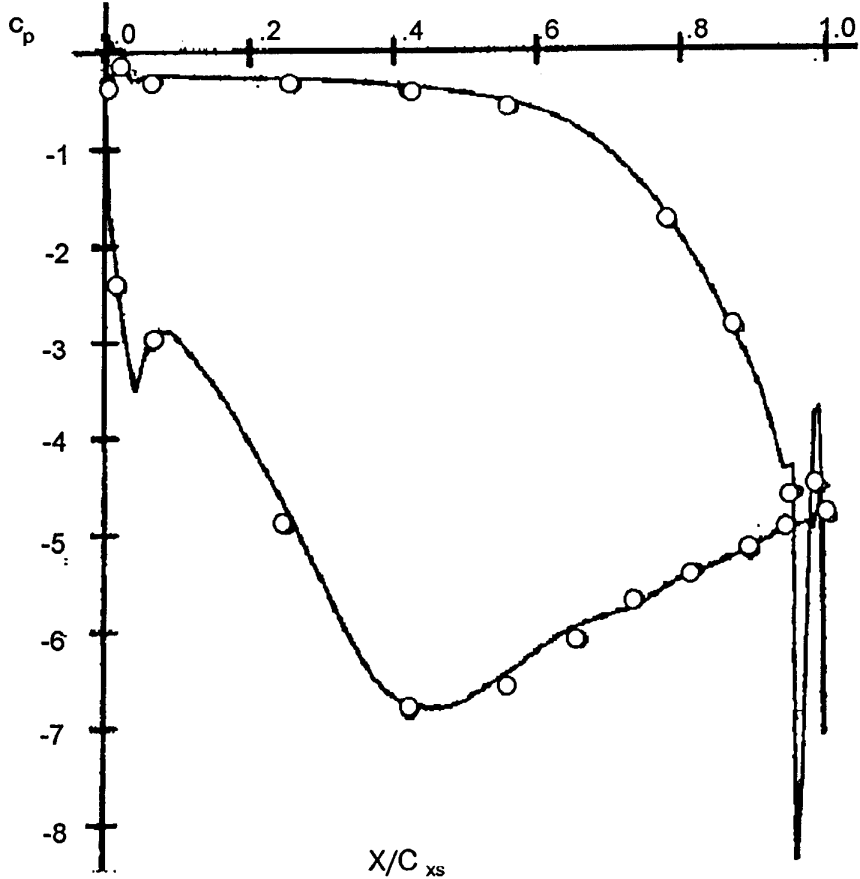


Fig. 37 The averaged stator surface pressure distribution
 O - experiment [22]

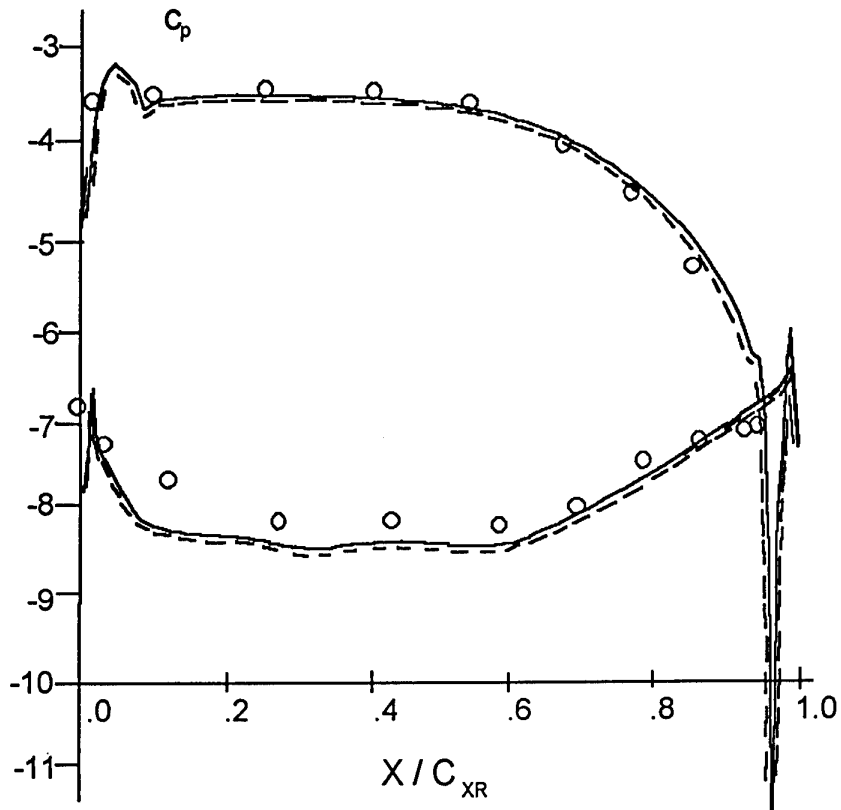


Fig. 38 The time-averaged rotor surface pressure distribution
○ - experiment [22]
— - 3-rd order accurate scheme
- - - 1-st order accurate scheme

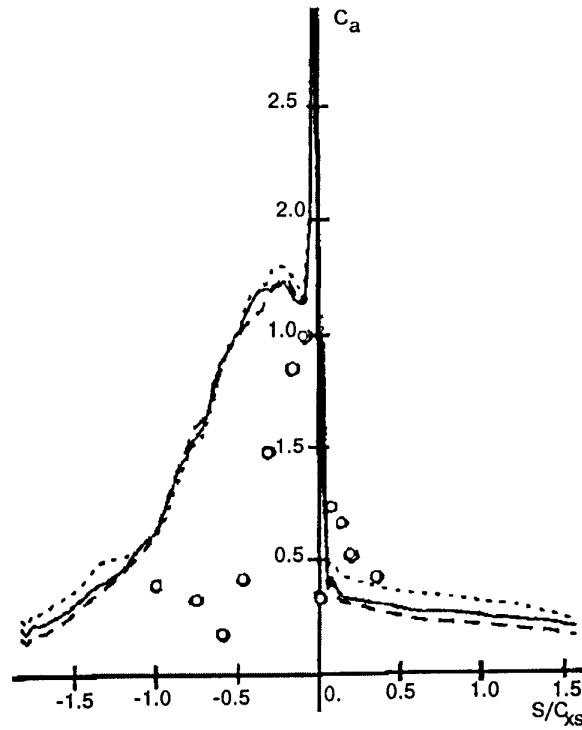


Fig. 39 Pressure amplitude coefficient distribution for stator

- - experiment [22]
- — — - 1-st order accurate scheme
- · · · - 2-nd order accurate scheme
- — — - 3-rd order accurate scheme

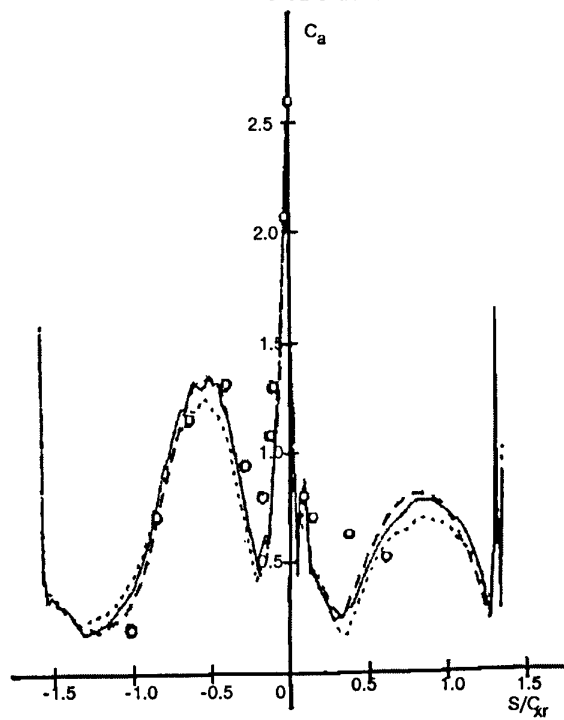


Fig. 40 Pressure amplitude coefficient distribution for rotor

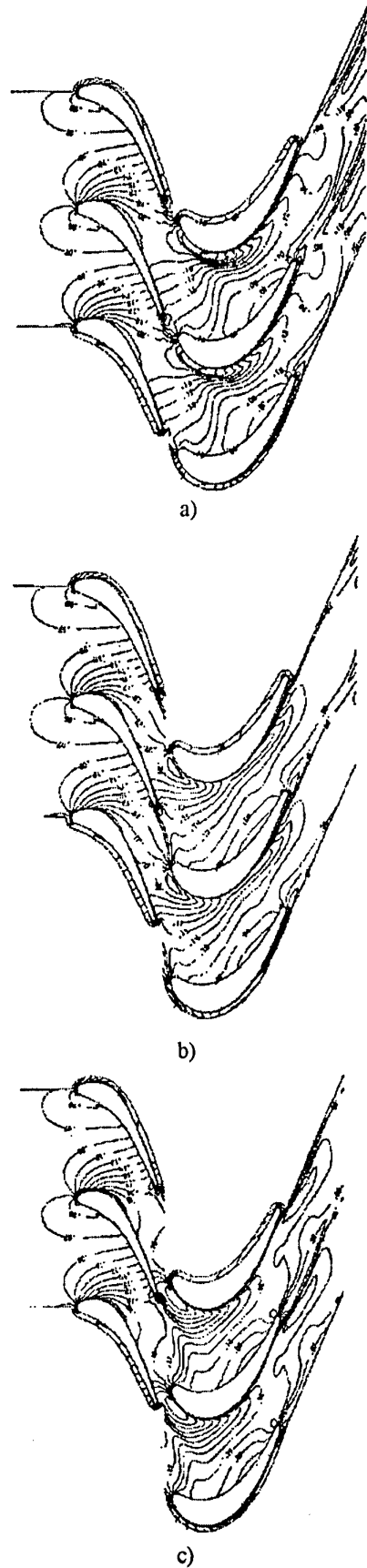


Fig. 41 Instantaneous Mach number contours at $t=0.23T$ (a), $t=0.567T$ (b), $t=0.9T$ (c)

Application of multidisciplinary models to the cooled turbine rotor design

by

Dr. V.K. Kostege, Prof. V.D.Venediktov, Dr. A.V. Granovskii
 CIAM (Central Institute of Aviation Motors)
 2, Aviamotornaya St.,
 Moscow, Russia, 111250

Abstract

A computer program for designing turbine vane and blade cooling systems is discussed. This program is based on the complex use of 2D and 3D gas dynamic, heat-transfer and thermostress models.

FEM Thermostress models are formatted based on geometry data from the computer design system. One-dimensional mass flow and conjugate thermal models are quickly created by using graphic dialogue regimes for different cooling systems. Quasi-3D and 3D thermostress models are used to carry out cooling system optimization or comparison of alternative cooling systems

Introduction

High temperature, spatial flow characteristics and film cooling systems, make for difficult problems for designing high work turbines. Design of vanes and blades is based on complex use of different models such as:

- inviscid, viscous and mixed 2D and 3D methods for calculation gasdynamic processes
- statistical (regression) method for calculation losses in turbine blades;
- methods of plane and spatial blade geometry generation;
- quasi-3D and 3D conjugate heat - transfer models;
- 2D and 3D stress-strain-state models

Designs are implemented in an iteration process using multiple simultaneous solutions of straight aerodynamic, heat transfer, and structural strength tasks.

Operation of a blade cascade under transonic conditions is characterized by a complex flow structure accompanied by local supersonic zones, inner and outer - edge shocks, and other phenomena. Designing a blade system of optimized construction (accounting for gas dynamics, strength, manufacturing technology, etc.) is a formidable, if not indeterminate, task. For this reason, when designing this equipment, which presently is mainly concerned with the geometry of the blade cascades and does not consider the specifics of actual operation, the blading may have a rather poor aerodynamic efficiency. Therefore, the shape of the blade passage must often be modified [1] when improving the turbine by increasing the aerodynamic efficiency of the blading.

The objective of existing methods for designing and optimizing compressor and turbine blade cascade is to provide separation and shock - free flow in the cascades. This is achieved by solving the inverse problem [2] and direct problems in the iterative process [3 - 6]. A certain preferred velocity distribution along the contour of the blade, ensuring minimum friction and wave losses, is the basis for calculations. Specifically, when designing supercritical blades for compressors [5], the convex surface of the blade is corrected at points where the maximum over expansion of the flow gives an intense shock wave capable of causing the separation of flow from interaction with the boundary layer.

Note that designing transonic blade cascades by solving the inverse problem has several disadvantages. The blade cascade obtained as a result of solving the inverse problem may fail to meet the requirements of blade cooling, structural strength of the blades, production techniques, etc.

A real modification of the blade cascade which meets these requirements may differ substantially from the optimal one. The numerous restrictions encountered by the designers necessitate that compromise solutions be taken. Therefore, it is best to carry out the design process in several stages, in which several direct and inverse problems are solved.

1. Linear blade cascade design

A multi-stage technique was recently developed at CIAM [7]. In the first stage, the optimum combination of free (variable) geometrical parameters of the cascade ensuring a low level of blade losses is selected, taking account of restrictions on the shape of the blades. This can be accomplished either based on design experience, using data from charts of experimental characteristics of planer cascades, or using statistical (regression) models, which generalize experimental data on losses in turbine blade cascades [8]. Such regression equations can be used as models to evaluate losses depending on the main geometrical parameters of the cascade and its operating conditions.

After selecting the optimal combination of geometrical parameters (with given restrictions) ensuring a low level of blade losses, a cascade may be constructed by employing any appropriate analytical method. This concludes the first stage of the design, which can be regarded as the solution to the inverse problem on the basis of statistical regression models.

In order to ensure minimal losses in a cascade of a particular shape, optimization is performed in the second stage using analytical (gas - dynamic) models, in particular by employing the method of realization [9], by calculating the boundary layer on the blades, and so on. The second stage also includes an analysis of the distribution of the effective velocity at the blade surface and in the blade passage, the intensity of the shock wave at the outlet from the cascade, and the susceptibility of the flow to separate. If necessary, the shape of the blade may be changed and all calculations may be repeated until a cascade with low blade losses and a favorable flow pattern is obtained.

As is well known, the flow, and consequently the aerodynamic efficiency, of the transonic cascade is greatly influenced by the shape of the suction side of the blade, particularly the distribution of its curvature in the region of the throat. Usually the shape of this section is characterized by the stagger angle. Calculations have shown that by redistributing the curvature of the suction side of the blade in the region of the throat, even at a constant stagger angle, the flow parameters in the cascade may be improved: specifically, maximal over expansion of the flow at the suction side may be substantially reduced [3].

The high sensitivity of the transonic flow to even minute changes in the blade contour, and the complexity of the flow pattern in the blade passage for transonic operating conditions do not allow general recommendations to be made regarding the preferred distribution of curvature along the contour of the blade, especially on the suction side of the blade. However, we may make the following qualitative assessment based on numerous calculations and experimental data: when correcting the blade contour, careful reduction of the intensity of the shock waves existing at the leading section of the suction side, which cause a thicker boundary layer at the suction side and its separation due to the shock near the trailing edge. Also, lengthy diffusing sections on the suction side should be avoided especially when the pressure in the flow near the wall at the trailing edge of the blade greatly exceeds the average pressure downstream of the cascade, because it contributes to the separation of the flow.

A monotonically accelerated flow along the suction side of the blade with small over expansion on the throat and velocity at the outlet of the suction side are the most favorable conditions.

To ensure aerodynamic optimization of the shape of the suction side, the second stage of the design should employ an automated method, in which the curvature of the surface is correlated to the local velocity of flow. Based on equations for planar gas flow expressed in physical coordinates (the x - axis is orthogonal to the stream lines), we obtain the following relationship:

$$d\lambda/\lambda = -dR/R = dK/K, \quad (1)$$

where R and $K = 1/R$ are the radius of curvature of the stream line and its curvature, respectively.

It follows that an increase in the curvature of the surface ($dR < 0$) at an arbitrary point on the suction side of the blade causes a local increase in the velocity of flow ($d\lambda > 0$), while reduced curvature causes a deceleration of flow (with $dR > 0$, $d\lambda < 0$). This phenomenon is qualitatively similar to the distribution of velocity in a vortex, that is, the local stream velocity is directly proportional to its curvature.

We optimize the shape of the suction side of the blade with the following parameters remaining invariant: chord l , pitch t , blade angle γ , throat section a_2 , thicknesses d_1 and d_2 of the leading and trailing edges, and with an invariant shape of the blade pressure side. Parameters such as the stagger angle and the maximum thickness of the blade may be subject to change in the course of optimization. The shape of the suction side of the blade is varied under the above conditions by redistributing the curvature along its contours.

A series of direct problems were solved in optimization by the realization method using an iterative process. At each design stage, we analyzed the calculated velocity distribution along the suction side of the blade, and corrected the distribution of curvature of the blade suction side according to the level of the velocity and character of the distribution. In accordance with the above mentioned influence of the curvature on the velocity (1), it varied at the nodes of the calculation

$$\hat{K}_i = K_i + \alpha(k - \lambda_{adi}) \quad (2)$$

where K_i and \hat{K}_i were the initial and final values for the curvature at the i - th node of the net;

$$k = \lambda_{adi} / \lambda_{2ad} \text{ and } \lambda_{adi} = \lambda_{adi} / \lambda_{2ad}$$

were the given and calculated values of the relative velocity λ_{ad} at the i - th point in the current iteration step.

Then the contour of the blade face was reconstructed using the changes distribution of the curvature, and the calculation net near the suction side was corrected retaining the orthogonality of the cells (in the calculation, the shape of the blade was given by the coordinates of nodes in the net within the blade passage). In the next iteration step, we used the flow parameters in the net cells of the previous stage to calculate the new velocity distribution λ_{ad} along the blade contour. This process was continued until a cascade was obtained with over expanded flow at the blade suction side: $\lambda_{\max} < 1.1$ to 1.15. Optimization of the shape of the blade suction side usually requires 5 to 7 iterations, in which variations are made in the blade curvature distribution using the relaxation coefficient $\lambda = 0.8$.

In each step we changed the shape of the blade suction side starting from a given point on its front, such as the point of tangency with the leading edge. At this point, the coordinates, the first derivative and the

curvature are maintained invariant during optimization. The shape of the blade side is reconstructed in accordance with the corrected curvature by numerical integration of an ordinary second-order differential equation using the Runge - Kutta - Feldberg technique. Here, the curvature is expressed through first and second derivatives as follows :

$$y'' - K(x)(1+y'^2)^{3/2} = 0 \quad (3)$$

The throat a_2 and the thickness of the trailing edge d_2 may be changed in the optimized cascade. Therefore, an additional correction of the distribution of the curvature on the blade side is necessary to maintain a_2 and d_2 at the level of the initial cascade. This keeps the flow rates of the gas and the cooling air in the optimized cascade invariant. The additional correction does not change the character of the distribution of the curvature on the blade side.

Fig. 1 illustrates how this method works by showing distributions of the curvature and the velocity along the contour of the blade suction side i in the course of the iteration process. Substantial over expansion of the flow appears in the initial cascade ($\lambda_{\max} = 1.41$) with a section having intensive diffusing flow. After performing corrections, the shape of the blade suction side was obtained with a small over expansion of flow ($\lambda_{\max} = 1.15$).

The iterations were made with a large relaxation coefficient ($\lambda = 1.15$) to obtain a vivid picture; this caused substantial redistribution of the blade suction side curvature as early as the third iteration step. The curvature became more pronounced in the zone of the trailing edge because of the conditions $a_2 = \text{const}$ and $d_2 = \text{const}$. However, this did not result in a substantial local increase in the diffusing ratio (Fig. 1b). Note that corrections may be stopped at any iteration step, which satisfies the requirements of the designer concerning the character of the flow and the shape of the blade.

Calculations of parameters for the boundary layer show that the momentum thickness in the corrected cascade is much less than in the initial cascade (Fig. 1c); it corresponds to a reduction in friction losses by $\delta \xi_{fr} = 0.01$ to 0.015 . From Fig. 1d we see that the maximum thickness is reduced in the optimized blade; however, the stagger angles δ and the wedge angle of the trailing edge ω_2 increase, which facilitates design of the blade cooling system.

In Fig. 2, the distribution of velocity λ_{ad} along the contours of the blade is shown for the initial and optimized cascades when $\lambda_{2ad} = 0.90$. Over expansions of the flow ($\lambda_{\max} = 1.22$) ending in a shock wave occurs in the initial cascade on the blade suction side near the geometric throat. A velocity distribution without a shock can be obtained for the correction of the blade in accordance with the method we have developed. There were only minor changes in

the distribution of the curvature and in the shape of the suction side of the blade (experimental data concerning cascade 2 are found in [8]).

The method proposed in this lecture was also used to reshape the root section of a turbine rotor cascade that had already been manufactured, in which substantial losses were noticed. When reshaping, besides correcting the curvature of the suction side of the blade, we slightly reduced the blade setting angle γ and the thickness of the trailing edge d_2 . The initial and optimized cascades were investigated experimentally for $Re \approx 10^6$ and a level of turbulence at the inlet of $\epsilon \approx 0.06$ to 0.08 .

Figure 3a shows the distribution of the curvature of the blade suction side in cascades 3 and 4, from which we see that the curvature at the middle of the blade is greater in cascade 3 than in cascade 4. The curvature of optimized cascade 4 is somewhat more pronounced near the throat than in cascade 3. This redistribution of curvature on the blade suction side resulted in a value for $\lambda_{2ad} = 0.72$ under working conditions (Fig. 3b) instead of substantial over expansion of the flow on the blade suction side in cascade 3 to $\lambda_{ad \max} = 1.03$, with subsequent deceleration in the elongated diffusion section to $\lambda_{ad} = 0.7$, and a reduced over expansion and diffusion ratio of the outlet section in cascade 4 ($\lambda_{\max} / \lambda_{2ad} = 1.2$ instead of 1.44 in cascade 3).

The unfavorable flow pattern on the blade suction side in cascade 3 causing the separation of the flow and substantial blade loss is clearly seen when examining the wall flow in cascades 3 and 4 (Fig. 4).

The flow was visualized by introducing a fast-drying dye upstream of the cascade for three to five seconds [11]. After drying, the dye traces produced a vivid picture of the wall currents under the operating conditions being studied. Fig. 4b shows that in optimized cascade 4 with $\lambda_{2ad} = 0.72$, the dye traces on the blade suction side studied coincide with the direction of stream lines indicate that the flow is regular, vortex-free, and continuous. Because separation was absent in cascade 4, the blade losses were much lower (by $\delta \xi_{bl} \approx 0.03 - 0.04$ as compared with the initial cascade 3), as shown in Fig. 3c.

The proposed method of aerodynamic optimization of transonic turbine blade cascades is based on the correlation of the velocity of the flow and the curvature of the surface being circumscribed, and can substantially accelerate work on improving turbine blade cascades. In some cases, this method will substantially reduce losses by slightly changing the geometry of the cascade and the blade system as a whole.

2. Designing of blade's cooling system

After generating the external blade surface, design of the blade cooling system, which provides the necessary blade surface temperature state for a given mass flow rate, is implemented. Application in the design stage of quasi-3D heat transfer models allows

comparitive analysis of alternative cooling systems, and optimization of the chosen cooling system. The profile part of the blade (after the aerodynamic design is complete) is described in terms of external contours of cross sections. Internal contours are set down for generating smooth internal cavities in some base section. Cavity sizes are regulated by giving wall thickness at some points of the external contours. The next step is the generation of internal contours for other blade sections by interpolation.

Existing information about the geometry is written in formats DXF or IGES and used in geometry simulation for generating cooling passages.

In dialog graphics regime partitions, matrix, injection holes and other elements can be generated. Contours, which include metal, form and create an input file for FE grid generation. Preparation of the full blade profile part geometry is provided by FE grid generation in all sections and by uniting all grids in one FE grid. Geometrical and FE models which have been described are implemented quickly and clearly, but final passage geometry is determined by an interactive process which demands designer's experience.

First check of geometry is the air mass flow characteristic of the blade's cooling system. Geometry is corrected until the correct air mass flow is obtained. Hydraulic model generation is carried out for regular structure (matrix, pin fin) automatically and for non regular structures in graphic dialog regime. Calculation of passage cross sectional areas and hydraulic diameters are implemented in "Edit" regime; or in the regime for the establishment of section connections; or when complete information about injection hole's (heat sources) is formed. Fig. 7 presents a copy of the picture on the display screen, appropriate to this regime of hydraulic model forming. Hydraulic resistance are calculated on the bases of given editor value of friction coefficients, or given in regime "Edit".

Heat transfer and air heating are calculated only for branches connected with FE grids.

For calculation of heat transfer in graphic dialog regime numbers A and n ($Nu = ARe^{**n}$) are given.

On Fig.8 gas boundary condition are presented (film cooling and boundary layer calculation)

For temperature field calculations in blade sections, the next input data are prepared:

distribution by height of gas temperature and pressure before the blade, gas pressure behind the blade;

air pressure and temperature on entrance in the blade's cooling system.

The blade's quasi-3D strength model is implemented on the FE grid, using temperature calculations, in conjunction with received temperature fields and gas and centrifugal forces.

References

1. Borisov F., Verevsky V., Ivanov M. et al. Three-Dimensional Profiling of the Nozzle Blade Cascade of the Last Stage in Large Steam Turbines, *Teploenergetika*, 1991, No. 8, pp. 51-54.
2. Sokolovski G., Gnesin V., Vanin V. Profiling Blade Cascades through Solving Inverse Problems, *Energeticheskoe Mashinostroenie*, Kharkov, 1984, No. 38.
3. Venediktov V.D., Granovskii A.V. Research into Transonic Turbine Blade Cascades and Possibilities for their Optimization by Numerical Methods, *Teploenergetika*, 1981, No.4, pp.37-40.
4. Stow P. The Development of Advanced Computational Methods for Turbomachinery Blade Design, *International Journal for Numerical Methods in Fluids*, 1989, Vol. 9, pp. 921-942.
5. Hobbs D.E., Weingold H.D. Application of The Method of Controlled Diffuser Ratio in the Design of Blade for Axial Multistep Compressors, *Energeticheskie Mashiny i Ustanovki*, Mir, Moscow, 1984, No.2.
6. Dulikravich D.S., Sobetskii Kh. Solution of the Problem of the Transonic Flow in Blade Cascades and Modification of the Shape of Blades for Eliminating Shock Waves in Blade Passages, *Aerokosmicheskaya Tekhnika*, Mir, Moscow, Vol. 1, No. 6, pp. 70-77.
7. Venediktov B.D. *Gazodinamika Okhlazhdaemykh Turbin* (Gas Dynamics of Cooled Gas Turbines), *Mashinostroenie*, Moscow, 1990.
8. Venediktov B.D., Granovskii A.V., Karelin A.M. et al. *Atlas Eksperimental'nykh Kharakteristik Ploskikh Reshetok Okhlazhdaemykh Gazovykh Turbin* (Cumulative Chart of Experimental Characteristics of Planar Blade Cascades of Cooled Gas Turbines), CIAM, Moscow, 1990.
9. Bogod A.B. Granovskii A.V., Karelin A.M. Increasing the Accuracy and Reducing the Time for Numerical Research into Transonic Gas Flows in Blade Cascades of Turbomachines, *Teploenergetika*, 1986, No.8, pp. 48-52.
10. Alecsin V.A., Soversheennyi V.D., Chikova S.P. Calculation of the Turbulent Boundary Layer with Permeable Sections, *Izv. Akad. Nauk SSSR, MZhG*, 1978, No., pp. 48-52.
11. Venediktov V.D., Granovskii A.V., Gurov V.L. A Method for Visualizing the Working Flow Passing through Blade Cascades of Turbomachines, *Otkrytoya Izobreteniya*, 1991, No. 19.

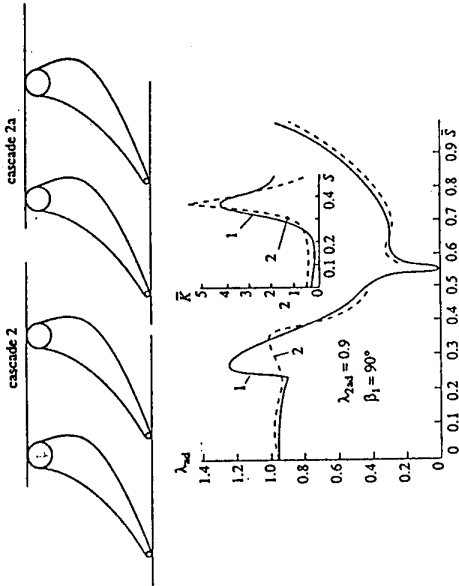


Fig. 2 Results of optimization of nozzle in cascade 2. Distribution of Laval number and suction side curvature
 1-initial cascade 2; 2- optimized cascade 2a.



Fig. 4

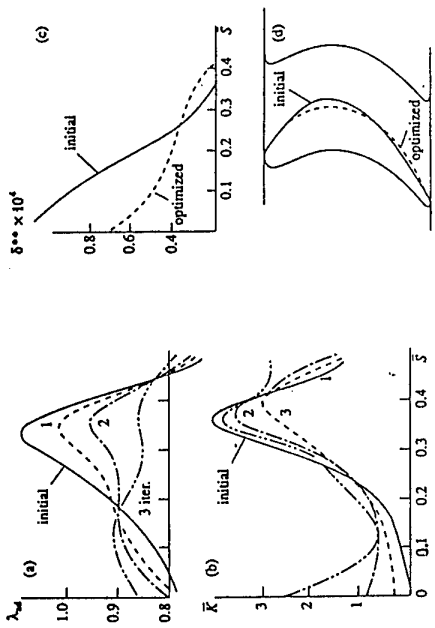


Fig. 1 Results of correcting the blade shape in cascade 1.
 a-Laval number along the blade suction side;
 b- dimension less curvature of suction side;
 c-distribution of the thickness of impulse loss;
 d- diagram of the initial and optimized cascades.

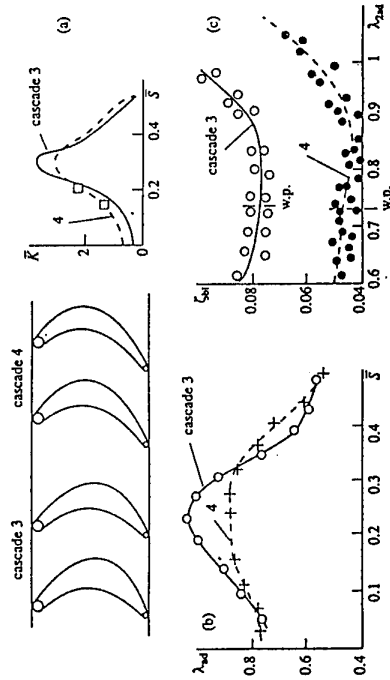


Fig. 3 Results of optimization of cascade 3.
 a- diagrams of cascade 3 and 4 and distribution curvature
 b- experimental distribution of Laval number;
 c- dependence of the coefficient losses on Laval number.

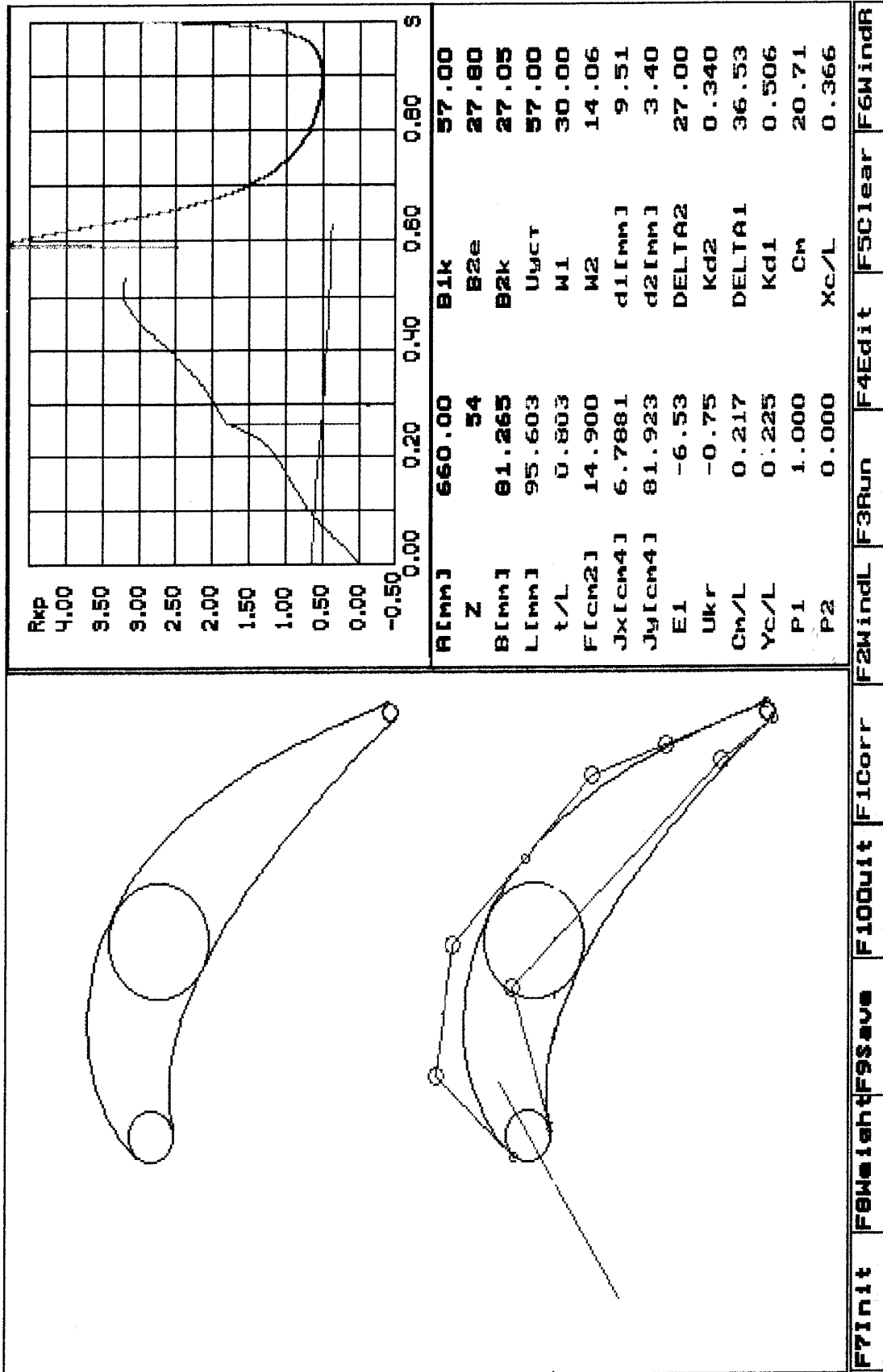


Fig. 5. Linear cascade turbine design.

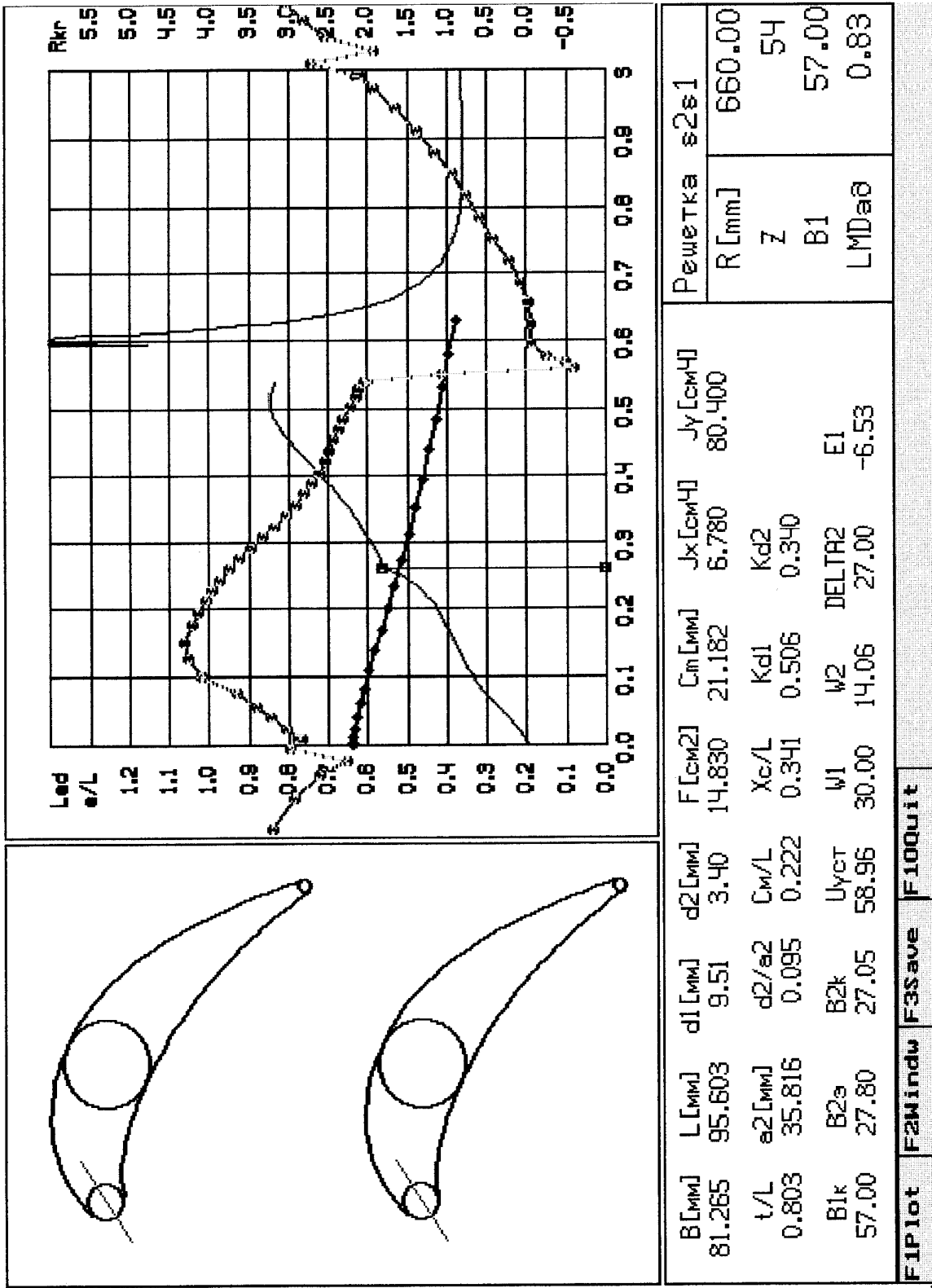


Fig. 6. Geometry and gasdynamic parameters linear turbine cascade.

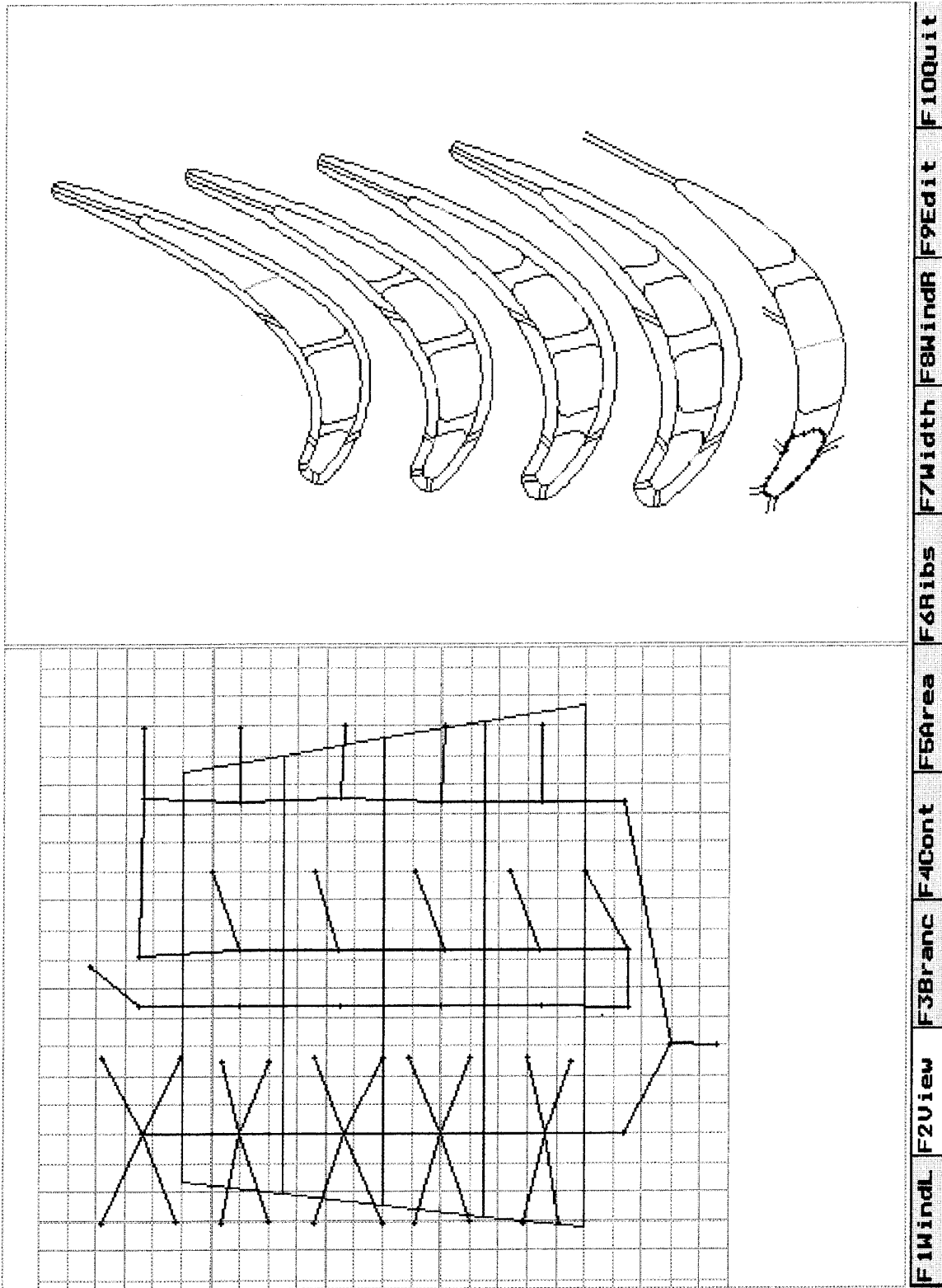
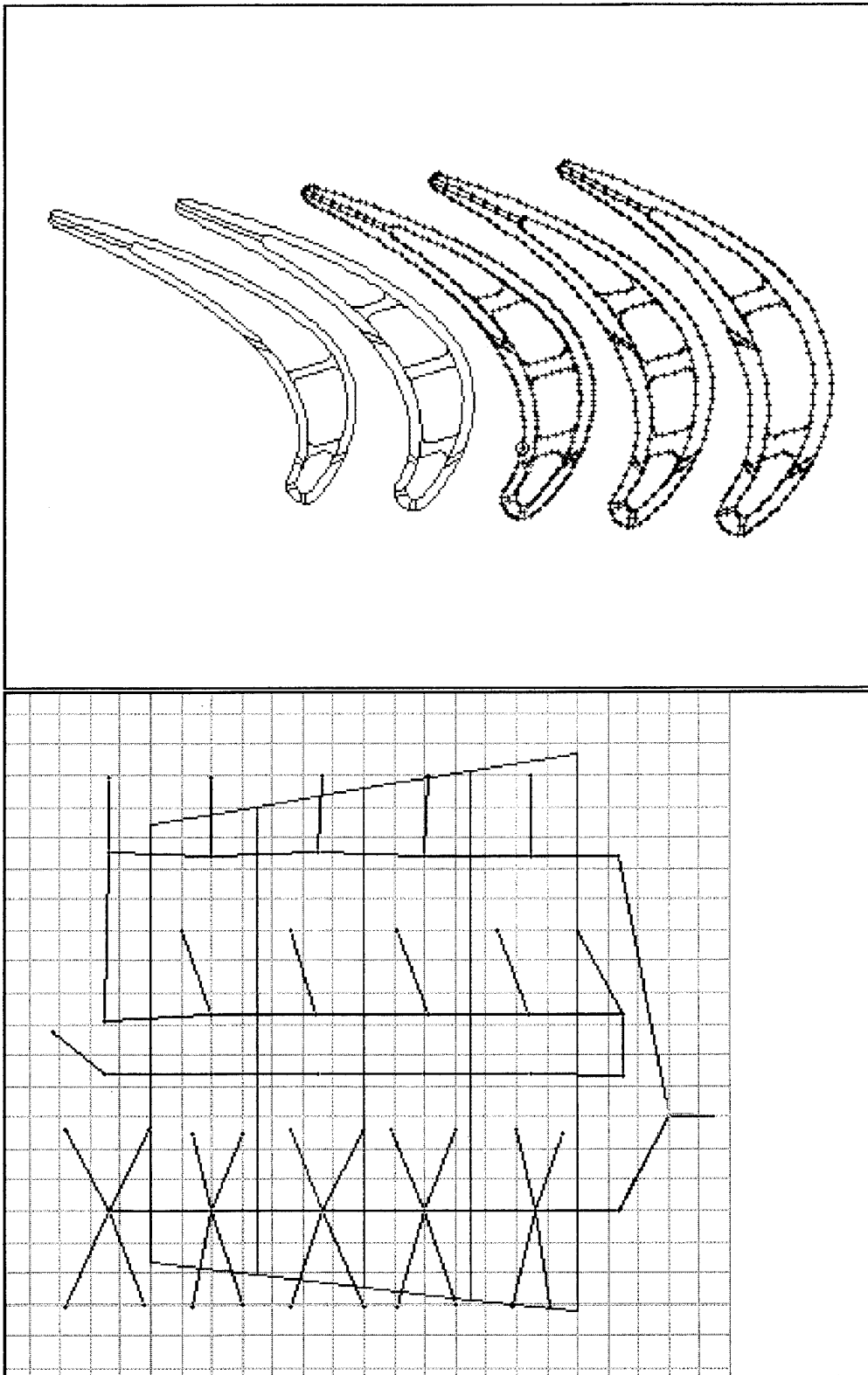
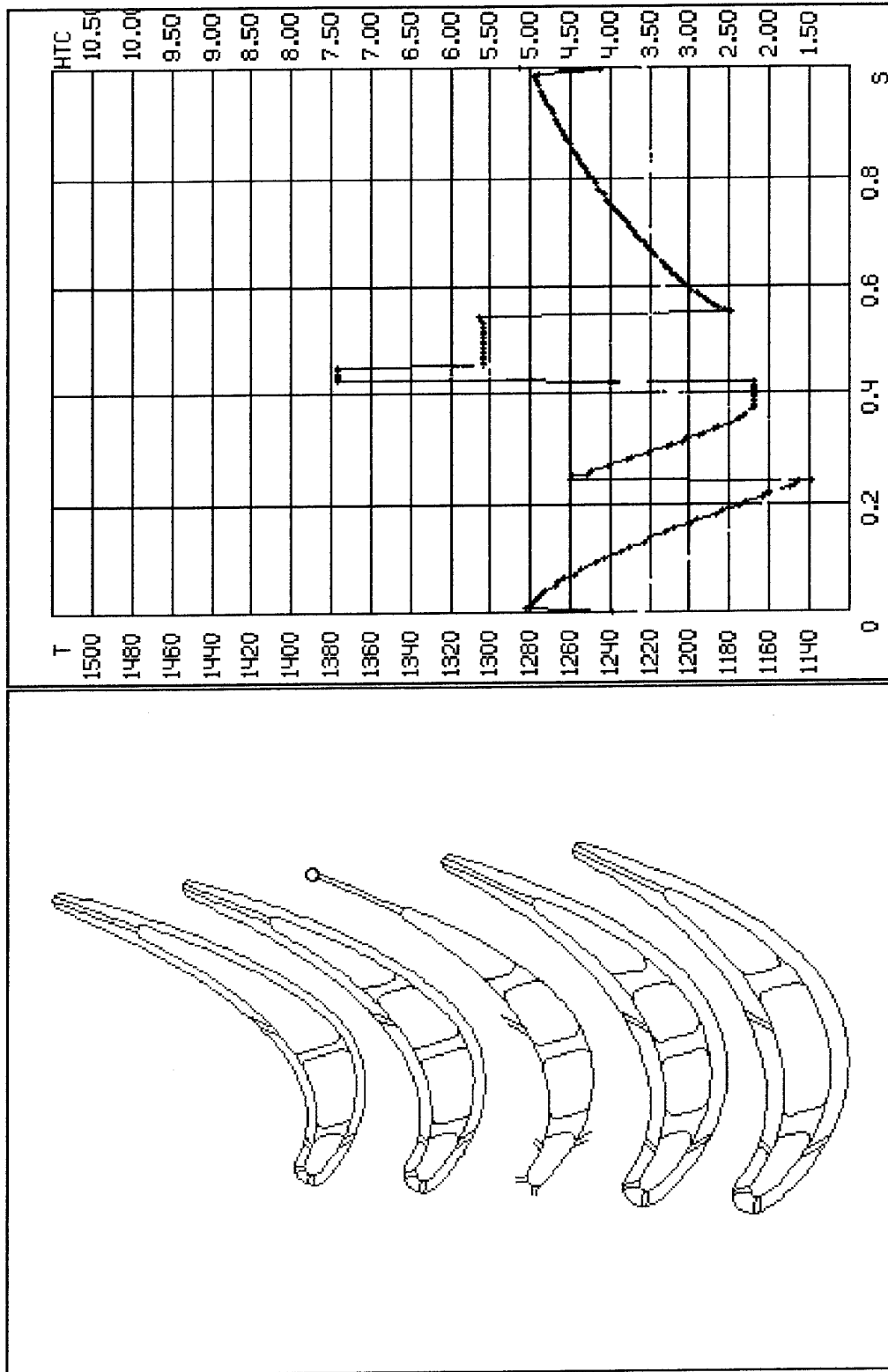


Fig. 7. Calculation of geometry characteristics of branch.



d	t	k	A					
0.25	1.30	1.00	0.00					
F1WindL	F2Deta1	F3Edit	F4Branc	F5Sect	F&Join	F7De1	F8WindR	F10Quit

Fig. 8. Input data for heat source.



S	T C	W/m2
0.000	1238.9	3569.5

F1Cont	F2WindL	F3Value	F4WindR	F5Nr. Rec	F10Quit
--------	---------	---------	---------	-----------	---------

Fig. 9. Boundary condition.

Verification of Multidisciplinary Models for Turbomachines

by

Dr. Kostege

CIAM (Central Institute of Aviation Motors)

2, Aviamotornaya ST.,

Moscow, Russia, 111250

Abstract

Accurate prediction of the temperature distribution in rotating blades is an important and difficult task. An approach for the verification of hydraulic and thermal models in real blades is discussed in the lecture. For static conditions, predicted local internal convective heat transfer coefficients on blades are corrected using a quasi-3D thermal-hydraulic model with the blade unsteady surface temperatures measured by the Thermovision system. External boundary conditions are corrected using the blade base surface temperatures measured by thermocouples on a hot static rig. The final identification of the models is carried out using measurements of the gas temperature distribution within the rotating blade passage, and the measured blade external surface temperature in the engine.

Introduction

With constantly increasing demands for engines maneuverability there is a resulting increase in the hostility of the internal engine environment. These very important problems inhibit turbine reliability for all operating regimes. From reference [1], in 40% of the cases tested, the hot section failures in the engine occurred on the working turbine blades. In aviation engines, failure of turbine blades occurs primarily under transient operating conditions. Because of this problem, thermal - stress blade predictions must be available for all flight regimes.

Predictions of static strength, fatigue life, and stator-rotor clearances are limited by the accuracy of calculation of the steady and unsteady temperature fields in turbine engines. Currently, the only means for obtaining enough reliable data for these temperature calculations is through the use of thermal-hydraulic models. Model validation and parameter specification are carried out through measurements on models, rigs, and engines.

1.1. Model identification for the blade profile

1.2. Methods of calculation

The flow regime and corresponding heat transfer in the core flow and in the cooling systems of turbine blades are complex. Because of the lack of reliable turbulent models and insufficient computing power, local heat transfer coefficients can not be accurately defined by computations alone. Experimental explorations of gas heat transfer coefficients on blades are made primarily on static rigs. Such explorations have taken place under rotating conditions, usually during stage design and development. Transfer of results from the static tests to the dynamic tests shows that it is impossible to guarantee the determination of heat transfer coefficients to high accuracy. Furthermore, these experimental explorations are implemented, as a rule, for a limited number of points, which presently do not satisfy demands for design.

Heat transfer coefficients in cooling system passages are usually explored in models. In a majority of the cases reviewed, results obtained from actual operating machines raised certain problems with respect to measured and predicted operation.

In Russia, the Zn - MATI method is widely implemented for the experimental determination of heat transfer coefficients [2, 3]. Heat exchange conditions are correlated to the height of a pure metal (Zn) crust, that has hardened on the external blade surface. The crust is formed by plunging the blade in pure molten metal (Zn). Crystallization takes place while air flows in cooling passages. Convective cooling occurs across moving boundaries. Here, a difficult problem is presented. The calculated heat transfer coefficient must be related to the boundary between liquid and solid Zn. Therefore, it is necessary to numerically compute the heat transfer to the blade cooling system.

The gas total temperature in the relative frame of a blade surface profile can be defined reliably only by direct temperature measurement. For example, the heat transfer coefficients on an uncooled blade can be determined with the help of MMTC (measuring maximum temperature crystallized), thermopaints and

other methods. These techniques are implemented in low temperature flow regimes.

Taking into account all the difficulties, more exact heat transfer coefficients can be defined on blade surfaces under working conditions through complex calculation and experimental observation in two stages:

First stage (static rig exploration).

- Working from the blade cooling system hydraulic model, a comparison is made of calculated results and experimental data from tests in water and tests in air.

- Blade cooling passage profil heat transfer coefficients are determined with solutions obtained from the method of liquid Zn crystallization (Zn - MATI).

- Gas heat transfer coefficients are determined by measuring the blade wall temperature during thermal cycling (for example by the "thin body method").

- Boundary conditions are checked and specified by comparing blade profile calculation results obtained by the quasi three-dimensional model and thermomentering results in real blade static rigs (convection - film cooling) and blades with closed injection holes.

Second stage (dynamic explorations).

- Gas temperature measurements are taken in the relative frame on the blade surface profile with no cooling

- Blade profile gas temperature measurements by MMTC sensing elements and other methods are taken.

- A series of temperature field parametric calculations on the blade profile (quasi three-dimensional model) is conducted with boundary conditions as measured under real conditions in static rig experiments, and compared with calculation results and thermomentering.

- Analysis of the calculations compared with experimental blade profile temperature is performed.

- The blade profile heat state models in the above calculations are based on quasi three-dimensional and three-dimensional thermal hydraulic models.

1.3. Methods of defining local heat transfer coefficients in real turbine cooling passages

The turbine blade cooling system performance (for example, the heat transfer coefficients inside passages) are defined as functions of known criteria, and using typical average heat exchange characteristics with available models.

Because of the complex flow in the cooling passages (turning, mixing and separation), their exist geometric differences between the blade and the model. Such discrepancies can cause a large difference between the blade's actual heat state and that calculated. This

makes it more difficult to properly design the cooling system and extend blade life.

In CIAM, the local heat transfer coefficients inside the blade passage are defined based on the "Zn - MATI" method, with the quasi three-dimensional thermal hydraulic model of the blade. During cooling of the melted Zn the temperature drops until the liquid-solid phase change point is reached. At the phase conversion surface, the temperature remains constant. As the surface moves during the phase change, the latent heat of the liquid-solid phase change is evolved. For definition of the separation boundary between the solid and the liquid Zn phases, a standard finite element method for the solution of the unsteady heat transfer equation is used. Inside the cooling passages, convective heat transfer boundary conditions are applied. However, in this solution, an effective heat capacity \bar{c} of Zn must be used.

$$\bar{c} = c + q\delta(\Delta)$$

The introduction of the effective heat capacity means that the process of crystallization takes place over a temperature interval.

For air mass flow in the blade's passages, the heat transfer coefficients are verified if the boundaries of crystallization coincide with experimental data for the entire blade profile.

At the present time, a more informative method of defining the local heat transfer characteristics inside the blade passages (or other experimental objects) is used.

This method, the Thermovision system, is based on a computational analyze of experimental data. During the calculation, the heat transfer coefficients are varied on separate boundaries. The unsteady blade surface temperature field is solved by the conjugate quasi three-dimensional technique.

Mode of study: The blades surface was covered with a special paint with a known emissivity. The blade was then heated to 300-350°C. After heating, cooled air (temperature 20°C) was quickly pumped trough the blade passages. The unsteady temperature of the external suction and pressure sides of the blade were measured by the Thermovision system (AGA - 782) with a frequency of one measurement set per second. The air mass flow was continuously recorded. In comparison with control thermocouples, the error of the unsteady temperature field measurement by the Thermovision system did not exceed +/- 3%.

1.4. Measurements of gas and blade temperature in engine

The experimental determination of the heat state in gas turbine engines was worked out at IAE by T.A.Kurchatova sensitive elements MMTC(measuring maximum temperature crystallized) [4]. The IAE application has several advantages : There are no congesting wires, small surfaces may be measured, and the maximum temperature can be measured. With the

help of MMTC, measurements of gas temperature, cooling air temperature in the small cooling passages of the blades, and the surface temperature of cooled blades is possible. The experience of the MMTC application has shown that data obtained under real engine conditions, without recalculation or simulation of the gas flow, can be used to understand the processes of the flow in turbine's gas channel.

1.5. Comparison of calculation and experimental data by blade's heat state

Consider a turbine blade with a cyclon matrix cooling system. The blade geometric and hydraulic models and the finite element grid for the blade middle section are shown in Fig 1.

The blade profile is given in 9 sections. Every section consists of 5 subregions. For example, the fifth section (middle) consists of the subregions numbered from 21 to 25. Subregions 23 and 24 represent the simulated heat transfer at the inlet and the exit of the cyclone passage, and subregion 25 represents the simulated heat transfer in the finned passages of the trailing edge. The finite element grid of the blade profile has 2278 boundary elements. The common number of subregions is 45, where 24 of these subregions represent heat sources.

The hydraulic model describes the blade cooling systems (i.e., that part of the hydraulic network appropriate to cooling). The regular part (matrices) of the hydraulic network is automatically generated by the model. Simultaneously, the blade sections and the calculated areas are branched and the hydraulic diameter cross sections of passages in the matrices are established.

Generation of irregular hydraulic branches is implemented in a graphic dialogue regime. Hydraulic resistance of radial passages is defined as

$$\xi = K\lambda \left(\frac{l}{D} \right)$$

where

$K = 10$ - coefficient, taking into account ribbed passage.

$\lambda = 0.04$ - friction coefficient of smooth passage.

l, D - length and hydraulic diameter of passage

The hydraulic resistances in matrix passages were calculated setting $K = 1$. Hydraulic branch resistance at the entrance and exit of the matrix passage are $\xi = 0.7$ and $\xi = 0.92$, respectively.

Resistances to air mass flow between the matrix passages on the blade pressure and suction sides are $\xi = 30$. Passages resistances on the entrance and the exit from the cyclone cavity are $\xi = 0.65$ and $\xi = 1.8$, respectively. Comparison of the calculations and the experimental mass flow characteristics of the blade cooling system show good agreement. The air mass flow

through blades was calculated to be $\alpha_1 = 2.9$ (0.8% of which is through the cyclone).

For the calculation of the heat transfer coefficients in the blade cooling system passages, well-known experimental correlations were used. Thus, in the cyclone cavity on the blade leading edge, surface correlations for a single jet impingement configuration [5] were used. This application has been confirmed by experiments (V. Saharov, CIAM). For other passages, the formula for heat transfer in turbulent regimes can be used with corrections to the entrance region of the flow, or roughness (passages with ribs).

$$Nu = 0.018 Re^{0.8} K$$

For passages with multiple ribs ($K = 2.2$), the calculation is made at the minimum section (A.Trishkin, CIAM). Figure 2 shows the thickness of the Zn crust (mid-span), distribution from the Zn-MATI method with closed injection passage. Agreement of calculated heat transfer coefficients increased by 10-20% in matrix passages. This was determined by taking into account the entrance region of the flow in the passage, $K = f(L/D)$.

It is very important to say that the calculation of the heat transfer coefficients in matrix passages was implemented for air mass flow values not confirmed by direct measurements. Only the inlet and exit air mass flow values were measured.

As we said before, the gas temperature radial distribution in front of the blade significantly changes in the blade passage. Considering the blade, Figure 3 shows the temperatures that were measured in rotating conditions on an engine. In three points (on leading and trailing edges of the pressure and the suction sides) of some sections of the non-cooled blade, the blade wall temperature was measured with the help of MMTC (V.Filippov). The gas temperature distribution on the pressure and the suction side were obtained from the three-dimensional heat conduction equation. Due to the heat flowing from the blade, the maximum difference of the blade metal wall temperature from the local gas recovery temperature is 10 - 15K.

Results of this measurements were used to obtain the gas temperature distribution in the passage between blades for the base flow regime.

Calculation of the film cooling on the blade suction side and gas heat transfer coefficients were conducted using the Laval number distribution $\lambda(s)$ along the blade section contour. Laval number distributions for root, middle and tip sections are shown in Figure 4. These results were obtained assuming inviscid three-dimensional flow.

Calculation of the local gas heat transfer coefficients was implemented while solving two-dimensional equations of boundary layer using an algebraic turbulent model (V. Sovershennyi). Figure 5 shows the comparison of calculated and measured

values of gas heat transfer coefficients on the static test rig. The measurement of the heat transfer coefficients was implemented with the help of the unsteady "thin body" method for the middle section of the blade (V.Pochuev, CIAM).

In Figure 6, some temperature calculation fields are shown for various blade sections on the external surface of the blade profile. Here the temperatures measured with the MMTTC technique are also shown on some points of the blade.

References

1. Tretyachenko G. Calculation of blade stress state on unsteady regimes. Kiev, Naukova Dumka, 1975.
2. Galkin M., Bojko A., Harin A. Method of determination of internal boundary condition in gas turbine cooled blade. Moscow. Mashinostroenie, 1978, No. 8.
3. Goreloff V., Goychenberg M., Malkoff V. The Investigation of Heat Transfer in Cooled Blades of Gas Turbines. AIAA, No. 90-2144, presented at the AIAA/SAE/ASME/ASEE 26th Joint Propulsion Conference, July 16-18, 1990, Orlando, FL
4. Karpuhin V., Nikolaenko B. Temperature measuring with using diamond. Moscow, Atomizdat, 1971.
5. Chupp R., Helms H., McFadden P., Brown T. Evaluation of internal Heat Transfer Coefficients for Impingement Cooled Turbine. Airfoils. Journal of Aircraft, Vol. 6, 1969.

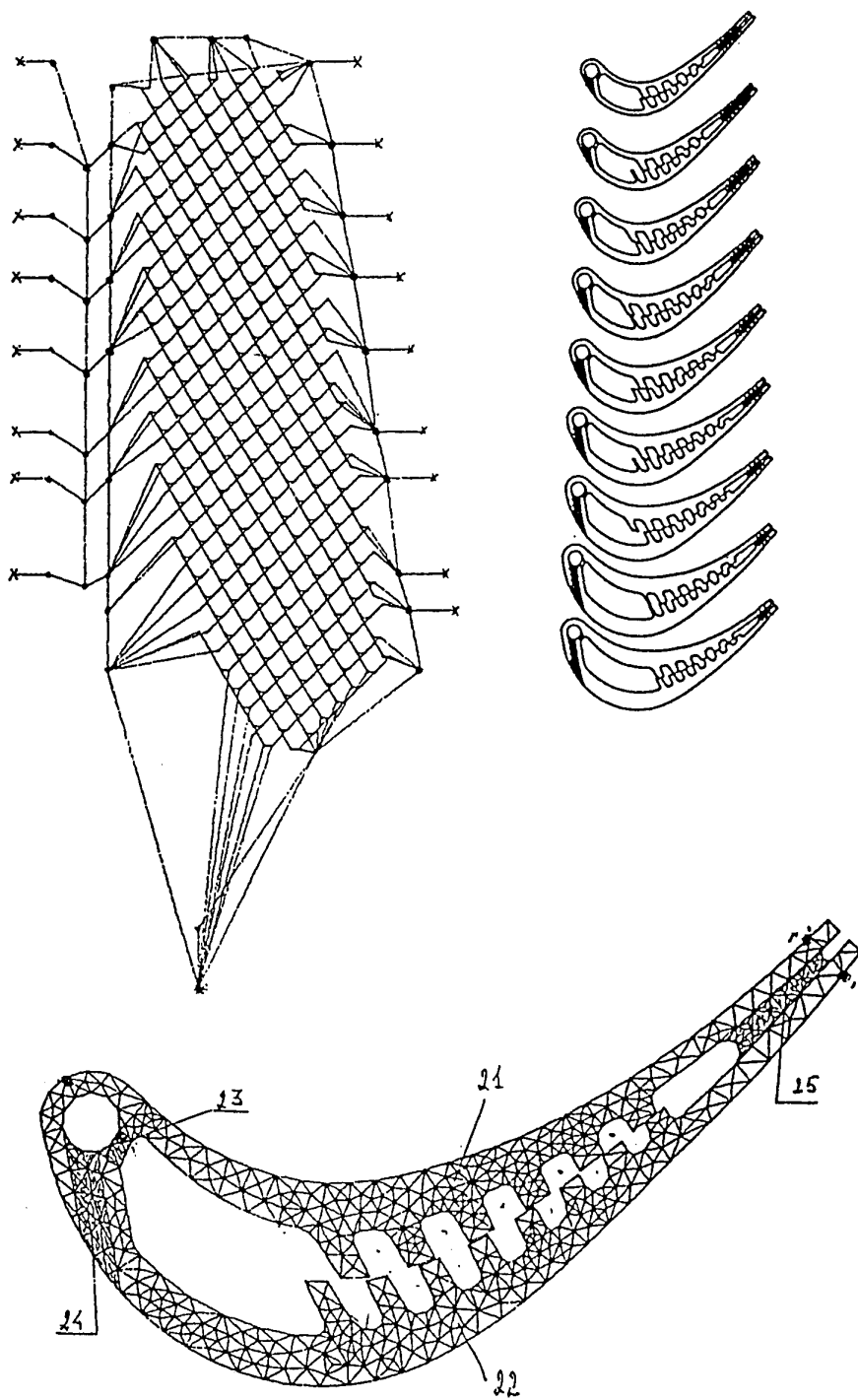


Fig-1 Hydraulic and geometrical models of cooled matrix blade.

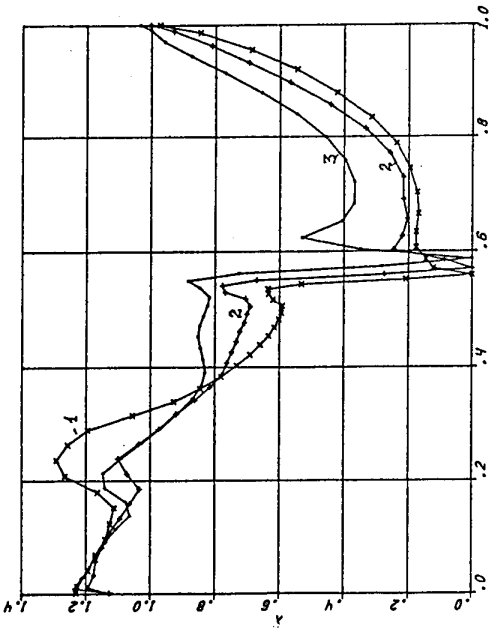


Fig. 4 Laval number distribution (tip, middle and hub section)

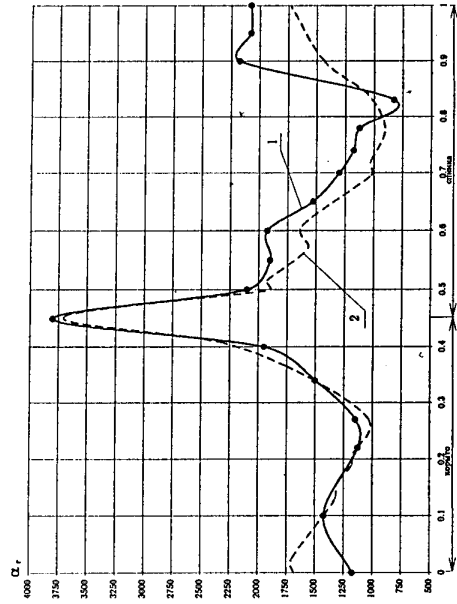


Fig. 5 Gas heat transfer coefficients (middle section)
1-experiment (static rig)
2-2D boundary layer calculation

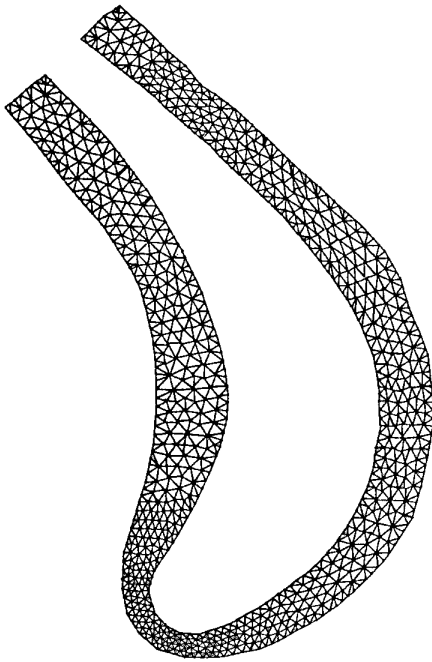


Fig. 2 Zn crust. Experimental data - Method Zn-NATI.

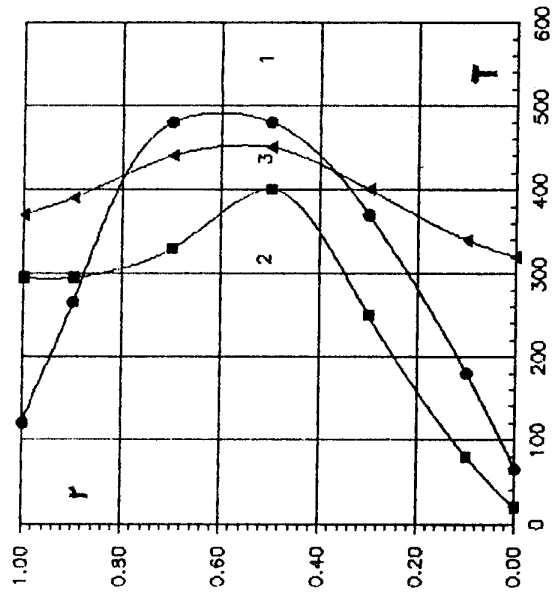


Fig. 3 Gas temperature distribution on blade
1-leading edge; 2-trailing edge
3-suction side; 3'-pressure side;

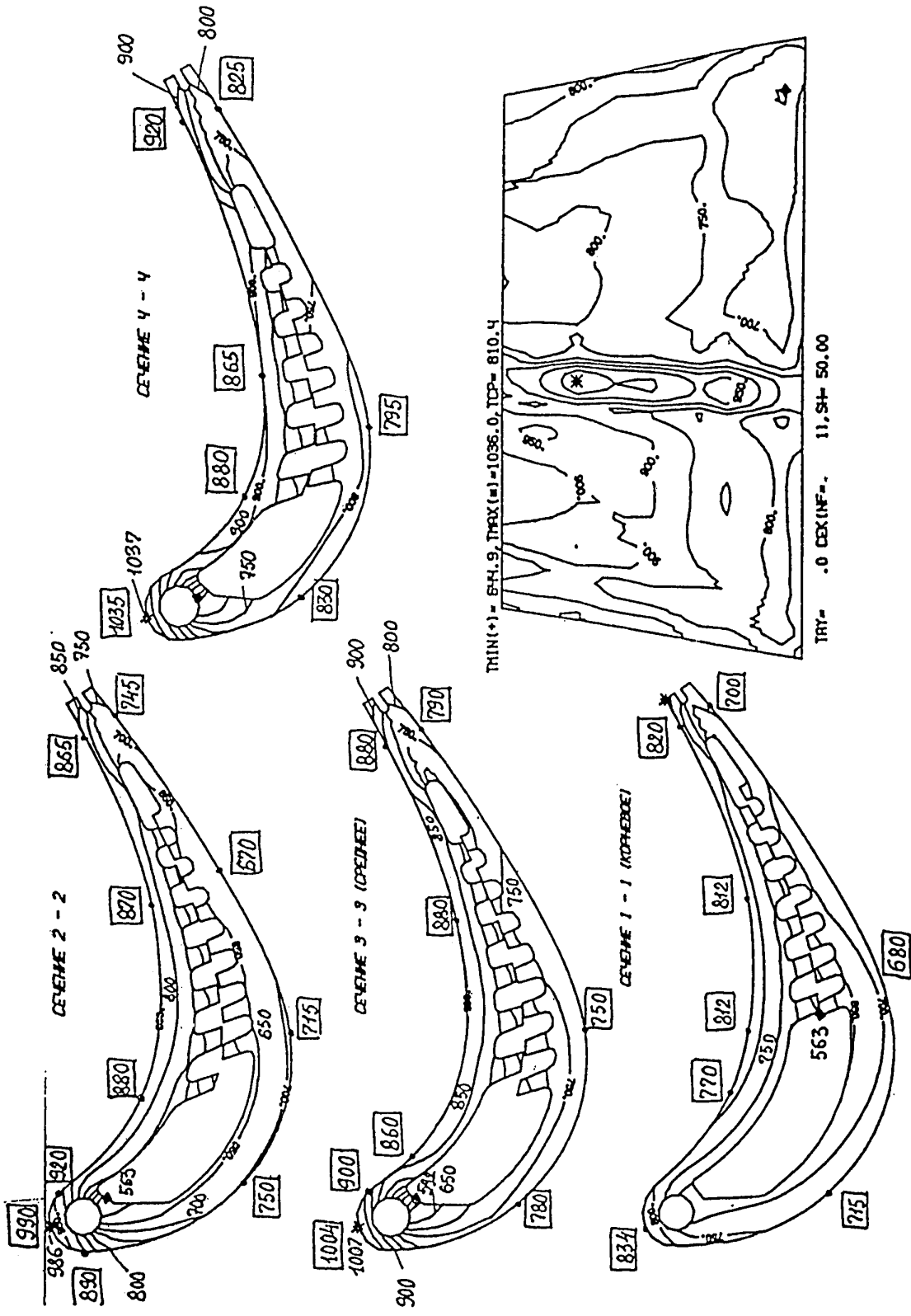


Fig-6 Steady temperature field in blade comparison numerical and experimental data.

Perspective problems of gas turbine engines simulation

by

Prof. M. Ja. Ivanov
 CIAM (Central Institute of Aviation Motors)
 2, Aviamotornaya St.,
 Moscow, Russia, 111250

Abstract

The purpose of the last lecture is to present the activity of CIAM in the field of the development of Computer Turbojet Test Technology based on aero-engine models of high 3D level. Using this technology the aero - engine design may be transformed into new quality. It's the predictions of steady and transient working processes, performances and efficiency on the first stage of engine design (without the real metal engine testing). These aero-engine models must accompany the whole engine life - from design to production and use on aircraft.

Introduction

The preceding lectures and also the quoted publications of last years have illustrated the modern advances of mathematical simulation of the physical processes in gas turbine engines and its components. In this lecture we'll formulate the nearest perspectives of development and application of this research direction.

First of all we would like to emphasize that now there is a real base of good enough computer test facilities to work out processes and performances investigations of different type of aero-engines (turbojet, turbofan, turboshaft and oth.). CIAM is realizing the development of modern Computer Turbojet Test Technology (CT³) - to create and validate new simulation software procedure to design and analyse aircraft engines. As a result of this CT³ program will be the creation and verification of the high levels computer test facilities for whole gas turbine engines. The CT³ system based on 2D and 3D simulations of aerodynamics, heat transfer and stress problems is described in this lecture.

The CT³ will allow high accuracy to simulate the real working processes on various regimes (take off, cruise, idling, autorotation and oth.) and influence of major parameters on engine efficiency. It will be a very convenient tool for engine performances prediction, such as the speed-altitude or part-load regime performances. The CT³ will determine also the equilibrium running lines, simulate different transient regimes. Wide application of the CT³ system on design engine stages allows to decrease greatly the time and cost of the engine development.

Another CT³ application will be non traditional methods of engine control systems. These new regulation methods will be based on the prediction of initial stages of nonstable engine working regimes (starting, surge, burning put or out and oth.) and allow to prevent nonstable processes at the initial steps.

In the frame of the considering research the special software system of scientific analysis and visualization is developed. This system conditionally named Scientific Operating System (SOS) allows us to improve greatly our analysis capabilities, as well as the ability to view portions or all of the numerical data, to have a static and animated 2D and 3D pictures in color presentation.

The achieved progress in aero-engine physical processes simulation may be used to design gas turbine engines and units of non aircraft application. As examples, in this lecture some results will be presented for a big steam turbine units for atomic power stations.

The computer 3D engine model must accompany the whole engine life - from design to production, uprated and modified versions, and to exploitation on aircraft. Estimation of necessary computer requirements for the realization of the CT³ shows us the first stage of CT³ may be developed using wide spread work stations with RISC processors.

1. Computer Turbojet Test Technology

CIAM owns a unique test facilities for research of real aero-engines and its components. Aircraft engines for different applications can be tested in simulated flight conditions up to altitude $H \approx 20$ km and flight Mach number $M \leq 3$. There are special rigs for testing small turbojet and turboshaft engines under simulated flight altitude - speed and climatic conditions and for gas dynamic, heat transfer and strength testing of gas turbine engine components.

In this section we consider the creation of the Computer Turbojet (Turbofan, Turboshaft and other turboengine) Test Technology - the CT³ system and its performances. The CT³ system must increase greatly the possibilities of our natural test rigs for researches of aircraft engines and its components.

We shall present the main peculiarities of developing the CT³ system. It is based on complex 2D and 3D mathematical simulations of aerodynamics, heat transfer and stress problems, described in this lecture .

After the thermodynamic design, when we have the drafted project, the CT³ system is included with the schematic diagram showed in fig.1. First of all CT³ allows to carry out the detail aerodynamic design of the whole gas turbine engine system. Here it's emphasized the main difference from traditional ways of engine system design.

Up to the present time the mathematical engine simulation used 1D and quasi-2D models [1-4], which demanded a long time for verification testing and development. Application of very accurate 2D and 3D models of the CT³ system allows to get more optimal aerodynamic project of engine system without continuous real engine testing.

On the first step CT³ applies for major steady regime simulations (the cruise and take off regimes). Here we can accurately simulate the equilibrium running points for a series of operating conditions and obtain performance curves of power output or thrust, and specific fuel consumption, when all components are linked together in an engine.

Analyzing these regimes, we can design a better variant of the working project and study off-design performances. Beginning from the off-design steady regimes (reduced and maximum powers, idling, autorotation and oth.) and having a better next variant of the working project we must analyze the very important off-design unsteady regimes (starting, surge, burning put or out and oth.). As a result of detail aerodynamic engine analysis we are very close to the optimum working engine flow passage project.

After that, also with the help of the perspective CT³ system we can carry out the mechanical detail analysis. On this step of design, there will be carefully solved heat transfer, stress, vibration, reliability and resource problems. Here we will deal with the finished engine project, which is used for the manufacturing of experience engine. The next step of wide using of the CT³ system will be an accompaniment of real ground and flight engine testing and its certification. The CT³ system must raise the engine testing to the new high quality level, where we will have essentially more information on all test regimes.

Lastly, the CT³ system will accompany also the engine production, exploitation and development of updated and modified engine versions. We would like to emphasize once more that the CT³ system must accompany the whole engine life and will be similar to an engine passport.

2. Scientific Operating System

When complex multidimensional problems are solved, the computer memory contains a large volume of numerical information. It's necessary to fulfill quickly enough the careful analysis of inputting and obtaining information with the help of special techniques. This analysis must be based on the new artificial intellectual systems and the modern graphic visualization systems, which are to be developed for work stations and personal computers.

At the time of writing, a new research group has been organized in CIAM headed by Dr. A.P.Tchiaston for the development of special software system of scientific analysis and visualization. This system conditionally named Scientific Operating System (SOS) will allow us to improve greatly our analysis capabilities. Shortly we would like to present the major peculiarities of this system.

At the first stage, the input information of complex 3D problems must be analyzed. The careful control of all inputted 3D objects and surfaces must be fulfilled. A researcher has the possibility to view any portion or the whole object of investigation. Fig.2-5 shows the SOS application for presentation of some pictures of gas turbine engine, its component and part of surfaces. In the same way, all initial problem data and boundary conditions must be verified.

At the second stage, the SOS application allows us to control the used computational grids. Fig.6,7 show the typical examples of these grids.

At the next stage, a researcher must have the possibility to analyze the computational process (convergence history, stability, accuracy and so on).

The main stage of SOS application is the scientific analysis of obtaining numerical data using the modern graphic visualization systems. We present here some typical pictures of such visualization and the special videofilm. The SOS system allows us to analyze in a very convenient form a steady and transient process of gas turbine engines and its components. A static and animated 2D and 3D pictures in color presentation are very impressive and can help obtain better solutions and give concrete recommendations for the engine design.

3. Some application for steam turbines design

High level of computational simulations developed in the aircraft engine design can be applied to construct and modify road and marine gas turbine engines, steam and gas turbine units of stationary power engineering.

One of the typical examples of this problem may be the increase of a big steam turbine efficiency. In many cases the detail study of using and producing power turbine shows the essential reserves in the increase of their aerodynamic efficiencies. In this section some typical results for redesign steam turbine stage are presented. Some real effects of multiphase phenomena in transonic flow are taken into account.

First, we consider the efficiency increase of the last stage of a big steam turbine (the low pressure cylinder). This stage had the meridional shape and radial blades of a vane and rotor as showed in fig.10, where also present pressure contour lines on suction sides of blades. With the help of 3D aerodynamic efficiency simulation was redesigned this last stage and proposed the new 3D bowed blades (fig.11). The new vane has blades with the axial bow in the upstream direction (upper part of blades) and with the radial bow near the hub. Fig. 12 and 13 show correspondently reaction distributions from hub to tip for major regime and two

partial regimes (mass flow ratio $\bar{G} = 0.5$ and $\bar{G} = 0.75$). There are no negative reaction for the modified stage. The modified stage has essentially lower total pressure losses and the stage efficiency increases on 2%. Details of showed researches were published in papers [5,6]. These examples have been demonstrated as one of the perspective problem of turbine simulation using complex 3D blade form in turbines for stationary power engineering.

The next perspective problem is the development of steam turbine simulation with real effects (the multiphase phenomena, condensation and oth.).

Gasdynamic multiphase phenomena in transonic flows caused by the phase transitions and strong interaction between phases is important for many practice problems such as steam turbines and nozzles, cryogenic turbomachinery, streams with dispended particles and aerosols. Below some numerical results are presented for multiphase inviscid problems based on Euler conservation equations for gas phase coupled with the equations of classical nucleation theory and microscopic or macroscopic droplet growth laws. Taking into account heat release, phase transition and strong interphase interactions such effects of high sensitive reaction as "condensation shock", periodic shock oscillations can be explained. Corresponding simulation of 2D and 3D multiphase flow was elaborated in CIAM by Drs. Ju. S. Kosolapov and A. S. Liberson [7,8].

Fig.14 shows pressure contour lines (with interval $\Delta p = 0.02$) for steam flow in cascade C-9012A with Mach number $M_2 = 1.2$. Condensation shock is pointed out by arrow. Correspondent distribution of pressure $\varepsilon = p/p_0$ along the section side is presented by Fig. 15 (solid line), compared with experimental data ("crosses"). A good agreement in almost all range, including condensation shock proves to be except at the trailing edge, where the viscous effects are significant. Dotted line depicts overcooling degree - ΔT , upper continuous thin line - rate of vapour β . It should be noticed that calculations by pure gas methodology without phase nonequilibrium effects lead to the essential errors in distribution of parameters below section with condensation shock effects. Fig.16 shows pressure countour lines for steam flow in cascade with $M_2 = 1.6$ and evolution of pressure (solid line) and rate of vapour (dotted line) along the suction side and correspondent line of periodicity. System of trailing edge shocks provides discontinuously evolution of stream getting more and more dry up with every current classical discontinuity breakdown.

Fig. 17 shows the mass concentration of the vapour phase for $M_2 = 1.2$ and 1.6. Notice that the vapour concentration is increased for higher Mach number.

In order to illustrate the accuracy of the developed method the steady flows of a spontaneously condensing water vapour in the plane nozzle were calculated [9].

Three regimes with the following total parameters at the inlet of the nozzle were examined:

$$p_0 = 0.7839 \text{ bar (common to all regimes),}$$

$$T_0 = 370 \text{ K (regime 1), } T_0 = 373 \text{ K (regime 2),}$$

$$T_0 = 377 \text{ K (regime 3, pure condensation shock).}$$

The nozzle flows are shown in fig. 18 for regime 1 Mach number contour lines ($\Delta M = 0.025$) (fig. 18,a), for regime 2 (fig. 18,b) and for regime 3 (fig. 18,c). There are the shock and subsonic flow behind it for regime 1, the local shock and subsonic region for regime 2 and only the condensation jump for regime 3.

The pressure distributions $\varepsilon = p/p_0$ along the axis of nozzle are shown in fig. 19 for regimes 1,2,3.

The crosses show the experimental data by D. Barshdorf [9]. Here we would like to finish the results presentation.

Conclusion

To direct readers' attention to important problems of the present Lecture Series we would like to formulate the following question: Can we create the gas turbine engine test cell, which allows us to measure all parameters and to observe going processes in any interesting point of flow passage? Some results of the Lecture Series show the principal possibility of such test cell creation. We have been convinced that Computer Turbojet Test Technology (CT³), based on the accurate 3D simulation of engine processes, can get results with more higher accuracy, then only experimental measurements. Let the real measurements of having limit points number (usually, about a few hundreds) coincide in the limits of demanding accuracy with their calculated values on the identified mathematical cell CT³. In this case we can with a sufficient confidence believe that the united system of real and mathematical (CT³) cells presents itself the new high level quality test facility measuring points number, equaled the points number of numerical grid, using in the CT³ system. Here in any point of measurements (in any computational cell) are registered all the parameters (for example, in a flow passage points - pressure, temperature, density and three component of velocity). At that time the proposed system allows to do transparent the all engine and to observe the research physical process in any region, in any point on display using impressive color graphic system. This can be related as well is gasdynamic process and also to heat transfer, stress, burning, deformation processes.

The CT³ system to develop an engine or a turbine power unit can essentially influence over their competition capacity. There is open the new advertisement possibilities. So all important performances can be presented very impressively using the transparent computer model. Special visual demonstration of the best sides of the article will carry out undoubly to a growth of the competition capacity.

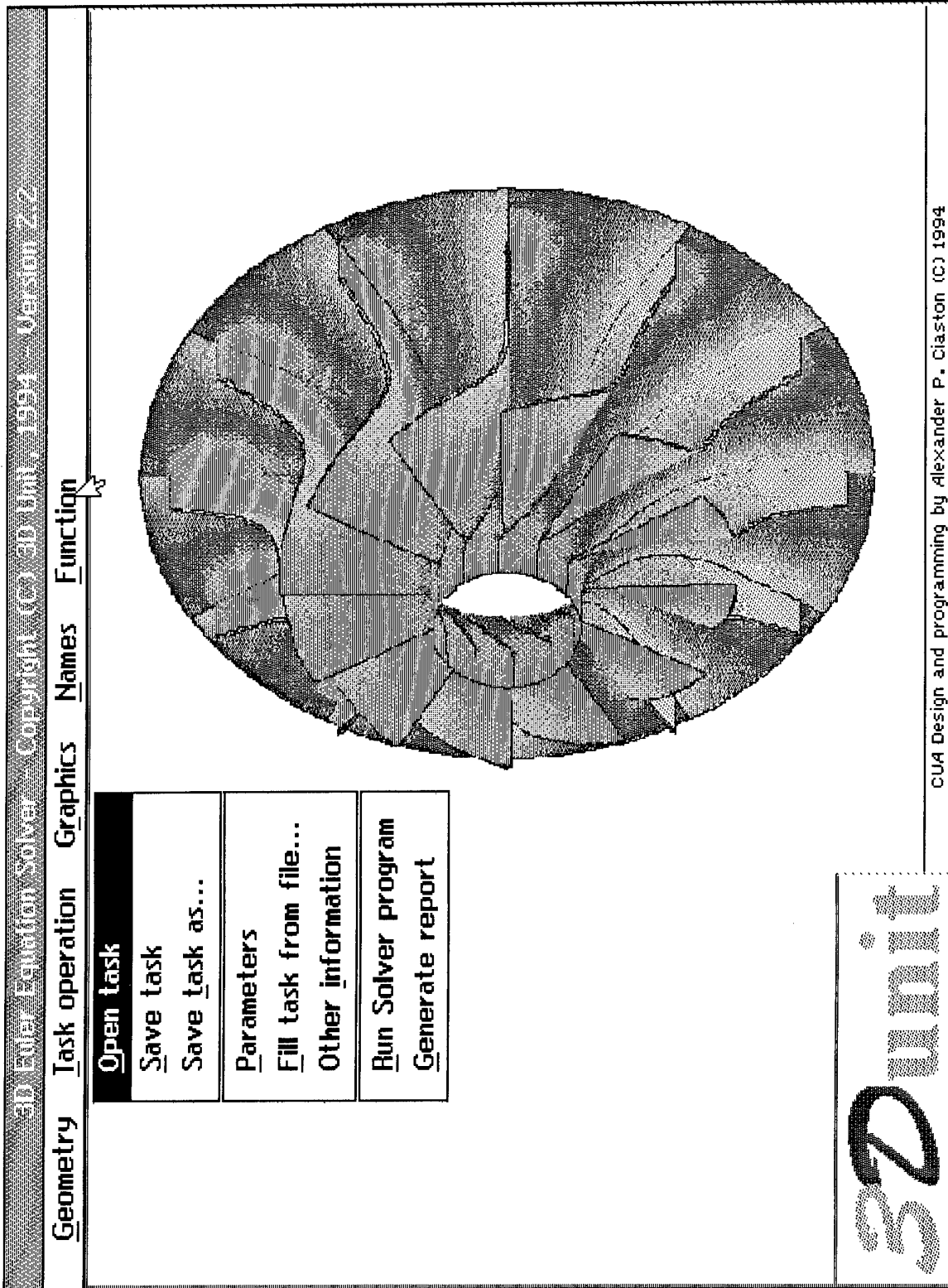
Moreover, the supply of engine or unit with its color 3D model will allow to get essentially clearer and **more** comfortable instructions, description of components and going processes. Simulation with the help of CT³ system of emergency situations will allow also to study the servicing personnel and to avoid the possible mistakes when emergency situations will be arised.

The enormous improvements in computing speed and storage capacity will have a major impact on widely spread of similar CT³ systems in engines and units design and exploitation.

kondensation reinen wasserdampfes in lavaldusen. Fossch. Ing.-Wes. 1971, Vol. 37, No. 5, pp. 146-157.

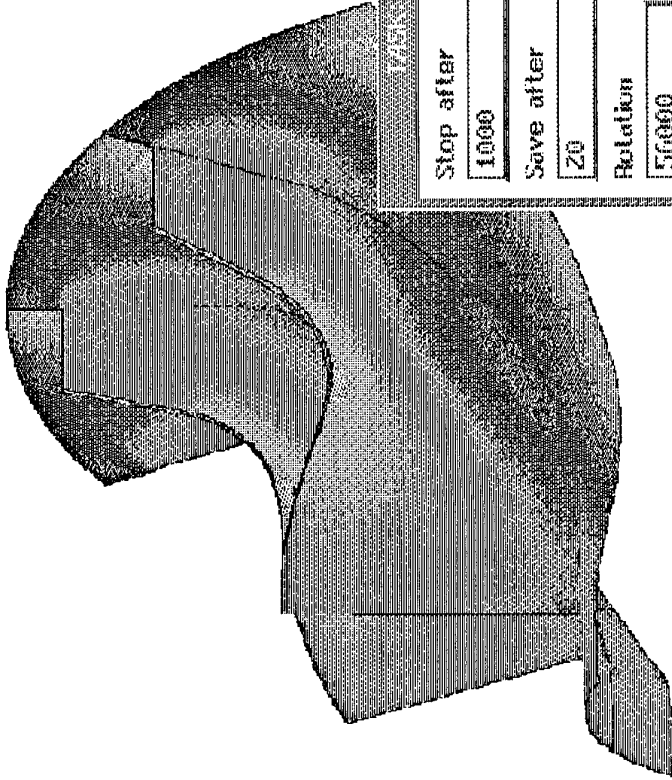
References

1. Klineberg J. M. Advances in computational design and analysis of airbreathing propulsion systems. Papers from the 9-th International Symposium on Air Breathing Engines. Sep. 3-8, 1989, pp. 3-17.
2. Karadimas G. Application of computational system to aircraft engine components development. Papers from the 9-th International Symposium on Air Breathing Engines. Sep. 3-8, 1989, 10p..
3. Rosen R., Bowditch D. N. The future challenge for aeropropulsion. NASA Technical Memorandum No. 105613, 1992, 12p..
4. Ogorodnikov D. A., Ivanov M. Ja., Sundurin V. G. Mathematical simulation for perspective aircraft engine design. Aircraft Technique, 1993, No.2-3, pp.1-15, (in Russian).
5. Borisov F. P., Verevsky V. I., Ivanov M. Ja., Trojanovsky B. M., Karelin A. M., Tchiaston A. P. 3D vane blade design of the last stage for high power steam turbine. Teploenergetica, 1991, No.8, pp. 51-54 (in Russian).
6. Borisov F. P., Ivanov M. Ja., Karelin A. M., Krupa V. G., Rudenko S. V. Application of inviscid and viscous flow simulation for high efficiency stage of steam turbine. Teploenergetica, 1993, No.5, pp.30-34 (in Russian).
7. Kosolapov Ju. S., Liberson A. S. Numerical simulation of stationary 2D spotted condensation steam flow in nozzles and turbine cascades based on implicit monotone relaxation scheme. Proceedings of the 1-st Russian National conference on heat transfer. Moscow, 1994 (in Russian).
8. Kosolapov Ju. S., Liberson A. S. Implicit monotone relaxation scheme for transonic aerodynamics including strong effects from heat addition. J. Comp. Math. and Math. Phys. (In Russian). In preparation.
9. Barshdorff D., Verlauf der zustads groben und gasdynamische zusammenhange bei der spontanen



CUA Design and programming by Alexander P. Ciaston (C) 1994

Fig.2 Working in the SOS Shell: 3D analysis of radial turbine vane



3Dunit

Task: d:\dynamic\turbine\data\unit1.tsk

Stop after	1000	Accuracy	0.0001	Start/Cont.	1
Save after	20	CFL number	4.		OK
Rotation	51000	Geometry file	d:\dynamic\turbine\data\unit1.gri		Cancel
Gas constant	287.8	Heat ratio	1.33		Arrays
Task comments:	Text example for radial turbine...				

Fig.3 Specifying parameters of calculation for radial turbine

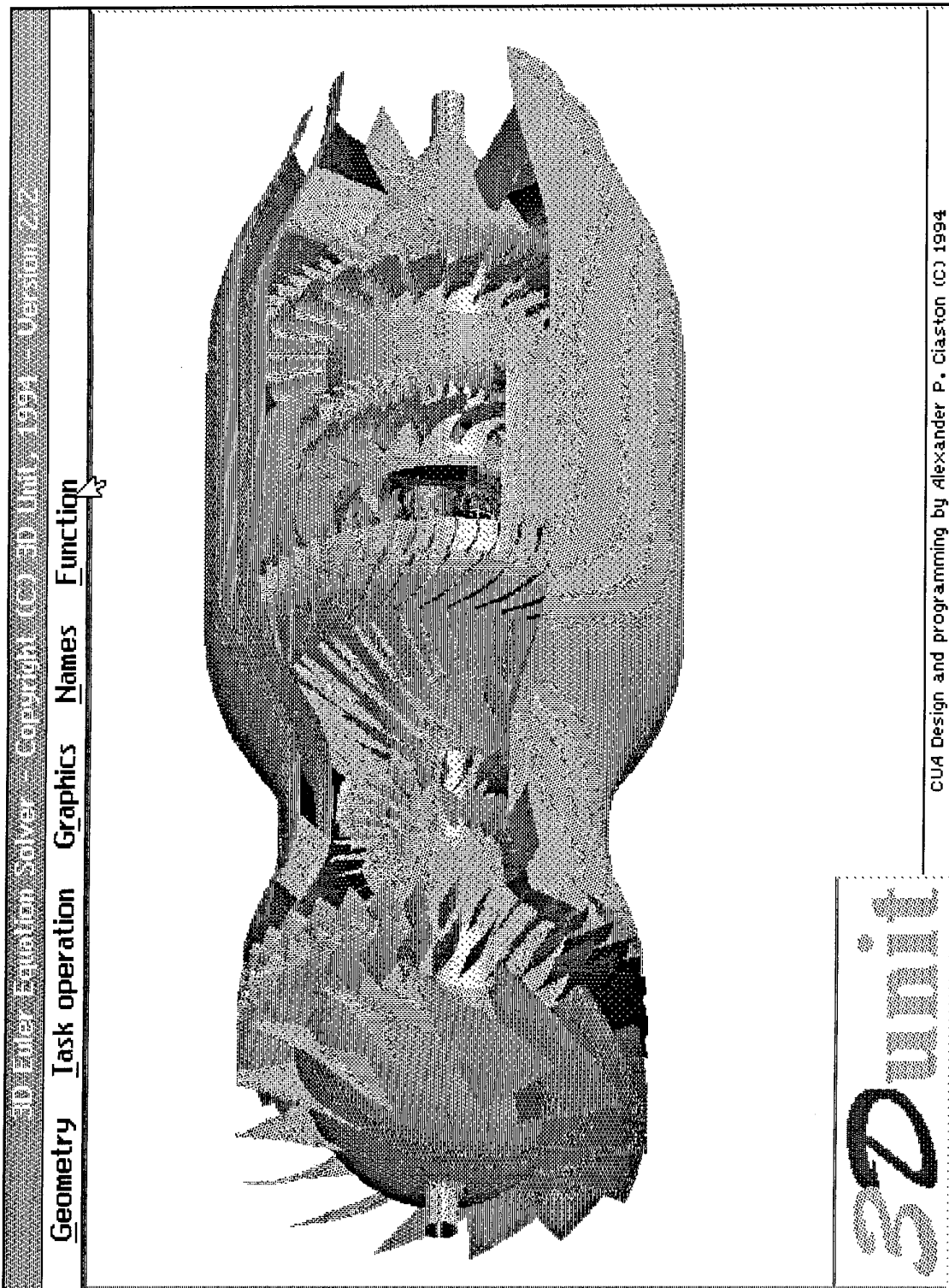
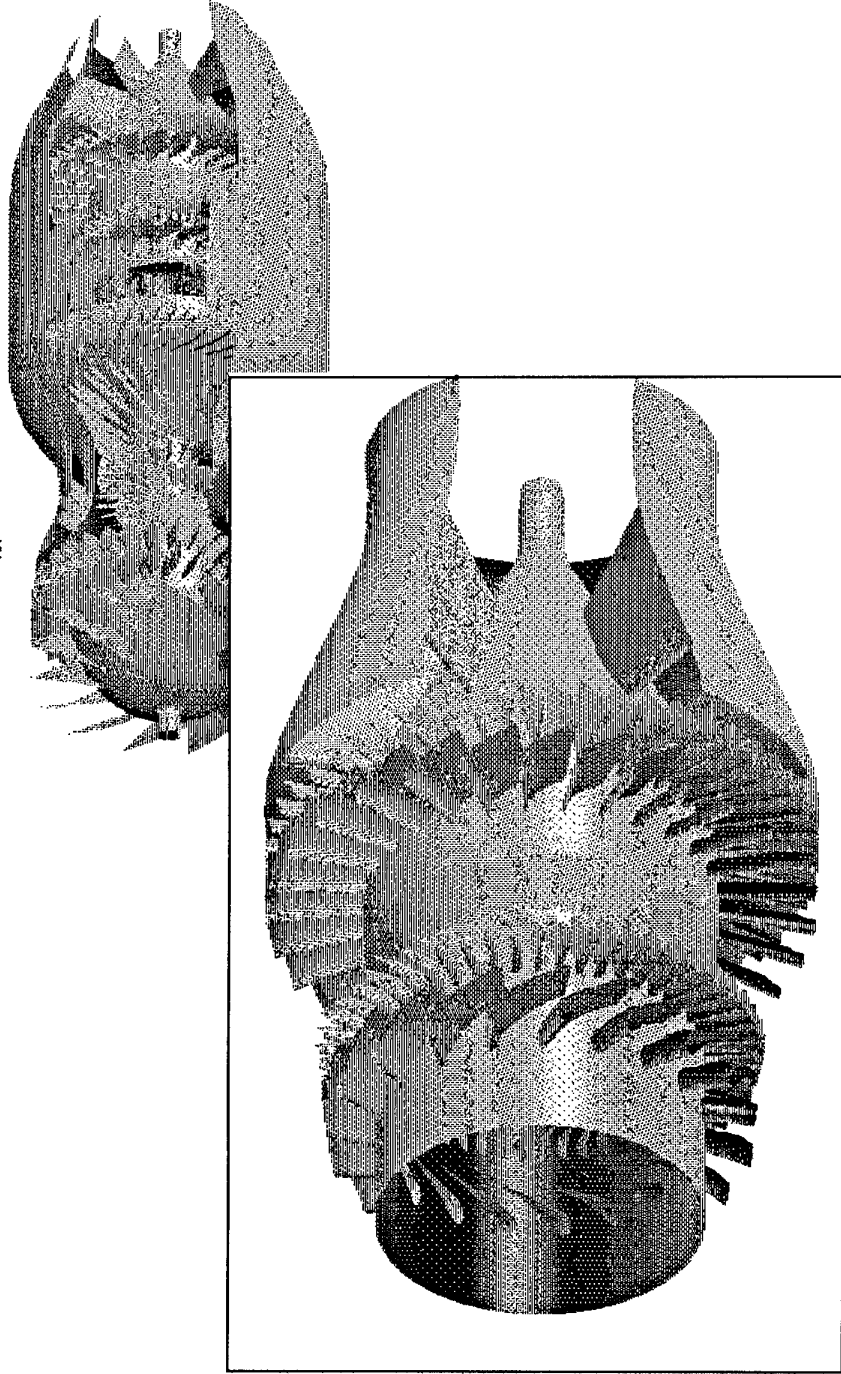


Fig.4 Looking through the whole engine

Geometry Task operation Graphics Names Function



3D unit

CUA Design and programming by Alexander P. Claston (C) 1994

Fig.5 Any component of engine can be investigated separately

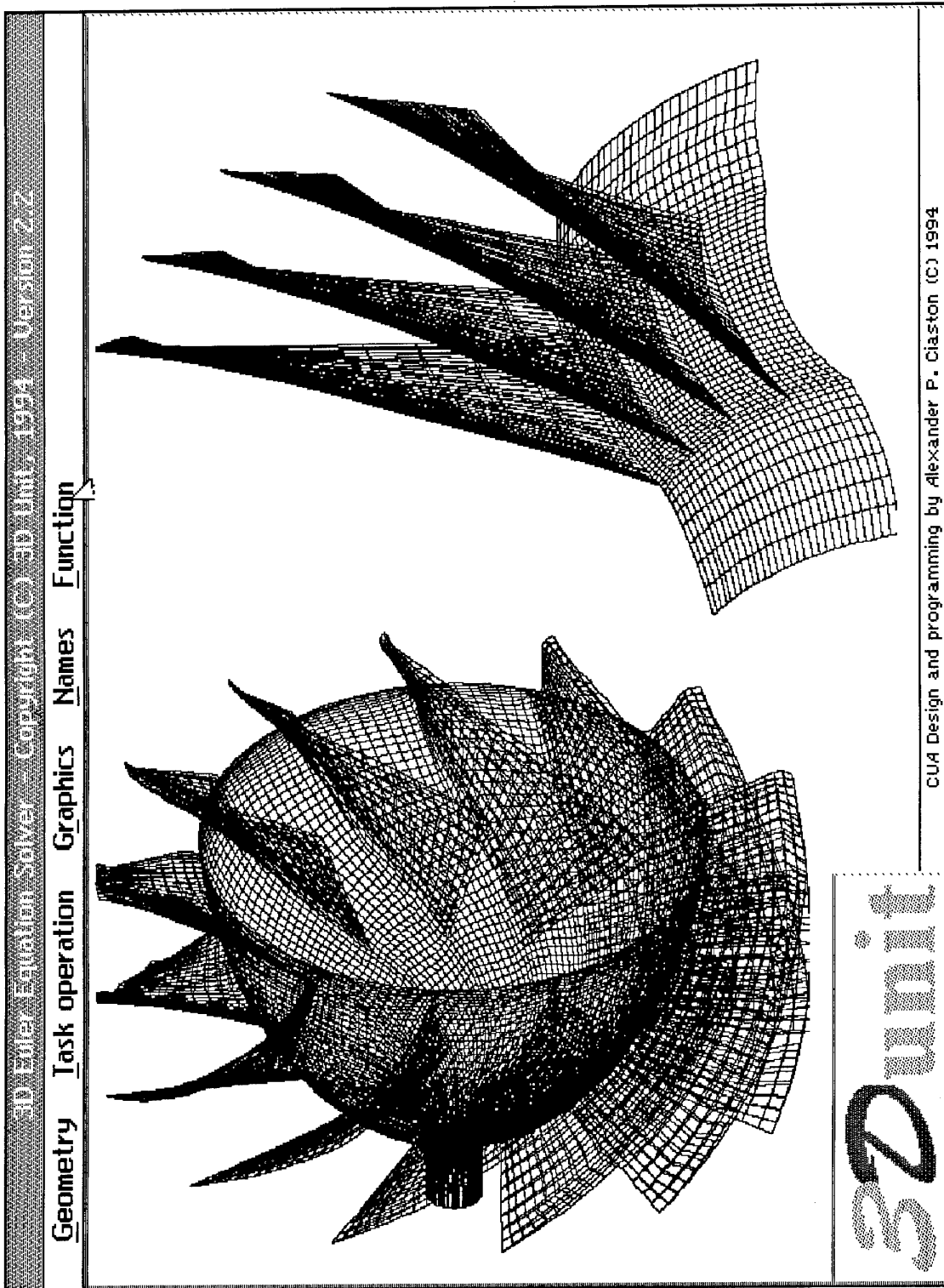
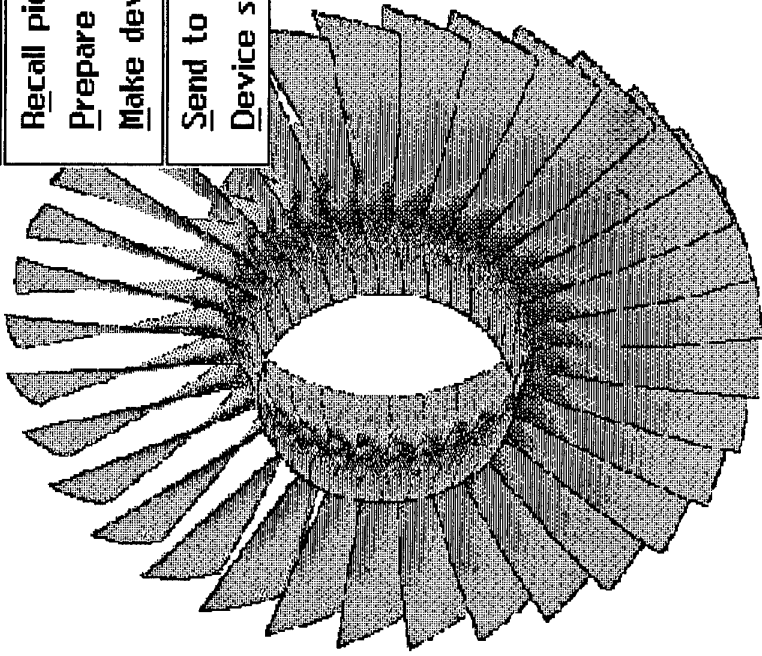


Fig. 6.7 Grid examples

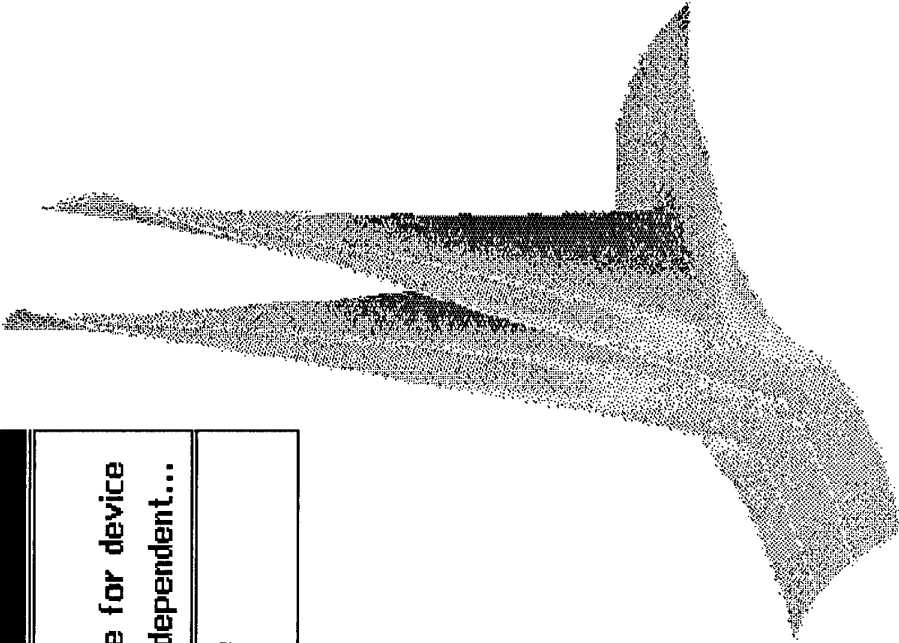
Geometry Task operation Graphics Names Function

Run graphics

- Recall picture
- Prepare picture for device
- Make device independent...
- Send to device
- Device setup



3D unit



CUA Design and programming by Alexander P. Claxton (C) 1994

Fig. 8.9 Analysis of numerical results: pressure distribution

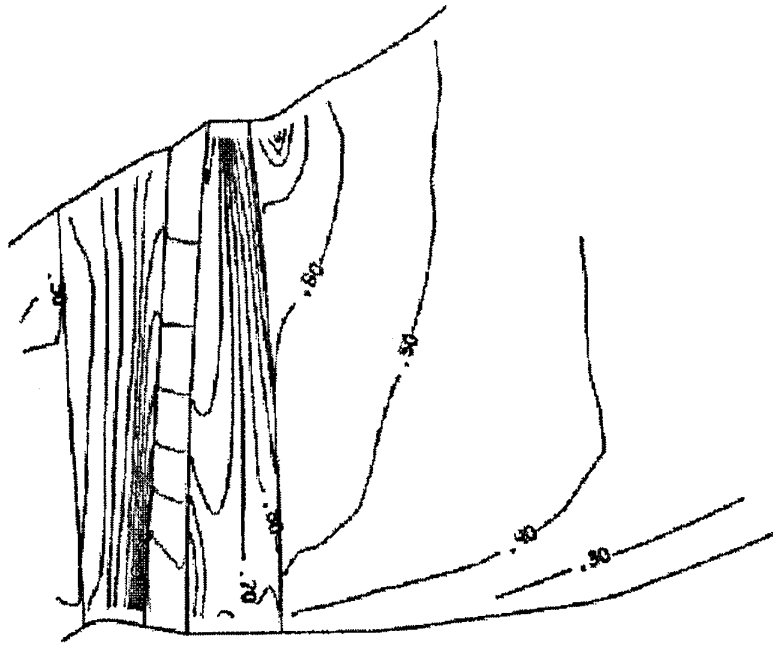


Fig. 10 Mach number contour lines on suction side for the initial variant of last stage of steam turbine.

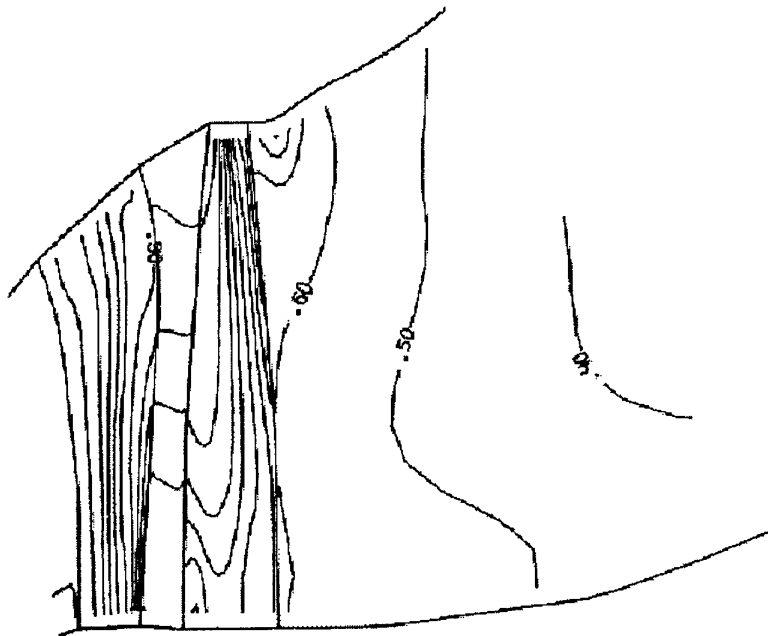


Fig. 11 Mach number contour lines on suction side. Modified variant.

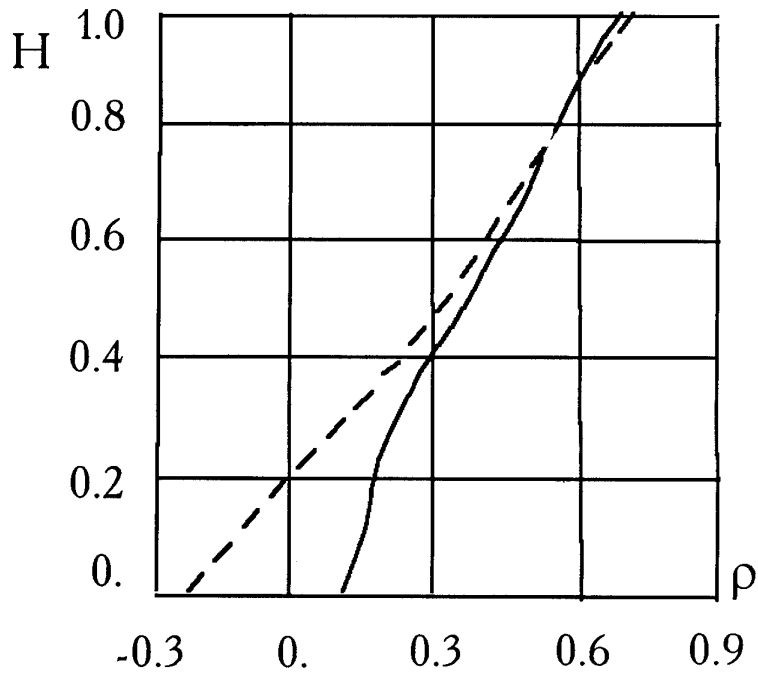


Fig. 12 Reaction distribution from hub to tip for major regime:
 - - - initial stage
 - - - modified stage

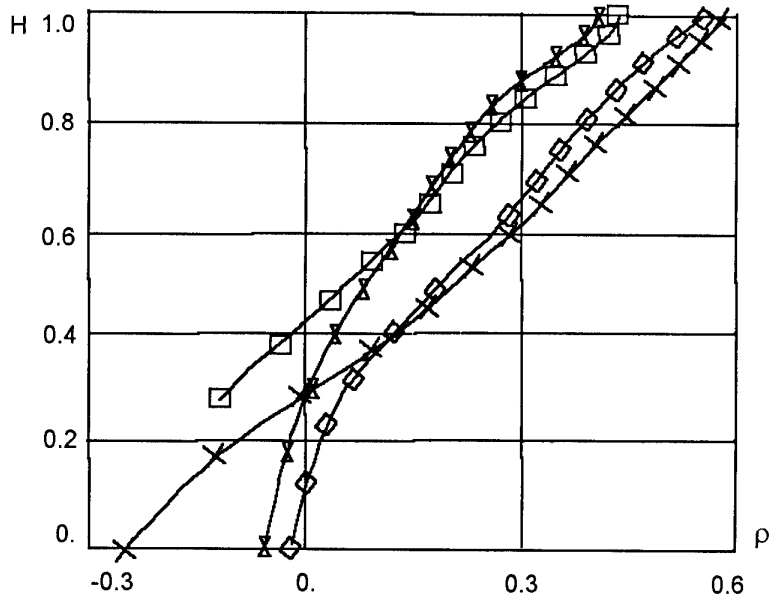


Fig. 13 Reaction distribution from hub to tip for partial regimes:

\times $\bar{G} = 0.75$ } the initial stage
 \square $\bar{G} = 0.5$ }
 \diamond $\bar{G} = 0.75$ } the modified stage
 \times $\bar{G} = 0.5$ }

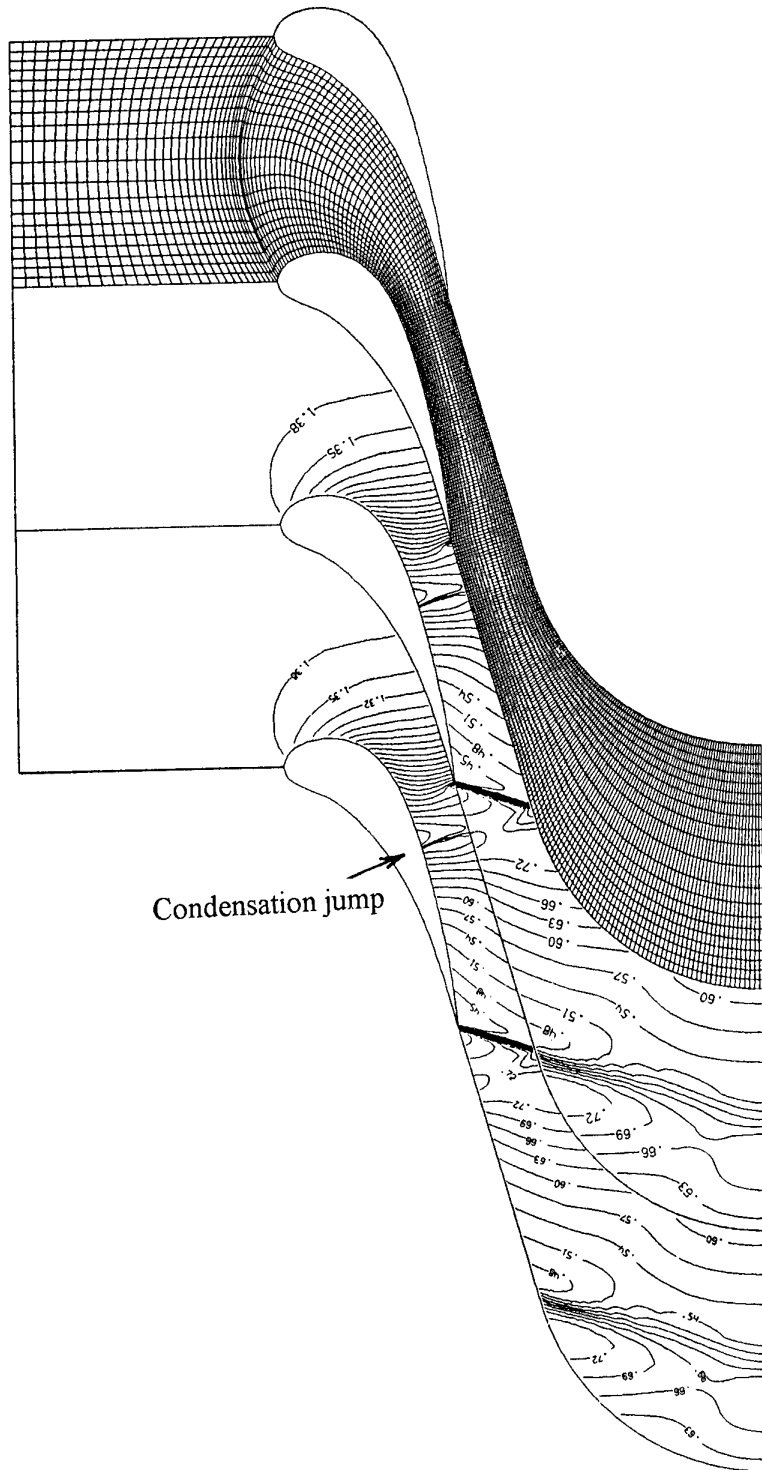


Fig. 14 Steam flow in cascade C-9012A. Pressure contour lines ($\Delta p = 0.02$), $M_2 = 1.2$

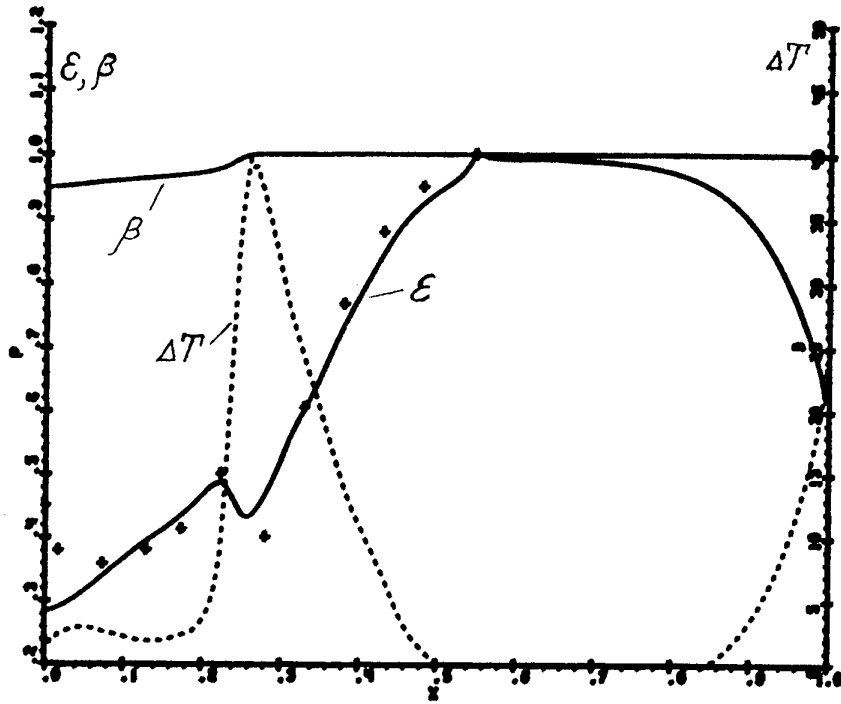


Fig. 15 Cascade surface pressure distribution $\varepsilon = p/p_0$:

----- calculation results
 + experimental results.

Distributions overcooling degree ΔT and rate of vapour β .

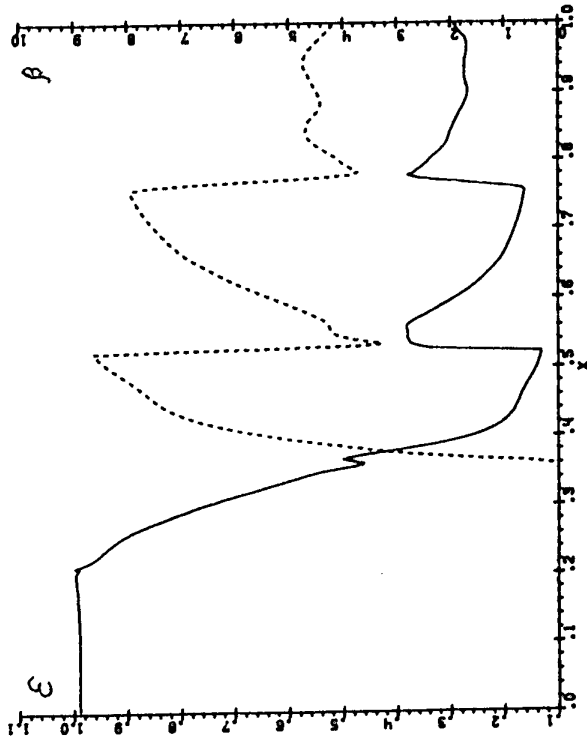
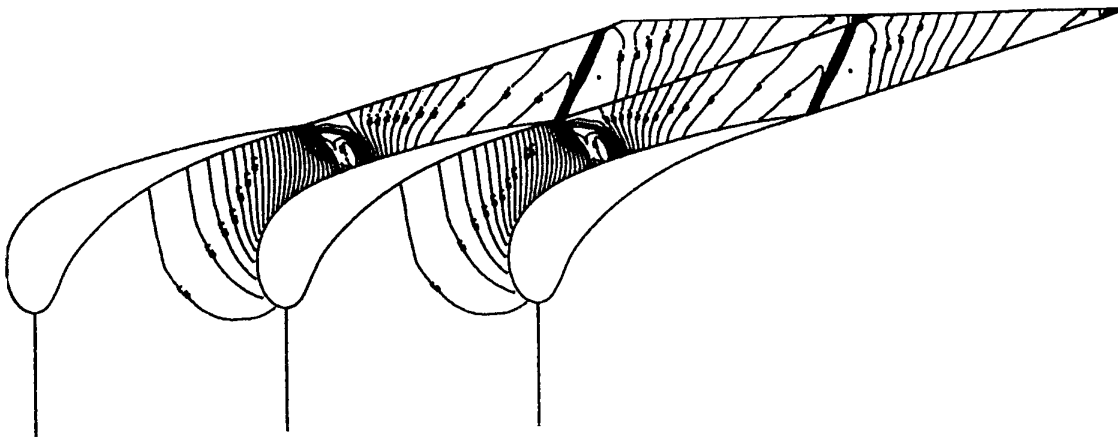


Fig. 16 (a) Pressure contour lines for $M_2 = 1.6$.
(b) Distributions pressure ϵ (solid line) and rate of vapour β (dotted line) along the suction side and the line of periodicity.

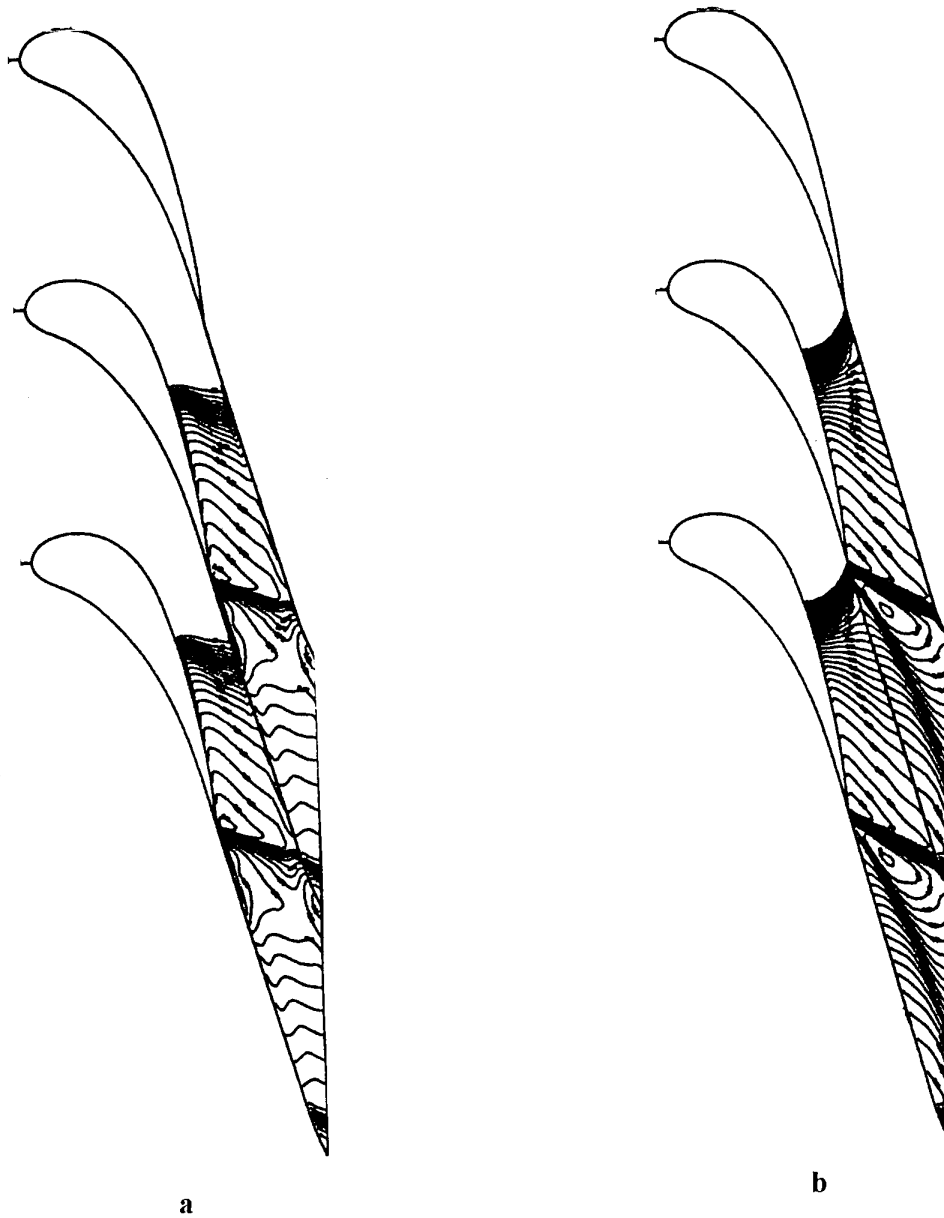
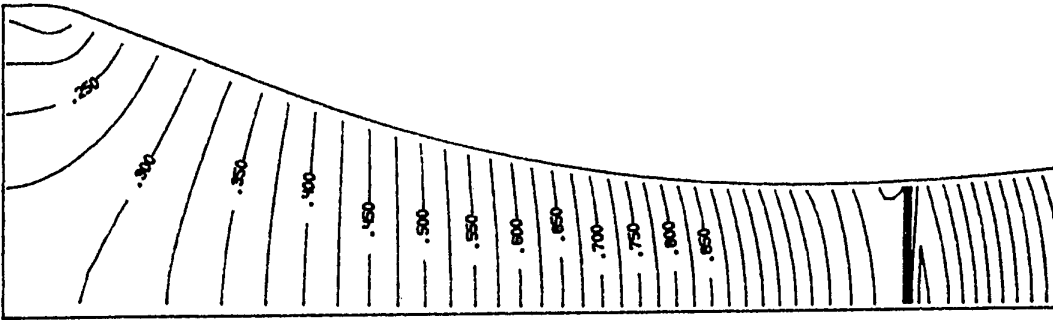
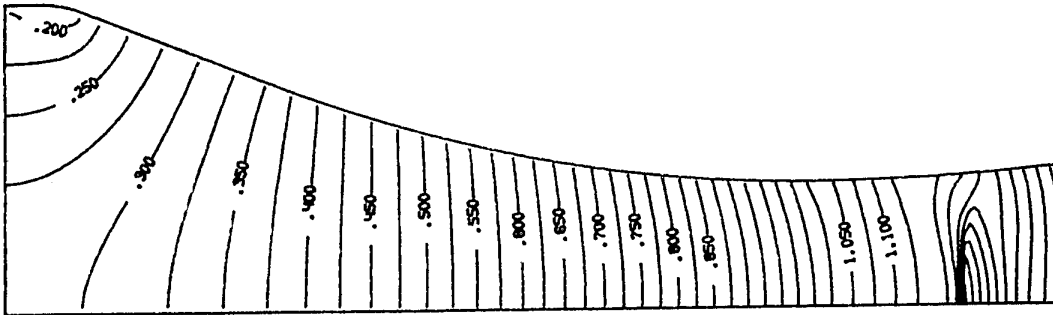


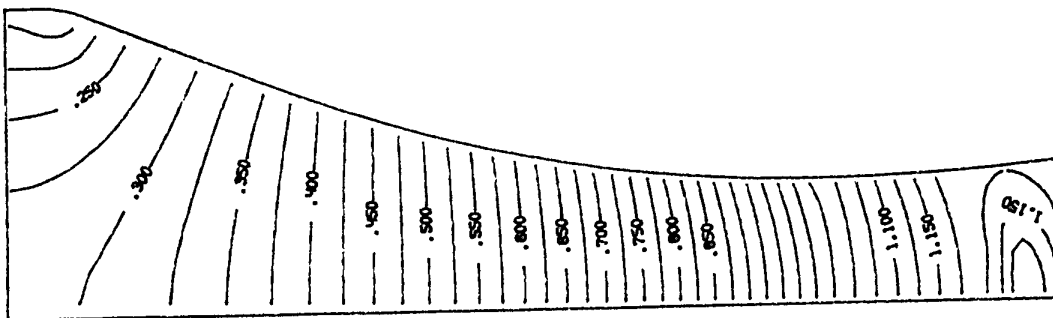
Fig. 17 Vapour mass concentration contour lines:
a) $M_2 = 1.2$, b) $M_2 = 1.6$



a



b



c

Fig. 18 Steam flow in nozzle:
 a) $T_0 = 370\text{ K}$, b) $T_0 = 373\text{ K}$ c) $T_0 = 377\text{ K}$

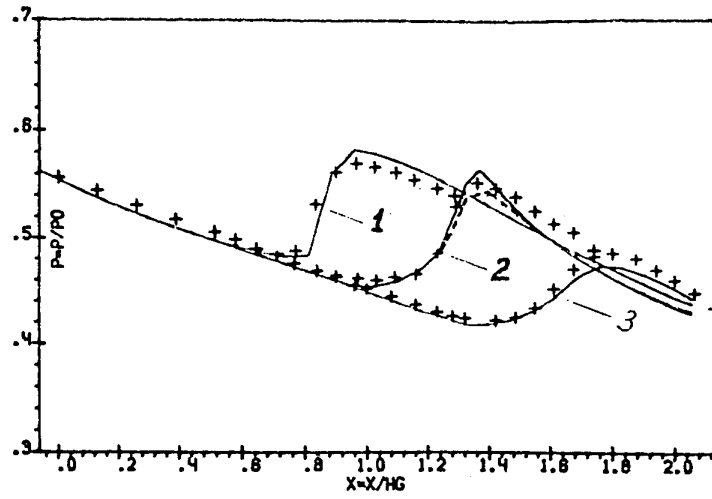


Fig. 19 Pressure distributions for regime 1,2,3:
----- numerical results
+++++ experimental data [9].

REPORT DOCUMENTATION PAGE

1. Recipient's Reference	2. Originator's Reference AGARD-LS-198	3. Further Reference ISBN 92-836-1008-3	4. Security Classification of Document UNCLASSIFIED
5. Originator	Advisory Group for Aerospace Research and Development North Atlantic Treaty Organization 7 rue Ancelle, 92200 Neuilly-sur-Seine, France		
6. Title	Mathematical Models of Gas Turbine Engines and their Components.		
7. Presented on	7-8 December 1994 in Cleveland, USA, 12-13 December 1994 in Wessling, Germany, and 15-16 December 1994 in Paris, France.		
8. Author(s)/Editor(s) Multiple	9. Date December 1994		
10. Author's/Editor's Address Multiple	11. Pages 192		
12. Distribution Statement	There are no restrictions on the distribution of this document. Information about the availability of this and other AGARD unclassified publications is given on the back cover.		
13. Keywords/Descriptors	Aircraft engines Gas turbine engines Components Mathematical models Aerodynamics Jet propulsion Numerical analysis Experimental data Thermal stresses		
14. Abstract	<p>This Lecture Series will present and discuss the scientific problems of modern mathematical simulation of gas turbine engines and their components.</p> <p>Some peculiarities of complex multicomponent and multidisciplinary models for whole flow passage of bypass gas turbine engine, core, multistage compressors and turbines, and other engine components will be studied.</p> <p>Solutions of steady and unsteady problems are given using high efficiency monotone numerical methods and the theoretical bases of these methods are presented.</p> <p>Many practical results of aerodynamic and thermostress simulations for engine components are shown. These results are compared widely with experimental data for accurate verification of developing computational codes.</p> <p>This Lecture Series, endorsed by the Propulsion and Energetics Panel of AGARD, has been implemented by the Technology Cooperation Programme.</p>		

<p>AGARD-LS-198 Advisory Group for Aerospace Research and Development North Atlantic Treaty Organization MATHEMATICAL MODELS OF GAS TURBINE ENGINES AND THEIR COMPONENTS Published December 1994 192 pages</p> <p>This Lecture Series will present and discuss the scientific problems of modern mathematical simulation of gas turbine engines and their components.</p> <p>Some peculiarities of complex multicomponent and multidisciplinary models for whole flow passage of bypass gas turbine engine, core, multistage compressors and turbines, and other engine components will be studied.</p>	<p>AGARD-LS-198</p> <p>Aircraft engines Gas turbine engines Components Mathematical models Aerodynamics Jet propulsion Numerical analysis Experimental data Thermal stresses</p>	<p>AGARD-LS-198 Advisory Group for Aerospace Research and Development North Atlantic Treaty Organization MATHEMATICAL MODELS OF GAS TURBINE ENGINES AND THEIR COMPONENTS Published December 1994 192 pages</p> <p>This Lecture Series will present and discuss the scientific problems of modern mathematical simulation of gas turbine engines and their components.</p> <p>Some peculiarities of complex multicomponent and multidisciplinary models for whole flow passage of bypass gas turbine engine, core, multistage compressors and turbines, and other engine components will be studied.</p>	<p>AGARD-LS-198</p> <p>Aircraft engines Gas turbine engines Components Mathematical models Aerodynamics Jet propulsion Numerical analysis Experimental data Thermal stresses</p>
<p>AGARD-LS-198 Advisory Group for Aerospace Research and Development North Atlantic Treaty Organization MATHEMATICAL MODELS OF GAS TURBINE ENGINES AND THEIR COMPONENTS Published December 1994 192 pages</p> <p>This Lecture Series will present and discuss the scientific problems of modern mathematical simulation of gas turbine engines and their components.</p> <p>Some peculiarities of complex multicomponent and multidisciplinary models for whole flow passage of bypass gas turbine engine, core, multistage compressors and turbines, and other engine components will be studied.</p>	<p>AGARD-LS-198</p> <p>Aircraft engines Gas turbine engines Components Mathematical models Aerodynamics Jet propulsion Numerical analysis Experimental data Thermal stresses</p>	<p>AGARD-LS-198 Advisory Group for Aerospace Research and Development North Atlantic Treaty Organization MATHEMATICAL MODELS OF GAS TURBINE ENGINES AND THEIR COMPONENTS Published December 1994 192 pages</p> <p>This Lecture Series will present and discuss the scientific problems of modern mathematical simulation of gas turbine engines and their components.</p> <p>Some peculiarities of complex multicomponent and multidisciplinary models for whole flow passage of bypass gas turbine engine, core, multistage compressors and turbines, and other engine components will be studied.</p>	<p>AGARD-LS-198</p> <p>Aircraft engines Gas turbine engines Components Mathematical models Aerodynamics Jet propulsion Numerical analysis Experimental data Thermal stresses</p>

<p>AGARD-LS-198 Advisory Group for Aerospace Research and Development North Atlantic Treaty Organization MATHEMATICAL MODELS OF GAS TURBINE ENGINES AND THEIR COMPONENTS Published December 1994 192 pages</p>	<p>AGARD-LS-198</p> <p>Aircraft engines Gas turbine engines Components Mathematical models Aerodynamics Jet propulsion Numerical analysis Experimental data Thermal stresses</p>	<p>AGARD-LS-198 Advisory Group for Aerospace Research and Development North Atlantic Treaty Organization MATHEMATICAL MODELS OF GAS TURBINE ENGINES AND THEIR COMPONENTS Published December 1994 192 pages</p>	<p>AGARD-LS-198</p> <p>Aircraft engines Gas turbine engines Components Mathematical models Aerodynamics Jet propulsion Numerical analysis Experimental data Thermal stresses</p>
<p>This Lecture Series will present and discuss the scientific problems of modern mathematical simulation of gas turbine engines and their components. Some peculiarities of complex multicomponent and multidisciplinary models for whole flow passage of bypass gas turbine engine, core, multistage compressors and turbines, and other engine components will be studied.</p>	<p>This Lecture Series will present and discuss the scientific problems of modern mathematical simulation of gas turbine engines and their components. Some peculiarities of complex multicomponent and multidisciplinary models for whole flow passage of bypass gas turbine engine, core, multistage compressors and turbines, and other engine components will be studied.</p>	<p>This Lecture Series will present and discuss the scientific problems of modern mathematical simulation of gas turbine engines and their components. Some peculiarities of complex multicomponent and multidisciplinary models for whole flow passage of bypass gas turbine engine, core, multistage compressors and turbines, and other engine components will be studied.</p>	<p>This Lecture Series will present and discuss the scientific problems of modern mathematical simulation of gas turbine engines and their components. Some peculiarities of complex multicomponent and multidisciplinary models for whole flow passage of bypass gas turbine engine, core, multistage compressors and turbines, and other engine components will be studied.</p>
<p>AGARD-LS-198 Advisory Group for Aerospace Research and Development North Atlantic Treaty Organization MATHEMATICAL MODELS OF GAS TURBINE ENGINES AND THEIR COMPONENTS Published December 1994 192 pages</p> <p>This Lecture Series will present and discuss the scientific problems of modern mathematical simulation of gas turbine engines and their components. Some peculiarities of complex multicomponent and multidisciplinary models for whole flow passage of bypass gas turbine engine, core, multistage compressors and turbines, and other engine components will be studied.</p>	<p>AGARD-LS-198</p> <p>Aircraft engines Gas turbine engines Components Mathematical models Aerodynamics Jet propulsion Numerical analysis Experimental data Thermal stresses</p>	<p>AGARD-LS-198 Advisory Group for Aerospace Research and Development North Atlantic Treaty Organization MATHEMATICAL MODELS OF GAS TURBINE ENGINES AND THEIR COMPONENTS Published December 1994 192 pages</p> <p>This Lecture Series will present and discuss the scientific problems of modern mathematical simulation of gas turbine engines and their components. Some peculiarities of complex multicomponent and multidisciplinary models for whole flow passage of bypass gas turbine engine, core, multistage compressors and turbines, and other engine components will be studied.</p>	<p>AGARD-LS-198</p> <p>Aircraft engines Gas turbine engines Components Mathematical models Aerodynamics Jet propulsion Numerical analysis Experimental data Thermal stresses</p>

<p>Solutions of steady and unsteady problems are given using high efficiency monotone numerical methods and the theoretical bases of these methods are presented.</p> <p>Many practical results of aerodynamic and thermostress simulations for engine components are shown. These results are compared widely with experimental data for accurate verification of developing computational codes.</p> <p>This Lecture Series, endorsed by the Propulsion and Energetics Panel of AGARD, has been implemented by the Technology Cooperation Programme.</p> <p>ISBN 92-836-1008-3</p>	<p>Solutions of steady and unsteady problems are given using high efficiency monotone numerical methods and the theoretical bases of these methods are presented.</p> <p>Many practical results of aerodynamic and thermostress simulations for engine components are shown. These results are compared widely with experimental data for accurate verification of developing computational codes.</p> <p>This Lecture Series, endorsed by the Propulsion and Energetics Panel of AGARD, has been implemented by the Technology Cooperation Programme.</p> <p>ISBN 92-836-1008-3</p>
<p>Solutions of steady and unsteady problems are given using high efficiency monotone numerical methods and the theoretical bases of these methods are presented.</p> <p>Many practical results of aerodynamic and thermostress simulations for engine components are shown. These results are compared widely with experimental data for accurate verification of developing computational codes.</p> <p>This Lecture Series, endorsed by the Propulsion and Energetics Panel of AGARD, has been implemented by the Technology Cooperation Programme.</p> <p>ISBN 92-836-1008-3</p>	<p>Solutions of steady and unsteady problems are given using high efficiency monotone numerical methods and the theoretical bases of these methods are presented.</p> <p>Many practical results of aerodynamic and thermostress simulations for engine components are shown. These results are compared widely with experimental data for accurate verification of developing computational codes.</p> <p>This Lecture Series, endorsed by the Propulsion and Energetics Panel of AGARD, has been implemented by the Technology Cooperation Programme.</p> <p>ISBN 92-836-1008-3</p>

Aucun stock de publications n'a existé à AGARD. A partir de 1993, AGARD détient un stock limité des publications associées aux cycles de conférences et cours spéciaux ainsi que les AGARDographies et les rapports des groupes de travail, organisés et publiés à partir de 1993 inclus. Les demandes de renseignements doivent être adressées à AGARD par lettre ou par fax à l'adresse indiquée ci-dessus. *Veuillez ne pas téléphoner.* La diffusion initiale de toutes les publications de l'AGARD est effectuée auprès des pays membres de l'OTAN par l'intermédiaire des centres de distribution nationaux indiqués ci-dessous. Des exemplaires supplémentaires peuvent parfois être obtenus auprès de ces centres (à l'exception des Etats-Unis). Si vous souhaitez recevoir toutes les publications de l'AGARD, ou simplement celles qui concernent certains Panels, vous pouvez demander à être inclut sur la liste d'envoi de l'un de ces centres. Les publications de l'AGARD sont en vente auprès des agences indiquées ci-dessous, sous forme de photocopie ou de microfiche.

CENTRES DE DIFFUSION NATIONAUX

ALLEMAGNE

Fachinformationszentrum,
Karlsruhe
D-76344 Eggenstein-Leopoldshafen 2

BELGIQUE

Coordonnateur AGARD-VSL
Etat-major de la Force aérienne
Quartier Reine Elisabeth
Rue d'Evere, 1140 Bruxelles

CANADA

Directeur, Services d'information scientifique
Ministère de la Défense nationale
Ottawa, Ontario K1A 0K2

DANEMARK

Danish Defence Research Establishment
Ryvangs Allé 1
P.O. Box 2715
DK-2100 Copenhagen Ø

ESPAGNE

INTA (AGARD Publications)
Pintor Rosales 34
28008 Madrid

ETATS-UNIS

NASA Headquarters
Code JOB-1
Washington, D.C. 20546

FRANCE

O.N.E.R.A. (Direction)
29, Avenue de la Division Leclerc
92322 Châtillon Cedex

GRECE

Hellenic Air Force
Air War College
Scientific and Technical Library
Dekelia Air Force Base
Dekelia, Athens TGA 1010

ISLANDE

Director of Aviation
c/o Flugrad
Reykjavik

ITALIE

Aeronautica Militare
Ufficio del Delegato Nazionale all'AGARD
Aeroporto Pratica di Mare
00040 Pomezia (Roma)

LUXEMBOURG

Voir Belgique

NORVEGE

Norwegian Defence Research Establishment
Attn: Biblioteket
P.O. Box 25
N-2007 Kjeller

PAYS-BAS

Netherlands Delegation to AGARD
National Aerospace Laboratory NLR
P.O. Box 90502
1006 BM Amsterdam

PORTUGAL

Força Aérea Portuguesa
Centro de Documentação e Informação
Alfragide
2700 Amadora

ROYAUME-UNI

Defence Research Information Centre
Kentigern House
65 Brown Street
Glasgow G2 8EX

TURQUIE

Millî Savunma Başkanlığı (MSB)
ARGE Dairesi Başkanlığı (MSB)
06650 Bakanlıklar-Ankara

Le centre de distribution national des Etats-Unis ne détient PAS de stocks des publications de l'AGARD.

D'éventuelles demandes de photocopies doivent être formulées directement auprès du NASA Center for AeroSpace Information (CASI) à l'adresse ci-dessous. Toute notification de changement d'adresse doit être fait également auprès de CASI.

AGENCES DE VENTE

NASA Center for
AeroSpace Information (CASI)
800 Elkridge Landing Road
Linthicum Heights, MD 21090-2934
Etats-Unis

ESA/Information Retrieval Service
European Space Agency
10, rue Mario Nikis
75015 Paris
France

The British Library
Document Supply Division
Boston Spa, Wetherby
West Yorkshire LS23 7BQ
Royaume-Uni

Les demandes de microfiches ou de photocopies de documents AGARD (y compris les demandes faites auprès du CASI) doivent comporter la dénomination AGARD, ainsi que le numéro de série d'AGARD (par exemple AGARD-AG-315). Des informations analogues, telles que le titre et la date de publication sont souhaitables. Veuillez noter qu'il y a lieu de spécifier AGARD-R-nnn et AGARD-AR-nnn lors de la commande des rapports AGARD et des rapports consultatifs AGARD respectivement. Des références bibliographiques complètes ainsi que des résumés des publications AGARD figurent dans les journaux suivants:

Scientific and Technical Aerospace Reports (STAR)
publié par la NASA Scientific and Technical
Information Division
NASA Headquarters (JTT)
Washington D.C. 20546
Etats-Unis

Government Reports Announcements and Index (GRA&I)
publié par le National Technical Information Service
Springfield
Virginia 22161
Etats-Unis
(accessible également en mode interactif dans la base de
données bibliographiques en ligne du NTIS, et sur CD-ROM)



AGARD holds limited quantities of the publications that accompanied Lecture Series and Special Courses held in 1993 or later, and of AGARDographs and Working Group reports published from 1993 onward. For details, write or send a telefax to the address given above. *Please do not telephone.*

AGARD does not hold stocks of publications that accompanied earlier Lecture Series or Courses or of any other publications. Initial distribution of all AGARD publications is made to NATO nations through the National Distribution Centres listed below. Further copies are sometimes available from these centres (except in the United States). If you have a need to receive all AGARD publications, or just those relating to one or more specific AGARD Panels, they may be willing to include you (or your organisation) on their distribution list. AGARD publications may be purchased from the Sales Agencies listed below, in photocopy or microfiche form.

NATIONAL DISTRIBUTION CENTRES

BELGIUM

Coordonnateur AGARD — VSL
Etat-major de la Force aérienne
Quartier Reine Elisabeth
Rue d'Evere, 1140 Bruxelles

CANADA

Director Scientific Information Services
Dept of National Defence
Ottawa, Ontario K1A 0K2

DENMARK

Danish Defence Research Establishment
Ryvangs Allé 1
P.O. Box 2715
DK-2100 Copenhagen Ø

FRANCE

O.N.E.R.A. (Direction)
29 Avenue de la Division Leclerc
92322 Châtillon Cedex

GERMANY

Fachinformationszentrum
Karlsruhe
D-76344 Eggenstein-Leopoldshafen 2

GREECE

Hellenic Air Force
Air War College
Scientific and Technical Library
Dekelia Air Force Base
Dekelia, Athens TGA 1010

ICELAND

Director of Aviation
c/o Flugrad
Reykjavik

ITALY

Aeronautica Militare
Ufficio del Delegato Nazionale all'AGARD
Aeroporto Pratica di Mare
00040 Pomezia (Roma)

LUXEMBOURG

See Belgium

NETHERLANDS

Netherlands Delegation to AGARD
National Aerospace Laboratory, NLR
P.O. Box 90502
1006 BM Amsterdam

NORWAY

Norwegian Defence Research Establishment
Attn: Biblioteket
P.O. Box 25
N-2007 Kjeller

PORTUGAL

Força Aérea Portuguesa
Centro de Documentação e Informação
Alfragide
2700 Amadora

SPAIN

INTA (AGARD Publications)
Pintor Rosales 34
28008 Madrid

TURKEY

Millî Savunma Başkanlığı (MSB)
ARGE Dairesi Başkanlığı (MSB)
06650 Bakanlıklar-Ankara

UNITED KINGDOM

Defence Research Information Centre
Kentigern House
65 Brown Street
Glasgow G2 8EX

UNITED STATES

NASA Headquarters
Code JOB-1
Washington, D.C. 20546

The United States National Distribution Centre does NOT hold stocks of AGARD publications.

Applications for copies should be made direct to the NASA Center for AeroSpace Information (CASI) at the address below. Change of address requests should also go to CASI.

SALES AGENCIES

NASA Center for
AeroSpace Information (CASI)
800 Elkridge Landing Road
Linthicum Heights, MD 21090-2934
United States

ESA/Information Retrieval Service
European Space Agency
10, rue Mario Nikis
75015 Paris
France

The British Library
Document Supply Centre
Boston Spa, Wetherby
West Yorkshire LS23 7BQ
United Kingdom

Requests for microfiches or photocopies of AGARD documents (including requests to CASI) should include the word 'AGARD' and the AGARD serial number (for example AGARD-AG-315). Collateral information such as title and publication date is desirable. Note that AGARD Reports and Advisory Reports should be specified as AGARD-R-*nnn* and AGARD-AR-*nnn*, respectively. Full bibliographical references and abstracts of AGARD publications are given in the following journals:

Scientific and Technical Aerospace Reports (STAR)
published by NASA Scientific and Technical
Information Division
NASA Headquarters (JTT)
Washington D.C. 20546
United States

Government Reports Announcements and Index (GRA&I)
published by the National Technical Information Service
Springfield
Virginia 22161
United States
(also available online in the NTIS Bibliographic
Database or on CD-ROM)

